Design and Verification of a Controlled Induced Mass Flow System

Alesha Saligram

A dissertation submitted to the Faculty of Engineering and the Built Environment, University of the Witwatersrand, Johannesburg, in fulfilment of the requirements for the degree of Master of Science in Engineering

27 March 2018

ABSTRACT

The Medium Speed Wind Tunnel (MSWT) of the Aeronautic Systems Competency (ASC) within the Council for Scientific and Industrial Research (CSIR) performs majority static stability wind tunnel testing. The facility does not have an active inlet simulation capability, or a pressure system to support such a capability. Airframes with air breathing engines are tested with inlets either covered with fairings or left open to operate in a passive mode. To expand the wind tunnel offerings to include an inlet test capability, an active inlet flow induction and metering system was required. An ejector driven duct was designed to provide simulated engine air flow at rates and conditions appropriate for the MSWT size and operating envelope. Integral to the design was a mass flow metering system featuring a translating conical plug. To reduce the risk and size footprint the ejector unit comprised 14 ejectors clustered around a hollow central core housing the mass flow plug support and drive system. The ESDU 92042 software was utilised as the design tool to develop the ejector geometry and Computational Fluid Dynamics (CFD) was employed as a verification and off-design performance prediction tool. The entrained mass flow rate predicted by the CFD model for the 14-ejector unit exceeded the predicted entrained mass flow rate determined by the ESDU 92042 software. Experimental tests were performed to determine the actual entrained mass flow rate of a single ejector in order to verify the design predictions of the CFD model. The maximum entrained mass flow rate determined from the experiment is greater than the maximum entrained mass flow rate predicted by the CFD model. The CFD model over-predicts the entrained mass flow rates of the ejector in the sub-critical mode and will envisage it to under-predict the entrained mass flow rates in the critical mode. The experimental results for the single ejector suggest that the designed operating envelope predicted for the parallel arrangement of 14 ejectors should be reached.

DECLARATION

I declare that this dissertation is my own unaided work, except where otherwise acknowledged. It is being submitted in fulfilment of the requirements for the degree of Master of Science in Engineering to the University of the Witwatersrand, Johannesburg. It has not been submitted before for any degree or examination to any other University.

Alesha Saligram

27 March 2018

CONTENTS

LIST OF FIGURES

LIST OF TABLES

LIST OF SYMBOLS

$\alpha\varepsilon$	Compound coefficient
β	Diameter ratio
β_c	Blockage correction factor
γ	Ratio of specific heats for air
δ_1^*/R_1	Boundary-layer displacement thickness
Δp	Differential pressure between static pressure of the conical inlet and atmospheric pressure
ΔP	Pressure drop
ε	Expansion ratio
2θ	Total diffuser expansion angle
θ_E	Exit angle
θ_N	Initial wall angle
μ	Dynamic viscosity
ρ	Fluid density
ρ_u	Upstream density
ϕ	Area ratio of enlargement
a_t	Speed of sound
A	Area
A_R	Ratio of the diffuser exit area to inlet area
A_s	Surface area
A^*	Throat area
A/A^*	Area ratio
C	Sutherland's constant
C_1	Geometry factors for laminar flow
$C_0, C_1 \dots C_{14}$	Coefficients
C_d	Discharge coefficient

C_t	Geometry factors for turbulent flows
C_{Df}	Free-air drag coefficient
e	Gas expansivity
E	Nozzle exit
ϵ/d	Relative roughness of the inner wall
f	Friction factor
G	Fluid mass velocity
h	Distance between radius
k	Velocity profile correction ratio
K	Length fraction of an ideal 15° conical nozzle
K_d	Diffuser loss factor
K_t	Total-pressure loss coefficient
L	Length of the channel between two pressure measurements
L_N	Nozzle length
m	Wake expansion factor
$\dot{m}$	Mass flow rate
$\dot{m}_c$	Corrected mass flow rate
$\dot{m}_p$	Primary stream mass flow rate
$\ddot{m}$	Secondary stream mass flow rate
M	Mach number
M_x	Supersonic Mach number before the shock
M_y	Subsonic Mach number after the shock
P_s	Static pressure
P_t	Total pressure
P_{t0}	Secondary stream pressure
P_{t1}	Primary stream pressure
P_{tx}	Stagnation pressure before shock
P_{ty}	Stagnation pressure after shock

P_{t1}/P_{t5}	Primary pressure ratio
P_{t5}/P_{t0}	Secondary pressure ratio
q	Dynamic pressure
q_m	Mass flow rate
Q	Volumetric flowrate
r_c	Circular arc radius
r_m	Secondary to primary mass flow ratio
R	Specific gas constant
R_1	Base radius
R_2	Top radius
Re	Reynolds number
R_E	Exit radius
R_t	Radius of the nozzle throat
s	Slant height
S	Frontal area of the body
T	Temperature
T_s	Static temperature
V	Velocity

1. INTRODUCTION

1.1 Research Background

Inlet tests form part of the integration process of an airframe and a propulsion system. The rated performance of a propulsion system is only achievable within a defined operating envelope that is expressed in terms of the quality of the airflow being delivered to the unit. The ideal uniform flow profile is distorted in terms of the total pressure distribution and degree of rotation (swirl) in the flow. These irregularities in the flow are produced by the interaction of the inlet flow with the external airframe and the duct leading to the engine. Significant inlet distortion levels lead to degraded performance of the engine and eventual surge or propulsion failure [1]. An inlet test is performed to quantify the distortion levels that are induced by a particular airframe and inlet duct combination. Appropriate matching of the results from such a test and the performance tests of the engine under similar conditions are required for the successful integration of an airframe and its propulsion system.

1.2 Research Motivation

Subsonic inlet testing has been performed at the Council for Scientific and Industrial Research (CSIR) with flow induction systems. Wind tunnel testing at the Medium Speed Wind Tunnel (MSWT) has been applied to static aerodynamic coefficient testing of airframes and airframe components. No attempts were made to simulate propulsion effects and any effects these may have on the aerodynamic measurements. In the case of air breathing propulsion systems, measures were taken to artificially cover the inlet region by a fairing in a way to cause minimal disturbance to the surrounding region. With no demand for modelling these effects, no augmented inlet flow simulation capability was developed for the MSWT. However, recently there has been a growing interest in the potential application of the MSWT to aerodynamic inlet flow simulations [1].

1.3 Objectives

- Design a mass flow quantity metering system that will allow for accurate control and measurement of airflow through an inlet for the Medium Speed Wind Tunnel conditions.
- A mass flow generation system should be designed to augment the required airflow through an inlet.
- The mass flow generation system should be able to perform at different angle of attacks in the Medium Speed Wind Tunnel.
- Computational Fluid Dynamics should be used as a verification and performance prediction tool to determine acceptable mass flow rates.
- Design and construction of an experimental test rig for the verification of the predicted computational results.

2. LITERATURE REVIEW

2.1 Inlet Test System

An inlet test system requires a mechanism to provide the required mass flow rate through the simulated inlet and some means of quantifying this flow rate. To accomplish this, two techniques have been utilized. The first technique is a long exhaust and measuring duct driven by a pressure sink such as an ejector, vacuum pump or vacuum chamber. The second technique employs a compact arrangement where a variable area mass flow device is operated in a choked mode via a close-coupled ejector.

The design of an inlet simulation system is not prescriptive and different approaches are undertaken by different test institutions. STARCS air inlet testing capability was developed for their transonic wind tunnel. They employed an inlet simulation system that used a ducted exhaust with a standard mass flow measurement system as illustrated in Figure 2-1.

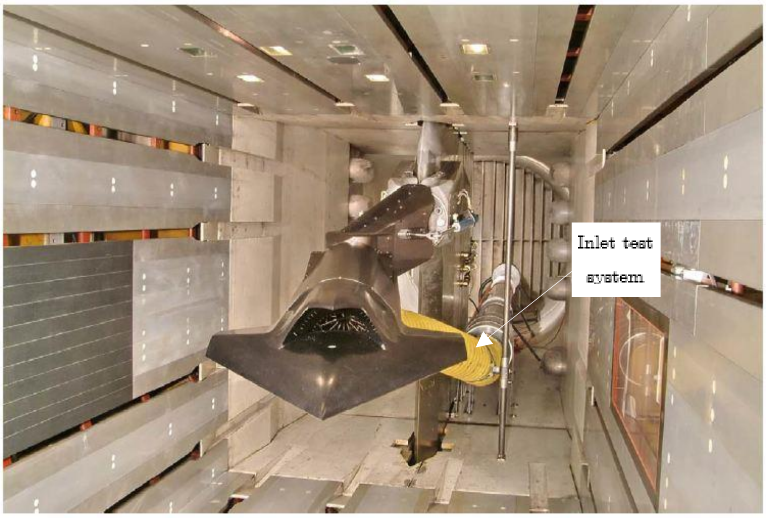

Figure 2-1 : STARCS air inlet testing capability in the transonic wind tunnel [2]

The different components that encompass their inlet test system are illustrated in Figure 2-2. A valve is used to control the air mass flow rate through the inlet. The air is then conditioned by a flow straightener and also by having a long onset distance with a straight pipe. The air mass flow rate measurement is accomplished by means of a venturi nozzle. An ejector is used to extract air through the inlet. This ejector is situated in the wind tunnel diffuser downstream of the choke section as illustrated in Figure 2-2. STARCS have designed and tested two different mass flow rate valves and several venturi nozzles for different mass flow rate regimes [2].

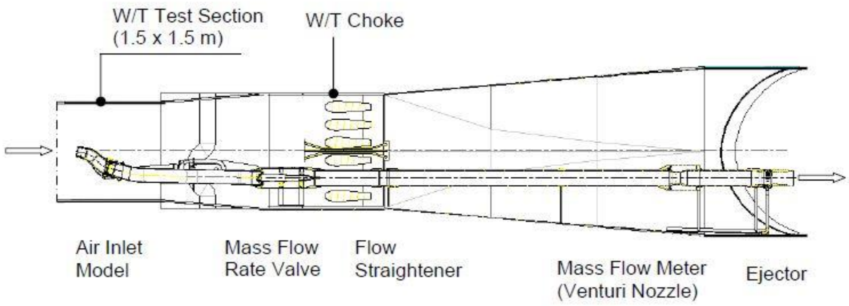

Figure 2-2 : Schematic of the air inlet test rig in the STARC transonic wind tunnel [2]

Standard mass flow measurement devices frequently require the inclusion of long upstream constant area ducting in order for the stated accuracy to be realised. Flow metering may be accomplished with an alternative system that is integral with the model, but in the ducted exhaust approach, a duct is still required to connect the model airflow duct to the pump device. The exhaust duct may be driven by a pump device located inside or outside of the tunnel. An arrangement like the one mentioned above presents undesirable additional structures, such as support bracing and piping, in the wind tunnel ducting increasing blockage and complicating model motion [1].

The second technique which uses a variable area mass flow device operated in a choked mode via a close-coupled ejector is the approach that is commonly undertaken. This technique has been applied in the transonic wind tunnels by Northrop, Calspan and National Aeronautics and Space Administration (NASA).

Northrop employs a plug valve system, illustrated in Figure 2-3, which is used for the metering and control of duct mass flows in wind tunnel inlet-airframe models. The plug valve system utilises the stability of choked flows which is accomplished by using a translating plug and an ejector system. The model houses the operating system which exhausts flow back into the tunnel circuit [3].

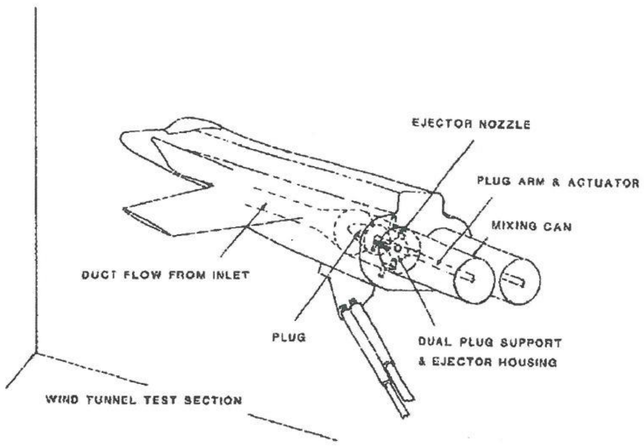

Figure 2-3: Inlet-airframe model with ejector augmented choking valve [3]

Inlet testing and research at the Calspan and the NASA Langley transonic wind tunnels employ a high pressure ejector and a mass flow plug to vary the airflow through the aircraft testing model. Their variable area mass flow device is the mass flow plug, whose position can be varied to allow for fine adjustments to the mass flow [4]. A compact inlet test arrangement in the Calspan transonic wind tunnel is illustrated in Figure 2-4 and the ejector mass flow system used at NASA is illustrated in Figure 2-5.

Figure 2-4 : Inlet test arrangement at the Calspan Transonic Wind Tunnel [4]

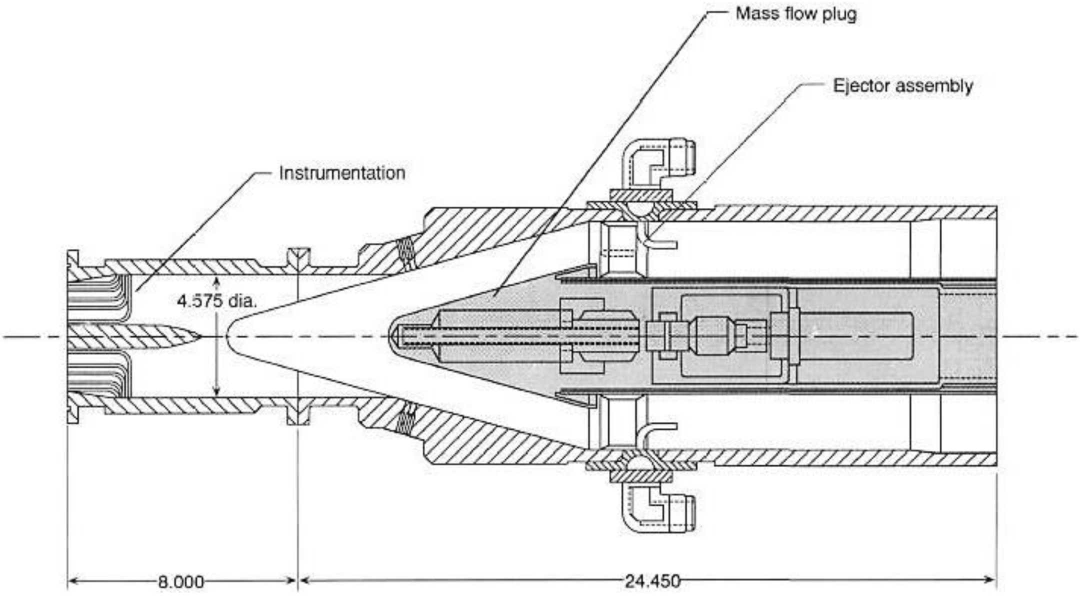

Figure 2-5 : Ejector mass flow system at NASA Langley (Dimensions are in inches) [5]

The compact arrangement of the above inlet test systems offers numerous advantages such as size, simpler support and potential inter-facility portability. This arrangement and technique is preferential for application in the Medium Speed Wind Tunnel (MSWT). An inlet test system fundamentally employs a mass flow generation system and a flow quantity and quality metering system. These systems will be discussed further more in the subsequent sections.

2.1.1 Mass Flow Generation System

Inlet test systems require a system to provide or augment the required airflow through an inlet under investigation over a range of test conditions. Wind tunnel test that are conducted at high Mach numbers may provide sufficient energy to drive air through an inlet system. However, at low Mach numbers there is insufficient pressure ratio across the inlet system to induce the desired airflow [6]. A high-pressure air-powered ejector is employed to provide or augment the required airflow through the inlet at the low Mach numbers.

2.1.1.1 Ejectors

Ejectors are devices that utilise a high energy fluid stream to entrain and accelerate a low energy fluid stream. These devices consist of no moving components and operate consuming little electrical or mechanical energy. The operation of an ejector relies on the principle of interaction between two fluid streams at different energy levels, in order to provide compression work. The high energy fluid stream is the motive flow or the primary flow stream (primary mass flow rate) whereas the low energy stream is the suction flow or the secondary flow stream (secondary/entrained mass flow rate) [7].

The ejector comprises of four components as illustrated in Figure 2-6. High energy fluid flows through the primary inlet which exits from sonic or supersonic nozzles and entrains the low energy fluid from the secondary inlet. A mixing duct is located after the primary inlet which is usually cylindrical with constant cross section. The high energy and low energy fluid streams are mixed by formation of a shear layer so that a uniform profile is produced at the end of the duct. A diffuser is located at the end of the ejector which reduces the fluid velocity and increases the pressure of the fluid to be discharged to the outlet [8]. With regards to the inlet test system, the ejector is typically located at the rear of the system downstream of the mass flow plug.

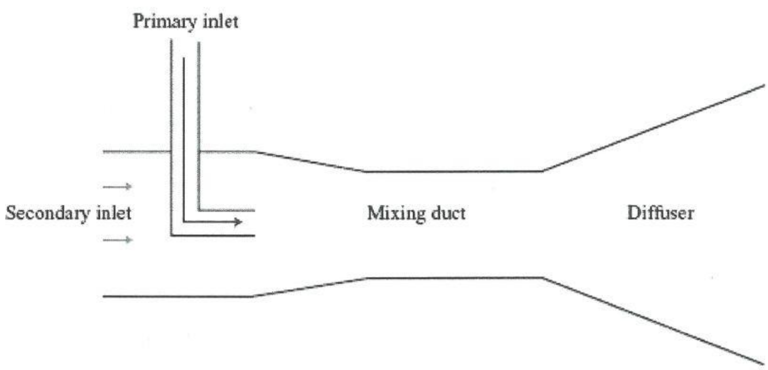

Figure 2-6 : Components of a basic ejector [1]

This ejector is known as a single nozzle ejector which is illustrated in Figure 2-7. In the single nozzle ejector mixing of the two fluid streams are completed in a long mixing duct. This is not suited for applications where there are space limitations.

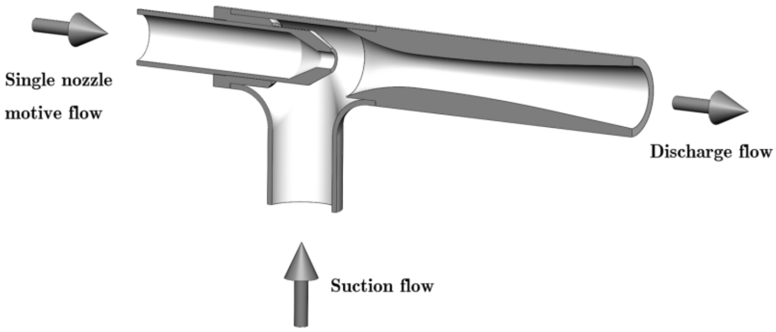

Figure 2-7 : Single nozzle ejector [9]

Ejector efficiency and compactness may be significantly improved by using more complex designs such as multi-nozzle or annular flow ejectors [10]. This is important in aeronautical applications where performance requirements and space limitations preclude the use of simple single nozzle applications. Single nozzle ejectors are considered adequate for use when low mass flows are required, however for high mass flow ratios a multi-nozzle or annular flow ejector is considered beneficial [10].

Multi-nozzle ejectors allow mixing of the two fluid streams to be completed in a shorter length, hence its suitability to applications where constraints are placed on the mixing duct length. This multi-nozzle ejector performance is greater although there are losses due to lower primary discharge coefficients and blockage which is caused by the multi-nozzle assembly [10]. An example of a six nozzle assembly is illustrated Figure 2-8(a) and the configuration of a nine nozzle ejector is illustrated in Figure 2-8(b).

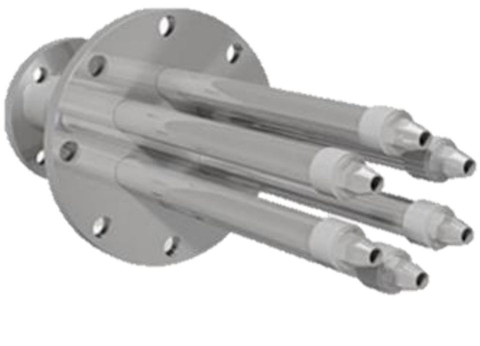

(a) Assembly of 6 nozzles [11]

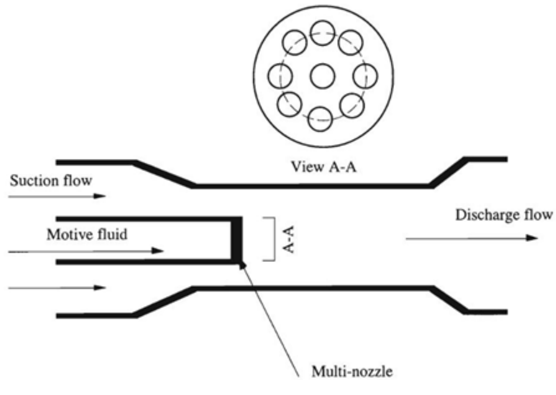

(b) Configuration of 9 nozzles [12]

Figure 2-8 : Multi-nozzle ejector

An experiment was conducted by Aissa [13] to study the effect of introducing multiple nozzles with and without swirl instead of one nozzle in the primary stream of an air ejector. Three nozzle configurations, illustrated in Figure 2-9, were tested: single nozzle, multiple nozzles with swirl and multiple nozzles without swirl. All nozzles were convergent having a 20° convergence cone angle. It was concluded from the experiment that utilising multiple nozzles instead of a single nozzle increased the ejector mass flow ratio and efficiency, and by introducing swirl in the flow resulted in an increase in the ejector mass flow ratio. Flow visualization was used to show that multiple nozzles with and without swirl resulted in a decrease in mixing length which would enable development of shorter ejectors [13].

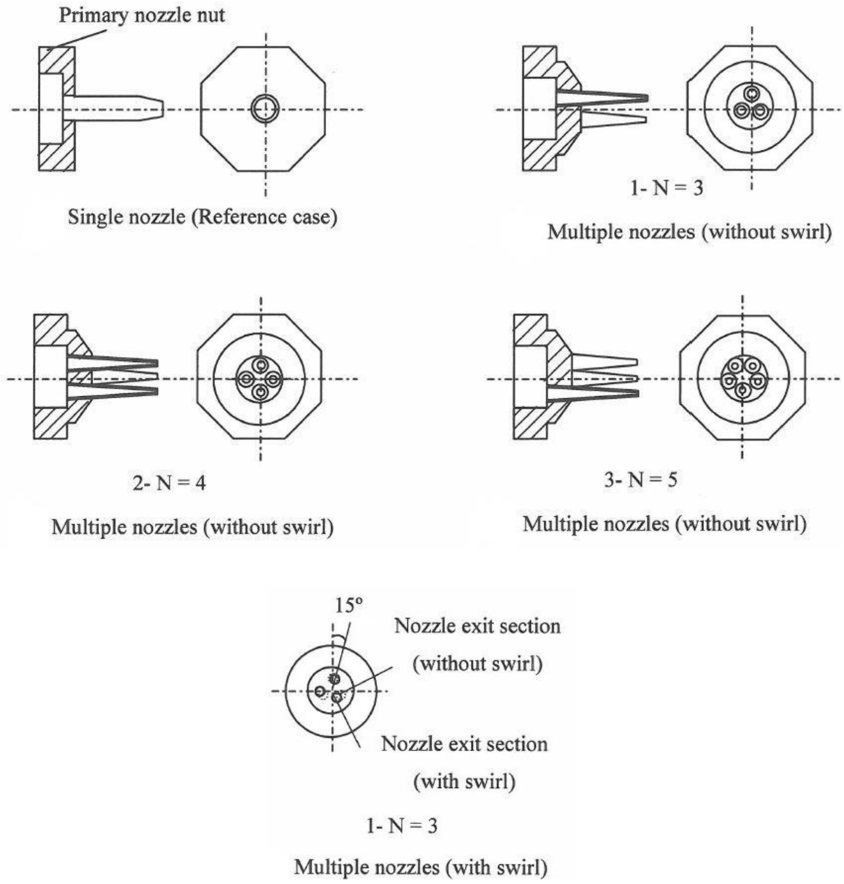

Figure 2-9 : Different primary nozzle(s) configurations [13]

Annular flow ejectors as illustrated in Figure 2-10 allows for the injection of the primary fluid through multiple nozzles which improves the mixing of the primary and secondary fluids resulting in a reduced mixing duct length thereby reducing losses. Caution should be taken when increasing the number of nozzles as blockage becomes more significant in this arrangement. Additional losses for this configuration may be incurred in the primary and secondary supplies due to the increased mechanical complexity of the ductwork [10].

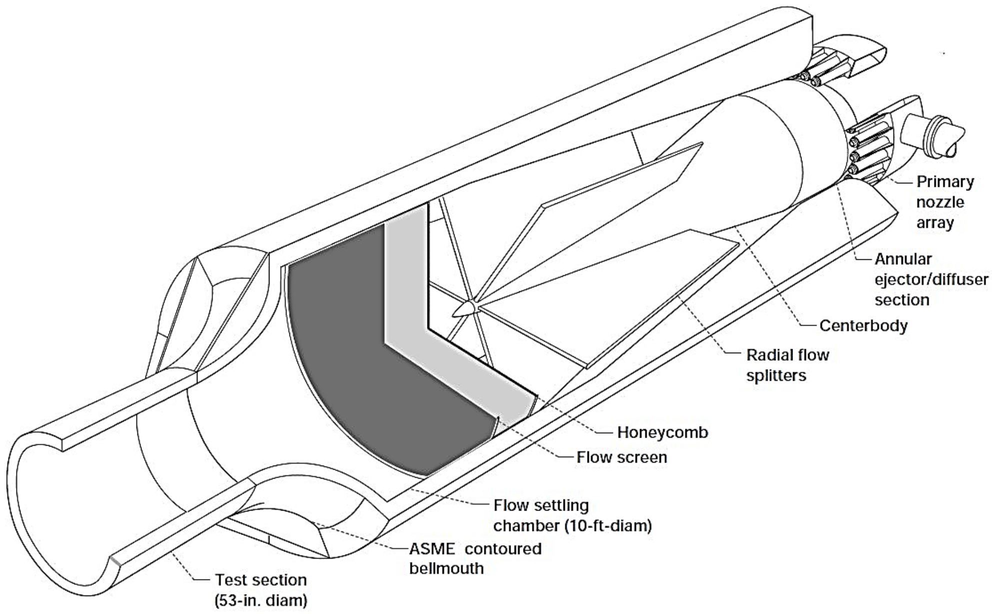

Figure 2-10 : NASA's NATR using an annular ejector with multiple nozzles [14]

2.1.1.2 Flow Regimes of Ejector Operation

In order to design for maximum ejector efficiency, the flow regimes of the ejector should be considered. There are a variety of flow regimes that are possible when designing an ejector, depending on operating conditions and the ejector geometry [15]. Flow regimes within an ejector of fixed geometry and the flow regimes within an ejector with fixed operating conditions are explained in this section with reference to the ejector illustrated in Figure 2-11 [15].

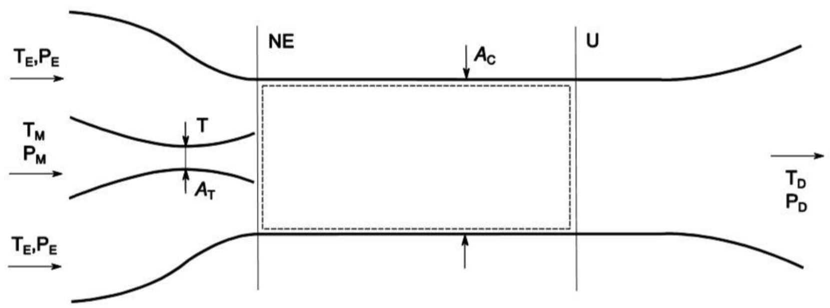

Figure 2-11 : Schematic diagram of an ejector [15]

Flow regimes within an ejector of fixed geometry revolves around the concept of critical backpressure, P_D^*. The primary nozzle throat area, the mixing duct area and the primary and secondary fluid states at the inlet to the ejector are fixed for this flow regime. A reversed flow region exists when the discharge pressure is too high to allow entrainment of the secondary fluid, the primary fluid partially flows towards the secondary inlet and the flow through the converging-diverging primary nozzle is overexpanded resulting in compression shocks. The reverse flow region is illustrated in Figure 2-12 [15] where P_D is to the right of point A on the x-axis. Unchoked entrainment occurs when the discharge pressure drops to point A in Figure 2-12, causing the compression shocks at the exit of the primary nozzle to weaken which allows the pressure at the primary nozzle exit, NE in Figure 2-11, to decrease and provoke entrainment of the secondary fluid [15]. Critical operation of the ejector occurs when the discharge pressure reaches P_D^* which allows a decrease in pressure upstream, causing the entrained flow to be accelerated to sonic speed within the mixing region. A choked regime occurs for discharge pressures below P_D^* and the entrainment ratio remains constant hence the entrained mass flow rate is constant. The primary flow remains choked at the primary nozzle throat and the entrained flow remains choked in the mixing region [15].

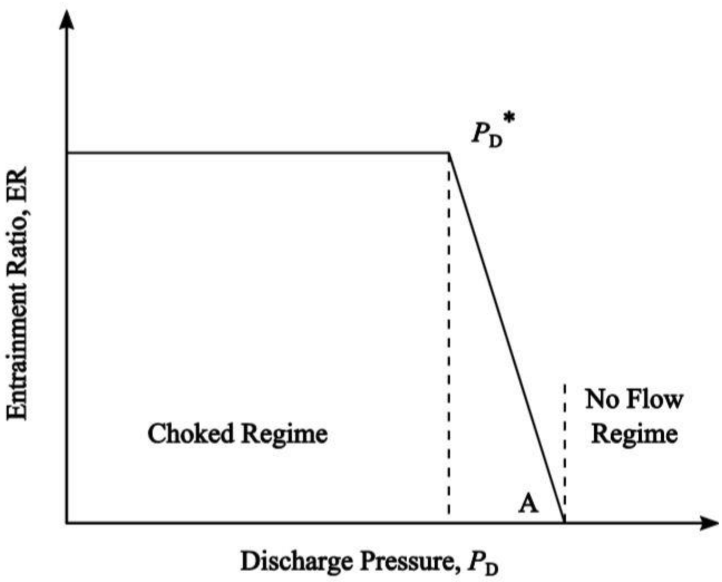

Figure 2-12 : Variation of entrainment ratio with discharge pressure [15]

Three flow regimes within an ejector with fixed operating conditions are identified which depend on the ejector geometry. A fixed inlet fluid state and a fixed discharge pressure is considered for this flow regime. For overexpanded flow the operating conditions are such that the primary fluid is choked at the primary nozzle throat and the secondary fluid is choked in the mixing duct. The area ratio of the mixing duct to primary nozzle throat area, φ, is small, such that the primary nozzle is overexpanded [15]. For perfectly expanded flow φ is reduced causing a higher entrainment ratio. The pressure at the uniform flow cross section, U in Figure 2-11 [15], as well as upstream of U decreases. When the primary nozzle is perfectly expanded, the compression shocks downstream of the primary nozzle weaken until they cease to exist, which results in an increase in the effective flow area of the secondary fluid and hence an increase in the entrainment ratio. At this point the φ is considered to be the optimal area ratio for a given set of inlet conditions and discharge pressure, the entrainment ratio is maximum and the static pressures of the primary and secondary fluid are equal at section NE [15]. For underexpanded flow φ is reduced below optimal which causes a decrease in entrainment ratio. The underexpanded primary jet spreads at the exit of the primary nozzle, restricting the flow area of the secondary fluid [15]. A flow structure in an ejector with an underexpanded primary nozzle and choked entrained flow is illustrated in Figure 2-13 [15]

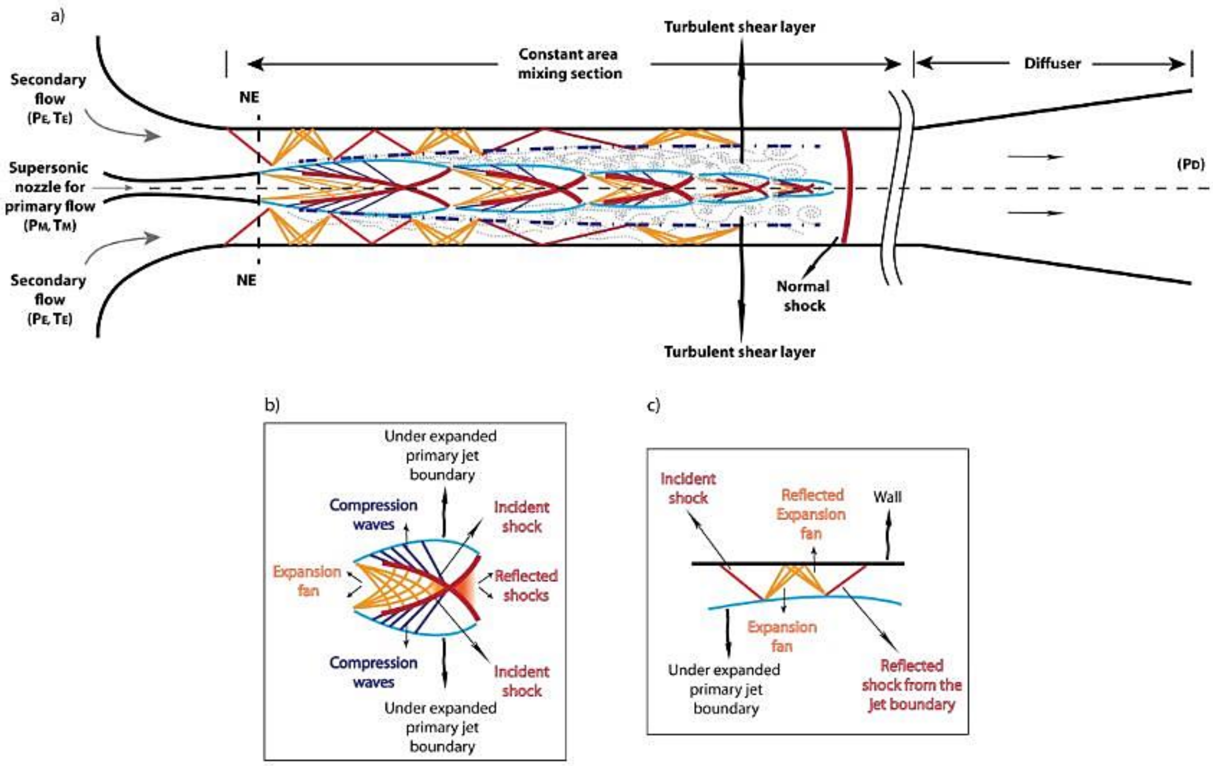

Figure 2-13 : Flow structure in an ejector with an underexpanded primary nozzle and choked entrained flow [15]

2.1.2 Flow Quantity Metering

Inlet tests are conducted at specific conditions that require quantification in order to properly establish corresponding operation points on engine performance maps. Hence a system is required to accurately measure and control the amount of airflow through an inlet.

Two methods have been noted for flow quantity metering. The first method employs a device that is operated in a chocked mode. This requires the throat *i.e.* the minimum area of the entire inlet duct system be at the device itself rather than at an upstream or downstream location [6]. Once the flow metering device is choked, the airflow through the system is a function of the area only. This means that the amount of airflow through the system can be varied by varying the area. In most flow metering devices the area is directly related to a measureable position of the choking device [6].

The second method employs a combination of pressure measurements taken at the engine compressor face to measure the mass flow through the inlet. Total pressure probes are situated at the compressor face. The average static to total pressure ratio at each probe is used to calculate the local Mach number which is converted to velocity. The mass flow element is then obtained by using the velocity, area and local air density. The total mass flow at the compressor face is achieved by summing up all the individual mass flow elements and then multiplying the sum by a discharge coefficient [6].

According to Davis et al. [6] the method employing a device operated in a choked mode is usually favoured for a flow quantity metering system as it provides a more accurate measurement of airflow through an inlet. Davis et al. [6] stated that the compressor face pressure method provides a less accurate measurement of airflow through an inlet and should be used as a check for the device operated in a choked mode.

2.1.2.1 Mass Flow Plug

The flow quantity metering system requires regulation to achieve various specific steady state flow rates. A translating conical mass flow plug, illustrated in Figure 2-14, is the most common device which combines a regulation function with a measurement function. The regulation function is achieved by the translational action of the conical plug fore and aft a restriction in the duct. The translation of the conical plug through the restriction in the duct results in a geometric converging-diverging nozzle and hence a geometric "throat" where choking can be achieved. Increasing and decreasing the duct throat area, by translation of the conical plug, results in a change of airflow through the duct. This approach implies an additional requirement of operating the conical plug with a sufficiently low back pressure to ensure that the plug remains choked [6].

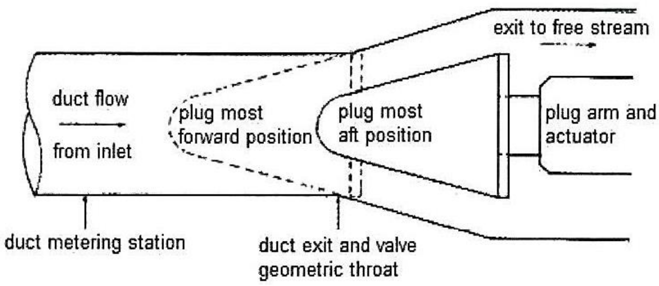

Figure 2-14 : Northrop schematic of a choking conical plug [3]

The area variation produced by the translation of the conical plug into a duct can be estimated from the system geometry and is illustrated in Figure 2-15 [1], showing the area reduction caused by plug extension. The metering function is achieved by correlating measurements of total and static pressure, temperature and conical plug position.

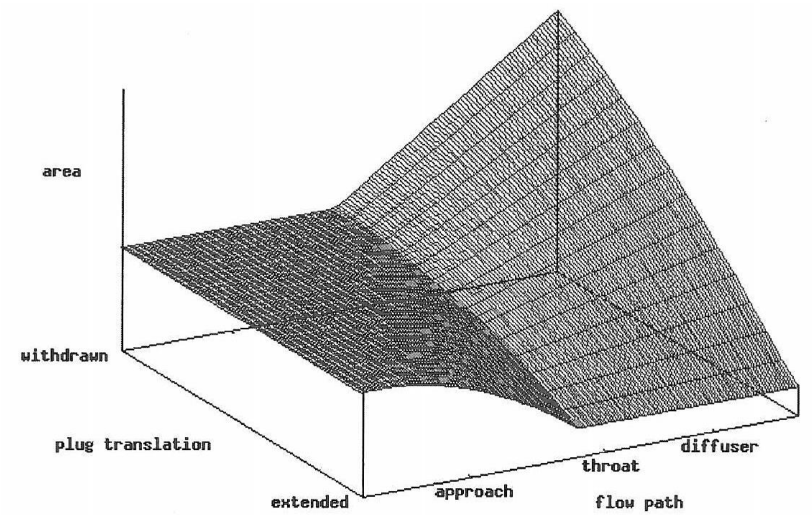

Figure 2-15 : Variable area converging-diverging nozzle achieved with plug translation [1]

The geometry of the conical mass flow plug and duct sizes are arbitrary but does have a demeanour on the sensitivity of the device as a mass flow meter and also on the overall system resistance. The relationship between mass flow rate and plug position is non-linear and is less sensitive for smaller duct sizes as shown on the graph in Figure 2-16.

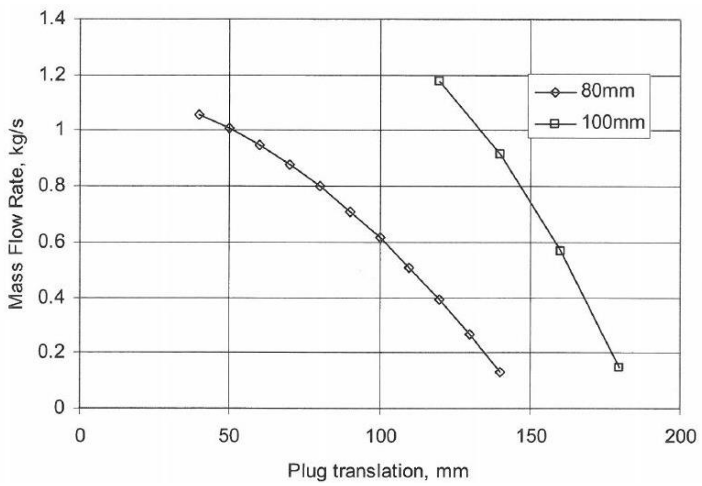

Figure 2-16 : Influence of throat duct size on mass flow plug sensitivity [1]

NASA Langley employs a translating conical plug, illustrated in Figure 2-5, with an approximate included cone angle of 30°. They use the conical mass flow plug to change the airflow, by changing the duct area as described above. The mass flow is computed from the ratio of the average flow plug exit static pressure to the average total pressure measured at the interface plane [5].

Northrop employs a choking plug valve system for the metering and control of duct mass flows, as illustrated in Figure 2-14. Boccadoro and Franco [3] from Northrop point out that the true throat area cannot be measured directly, hence a calibration exercise was performed against an appropriate standard by means of a displacement transducer. This would effectively allow the throat area to be expressed as a function of the conical plug axial position.

Boccadoro and Franco state that with choked flow at the throat, each position of the conical plug corresponds to a specific mass flow rate. This mass flow rate will be insensitive to changes in the back pressure and will be a function only of the upstream total pressure and temperature [3]. This would be the preferred mode of operation as it removes the dependency of the mass flow on the throat static pressure [1].

2.1.3 Flow Quality Metering

For an inlet test, flow quality metering is accomplished by employing a pressure rake array which is located at the "aerodynamic interface plane" (AIP). The AIP is the location of the instrumentation plane used to define inlet distortion and performance at the aerodynamic interface between the inlet and the engine. It is required that the AIP be located in a circular or annular section of the inlet duct as close as practical to the engine-face plane which is defined by the leading edge of the most upstream engine strut, vane or blade row [16]. According to the Society of Automotive Engineers (SAE) Aerospace Recommended Practice ARP-1420, a typical pressure rake array for measuring inlet recovery and distortion should be employed [16]. The pressure rake array utilises eight rakes spaced 45° apart with five probes on each rake as illustrated in Figure 2-17(a). The probes are located at the centroid of five rings, illustrated in Figure 2-17(b), with each ring representing an equal area of the AIP. The arrangement of the rakes at 45° allows for the measurement of the circumferential distortion component whereas the arrangement of the probes at the centroid of the rings allow for the radial distortion component to be determined [6].

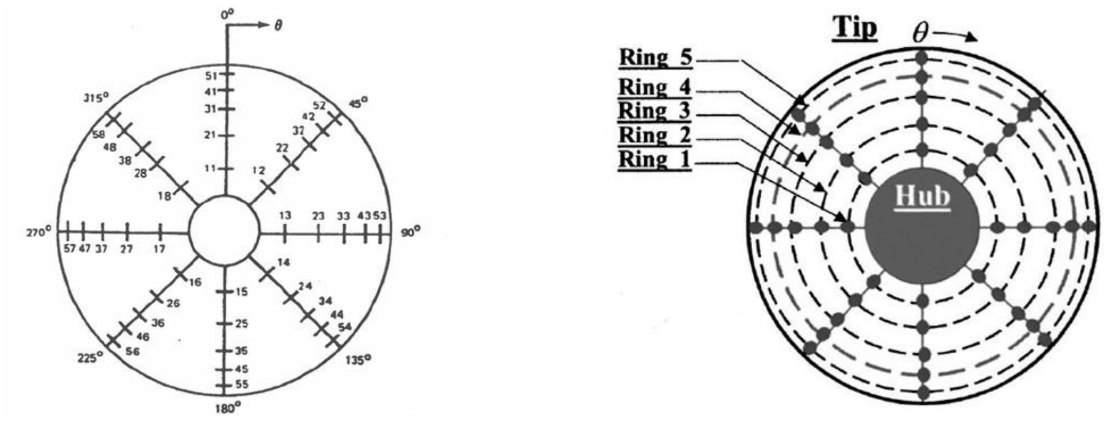

(a) Rake and probe orientation [16]

(b) Probe location on each ring [6]

Figure 2-17 : Standard SAE 40-port pressure rake array

An inlet pressure rake, illustrated in Figure 2-18, was designed and built according to the specifications of SAE ARP 1420 to perform inlet distortion measurements during taxi tests of an

Unmanned Aerial Vehicle (UAV) [17]. It was found that the maximum blockage of the rake structure amounted to 8% of the inlet area. The 8% blockage was due to the location of the rakes and supporting structure in a constant area duct and this limitation generally applies to all flying applications. However, scaled applications may make use of a diffuser downstream of the AIP so that the structural support of the rake does not cause too much blockage [1].

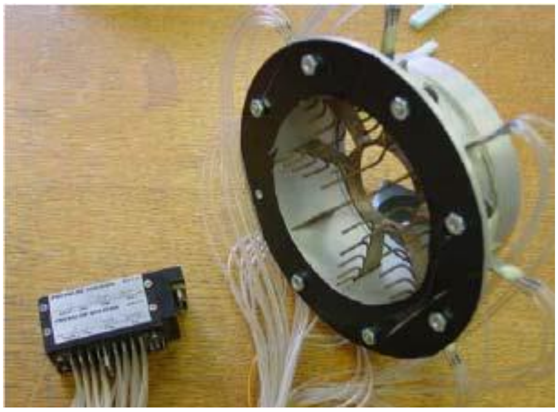

Figure 2-18 UAV 40 port pressure rake [17]

2.2 One-Dimensional Ejector Theory

In 1939, Flügel [18] presented a one-dimensional analysis of the mixing of two gas streams by applying the equations of continuity, momentum and energy to the design of ejectors. Two models were considered by Flügel [18], mixing at constant cross-sectional area and mixing at constant pressure, however the published results of his calculations were insufficient [18]. In 1950, Keenan et al. [18] presented a one-dimensional theoretical and experimental analysis of an ejector. Their model was based on ideal gas thermodynamics and the principles of mass, momentum and energy conservation. The analysis considered a constant-area mixing model and a constant-pressure mixing model, which became the foundation of ejector design. To simplify the analysis, Keenan et al. [18] assumed the primary stream and secondary stream have the same molecular weight and ratio of specific heats, and the shear forces between the streams and the walls are zero.

Keenan et al. [18] showed that the results of a constant-area mixing model analysis agreed with the experimental results and concluded that the method of analysis is adequate to represent reality. They stated that it was difficult to obtain an accurate comparison between the analysis and experiment of a constant-pressure mixing model. This was due to the curved shape and dimensions of the constant-pressure mixing section being difficult to accurately design.

2.2.1 Constant-Area Mixing Model

The mixing in a constant-area ejector, as illustrated in Figure 2-19, occurs between section 1 and 3. Section 1 is the exit plane of the primary nozzle which is situated within the constant-area mixing section. The mixing process of the primary stream and secondary stream starts at section 1 and completes at section 3, the exit of the mixing chamber. During the ejector operation an aerodynamic throat could occur in the mixing chamber. When the static pressure of the primary stream is higher than that of the secondary stream between sections 1 and 2, this causes the primary stream to expand against the secondary stream [24]. The primary stream acts as an aerodynamic nozzle for the secondary stream and causes the aerodynamic throat to form. The secondary stream could be choked at the aerodynamic throat if the downstream pressure is low enough [24].

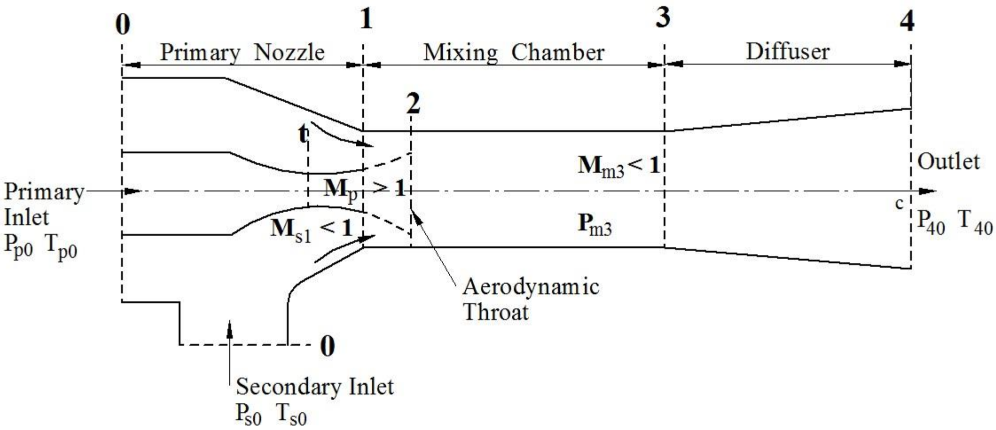

Figure 2-19 : Schematic of constant-area ejector model [24]

2.2.2 Constant-Pressure Mixing Model

The mixing in a constant-pressure ejector, as illustrated in Figure 2-20, occurs between sections 1 and 2. Mixing of the primary stream and the secondary stream occurs in a chamber, between section 1 and 2, with constant uniform pressure. A normal shock wave occurs in the constant area chamber, between section 2 and 3, if the velocity of the fully mixed flow is supersonic at section 2. The static pressure of the mixed flow leaving section 3 at uniform subsonic velocity is increased in the diffuser [24].

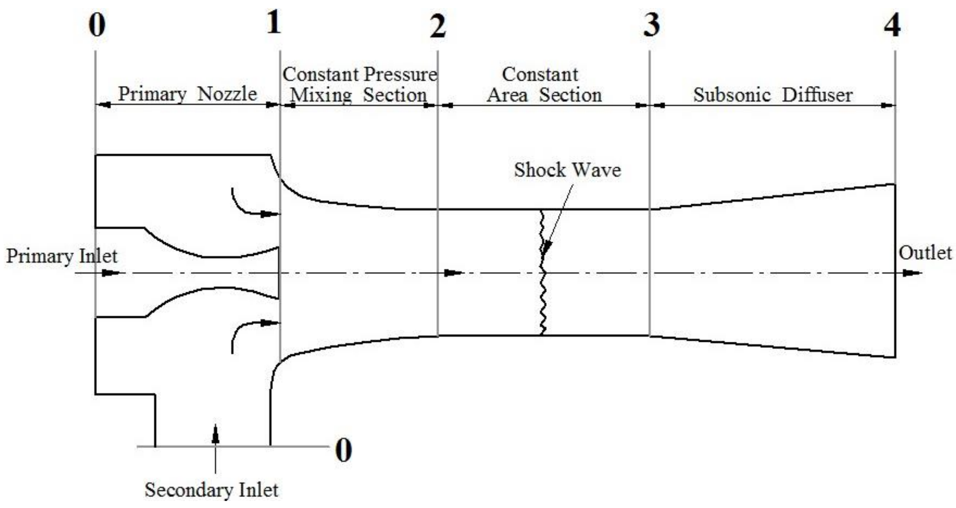

Figure 2-20 : Schematic of constant-pressure ejector model [24]

2.3 ESDU 92042

Engineering Science Data Unit (ESDU) 92042 describes a computer software for the design and performance of gas ejectors. The ESDUpac A9242 computer software integrates one-dimensional flow theory and data from previous experiments to design an ejector.

The software provides the following design and performance prediction procedures [10].

a) Quick Design Procedure - This method requires the input of the entry and required pressures, temperatures, mass flow rates and dimensions. The software calculates the primary nozzle and exit dimensions, using empirical data for air-air ejectors. This method is restricted to ejectors with constant area mixing and air as both working fluids.
b) Detailed Design Procedure - This method requires the input of the entry and required pressures, temperatures, mass flow rates, dimensions and loss factors as well as user defined constraints on the flow conditions. The software calculates the primary nozzle and exit dimensions, and flow conditions throughout the ejector using one-dimensional flow theory.
c) Performance Prediction Calculation - This method requires the input of the ejector dimensions, loss factors and a range of entry flow conditions. The software calculates the outlet conditions and the flow conditions throughout the ejector using one-dimensional flow theory.

A typical gas ejector configuration employed by the ESDU software for the design and performance of an ejector is illustrated in Figure 2-21. The design procedures optimises for the shortest mixing duct length for complete mixing of the primary and secondary streams and for the highest efficiency. The ESDU ejector design procedures determine performance at the primary nozzle 'on-design' point, *i.e.* the conditions under which the primary static pressure matches the secondary static pressure at the nozzle exit plane [1]. ESDU states that an ejector may be required to operate over a range of primary pressures or secondary Mach numbers, in which case estimates of 'off-design' performance must be pursued [10]. The ESDU software can only be applied to designs were the secondary to primary mass flow ratio, r_m, ranges from 0.05 to 1, as illustrated in Figure 2-22. Mass flow ratios that do not lie in this range results in data being less reliable.

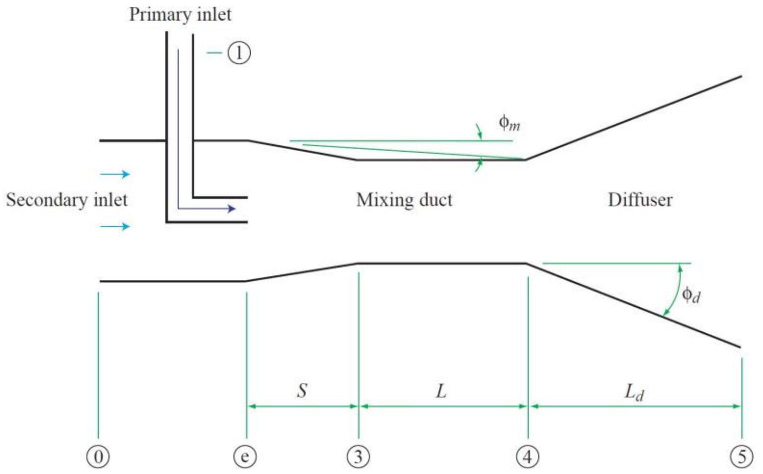

Figure 2-21 : Ejector configuration used by ESDUpac A9242 [10]

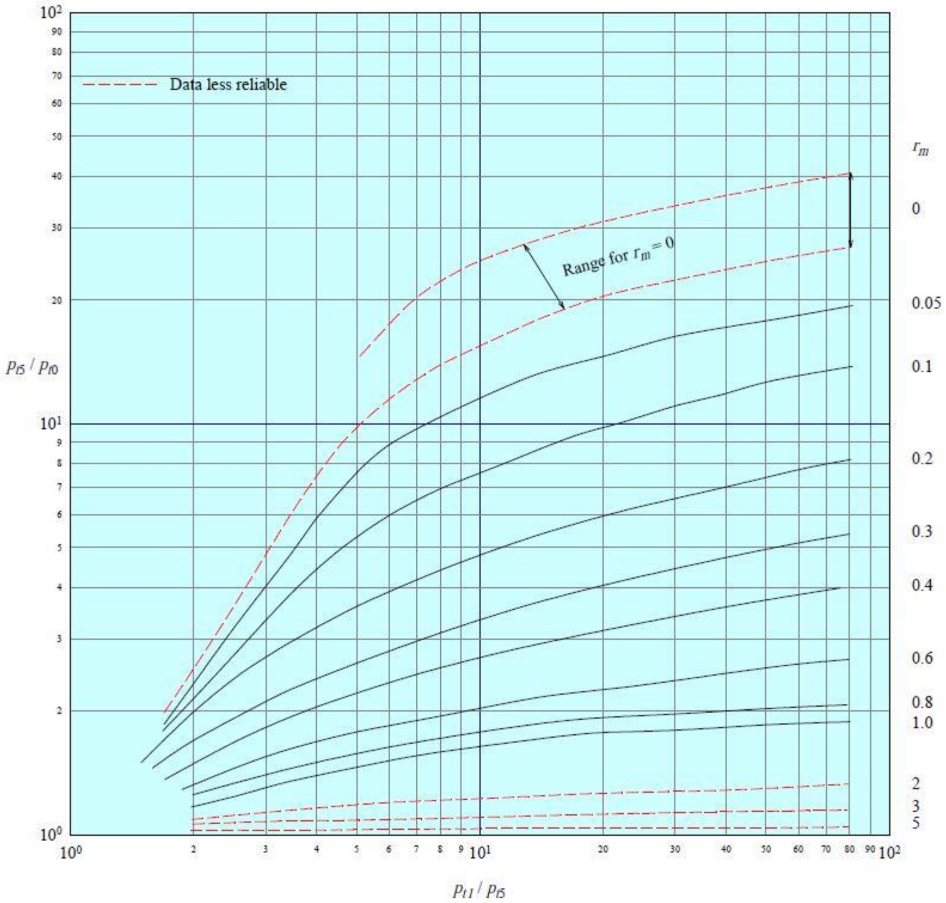

Figure 2-22 : Optimum performance relationship between pressure ratios and mass flow ratio [10]

A few mechanical design considerations were made by ESDU that are worth stating. The secondary inlet and primary nozzle assembly should be designed for minimum loss in order to achieve good performance. ESDU [10] states that the secondary flow should be ducted into a plenum chamber and thence into the mixing duct via a bellmouth entry. However, if space is limited a conical entry may be employed. When employing a conical entry, the optimum included angle for the conical inlet should lie between 20° to 30° to ensure that the ejector performance does not degrade substantially in comparison to ejectors that employ bellmouth entries. The junction between the conical entry and the mixing duct should be radiused for minimum losses [10].

ESDU [10] recommends a convergent-divergent primary nozzle, provided the primary pressure is sufficiently high to enable it to operate correctly. The convergent-divergent nozzle should have a sharp lip so that there is no wake and an internal smooth surface to reduce friction losses. According to ESDU [10] the mixing duct need not be cylindrical. However, square and rectangular section ducts having sharp corners would produce unstable flow. The surface finish of the mixing duct affects the efficiency and the secondary mass flow; hence a smooth surface finish is required to reduce friction [10]. ESDU [10] states that the diffuser included angle is recommended to lie in the range 6° to 10° and that it is not worthwhile radiusing the mixing duct and diffuser junction for these angles.

2.4 Nozzle Design

The primary nozzle employed in an ejector according to ESDU [10] is shown schematically in Figure 2-23. The nozzle has two distinct sections: a convergent section where the gas is accelerated to sonic conditions at the nozzle throat, followed by a divergent section that accelerates the gas from sonic to supersonic conditions. Of particular significance is the nozzle contour, which is designed to cancel shock waves that develop in the nozzle due to the supersonic flow of gases through it [19].

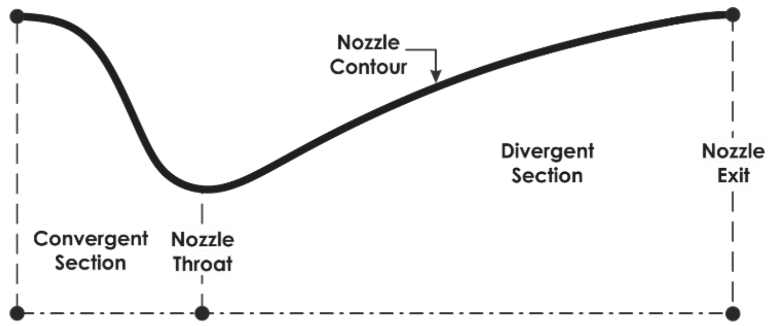

Figure 2-23 : Schematic of a convergent- divergent nozzle [19]

2.4.1 Supersonic Nozzle Contours

A numerical technique that is able to define the wall boundaries in supersonic flow is known as the Method of Characteristics (MOC), which is commonly combined with calculus and used for the development of the wall contours of bell-nozzles for maximum thrust performance [20]. Two nozzle profiles viz. Minimum Length Nozzle (MLN) and Rao [22] Thrust Optimised Parabolic (TOP) nozzle were considered for the supersonic nozzle contour.

2.4.1.1 Minimum Length Nozzle

The method of characteristics provides a technique for designing the contour of a supersonic nozzle for shockfree isentropic flow as illustrated in Figure 2-24 [21]. In the convergent section of the nozzle, the subsonic flow is accelerated to sonic conditions at the throat region. A sonic line illustrated by the dashed line from *a* to *b* in Figure 2-24 is generally curved, however for most applications it is assumed to be straight. Downstream of the sonic line an expansion section occurs where expansion waves are generated and propagate across the flow downstream as they reflect from the opposite wall of the nozzle. The expansion region *acejb* is defined as a non-simple region, consisting of both left and right running curved characteristic lines. The angle of the nozzle wall with respect to the *x* direction, θ_w, increases in the expansion section and reaches a maximum at the inflection point, *c*, of the nozzle contour as illustrated in Figure 2-24 [21]. Downstream of point *c*, θ_w decreases until the wall becomes parallel to the *x* direction at point *d* and *f*. The section from *c* to *d* denotes the straightening section which is designed to cancel all the expansion waves generated in the expansion section. The regions *cde* and *jef* in the straightening section covers the characteristics of only one family and is described as a simple region where the characteristic lines are straight. Downstream of points *def* the flow is uniform and parallel at the desired Mach number [21].

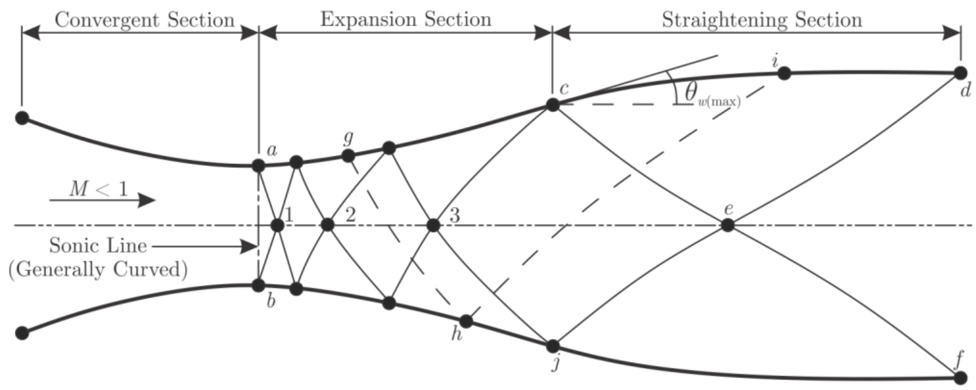

Figure 2-24 : Schematic of a supersonic nozzle designed by the method of characteristics [21]

The supersonic nozzle as illustrated in Figure 2-24 is typically used in wind tunnels where high-quality and uniform flow is desired in the test section which is downstream of section *def*. Wind tunnel nozzles are generally long with a relatively slow expansion. However, long nozzles with a slow expansion are not suitable for certain nozzles such as a rocket nozzle. In these cases a short nozzle is required in order to minimize weight. A minimum length nozzle allows for rapid expansion to produce short nozzles that minimize weight. In a minimum length nozzle, the expansion section shown in Figure 2-24 is shrunk to a point and the expansion takes place through a centred Prandtl-Meyer expansion wave emanating from a sharp corner, point *a*, at the throat with an angle $\theta_{w,max}$ as illustrated in Figure 2-25 [21]. Unlike the nozzle in Figure 2-24 where multiple reflections of the expansion waves occurred from the wall along *ac*, the minimum length nozzle encounters only two systems of waves, right-running waves emanating from point *a* and the left-running waves emanating from point *d* in Figure 2-25 [21]. As a result of no multiple reflections, $\theta_{w,max}$ in a minimum length nozzle must be larger than $\theta_{w,max}$ in Figure 2-24 for the same exit Mach number. The length, *L*, of the supersonic nozzle is a minimum to ensure shockfree isentropic flow occurs [21].

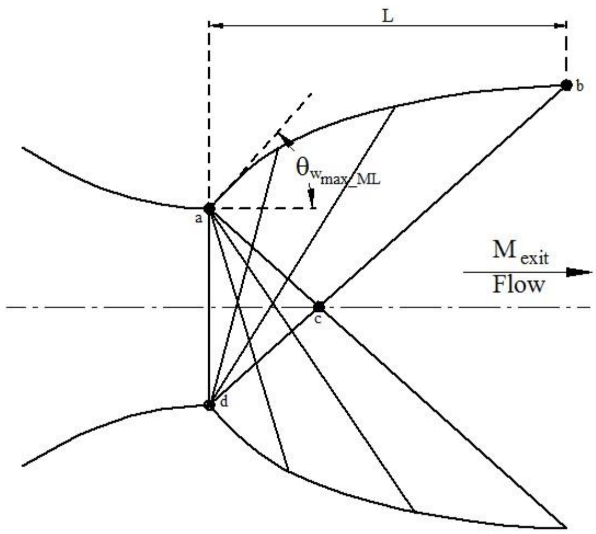

Figure 2-25 : Schematic of a minimum length nozzle [21]

2.4.1.2 Rao TOP Nozzle

Rao [22] developed a rapid technique to approximate nozzle designs for optimum thrust, which was derived from extensive MOC computations of various bell-nozzles. This technique is referred to as the parabolic approximation of optimum thrust nozzles, and the resulting bell-nozzles are known as Rao Thrust Optimised Parabolic (TOP) nozzles.

The parabolic approximation to bell-nozzles has the design configuration shown in Figure 2-26, where the entrance curve upstream of the nozzle throat, t, is a circular arc with a radius of $r_c = 1.50R_t$, where R_t is the radius of the nozzle throat in the axisymmetric nozzle. The divergent section consists of two parts: the expansion section that lies between t and the inflection point N, which has a circular radius of $r_{es} = 0.382R_t$ and produces an initial wall angle at N of θ_N; and the straightening section, which has a parabolic wall contour referred to as the terminal curve, terminating at the nozzle exit, E, at an exit angle of θ_E and an exit radius of $R_E = \sqrt{\varepsilon}R_t$. The expansion ratio ε relates R_t to R_E, thereby fixing flow conditions at the nozzle exit and the nozzle length, L_N [19].

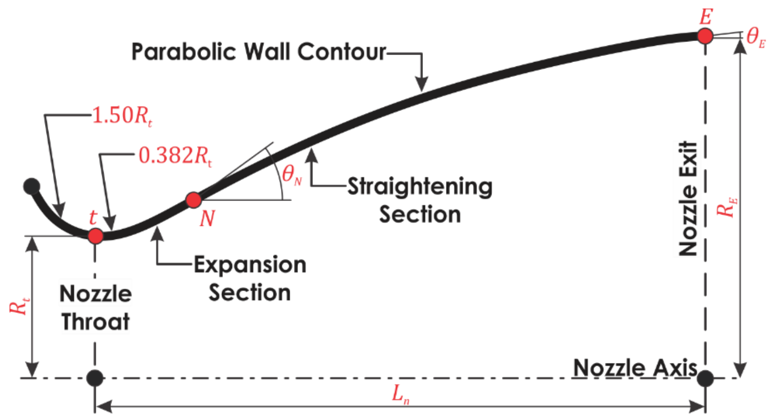

Figure 2-26 : Typical design configuration for the parabolic approximation to optimum thrust nozzles developed by Rao [22]

The length of the nozzle can be approximated using Equation 2.1 [19], where K is the length fraction of an ideal 15° conical nozzle.

$$L_n = \frac{K(\sqrt{\epsilon} - 1)R_t}{tan\theta_E} \tag{2.1}$$

The initial entrance angle of the parabolic terminal curve, θ_n, relates to the expansion ratio for specific length fractions, K, as illustrated in Figure 2-27, while the nozzle exit angle, θ_E, correlates to specific expansion ratios for specified K values as presented in Figure 2-28 [19]. A suitable length fraction is selected such that L_n meets geometric design requirements, allowing θ_n and θ_E to be evaluated.

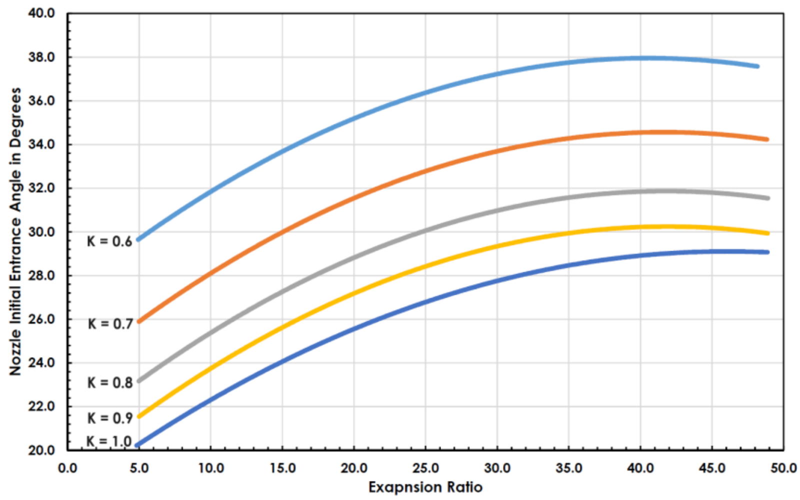

Figure 2-27: Rao Thrust Optimised Parabola (TOP) nozzle initial entrance angle for various expansion ratios and length fractions [19]

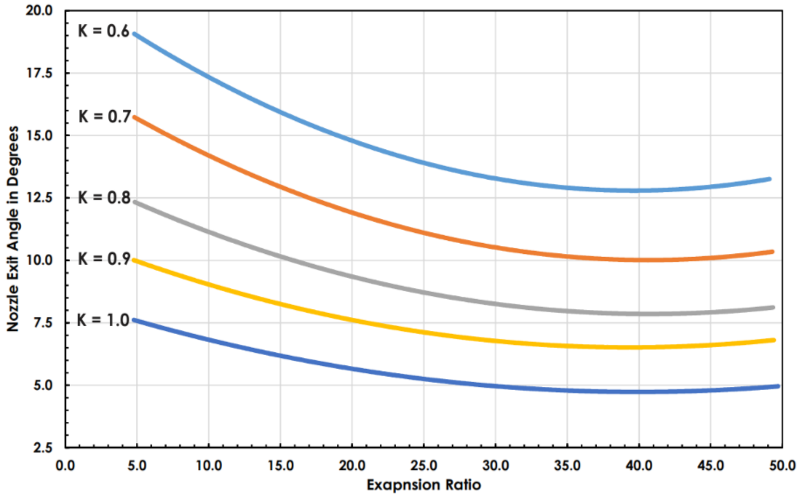

Figure 2-28: Rao Thrust Optimised Parabola (TOP) nozzle exit angle for various expansion ratios and length fractions [19]

The second-degree polynomial defining the TOP nozzle is expressed in Equation 2.2 [19], and when normalised, the coefficients can be determined by four independent variables *i.e.* ε, K, θ_n and θ_E [23]

$$\left(\frac{R}{R_t} + a\frac{X}{R_t}\right)^2 + b\frac{X}{R_t} + c\frac{R}{R_t} + d = 0 \tag{2.2}$$

The boundary conditions that are applied to resolve the coefficients of the polynomial terminal curve are defined in Equations 2.3 to 2.6 [19], where S1 signifies the entrance curve upstream of the nozzle throat, S2 signifies the expansion section and S3 signifies the straightening section with referenced to Figure 2-26.

$$S2(N) = S3(N) \tag{2.3}$$

$$\frac{dS2}{dX}(N) = \frac{dS3}{dX}(N) = tan\theta_N \tag{2.4}$$

$$S3(E) = R_E \tag{2.5}$$

$$\frac{dS3}{dX}(E) = tan\theta_E \tag{2.6}$$

The Matlab code presented in APPENDIX A.2 [19] determines the Rao TOP nozzle profile by employing the above method. The code requires specific inputs as shown in Figure 2-29 the first block of the process flow diagram which are used to determine the expansion ratio. The length factor and expansion ratio are used to compute suitable inflection point and nozzle exit angles. Subsequently, the entrance curve, S1, expansion curve, S2, and parabolic terminal curve, S3, are computed by applying the necessary boundary conditions.

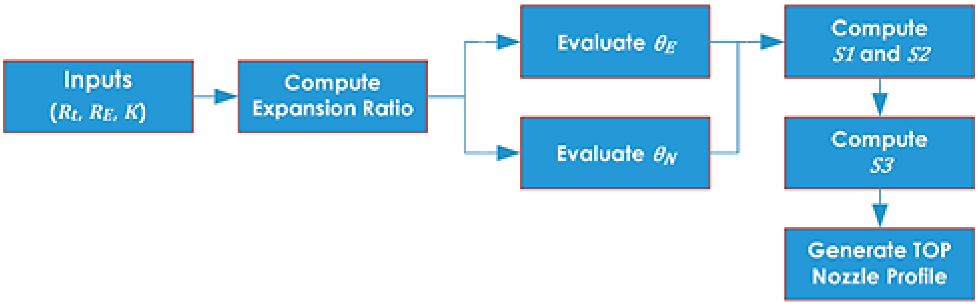

Figure 2-29 : Flow diagram of the process used to determine Rao TOP nozzle profiles using Matlab code

2.5 Medium Speed Wind Tunnel

The mass flow system is to be designed for the MSWT and ultimately manufactured and implemented to allow for inlet testing. The MSWT, illustrated in Figure 2-30, is a closed circuit, variable pressure, continuous wind tunnel. It has a Mach number range from 0.2 to 1.4, a test section dimension of 1.5m x 1.5m x 4.5m and a stagnation pressure range from 20kPA to 250kPa. The facility is used to do captive trajectory tests, high angle of attack tests, force and pressure measurements, flow visualisation, flutter testing, dynamic testing and aerodynamic damping tests [25]. The wind tunnel has 3 support systems namely flow field probe system (FFPS) which has 6 degrees of freedom, sidewall support which has 1 degree of freedom and main model support (MMS) which has 2 degrees of freedom.

Figure 2-30 : Medium Speed Wind Tunnel

3. DESIGN OF A CONTROLLED INDUCED MASS FLOW SYSTEM

The technique that employs a compact arrangement, where a variable area mass flow device is operated in a choked mode via a close-coupled ejector, is favoured for the Medium Speed Wind Tunnel (MSWT). The Council for Scientific and Industrial Research (CSIR) requires the system to be designed for an "aerodynamic interface plane" (AIP) of 80mm. A pressure rake array will be supplied by the CSIR which will facilitate the flow quality metering of the system.

The subsequent sections will detail the design of the flow quantity metering system and mass flow generation system.

3.1 Design of the Flow Quantity Metering System

The method employing a device operated in a choked mode is usually favoured for a flow quantity metering system as it provides a more accurate measurement of airflow through an inlet. The variable area mass flow device that will be employed is a translating conical mass flow plug as described in Section 2.1.2.1, which will be operated in a choked mode. A similar mass flow plug employed by NASA Langley and Northrop, as illustrated in Figure 2-5 and Figure 2-14 respectively, will facilitate the design.

3.1.1 Area Distribution

The mass flow system is designed for an AIP of 80mm. It is required that the maximum Mach number at the engine face, or the AIP, be in the range of 0.4 and 0.6 [26]. Using this information the desired throat areas are determined by using Equation 3.1 [27].

$$\frac{A}{A^*} = \frac{1}{M}\left(\frac{2\left(1+\frac{\gamma-1}{2}M^2\right)}{\gamma+1}\right)^{\frac{\gamma+1}{2(\gamma-1)}} \tag{3.1}$$

Where, A is the AIP area, A^* is the throat area and γ is the ratio of specific heats for air. The determined throat area should be the cross sectional area at the "geometric throat" of the duct as illustrated in Figure 3-1. The area of the geometric throat needs to be less than the AIP area to ensure choked flow. A 75mm geometric throat diameter satisfies this requirement. A 30° cone angle was deemed to be the most feasible angle as this resulted in a slender conical plug. In addition, this angle allows for a reasonable linear plug displacement to be achieved. The dimensioned conical mass flow plug located in the duct is illustrated in Figure 3-2. The translation of the plug will be achieved by a linear actuator located in an annulus behind the conical mass flow plug.

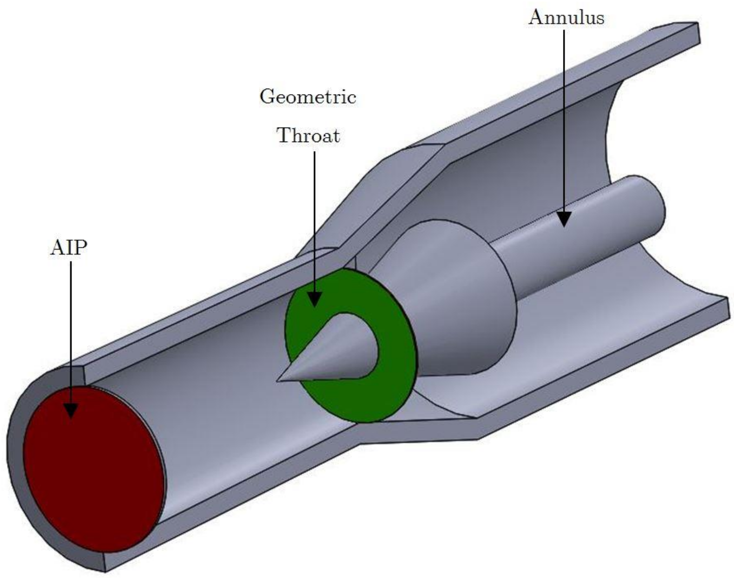

Figure 3-1 : Schematic of conical mass flow plug

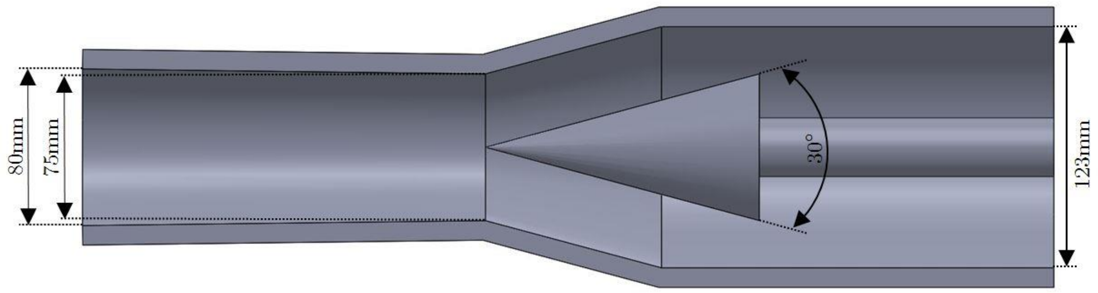

Figure 3-2 ; Conical mass flow plug dimensions

An Excel spreadsheet was used to develop a model to calculate the area distribution along the duct for various plug displacements. The cross sectional area along the duct was calculated at increments of 1mm. The area along the duct was calculated using the area of a circle where applicable, whereas the area around the plug was calculated using the surface area of a conical frustum. A conical frustum, illustrated in Figure 3-3, is a frustum created by slicing the top off a cone, with the cut made parallel to the base [28]. The surface area, A_s, is calculated using Equation 3.2 [28].

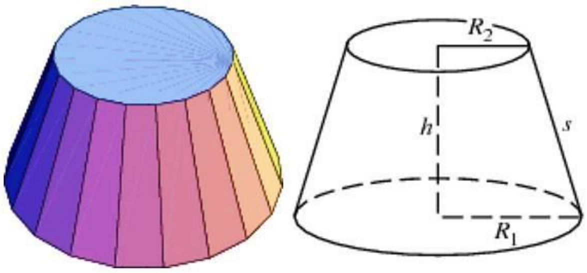

Figure 3-3 : Conical Frustum [28]

$$A_s = \pi(R_1 + R_2)s \\ = \pi(R_1 + R_2)\sqrt{(R_1 - R_2)^2 + h^2} \tag{3.2}$$

3.1.2 Determination of Backpressure

An analysis was conducted to determine the target backpressure, *i.e.* the pressure aft of the cone, to ensure choked conditions at the geometric throat for all wind tunnel stagnation pressures. In order for the target backpressure to be determined, the pressure losses incurred by channelling the secondary flow through the duct were calculated. These pressure losses are illustrated graphically in Figure 3-4.

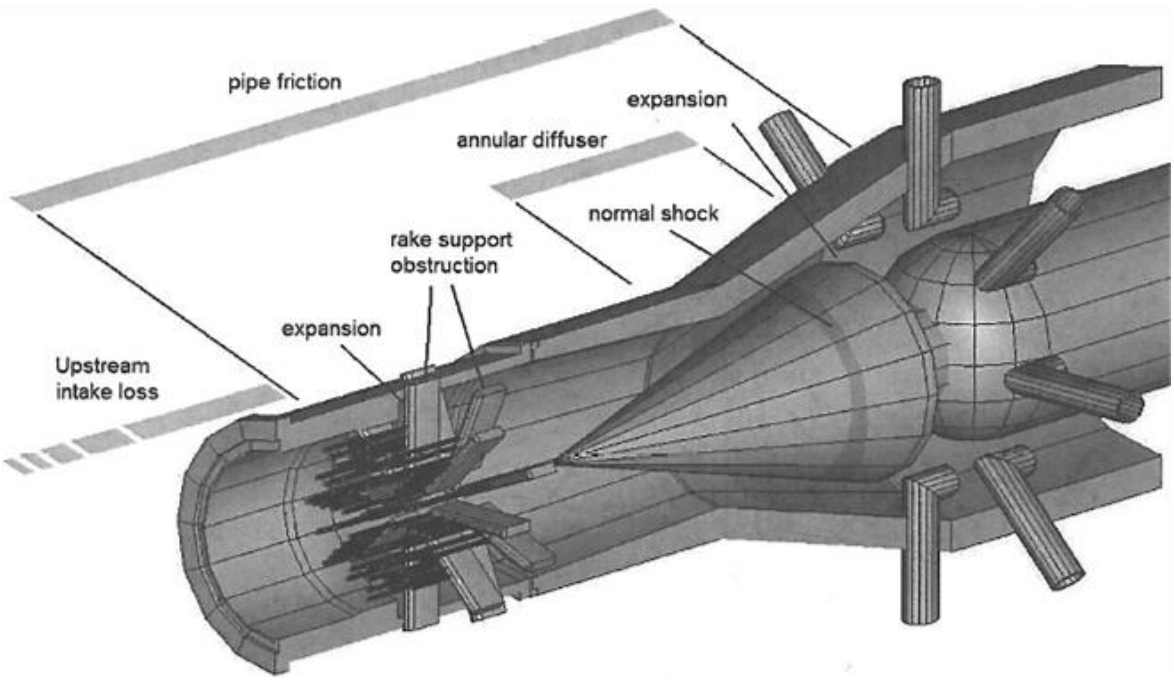

Figure 3-4 : Pressure loss model of a conceptual rake array with a close-coupled ejector driven by choked mass flow plug [1]

The pressure losses incurred by channelling the secondary flow through the duct comprise of the following:

- Intake Loss - Classical inlet losses are mainly dominated by friction and lip separation at off-design conditions and have a pressure recovery of 98%. S-duct inlets experience additional losses due to the curvature of the duct. An experiment by Tournier *et al* [29] on the flow control in an S-duct inlet found that the pressure recovery up to the design point, where mass flow equals 1.67kg/s, stays above 97% and then decreases at off-design conditions, where mass flow equals 2kg/s, to reach 94%. Pressure recovery for a poorly matched inlet-engine combination may result in poor pressure recoveries of order 90% or less at high mass flows as determined by Saltzman [30]. However with a modified system the pressure recovery improved to over 97%. A design pressure recovery estimate of 90% will be utilised in the pressure model to depict the worst case scenario. This loss represents a loss at design engine mass flow rates and for the appropriate inclusion into the pressure loss model, it has to be non-dimensionalised with dynamic pressure to avoid predicting high losses under reduced throttle simulations [1].
- Pipe Friction - This was calculated using Churchill's explicit formulation of the characteristic Moody Diagram for pipe friction. The pressure drop, ΔP, caused by pipe friction is calculated using Equation 3.3 [31]

$$\Delta P = f \rho G^2 \frac{L}{d} \tag{3.3}$$

where

$$f = \left[\left(\frac{C_1}{Re}\right)^{12} + \frac{1}{(A+B)^{3/2}}\right]^{1/12} \tag{3.4}$$

$$A = \left\{\frac{1}{\sqrt{C_t}} \ln\left[\frac{1}{(7/Re)^{0.9} + 0.27\,\epsilon/d}\right]\right\}^{16} \tag{3.5}$$

$$B = \left(\frac{37530}{Re}\right)^{16} \tag{3.6}$$

with f representing friction factor, G is the fluid mass velocity, L is the length of the channel between two pressure measurements, $C_1 = 8$ and $C_t = 1/2.457^2$ are geometry factors for laminar and turbulent flows for circular tubes respectively, ϵ/d being the relative roughness of the inner wall, Re representing Reynolds number defined by the duct diameter calculated using Equation 3.7 [32]

$$Re = \frac{\rho V d}{\mu} \tag{3.7}$$

where

$$\mu = \mu_0 \frac{T_0 + C}{T + C}\left(\frac{T}{T_0}\right)^{3/2} \tag{3.8}$$

$$\rho = \frac{P_s}{RT_s} \tag{3.9}$$

with μ representing dynamic viscosity at input temperature T, μ_0 representing the reference viscosity at the reference temperature T_0, Sutherland's constant C for the gaseous material, P_s and T_s representing static pressure and temperature, specific gas constant $R = 287.1 J/kg.K$ [27]. For standard air as the gaseous material, $C = 120$, $T_0 = 291.15K$ and $\mu_0 = 0.01827 \times 10^{-3} Pa.s$ [33]

- Expansion – Two sudden expansions occur in the system. The first occurs downstream of the AIP where the duct is expanded to house the rake support structure and the second occurs at the base of the translating mass flow plug. The pressure loss due to the expansion, P_{loss}, was calculated using Equation 3.10, where the total-pressure loss coefficient, K_t, was evaluated according to ESDU [34]

$$P_{loss} = K_t q \tag{3.10}$$

where

$$q = \tfrac{1}{2}\gamma P_s M^2 \tag{3.11}$$

with q representing dynamic pressure, P_s representing static pressure, M representing Mach number. K_t is determined by the following steps: $\left(\frac{V}{a_t}\right)_2$ is calculated from Equation 3.12 using the quadratic formula and substituted into Equation 3.13 to determine M_2, which is used to calculate $\frac{P_{t2}}{P_2}$ by using Equation 3.14, hence K_t is calculated using Equation 3.16 noting that $\frac{P_{t2}}{P_{t1}} = \frac{P_1}{P_{t1}}.\frac{P_{t2}}{P_2}.\frac{P_2}{P_1}$. The area ratio of enlargement is represented by $\phi = A_1/A_2$ where A_1 and A_2 represents the cross-sectional area before and after the enlargement plane.

$$\left(\frac{V}{a_t}\right)_2^2 - \left(\frac{V}{a_t}\right)_2 \left[\frac{2}{(\gamma+1)\phi\left(\frac{V}{a_t}\right)_1}\left\{1 + \left(\frac{V}{a_t}\right)_1^2\left(\gamma\phi - \frac{\gamma-1}{2}\right)\right\}\right] + \frac{2}{\gamma+1} = 0 \tag{3.12}$$

$$\frac{V}{a_t} = M\left(1 + \frac{\gamma-1}{2}M^2\right)^{-1/2} \tag{3.13}$$

$$P_t = P_s\left(1 + \frac{\gamma-1}{2}M^2\right)^{\gamma/\gamma-1} \tag{3.14}$$

$$\frac{P_{s2}}{P_{s1}} = \phi\frac{\left(\frac{V}{a_t}\right)_1}{\left(\frac{V}{a_t}\right)_2}\left[\frac{1 - \frac{\gamma-1}{2}\left(\frac{V}{a_t}\right)_2^2}{1 - \frac{\gamma-1}{2}\left(\frac{V}{a_t}\right)_1^2}\right] \tag{3.15}$$

$$K_t = \frac{P_{t1} - P_{t2}}{\frac{1}{2}\rho_1 V_1^2}$$
$$= \frac{1 - (P_{t2}/P_{t1})}{\frac{1}{2}\gamma(P_{s1}/P_{t1})M_1^2} \tag{3.16}$$

- Rake Supports – Two rake support arrays, each with 8 arms, are located sequentially to reduce blockage in the expanded duct downstream from the AIP. The pressure loss, ΔP_t, due to the rake supports are estimated using Equation 3.17 from ESDU [35]

$$\Delta P_t = \frac{1}{2}\rho V^2 k \left(\frac{S}{A}\right) \beta_c C_{Df} \tag{3.17}$$

where

$$\beta_c = {}^{1}\!/_{(1 - m\,S/A)} \tag{3.18}$$

with β_c representing a blockage correction factor, k representing the velocity profile correction ratio which is unity for uniform flow, C_{Df} representing the free-air drag coefficient, S representing the frontal area of the body, A representing the cross-sectional area of the pipe, m representing the wake expansion factor which tends to unity for ${}^{S}\!/_{A} > 0.1$.

- Annular Diffuser – The location of the cone in a diverging duct creates an annular diffuser with associated losses for the subsonic flow downstream from the normal shock. Subsonic-diffuser data was characterised from NACA RM-L56F05 [36] by a surface fit, as illustrated in Figure 3-5, and is defined by a 4th order polynomial with two variables, an angle parameter, 2θ and a boundary-layer displacement thickness, δ_1^*/R_1.

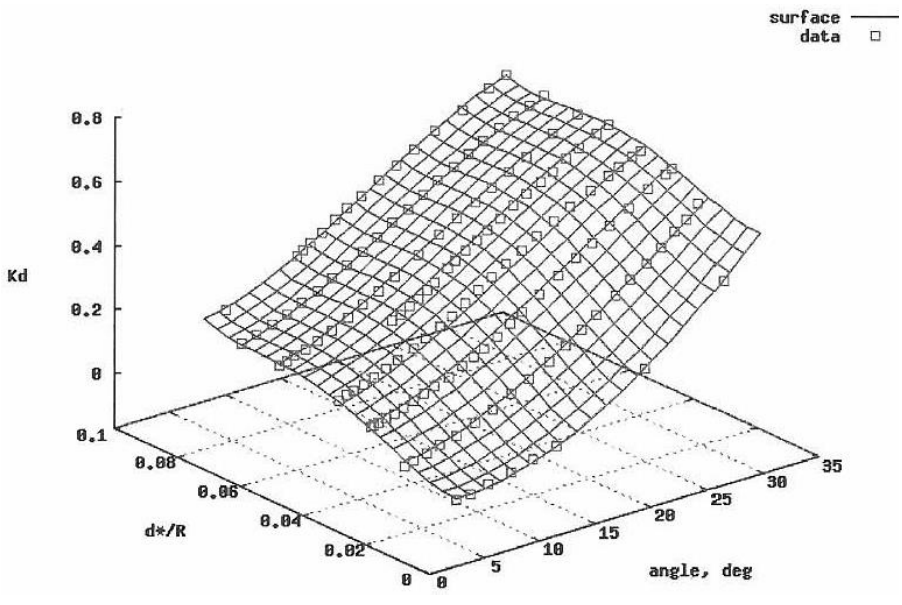

Figure 3-5 : Derived annular diffuser loss factor model, excluding friction [1]

The pressure loss, ΔP_t, is calculated using Equation 3.19 [36]

$$\Delta P_t = K_d q \left(1 - \frac{1}{A_R}\right)^2 \tag{3.19}$$

where A_R is the ratio of the diffuser exit area to inlet area, K_d represents a diffuser loss factor which is calculated using the 4th order polynomial in Equation 3.20 [1]

$$\begin{aligned} K_d = \; & C_0 + C_1 x + C_2 x^2 + C_3 x^3 + C_4 x^4 + C_5 y + C_6 y^2 + C_7 y^3 + C_8 y^4 \\ & + C_9 x^3 y + C_{10} x^2 y^2 + C_{11} x y^3 + C_{12} x^2 y + C_{13} x y^2 + C_{14} x y \end{aligned} \tag{3.20}$$

where

$x = 2\theta$
$y = \delta_1^*/R_1$
C_0 = 4.0975E-02
C_1 = -8.0922E-03
C_2 = 1.0993E-03
C_3 = -9.8590E-06
C_4 = 4.9515E-08
C_5 = -2.8964E+00
C_6 = 3.2265E+02
C_7 = -6.0759E+03
C_8 = 3.5287E+04
C_9 = -2.3226E-04
C_{10} = 1.5764E-01
C_{11} = 4.9412E+00
C_{12} = -8.7586E-03
C_{13} = -6.0306E+00
C_{14} = 5.2686E-01

- Normal Shock – The arrangement of a conical mass flow plug in a duct as illustrated in Figure 3-4, creates a converging-diverging duct where, with appropriate geometry and back pressure, the flow will go sonic at the throat and accelerate to supersonic in the diverging section. With an appropriate backpressure, the flow will decelerate to subsonic conditions through a normal shock at some point in this diverging section. The stagnation pressure ratio across the shock, P_{ty}/P_{tx}, is calculated using Equation 3.21 [27] which will allow for the determination of the pressure loss due to the normal shock.

$$\frac{P_{ty}}{P_{tx}} = \left[\frac{\frac{\gamma+1}{2} M_x^2}{1 + \frac{\gamma-1}{2} M_x^2}\right]^{\frac{\gamma}{\gamma-1}} \left[\frac{2\gamma}{\gamma+1} M_x^2 - \frac{\gamma-1}{\gamma+1}\right]^{\frac{1}{1-\gamma}} \tag{3.21}$$

Where M_x represents the supersonic Mach number before the shock. This Mach number is determined by an iterative process. With the area along the duct determined earlier in the Excel model, the area ratio A/A_t was calculated by dividing the area with the minimum throat area. The supersonic Mach number, M_x, was determined by calculating the area ratio, $A/A_{t_{sup}}$, using Equation 3.1, such that $A/A_t - A/A_{t_{sup}} \to 0$.

An Excel spreadsheet was used to develop a model that would enable the determination of the target backpressure and the mass flow rate for choked conditions at various wind tunnel stagnation pressures and mass flow plug positions. The backpressure and mass flow rate was determined by an iterative process as described by the flowchart in Figure 3-6.

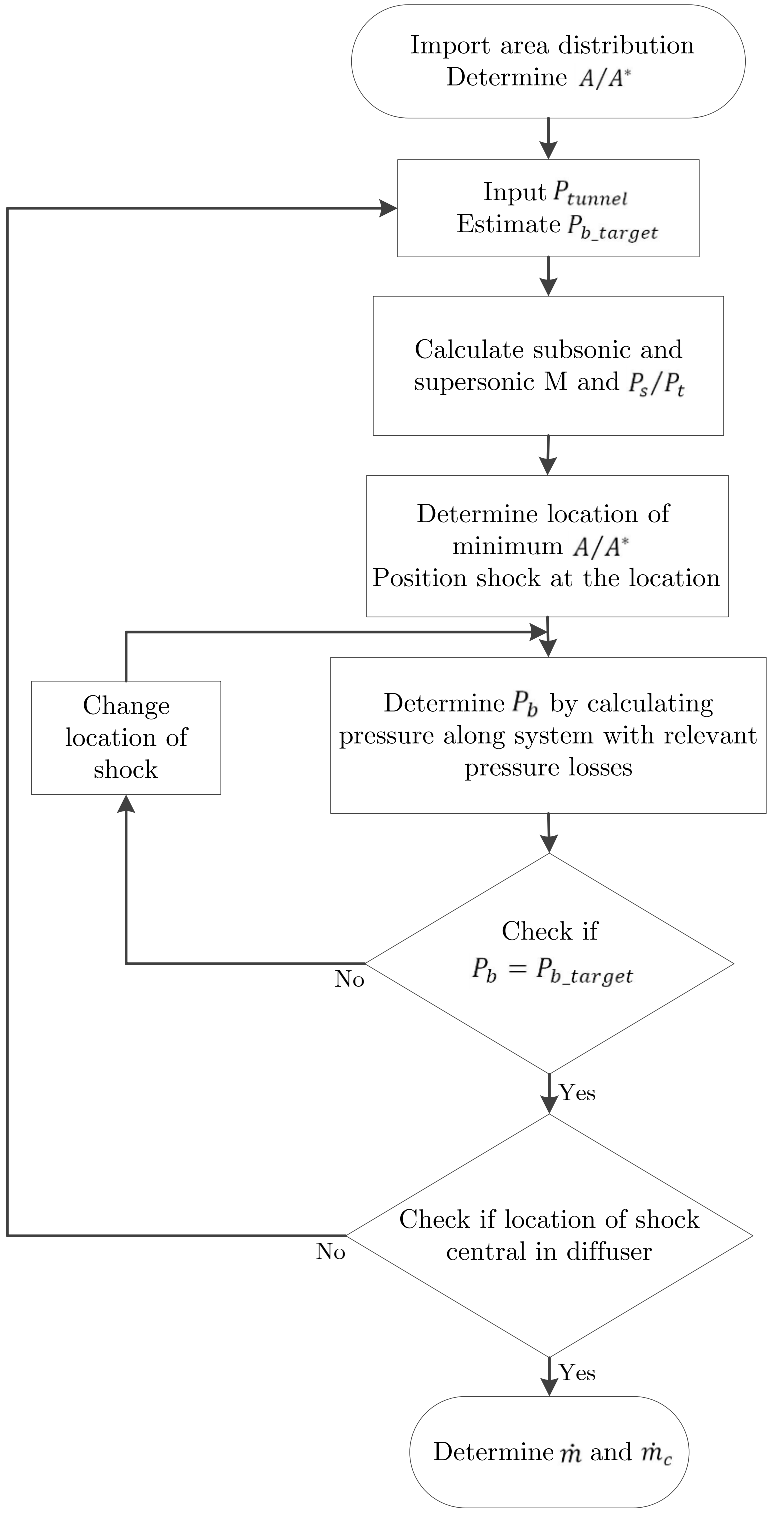

Figure 3-6 : Flowchart showing the determination process of backpressure and mass flow rate

The area distribution determined in Section 3.1.1 was imported into the Excel model. The throat area, A^*, was determined by finding the minimum area along the system. The area ratio, A/A^*, along the system was determined by dividing the area with A^*. The model requires the input of the wind tunnel stagnation pressure, P_{tunnel}, and an estimate of the target backpressure, P_{b_target}. The Mach number along the duct is subsonic upstream of the throat and downstream of the shock, and supersonic from the throat to the shock.

The area ratios for a range of subsonic Mach numbers were determined using Equation 3.1 as illustrated by the blue dots in Figure 3-7. Regression analysis was performed to determine the most feasible curve fit as shown by the red curve illustrated in Figure 3-7. The curve is defined by Equation 3.22

$$\begin{aligned}\frac{A}{A^*_{sub}} = {} & 5.78704 \times 10^{-1} M^{-1} + 3.47222 \times 10^{-1} M + 6.94444 \times 10^{-2} M^3 \\ & + 4.62963 \times 10^{-3} M^5\end{aligned} \tag{3.22}$$

where A/A^*_{sub} represents the subsonic area ratio, M represents the subsonic Mach number.

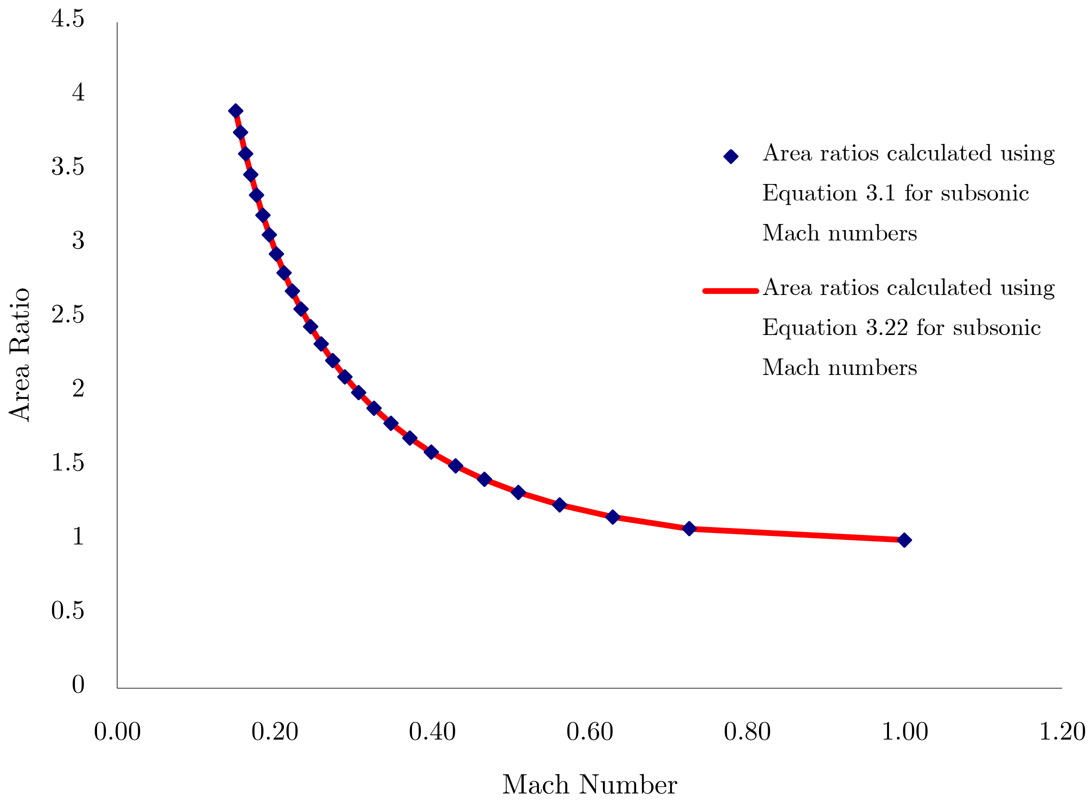

Figure 3-7 : Area ratio determined two ways for subsonic Mach numbers

The subsonic Mach number, for the model, was determined by an iterative process where the area ratio, A/A^*_{sub}, was calculated using Equation 3.22, such that $A/A^* - A/A^*_{sub} \rightarrow 0$.

The supersonic Mach number is determined by an iterative process where the area ratio, A/A^*_{sup}, is calculated using Equation 3.1, such that $A/A^* - A/A^*_{sup} \rightarrow 0$. The subsonic Mach number after the shock, M_y, is calculated using Equation 3.23 [27]

$$M_y^2 = \frac{M_x^2 + \frac{2}{\gamma - 1}}{\frac{2\gamma}{\gamma - 1} M_x^2 - 1} \tag{3.23}$$

where M_x represents the supersonic Mach number before the shock. The pressure ratio, P_s/P_t, is calculated using Equation 3.24 [27]

$$\frac{P_s}{P_t} = \left(1 + \frac{\gamma - 1}{2} M^2\right)^{\gamma/_{1-\gamma}} \tag{3.24}$$

where M represents the relevant Mach number. The initial location of the shock was at the minimum A/A^*, *i.e.* the throat, along the duct. The position of the normal shock in the annular diffuser is moved from the throat region downstream until the pressures behind the mass flow plug matches the target backpressure. The backpressure was determined by calculating the relevant pressures losses along the duct as described earlier in this section. The calculated backpressure was analysed against the target backpressure. If the calculated backpressure did not match the target backpressure, the location of the shock was moved downstream in the diffuser and the backpressure was recalculated. However, if the calculated backpressure equalled the target backpressure, the position of the shock was analysed. For a low backpressure, *i.e.* high-pressure difference, the shock advances far into the annular diffuser which leads to an unreasonable demand on the performance required from the ejector. For a high backpressure, *i.e.* low-pressure difference, the shock moves upstream towards the throat but cannot be allowed to disappear altogether or else the benefits of using a choked plug are lost. An appropriate location of the shock was estimated to be at the centre of the diffuser. If the location of the shock was not approximately central in the diffuser, the estimated back pressure was required to be increased or decreased according to the location of the shock. However, if the shock location was central in the diffuser, the mass flow rate was calculated using Equation 3.25 [27] as the flow is choked at the throat.

$$\begin{aligned} \dot{m} &= \rho A V \\ &= \frac{P_s}{RT_s} V A^* \end{aligned} \tag{3.25}$$

where P_s represents the static pressure, which was calculated using the pressure ratio from Equation 3.24 multiplied by the stagnation pressure, A^* represents the area at the throat, R is the specific gas constant $R = 287.1 J/kg.K$ [27], T_s represents the static temperature, which was determined using the temperature ratio from Equation 3.26 [27] multiplied by the stagnation temperature $T_t = 315K$, and V represents the velocity which was calculated using Equation 3.27 [27]

$$\frac{T_s}{T_t} = \left(1 + \frac{\gamma - 1}{2} M^2\right)^{-1} \tag{3.26}$$

$$\begin{aligned} V &= Ma \\ &= M\sqrt{\gamma R T_s} \end{aligned} \tag{3.27}$$

The corrected mass flow rate was calculated using Equation 3.28 [37]

$$\dot{m}_c = \frac{\dot{m}\sqrt{\theta_t}}{\delta_t} \tag{3.28}$$

where

$$\theta_t = \frac{T_t}{T_{ref}} \tag{3.29}$$

$$\delta_t = \frac{P_t}{P_{ref}} \tag{3.30}$$

with the reference temperature $T_{ref} = 288.15K$ and reference pressure $P_{ref} = 101.325kPa$ [38]. The above process allows for the pressures, temperatures and Mach number along the duct to be determined as well as the mass flow rate through the system. These parameters are required to facilitate the design of an ejector. Table 3-1 provides the resulting mass flow rates and target backpressures for various wind tunnel stagnation pressures and mass flow plug displacements. A negative plug displacement depicts the mass flow plug translating upstream towards the AIP.

Table 3-1 : Resulting mass flow rates and target backpressure for various wind tunnel stagnation pressures and plug displacements

P_{tunnel} [kPa]	Plug Displacement [mm]	$\dot{m}$ [kg/s]	$\dot{m}_c$ [kg/s]	P_{b_target}[kPa]
240	-95	1.20	0.53	180
	-70	1.60	0.71	165
	-30	1.91	0.84	140
200	-95	1.00	0.53	160
	-70	1.33	0.71	145
	-30	1.59	0.84	125
150	-95	0.75	0.53	120
	-70	1.00	0.70	110
	-30	1.19	0.84	100
100	-95	0.50	0.53	80
	-70	0.67	0.70	75
	-30	0.79	0.84	70
50	-95	0.25	0.53	40
	-70	0.33	0.70	35
	-30	0.40	0.84	30

3.2 Design of the Mass Flow Generation System

An ejector, as described in Section 2.1.1.1, will be employed as the mass flow generation system. The constant-area mixing model, as described in Section 2.2.1, was chosen as the design for an ejector. The ejector was designed using the ESDU 92042 computer software described in Section 2.3 and verified using Computational Fluid Dynamics (CFD) as outlined in the subsequent sections. The method used to design the ejector is explained in the Design Methodology subsection.

3.2.1 ESDU 92042

3.2.1.1 Quick Design Procedure

The quick design procedure from ESDU 92042 was the method employed to design an ejector. This method is restricted to ejectors with constant-area mixing and air as both working fluids. A schematic of a typical ejector configuration is shown in Figure 3-8 (a) and a parallel sided mixing duct, *i.e.* constant-area mixing, is illustrated in Figure 3-8 (b).

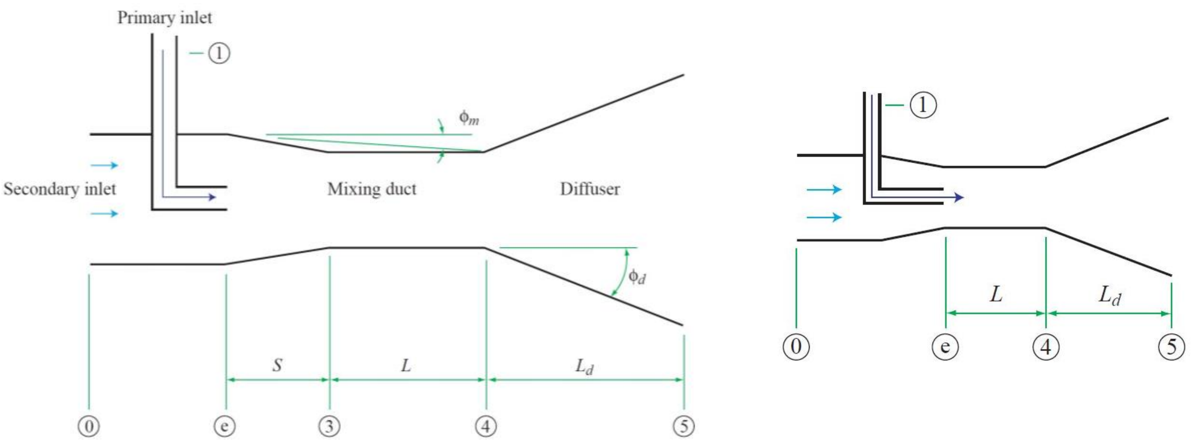

(a) Ejector configuration

(b) Constant-area mixing duct, with S=0

Figure 3-8 : ESDU 92042 schematic ejector [10]

The primary inlet represents high-pressured air from a compressor. Two compressor pressures, 12bar and 25bar, were analysed for the design of an ejector. The 12bar compressor pressure can be supplied by the existing High Speed Wind Tunnel and the 25bar compressor is the maximum portable supply pressure that can be rented. The 12bar compressor has an outlet temperature of 313.1K and a mass flow rate of 1.28kg/s, whereas the 25bar compressor has an outlet temperature of 383.1K and a mass flow rate of 0.554kg/s. The secondary inlet represents the conditions aft of the conical mass flow plug which were determined by the process described in Section 3.1.2. The diameter at the exit plane of the diffuser was required to be equal to the diameter aft of the plug, as illustrated in Figure 3-2 *i.e.* 0.123m, to allow for a slender designed system.

The quick design procedure requires input data of pressures, temperatures, mass flow rates and dimensions in order for an ejector to be design. The input data required for the quick design procedure are listed in Table 3-2.

Table 3-2 : Input data required for quick design procedure

P_{t0}	Secondary stream entry total pressure. This is the determined target backpressure from Section 3.1.2.
P_{t1}	Primary stream entry total pressure. This is the pressure from the compressor.
$\dot{m}''$	Secondary stream mass flow rate. This is the determined mass flow rate from Section 3.1.2.
$\dot{m}'$	Primary stream mass flow rate. This is the mass flow rate of the compressor.
$\dot{m}'' + \dot{m}'$	Mixing duct mass flow rate.
T_{t0}	Secondary flow entry total temperature. This is the temperature determined from Section 3.1.2.
T_{t1}	Primary flow entry total temperature. This is the temperature of the air from the compressor.
$(S+L)/d_4$	Mixing duct length to diameter ratio. A value in the range $8 \leq (S+L)/d_4 \leq 10$ is recommended to achieve complete energy mixing under most conditions.
d_5	Diffuser exit diameter.
$\lvert\phi_d\rvert$	Diffuser wall angle. A value in the range $3 \leq \phi_d \leq 5$ is recommended.

The quick design method calculates the diffuser exit pressure and determines the overall areas and lengths of the primary nozzle, mixing duct and diffuser. The output results determined from the quick design procedure are listed in Table 3-3.

Table 3-3 : Output results from quick design procedure

P_{t5}	Diffuser exit total pressure.
P_{t1}/P_{t5}	Primary pressure ratio.
P_{t5}/P_{t0}	Secondary pressure ratio.
P_{t1}/P_{t0}	Primary to secondary pressure ratio.
A_{th}	Primary nozzle throat area.
A_e	Primary nozzle exit area
A_e/A_{th}	Primary nozzle exit area to throat area ratio.
A_4	Mixing duct cross-sectional area.
A_5	Diffuser exit area.
$S+L$	Mixing duct length (S=0 for constant-area mixing duct)
L_d	Diffuser length.
L_d/d_4	Diffuser length to diameter ratio.

The ESDU 92042 software can only be applied to designs where the secondary to primary mass flow ratio ranges from 0.05 to 1, as illustrated in Figure 2-22. Mass flow ratios that do not lie in this range results in data being less reliable. A maximum mass flow ratio of 2 is allowed by ESDU for the design of an ejector, however the data obtained for the design will be less reliable. ESDU 92042 does not determine an ejector design for mass flow ratios greater than 2.

3.2.1.2 Performance Prediction Calculation

The performance prediction calculation from ESDU 92042 [10] determines the outlet conditions and the flow conditions throughout the ejector given the physical dimensions of the ejector determined by the quick design procedure. The performance prediction procedure requires input of the ejector dimensions, loss factors and a range of entry flow conditions in order for the performance of the ejector to be determined. ESDU 92042 states that the output from the design evaluation is taken as the input for a performance prediction calculation and the results obtained for the performance parameters agree with the initial data input, within the computational accuracy available [10]. The input data required for the performance prediction procedure are listed in Table 3-4 with reference to Figure 3-8.

Table 3-4 : Input data required for performance prediction calculation

γ'	The ratio of the specific heat capacities of the primary gas.
R'	The gas constant of the primary gas.
γ''	The ratio of the specific heat capacities of the secondary gas.
R''	The gas constant of the secondary gas.
C_D	Primary nozzle discharge coefficient accounts for losses in the primary nozzle.
K	Mixing duct momentum loss factor allows for all losses in the mixing duct. For a single nozzle ejector a value of $K = 0.87$ may be taken.
η_d	Diffuser total pressure recovery $\eta_d = P_{t5}/P_{t4}$ with typical values in the range 0.9 to 0.96.
η_i	Secondary flow inlet efficiency $\eta_i = P''_{te}/P_{t0}$.
A_{ME}	Area ratio $A_{ME} = A_4/A_e$.
d_{th}	Primary nozzle throat diameter.
d_e	Primary nozzle exit diameter.
d_4	Mixing duct diameter.
d_5	Diffuser exit diameter.
$(S+L)/d_4$	Mixing duct length to diameter ratio.
L_d/d_4	Diffuser length to diameter ratio.
P_{t1}	Primary nozzle entry total pressure.
T_{t1}	Primary nozzle entry total temperature.

P_{t0}	Secondary stream entry total pressure.
T_{t0}	Secondary stream entry total temperature.

The performance prediction calculates the diffuser exit pressure, the primary and secondary stream mass flow rates and the Mach number at various planes. The output results determined from the performance prediction procedure are listed in Table 3-5.

Table 3-5 : Output results from performance prediction calculation

P_{t5}	Diffuser exit total pressure.
P_{t1}/P_{t5}	Primary pressure ratio.
P_{t5}/P_{t0}	Secondary pressure ratio.
$\dot{m}''$	Secondary stream mass flow rate.
$\dot{m}'$	Primary stream mass flow rate.
M_3'	Primary nozzle exit Mach number.
M_3''	Secondary stream Mach number at nozzle exit plane.
M_4	Stream Mach number at mixing duct exit plane.
M_5	Stream Mach number at diffuser exit plane.

3.2.2 Computational Method

CFD simulations were performed to validate the ESDU 92042 software and evaluate the mass flow rates for different wind tunnel total pressures for different designs. Two-dimensional and three-dimensional simulations were performed for different designs with certain aspects of the analysis being common in both simulations. The two-dimensional and three-dimensional simulations (pre-processing, processing and post processing) were computed using the commercially available flow solver, STAR-CCM+ V9.06, where a coupled-flow solver was employed with the equation of state of the fluid being modelled as an ideal gas. The solver settings for three-dimensional simulations were updated to enable the continuity convergence accelerator, grid sequencing initialization and AMG linear solver [39].

The ejector geometry was determined using ESDU 92042 software, as described in Section 3.2.1, and generated using SolidWorks V16 Computer Aided Design (CAD) software. Two nozzle designs were explored for the primary nozzle, namely a minimum length nozzle as described in Section 2.4.1.1 and a Rao TOP nozzle as described in Section 2.4.1.2. The minimum length nozzle and the Rao TOP nozzle were determined using the Matlab codes as represented in Appendix A.1 [40] and Appendix A.2 [19] respectively. The Matlab codes determine the points that represent the nozzle contour. These points were imported into SolidWorks V16 as a curve in order to generate the primary nozzle geometry. The ejector geometry was saved as a parasolid and imported into STAR-CCM+.

3.2.2.1 Grid Sensitivity Studies

The two-dimensional simulations employed a hexahedral mesh, which was first generated in three-dimensional and converted into a two-dimensional mesh. The generated hexahedral mesh provided a high-quality grid with minimal cell skewness. A polyhedral mesh was employed for the three-dimensional simulations, with a refined boundary layer mesh along the inner walls to improve the accuracy of the flow solution. The polyhedral mesher provides a balanced solution for complex mesh generation problems by approximately reducing the cell count by five times as compared to a tetrahedral mesh. The surface remesher tool was employed to re-tessellate the surfaces of the imported geometry. This allows the overall quality of the surfaces to be improved which results in an optimised mesh generation process. A mesh refinement was generated using a volumetric control with a cylinder volume shape in the primary nozzle and mixing duct zone [41].

Grid sensitivity studies were completed for the three-dimensional simulations to ensure that the results were independent of the grid resolution of the simulations. Figure 3-9 illustrates the entrained mass flow rate of an ejector at $P_{tunnel} = 100kPa$ and wind tunnel conditions at $M = 0.8$ for various grid sizes. A non-dimensional grid size (G) was calculated by normalising the minimum element size for each grid by the finest grid's minimum element size. A second order polynomial curve was fitted to the entrained mass flow rate data in order to extrapolate the entrained mass flow rate at $G = 0$, which was used as a reference point to determine whether solutions were grid independent.

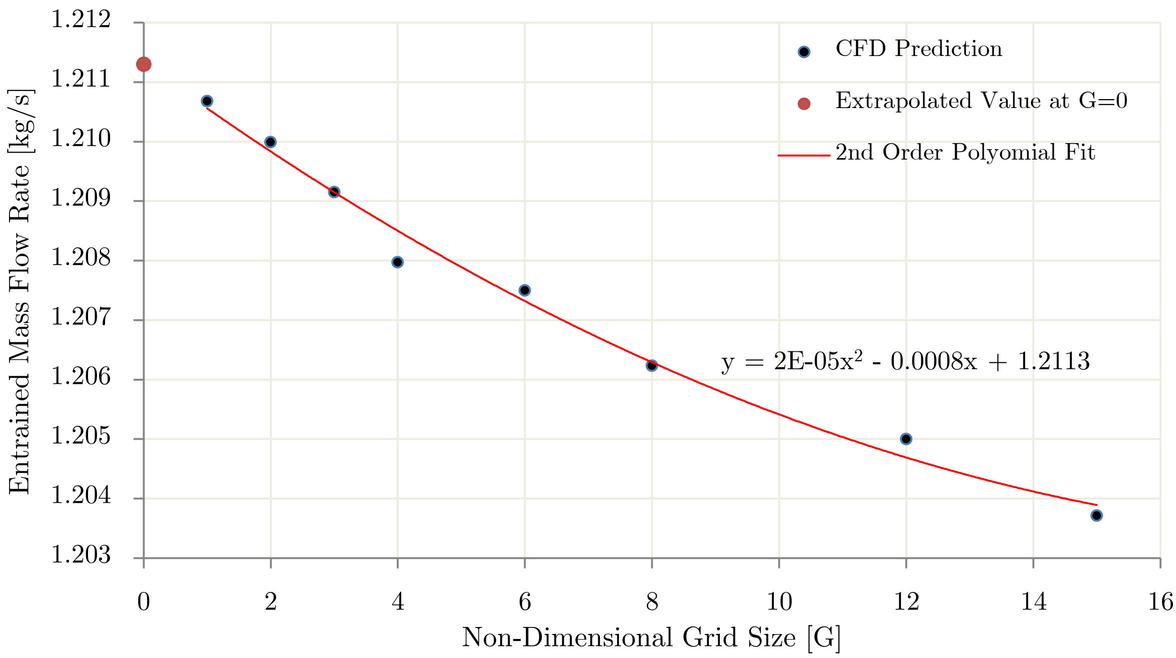

Figure 3-9 : Grid convergence study of an ejector at $P_{tunnel} = 100kPa$ and wind tunnel conditions at $M = 0.8$

The maximum acceptable deviation of the entrained mass flow rate must be within $\pm 0.5\%$ of the value at $G = 0$. Figure 3-10 illustrates that any solution computed on grids with sizes of $G \leq 8$ will have an acceptable discretisation error. For flow diagnostics purposes, all solutions were computed at a non-dimensional grid size of 4 *i.e.* base size of 40mm.

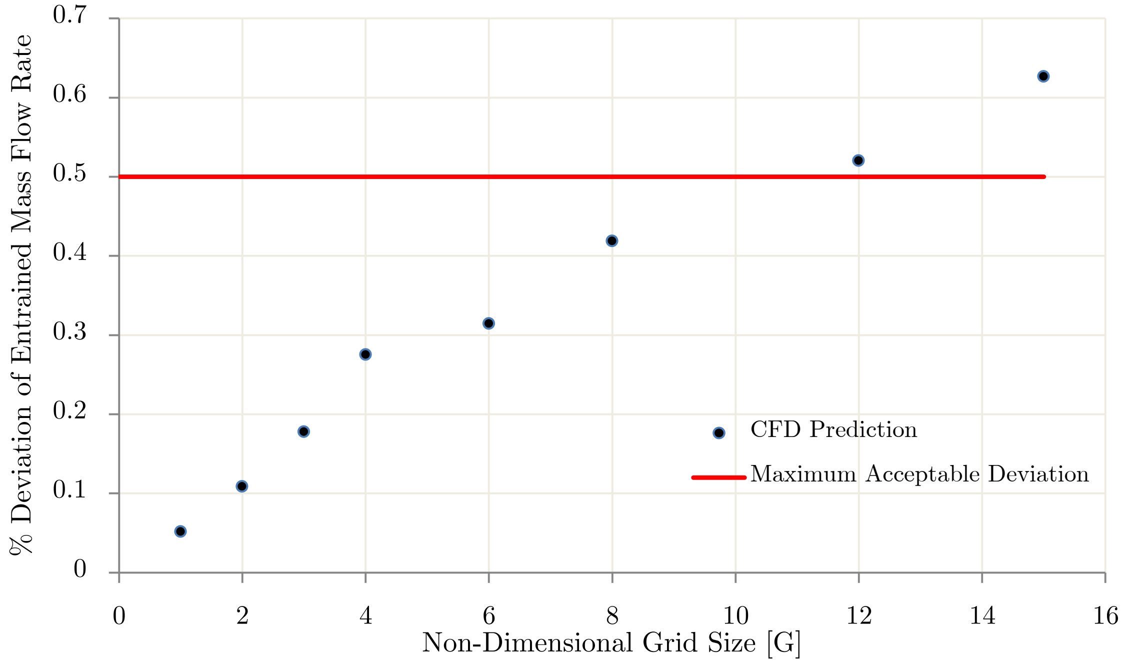

Figure 3-10 : Percentage deviation of the entrained mass flow rate for various grid sizes

3.2.2.2 Turbulence Modelling

STAR-CCM+ has several turbulence models with the most common models being k-epsilon, k-omega and Spalart-Allmaras. The Spalart-Allmaras [41] turbulence model yields the best results for attached boundary layers and flows with mild separation such as flow over a wing, fuselage or other aerospace external flow applications. However, the model is not suited to applications involving jet-like free-shear regions, hence the two-equation k-epsilon and k-omega models should be examined. The k-epsilon and k-omega models are similar in that two transport equations are solved, but differ in the choice of the second transported turbulence variable. The k-omega turbulence model is sensitive to inlet boundary conditions for internal flows, a problem that does not exist for the k-epsilon turbulence model [41]. Hence the Reynolds Averaged Navier Stokes (RANS) equations were solved along with the k-epsilon turbulence model as internal flows are simulated.

3.2.2.3 Wall y⁺ Strategy

In addition to the grid sensitivity studies, the non-dimensional wall distance (y^+) values were monitored to determine the appropriate grid configuration for the selected turbulence model. The Realizable k-epsilon two-layer model was employed, this model offers the most mesh flexibility and has an all-y^+ wall treatment. The all-y^+ wall treatment attempts to emulate the high-y^+ wall treatment for coarse meshes and the low-y^+ wall treatment for fine meshes. The high-y^+ treatment assumes that the near-wall cell lies within the logarithmic region of the boundary layer and the low-y^+ treatment assumes that the viscous sublayer is properly resolved. The Realizable k-epsilon two-layer model provides good results on fine meshes *i.e.* $y^+ \leq 1$ and coarse meshes *i.e.* $y^+ \geq 30$, and also produces the least inaccuracies for intermediate meshes *i.e.* $1 < y^+ < 30$ [41]. The wall y^+ value for the solution of an ejector at a non-dimensional grid size of 4 is illustrated in Figure 3-11. Figure 3-12 illustrates the values of $y^+ \geq 30$ of an ejector at a non-dimensional grid size of 4. Since the Realizable k-epsilon two-layer model employs an all-y^+ wall treatment and the obtained y^+ values for the solution of an ejector satisfies the y^+ values for the selected turbulence model, simulations were deemed acceptable for the selected grid configuration.

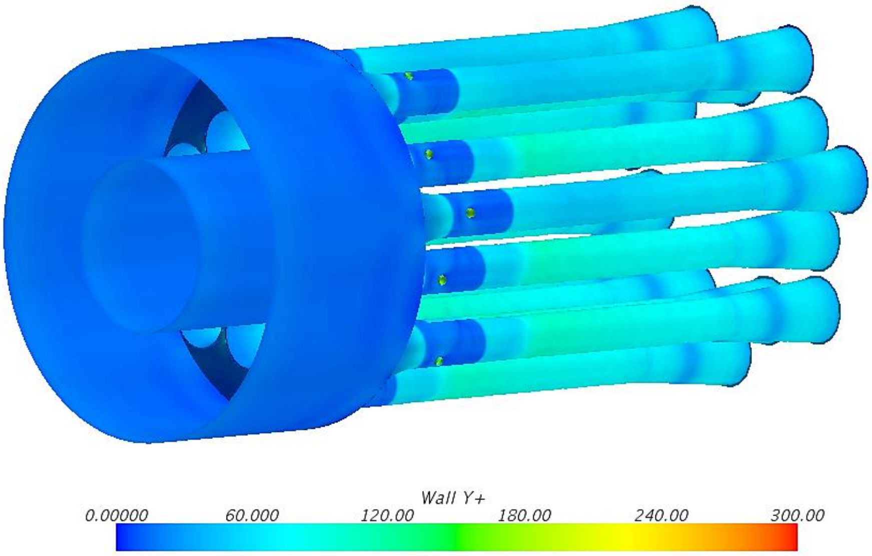

Figure 3-11 : Wall y^+ values at a non-dimensional grid size of 4 for an ejector

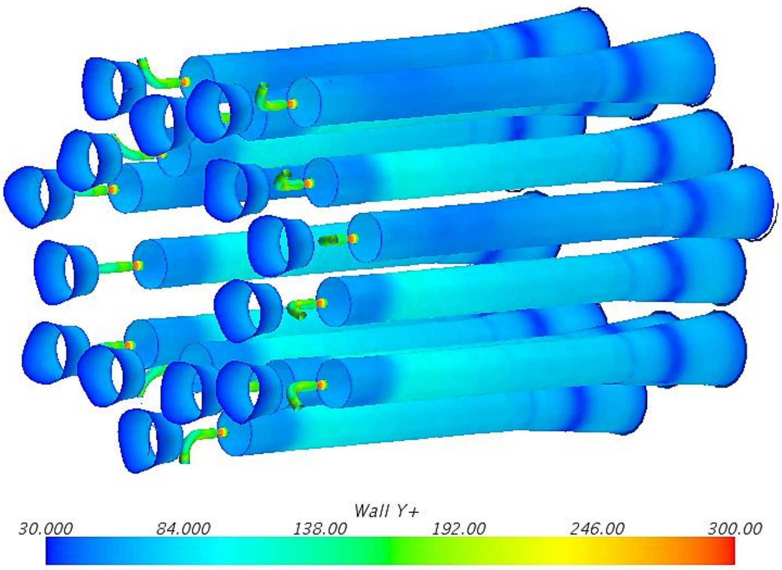

Figure 3-12 : Wall $y^+ \geq 30$ at a non-dimensional grid size of 4 for an ejector

3.2.3 Design Methodology

Davis *et al* [6] indicated that the most critical case for sizing any flow generation system is at static and low Mach numbers; and high-pressure conditions. Hence, the ejector was designed for static tests under the pressure conditions of the MSWT. The design of the ejector was achieved by an iterative process involving ESDU 92042 computer software and CFD simulations. Figure 3-13 describes the processes followed to design an ejector to meet the mass flow rate requirements from the flow quantity metering analysis in Section 3.1.

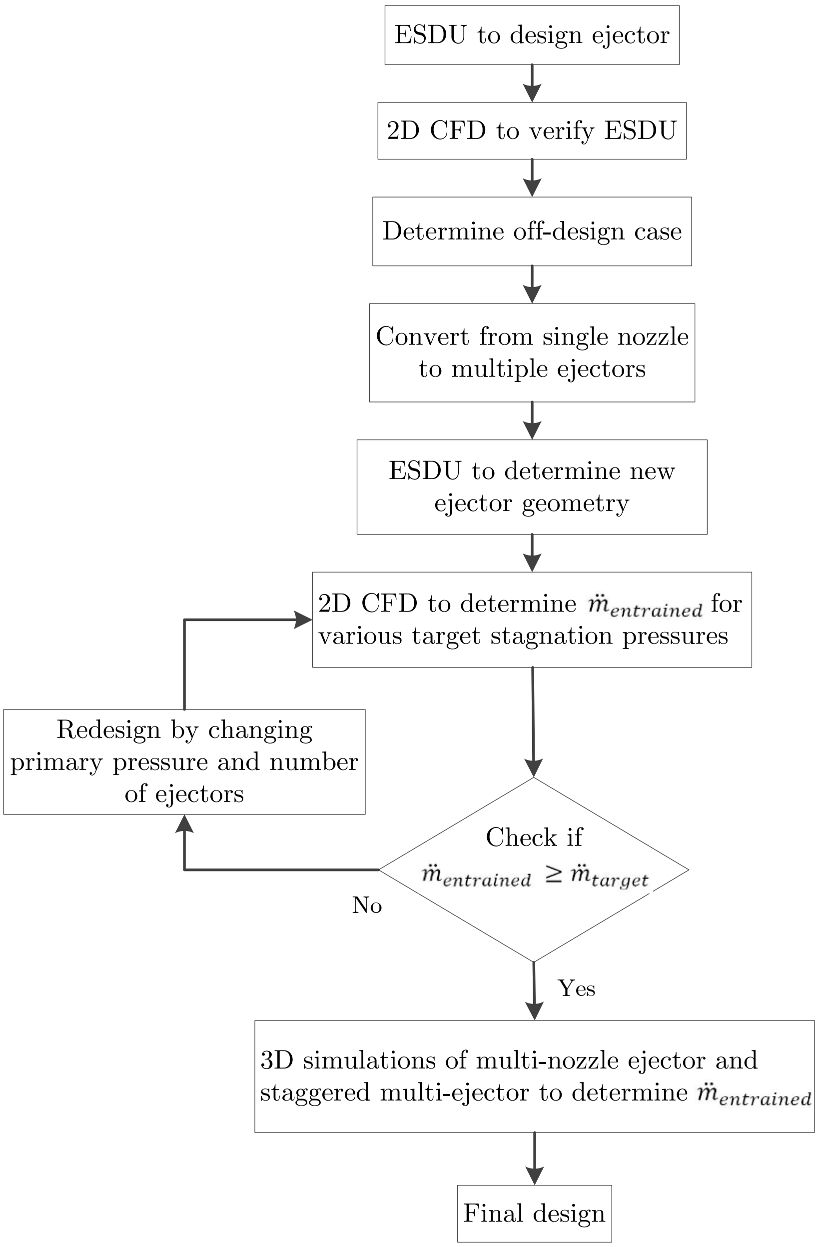

Figure 3-13 : Flowchart showing the design process of an ejector

The ejector was designed using ESDU 92042 computer software, as described in Section 3.2.1. The diffuser wall angle range was investigated, which led to $\phi_d = 5$ deemed feasible as it resulted in a shorter diffuser therefore a shorter ejector being designed. Two primary pressures, 25bar and 12bar, were considered as stated in Section 3.2.1.

Two-dimensional CFD simulations, as described in Section 3.2.2, were performed for 25bar and 12bar primary pressure ejector designs to validate the ESDU 92042 software. Multiple two-dimensional simulations were performed employing various secondary stream entry total pressures, P_{t0}. The geometry of an ejector designed by ESDU 92042 employed in the simulation with the specified boundary conditions is illustrated in Figure 3-14. Since we are concerned with the air flow inside the ejector, an external fluid domain boundary was not required. The inlets to the fluid domain were specified as stagnation inlets, with the secondary inlet boundary conditions set as the input data P_{t0} and T_{t0} from Table 3-2 and the nozzle inlet boundary conditions set as either 25bar or 12bar primary pressure with their respective temperatures as stated in Section 3.2.1. The outlet was specified as a pressure outlet with static conditions determined using the exit pressure P_{t5} calculated by ESDU 92042 and the total mass flow rate, $\dot{m}'' + \dot{m}'$, at the diffuser exit. The ejector and nozzle walls were specified as non-slip solid walls and an axisymmetric plane was used which segmented the flow domain. A hexahedral mesh was employed to the two-dimensional simulations, with the hexahedral mesh around the minimum length nozzle section shown in Figure 3-15.

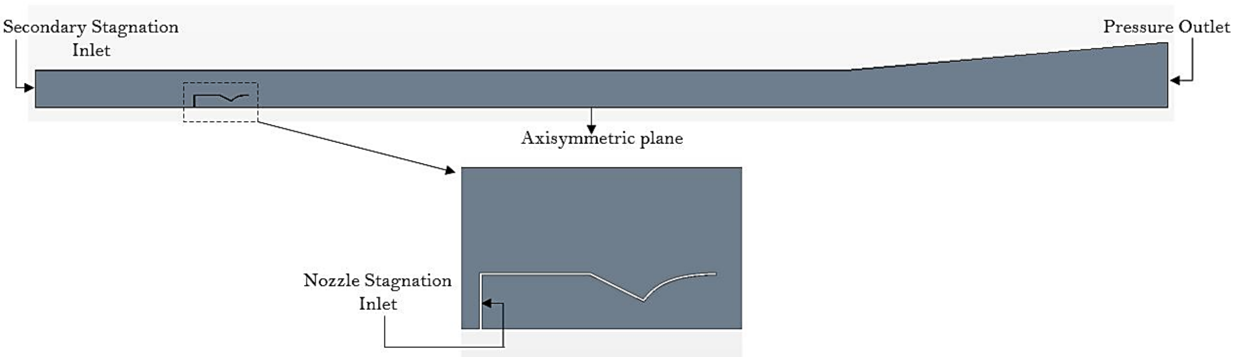

Figure 3-14 : Two-dimensional ejector geometry required as an input for CFD with specified boundary conditions

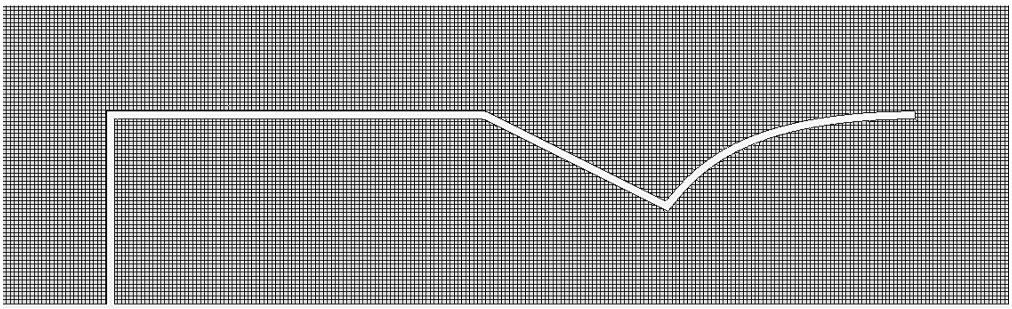

Figure 3-15 : Hexahedral mesh around the minimum length nozzle employed for two-dimensional simulations

ESDU determines the optimum ejector design for a specific set of input data therefore for various secondary pressures, primary pressures and mass flow rates, multiple ejector designs are established. An "off-design" case had to be determined *i.e.* one ejector geometry that would be able to entrain the specified target mass flow rates, as listed in Table 3-1, at different secondary stream total pressures. The "off-design" case was determined by analysing each ejector design obtained by ESDU 92042, to determine which geometrical factors where significantly different. It was established that the mixing duct cross-sectional area was the most significant factor that changed between each ejector design. Two-dimensional CFD simulations, as described in Section 3.2.2 and above, were performed employing a test matrix that was determined by the Modern Design of Experiments (MDOE) method. This test matrix, outlined in Table 3-6, has two factors, mixing duct diameter and secondary stream entry total pressure, and 3 levels per factor *i.e.* minimum (-1), intermediate (0) and maximum (1) which results in 9 CFD simulations. The results from the CFD simulations performed indicated that the minimum mixing duct diameter ejector design was the only ejector to entrain mass flow for the various secondary stream entry total pressures, therefore this ejector was considered to be the "off-design" case.

Table 3-6 : Test Matrix for determining off-design case

	Mixing Duct Diameter	**Secondary Stream Total Pressure**
CFD Simulation	**Factor 1**	**Factor 2**
1	0	1
2	-1	1
3	-1	-1
4	0	-1
5	0	0
6	1	-1
7	-1	0
8	1	0
9	1	1

Since the ejector forms part of a system that will be employed into the MSWT, a simple single nozzle ejector would not be suitable as there are space limitations in the wind tunnel. To overcome the space limitations, the single nozzle 'off-design' ejector was converted into multiple smaller ejectors and hence into a multi-nozzle ejector. The number of smaller multiple ejectors were found by equating the area of the diffuser exit plane of the 'off-design' ejector to the total combined area of the diffuser exit plane of the smaller ejectors. Figure 3-16 and Figure 3-17 illustrates that two configurations would satisfy the above area comparison such that $A_1 = A_2$. The ESDU 92042 software, as mentioned in Section 3.2.1, was used to determine the ejector geometry for both configurations. It should be noted that the translation of the mass flow plug is achieved by a linear actuator located in the annulus, hence the mixing duct and annulus cross-sectional area were analysed to determine the space available for the actuator. Configuration 2 was deemed feasible as it resulted in a more compact system being developed and has the desired space available for the linear actuator.

Configuration 1 – 4 ejectors

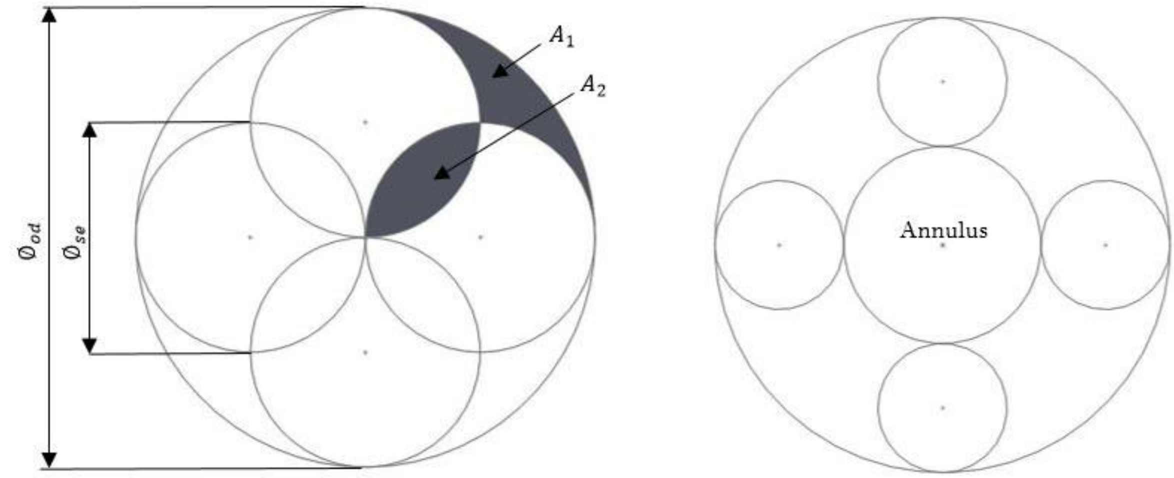

(a) Diffuser exit plane of the 'off-design' ejector to determine area

(b) Mixing duct plane with 4 ejectors

Figure 3-16 : Diffuser exit plane of the 'off-design' ejector and mixing duct plane with 4 ejectors

Configuration 2 – 9 ejectors

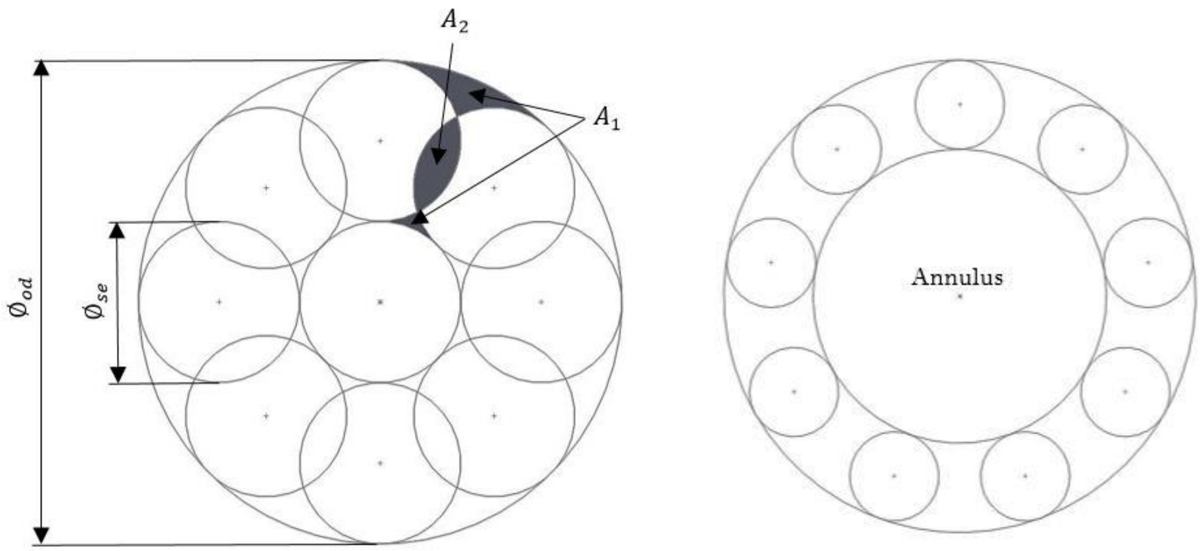

(a) Diffuser exit plane of the 'off-design' ejector to determine area

(b) Mixing duct plane with 9 ejectors

Figure 3-17 : Diffuser exit plane of the 'off-design' ejector and mixing duct plane with 9 ejectors

Two-dimensional CFD simulations, as described in Section 3.2.2 and above, were performed with the ejector geometry of configuration 2 to determine the entrained mass flow rates obtainable at various target stagnation pressures. A check was performed to determine if the entrained mass flow rates of the ejector design met the target mass flow rates from Table 3-1 for the various target stagnation pressures. It was established that the entrained mass flow rate determined with the ejector geometry of configuration 2 did not meet the target mass flow rates.

It should be noted that the ejector was designed at maximum primary pressure and maximum primary mass flow rate, therefore if the determined entrained mass flow rates did not correlate to the target mass flow rates, there is no means of increasing the entrained mass flow rate. However, if the ejector is redesigned at a lower primary pressure and lower primary mass flow rate, this will allow the entrained mass flow rate to increase since the compressor will be able to supply a higher primary pressure and mass flow rate. If the ejector is redesigned at a lower primary pressure, this will allow for the ejector to be run at a higher primary pressure entraining more mass flow and redesigning at a lower primary mass flow rate will allow for the addition of ejectors if the entrained mass flow rates did not meet the target mass flow rates.

Therefore, the ejector was redesigned using the ESDU 92042 software, as mentioned in Section 3.2.1, with a primary pressure of 20bar and a primary mass flow rate of 0.277kg/s. Two-dimensional CFD simulations, as described in Section 3.2.2 and above, were performed with the redesigned ejector geometry simulating maximum primary pressure conditions to determine the entrained mass flow rates obtainable at various target stagnation pressures.

A check was performed to determine if the entrained mass flow rates of the new ejector design met the target mass flow rates from Table 3-1 for the various target stagnation pressures. It was established that the entrained mass flow rate determined with the redesigned ejector did not meet the target mass flow rates, hence the option of increasing the number of ejectors were explored.

The maximum number of ejectors were determined by dividing the total available mass flow rate (0.554kg/s) by the primary mass flow rate obtained at the maximum primary pressure (25bar) simulation. It was established that 14 ejectors would be employed as it results to the maximum available primary mass flow rate. The entrained mass flow rate for the configuration employing 14 ejectors met or exceeded the target mass flow rates. The configuration employing 14 ejectors was used to develop a multi-nozzle ejector and a staggered multi-ejector.

The multi-nozzle ejector, as illustrated in Figure 3-18(a), was obtained by combining the mixing duct areas of the 14 ejectors which resulted in the total mixing duct area. Since the mixing duct need not be cylindrical, as mentioned in Section 2.3, an annular mixing duct was utilised which would allow for the linear actuator to be situated in the annulus, as illustrated in Figure 3-18(b). The area ratio A_5/A_4 and diffuser wall angle $\phi_d = 5$, obtained from ESDU, was used to determine the diffuser geometry. The primary nozzles were spaced equally and arranged in an annular ring, as illustrated in Figure 3-18(c).

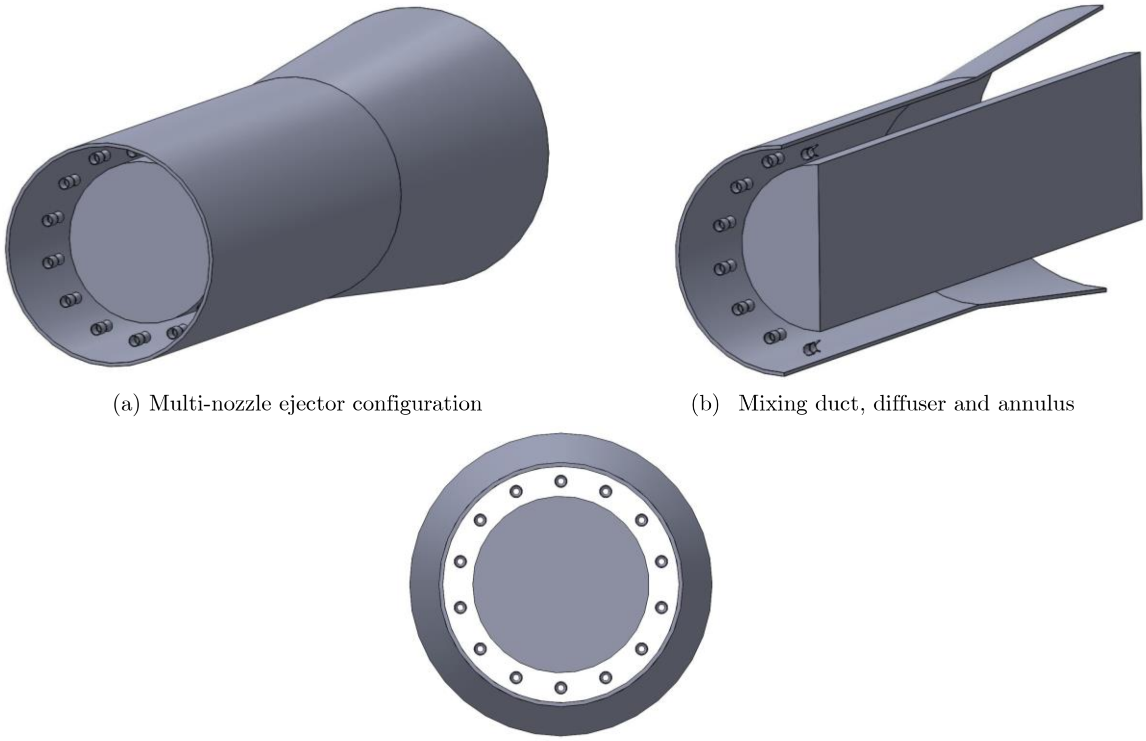

(a) Multi-nozzle ejector configuration (b) Mixing duct, diffuser and annulus

(c) Primary nozzle arrangement

Figure 3-18 : Multi-nozzle ejector

Three-dimensional CFD simulations, as described in Section 3.2.2, were performed to determine the entrained mass flow rate for various secondary stream entry total pressures. A segment of the multi-nozzle ejector was employed in the simulation with the specified boundary conditions illustrated in Figure 3-19. The air flow inside the multi-nozzle ejector was model with the air exiting into the wind tunnel. The inlets to the fluid domain were specified as stagnation inlets, with the secondary inlet boundary conditions set as the input data P_{t0} and T_{t0} from Table 3-2 and the primary nozzle inlet boundary conditions set as 25bar primary pressure with the corresponding temperature as stated in Section 3.2.1. The outlet was specified as a pressure outlet with static conditions corresponding to the MSWT at M=0.6 and P_{t0} from Table 3-2. The ejector, primary nozzle and annulus walls were specified as non-slip solid walls and a symmetry boundary was used since the multi-nozzle ejector is symmetrical. A polyhedral mesh was employed to the three-dimensional multi-nozzle simulations as mentioned in Section 3.2.2.1, with the polyhedral mesh around the Rao primary nozzle section shown in Figure 3-20.

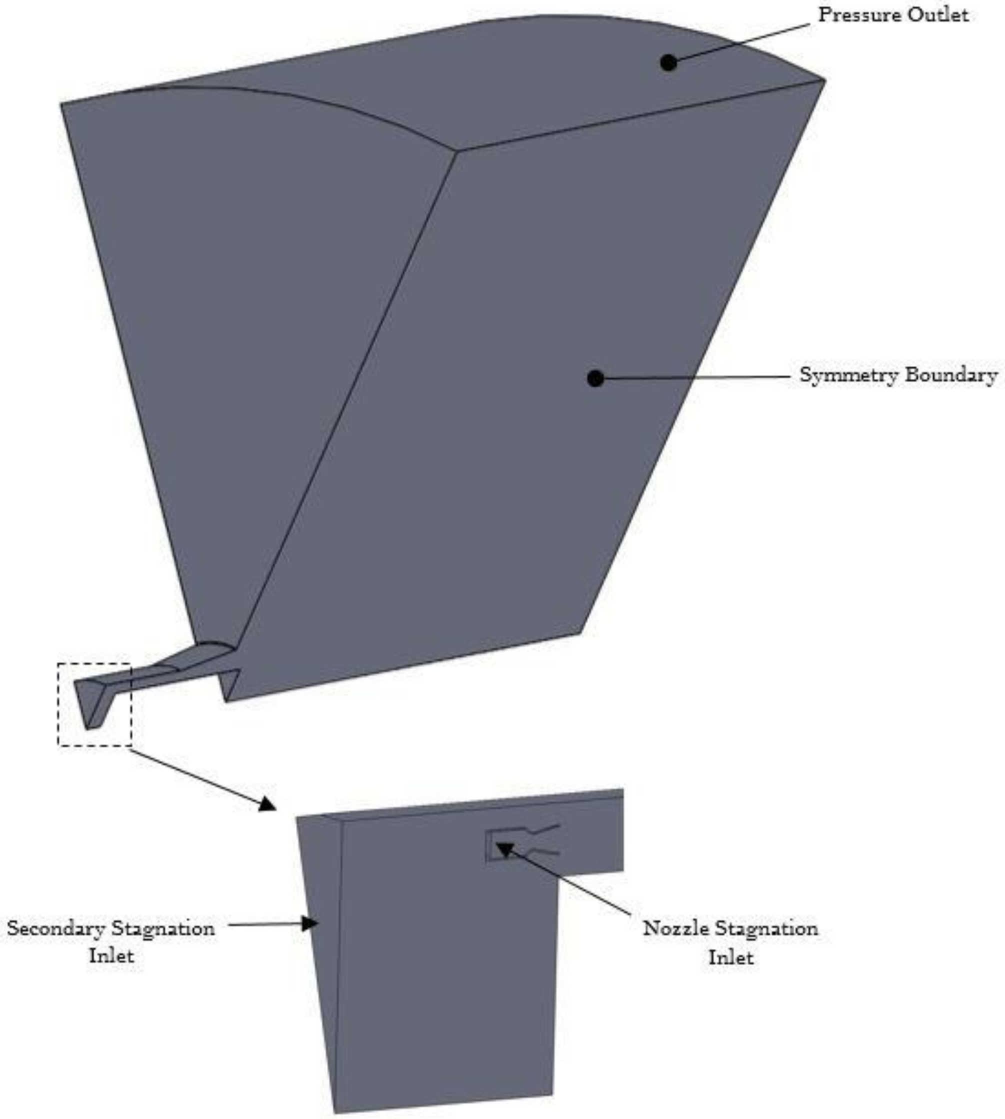

Figure 3-19 : Three-dimensional segment of a multi-nozzle ejector geometry required as an input for CFD with specified boundary conditions

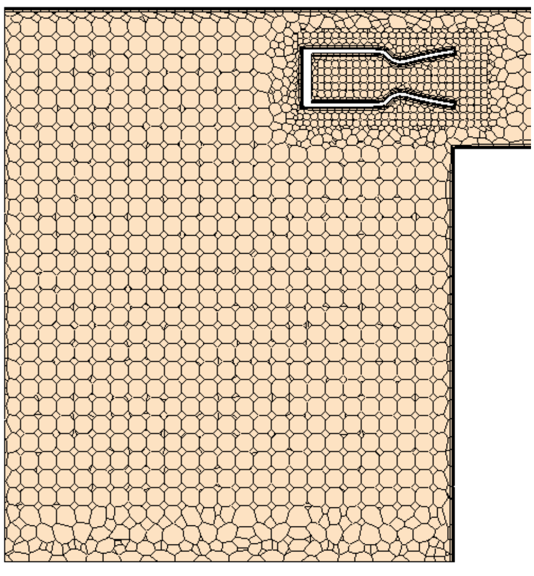

Figure 3-20 : Polyhedral mesh around the Rao nozzle employed for three-dimensional multi-nozzle ejector simulations

The staggered multi-ejector, as illustrated in Figure 3-21(a), employs 14 individual ejectors arranged around an annulus as illustrated in Figure 3-21(b). The ejector employed in the staggered multi-ejector configuration is illustrated in Figure 3-21(c) with a 30° included angle conical inlet employed before the mixing duct as mentioned in Section 2.3.

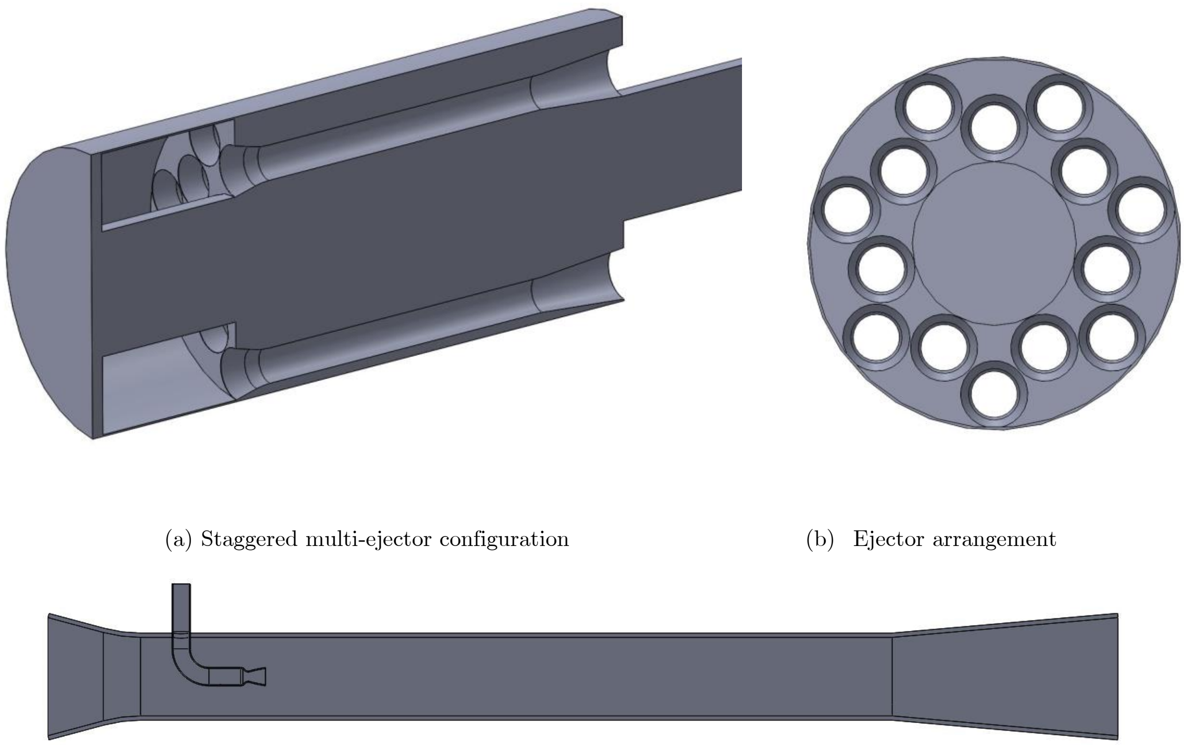

(a) Staggered multi-ejector configuration

(b) Ejector arrangement

(c) Ejector configuration for the staggered multi-ejector

Figure 3-21 : Staggered multi-ejector

Three-dimensional CFD simulations, as described in Section 3.2.2, were performed to determine the entrained mass flow rate for various secondary stream entry total pressures. The three-dimensional geometry of the staggered multi-ejector employed in the simulations with the specified boundary conditions is illustrated in Figure 3-22. The air flow inside the staggered multi-ejector was model with the air exiting into the wind tunnel. The inlets to the fluid domain were specified as stagnation inlets, as illustrated in Figure 3-22(a), with the secondary inlet boundary conditions set as the input data P_{t0} and T_{t0} from Table 3-2 and the nozzle inlet boundary conditions set as 25bar primary pressure with the corresponding temperature as stated in Section 3.2.1. The outlet was specified as a pressure outlet, as illustrated in Figure 3-22(c), with static conditions corresponding to the MSWT at M=0.8 and P_{t0} from Table 3-2. The ejector, primary nozzle and annulus walls were specified as non-slip solid walls illustrated in Figure 3-22(b). A polyhedral mesh as shown in Figure 3-23 was employed to the three-dimensional multi-ejector simulations as mentioned in Section 3.2.2.1.

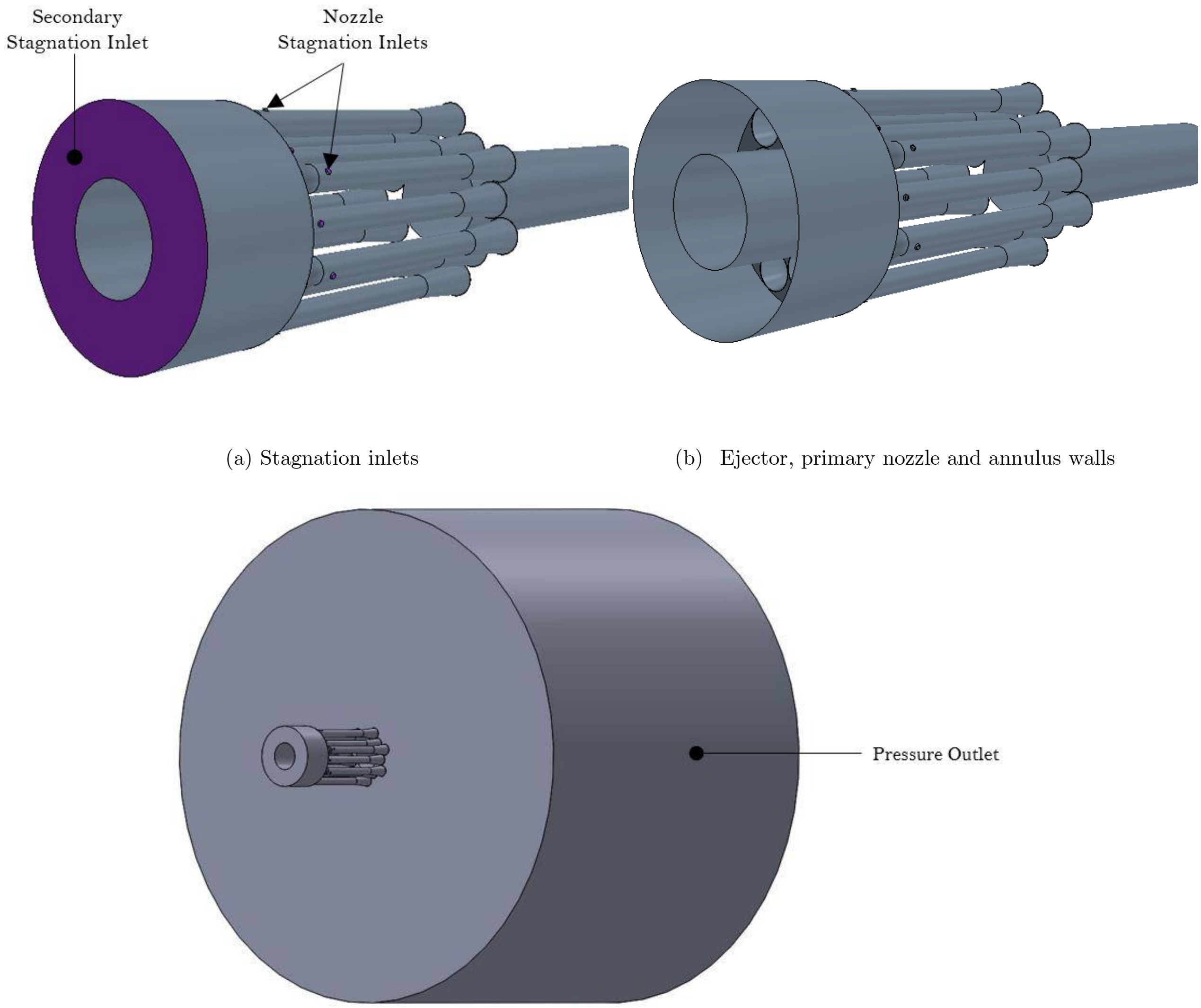

(a) Stagnation inlets

(b) Ejector, primary nozzle and annulus walls

(c) Pressure outlet

Figure 3-22 : Three-dimensional geometry of the staggered multi-ejector required as an input for CFD with specified boundary conditions

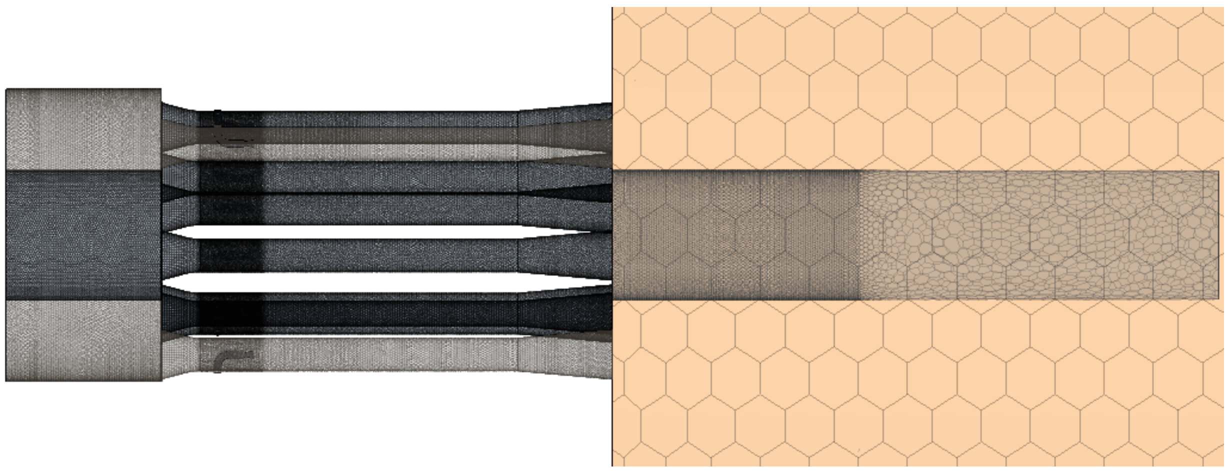

Figure 3-23 : Polyhedral mesh employed for three-dimensional multi-ejector simulations

3.3 Final Design

The controlled induced mass flow system, as illustrated in Figure 3-24, employs a translating conical mass flow plug as a flow quantity metering system and a staggered multi-ejector as the mass flow generation system. The system was designed for an AIP of 80mm with a rake array located aft of the AIP to provide the flow quality metering. A 25bar auxiliary compressor provides 0.554kg/s of air which is ducted into a plenum thence to the primary nozzle of the 14 individual ejectors. The high energy primary flow passes through a Rao nozzle entraining and accelerating the low energy secondary flow upstream of the AIP. The conical mass flow plug is operated in a choked mode to provide an accurate measurement of airflow through an inlet. The translation action of the conical mass flow plug is achieved by a linear actuator housed in the annulus which would allow for the regulation of mass flow. The secondary flow is ducted into a plenum chamber and thence into the mixing duct of the 14 ejectors via a conical inlet. The diffuser located at the end of the ejector reduces the fluid velocity and increases the pressure of the fluid to be discharged into the MSWT.

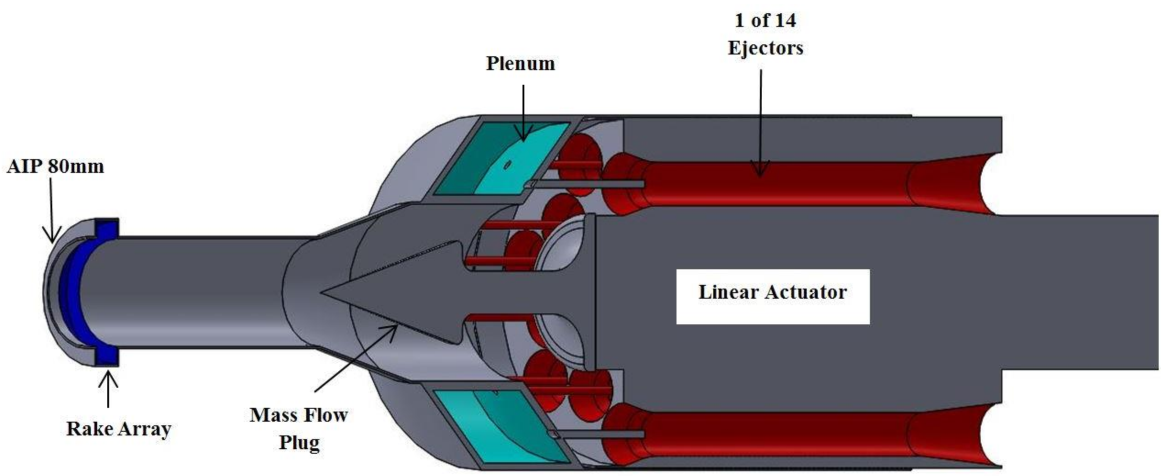

Figure 3-24 : Final design of a controlled induced mass flow system

CFD simulations were performed to determine the effects a skewed inlet velocity profile and inclined exit conditions relative to the free stream wind tunnel test section conditions have on the entrained mass flow rate for the staggered multi-ejector.

3.3.1 Skewed Inlet Velocity Profile With/Without Inclined Exit

Three-dimensional CFD simulations, as described in Section 3.2.2, were performed to determine the entrained mass flow rate for a skewed secondary inlet velocity profile with and without an inclined exit. CFD simulations without an inclined exit were firstly performed. The three-dimensional geometry of the skewed inlet velocity staggered multi-ejector employed in the simulations with the specified boundary conditions is illustrated in Figure 3-25. The air flow inside the staggered multi-ejector was model with the air exiting into the wind tunnel. The inlets to the fluid domain were specified as stagnation inlets, as illustrated in Figure 3-25(a). The secondary inlet total pressure was determined by obtaining the static pressure at the secondary inlet from a previous solution hence calculating the Mach number. By varying the Mach number, such that Ring 1 Mach number is 1.5 times the original Mach number and Ring 5 Mach number is 0.5 times the original Mach number, the total pressure is determined using Equation 3.14. The nozzle inlet boundary conditions were set as 25bar primary pressure with the corresponding temperature as stated in Section 3.2.1. The outlet was specified as a pressure outlet, as illustrated in Figure 3-22(c), with static conditions corresponding to the MSWT at M=1.2 and P_{t0} from Table 3-2. The ejector, primary nozzle and annulus walls were specified as non-slip solid walls illustrated in Figure 3-25(b). A polyhedral mesh was employed to the three-dimensional multi-ejector simulations as mentioned in Section 3.2.2.1.

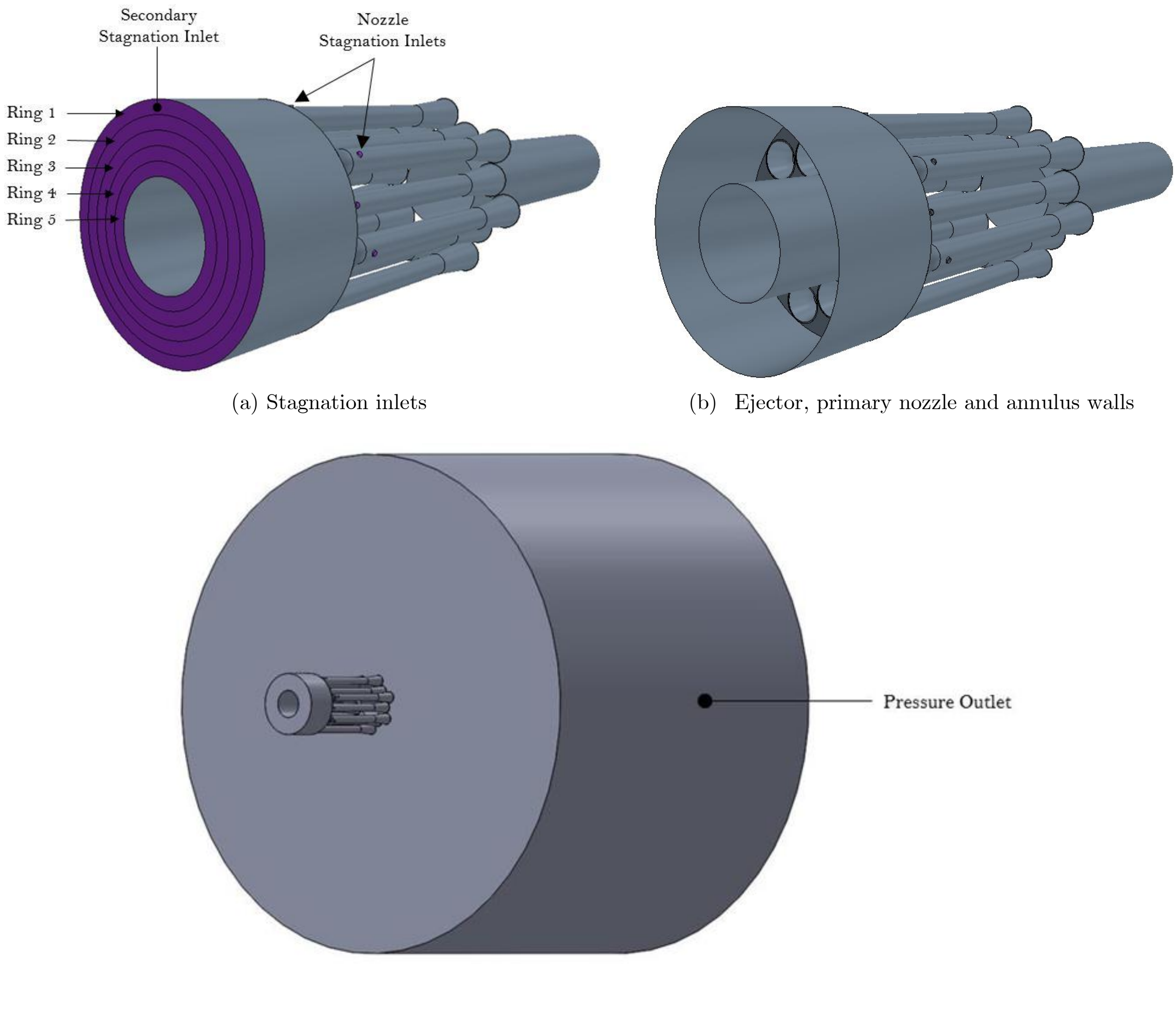

(a) Stagnation inlets

(b) Ejector, primary nozzle and annulus walls

(c) Pressure outlet

Figure 3-25 : Three-dimensional geometry of the skewed inlet velocity staggered multi-ejector required as an input for CFD with specified boundary conditions

The CFD simulations with a 30° inclined exit were performed using the geometry of the skewed inlet velocity as shown in Figure 3-25. The boundary conditions for the stagnation inlets and walls were specified as per the skewed inlet velocity without an inclined exit. However the outlet was specified as free stream with a flow direction at 30° and static conditions corresponding to the MSWT at M=1.2 and P_{t0} from Table 3-2.

4. EXPERIMENTAL METHOD

The mass flow rates of the staggered multi-ejector design were required to be verified experimentally. Staggered multi-ejector design employs 14 single identical ejectors therefore a single ejector was manufactured and tested to determine the entrained mass flow rate and the primary mass flow rate. The configuration of a single ejector employed in the staggered multi-ejector design with the required mass flow rate determination points is illustrated in Figure 4-1. The experimental test rig designed, the layout for the determination of mass flow rates and the experimental methodology followed are outlined in the subsequent sections.

Figure 4-1 : Configuration of a single ejector with required mass flow rate determination points

4.1 Experimental Test Rig

To determine the mass flow rates of the ejector, a test rig was designed and manufactured integrating the ejector configuration illustrated in Figure 4-1. The determination of the entrained mass flow rate at the inlet of the ejector was achieved by employing a conical inlet. The primary mass flow rate exiting the nozzle is determined by calculating the total mass flow rate at the exit and hence subtracting the entrained mass flow rate from the inlet. The total mass flow rate at the exit was determined by employing a meter run which consists of an orifice plate with flange taps. The subsequent sections outline the conical inlet, meter run and ejector designed for the experiment.

4.1.1 Conical Inlet

The conical inlet was designed and manufactured according to ISO 5801:2007(E) and can only be used when drawing air from an open free space and if Reynolds number, Re_d, is greater than 20 000 [42]. The conical inlet dimensions and tolerances according to ISO 5801:2007(E) are illustrated in Figure 4-2 with $d = 50mm$ and PT representing four wall pressure tappings.

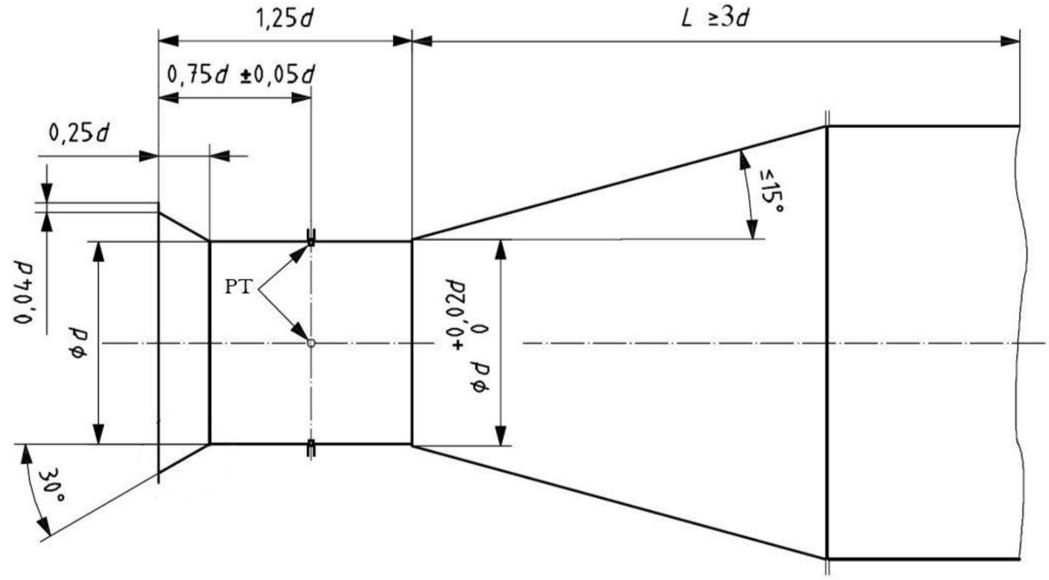

Figure 4-2 : Geometry of conical inlet [42]

According to ISO 5801:2007(E) there should be no external obstruction to the free movement of the air entering the inlet and the velocity of any cross-currents should not exceed 5% of the nozzle throat velocity. The conical inlet can be used uncalibrated for a pressure difference of up to 4kPa. The mass flow rate, q_m, is determined by using Equation 4.1 [42]

$$q_m = \alpha\varepsilon\pi\frac{d^2}{4}\sqrt{2\rho_u\Delta p} \tag{4.1}$$

where $\alpha\varepsilon$ is the compound coefficient dependent on Reynolds number, Re_d, and is plotted in Figure 4-3, d represents the diameter of the conical inlet, ρ_u represents the upstream density which is determined according to Equation 3.9, Δp represents the differential pressure between the static pressure of the conical inlet and atmospheric pressure. Approximation uncertainties in the mass flow rate calculations are mainly associated with the compound coefficient value. According to ISO 5801:2007(E) the basic uncertainty when $Re_d > 3 \times 10^5$ is $\pm 1.5\%$ and for $2 \times 10^4 < Re_d < 3 \times 10^5$ is $\pm\left(\frac{2\times10^4}{Re_d} - \frac{1}{15}\right)\%$ [42].

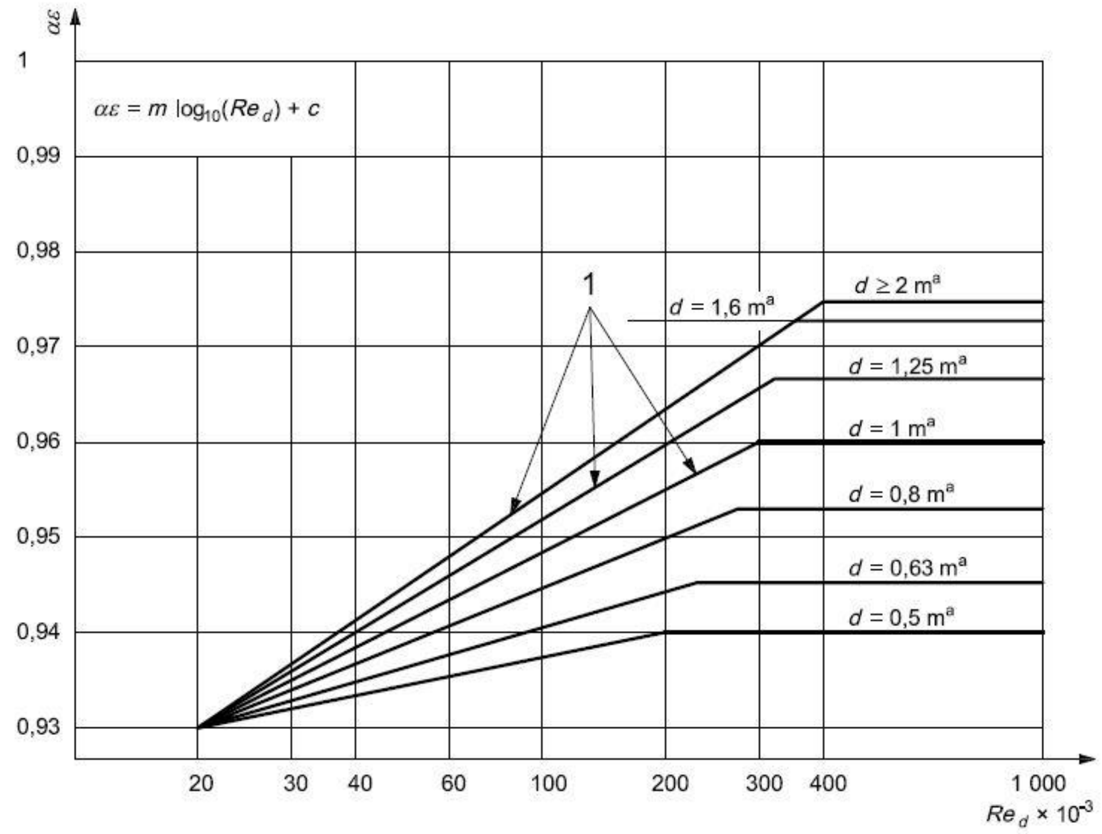

Key

1 curves for different duct diameters

$\alpha\varepsilon$ compound coefficient

$Re_d \times 10^{-3}$ Reynolds number

NOTE 1 For $d \leqslant 0{,}5$ m: $m = 0{,}010\ 00$; $c = 0{,}887\ 0$; $\alpha\varepsilon$ max. = 0,94.

NOTE 2 For $0{,}5\ \text{m} < d \leqslant 2$ m: $m = 0{,}009\ 63 - 0{,}047\ 83d + 0{,}012\ 86d^2$; $c = 0{,}971\ 5 - 0{,}205\ 8d + 0{,}055\ 33d^2$; $\alpha\varepsilon$ max. $= 0{,}913\ 1 + 0{,}062\ 3d - 0{,}015\ 67d^2$.

NOTE 3 For $d \geqslant 2$ m: $m = 0{,}034\ 59$; $c = 0{,}781\ 2$; $\alpha\cdot\varepsilon$ max. = 0,975.

[a] Duct diameter.

Figure 4-3 : Compound coefficients of conical inlets [42]

4.1.1.1 Pressure Tappings

The pressure tappings were constructed according to ISO 5801:2007(E). Each pressure tapping takes the form of a hole through the wall of the airway as illustrated in Figure 4-4. The bore diameter, a, is required to be not less than 1.5mm, not greater than 5mm and not greater than $0.1D$, where D is the airway diameter [42].

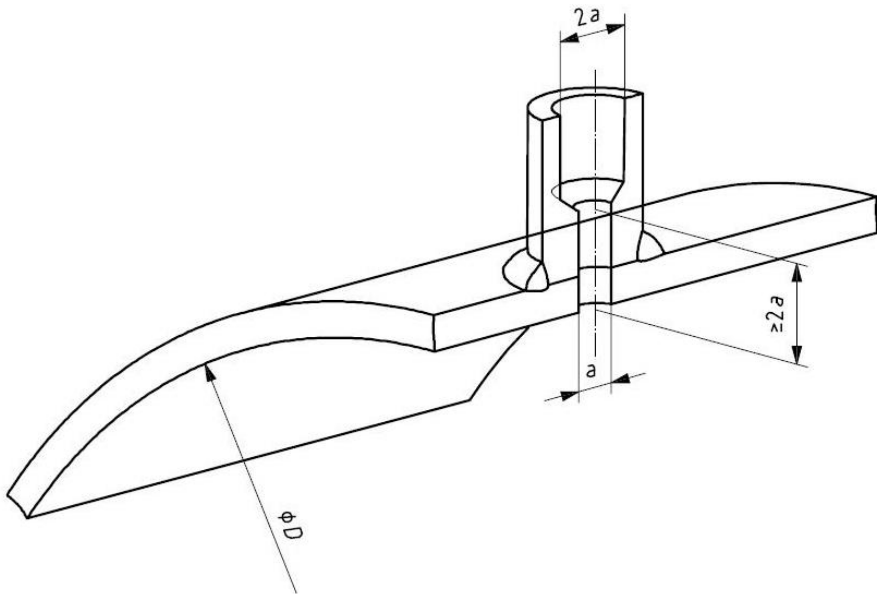

Figure 4-4 : Construction of wall pressure tappings [42]

4.1.1.2 Conical Inlet Design

The conical inlet was designed and manufactured for an inner diameter $d = 50mm$. The material used for the manufacturing of the conical inlet was aluminium alloy 6082-T6. The pressure tappings were manufactured for a bore diameter $a = 2.2mm$.

The conical inlet incorporates space for the primary nozzle, a primary nozzle support structure and a primary nozzle clamp mechanism without affecting the design standards of ISO 5801:2007(E). Detailed manufacturing drawings of the conical inlet are presented in APPENDIX B. Four M5 x 4mm tubing push-in fittings were screwed into the pressure tappings to allow for the determination of the differential pressure, Δp. The four push-in fittings were linked together by T shaped connectors and 4mm tubing as illustrated in Figure 4-5. The manufactured conical inlet assembled for the experiment is illustrated in Figure 4-6.

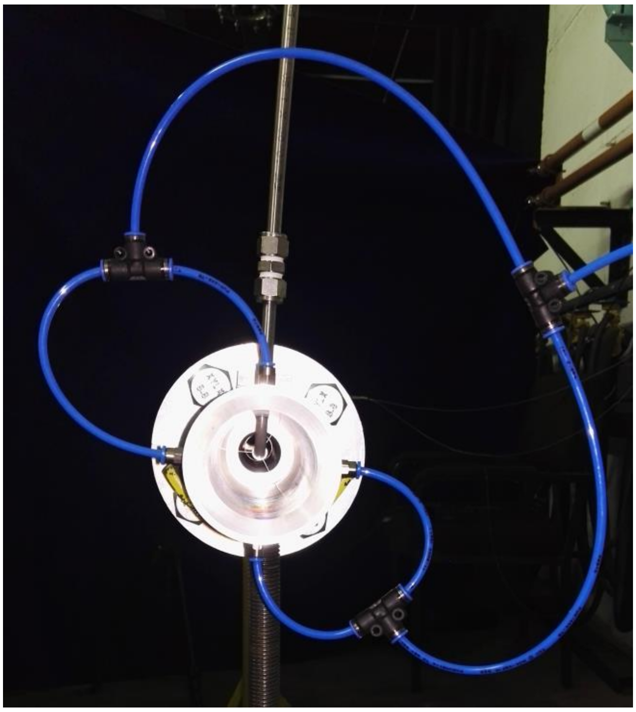

Figure 4-5 : Resulting pressure tappings and connection of tubing for static pressure measurement

Figure 4-6 : Manufactured conical inlet

4.1.2 Meter Run

The total mass flow rate at the exit is measured using a meter run, illustrated in Figure 4-7, supplied by a company WIKA Instruments. The meter run encompasses an orifice plate designed for a specific mass flow rate range and flange pressure tappings across the orifice plate.

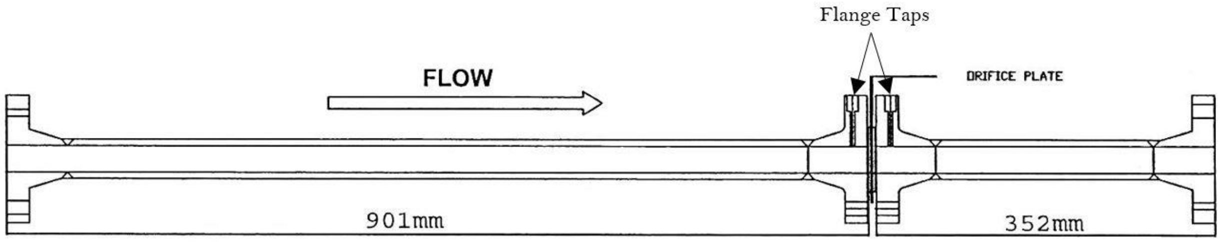

Figure 4-7 : Meter run for total mass flow rate measurement

The total mass flow rate, $\dot{m}_{total}$, is determined by Equation 4.2 where the volumetric flowrate, Q, is calculated according to ASME MFC-14M-2001 standard.

$$\dot{m}_{total} = \rho Q \tag{4.2}$$

For flange taps the configuration illustrated in Figure 4-8 as specified by the ASME MFC-14M-2001 standard is used in the determination of the volumetric flowrate, Q.

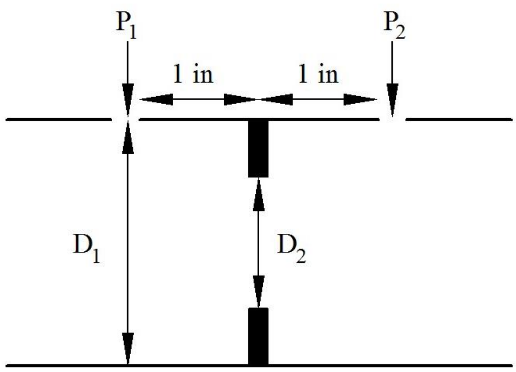

Figure 4-8 : Flange taps configuration [43]

The volumetric flowrate, Q, is determined by using Equation 4.3 [43]

$$Q = eC_dA_2\frac{\sqrt{2\Delta P/\rho}}{\sqrt{1-\beta^4}} \tag{4.3}$$

where

$$e = 1 - \frac{\Delta P}{\gamma P_1}(0.41 + 0.35\beta^4) \tag{4.4}$$

$$C_d = [0.598 + 0.468(\beta^4 + 10\beta^{12})]\sqrt{1-\beta^4} + (0.87 + 8.1\beta^4)\sqrt{\frac{1-\beta^4}{Re_1}} \tag{4.5}$$

$$A_2 = \frac{\pi D_2^2}{4} \tag{4.6}$$

$$\beta = \frac{D_2}{D_1} \tag{4.7}$$

with e representing gas expansivity, ΔP is the pressure drop across the orifice, C_d representing the discharge coefficient, A_2 is the cross sectional area of the orifice, β being the diameter ratio, Re_1 representing Reynolds number defined by the pipe diameter calculated using Equation 4.8 [43]

$$Re_1 = \frac{D_1 V_1 \rho}{\mu} \tag{4.8}$$

where

$$V_1 = \frac{Q}{A_1} \tag{4.9}$$

with D_1 representing the diameter of the pipe, V_1 is the velocity in the pipe, A_1 is the cross sectional area of the pipe, μ is the gas viscosity calculated using Equation 3.8, ρ representing the gas density calculated using Equation 3.9. An excel spreadsheet [43] was obtained that calculates the flowrate from a small-bore gas orifice meter using the ASME MFC-14M-2001 standard. The gas viscosity and gas density equations from the excel spreadsheet were modified to Equation 3.8 and Equation 3.9 respectively. The input parameters required by the excel spreadsheet are upstream pressure, downstream pressure and downstream temperature. Equation 4.2 to Equation 4.9 are determined by an iterative solution using the goal seek function. Goal seek uses an initial guess value for the Reynolds number to calculate the discharge coefficients and uses this to determine the flowrate. The calculated flowrate is then used to determine the Reynolds number. Goal seek then automatically adjusts the guess and calculated values of the Reynolds number until the difference between the guess and calculated Reynolds number is approximately zero [43].

4.1.3 Ejector Design

The ejector illustrated in Figure 4-1 was manufactured in various parts. The conical entry and mixing duct was combined and manufactured into one part which will attached to the conical inlet mentioned in Section 4.1.1. The material used for the manufacturing of the conical entry and mixing duct was aluminium alloy 6082-T6. Detailed manufacturing drawings of the conical entry and mixing duct are presented in APPENDIX B.

The diffuser was manufactured incorporating a transition section which would allow for equal diameter at the interface plane where the diffuser exit and meter run inlet meet. The material used for the manufacturing of the diffuser was aluminium alloy 6082-T6. Detailed manufacturing drawings of the diffuser are presented in APPENDIX B.

The primary nozzle was manufactured in three parts, as illustrated in Figure 4-9, to allow for easy assembly as well as to provide compatibility with other primary nozzle profiles. The primary nozzle profile part, *i.e.* the smallest part in Figure 4-9, was manufactured with a greater wall thickness to accommodate for the thread. The material used for the manufacturing of the primary nozzle was stainless steel 304. Detailed manufacturing drawings of the primary nozzle are presented in APPENDIX B.

Figure 4-9 : Primary nozzle manufactured in three parts

A support structure for the primary nozzle was designed to constrain the nozzle from any lateral or rotational movement and to align the primary nozzle centrally. The support structure is concentrically located in the conical inlet. The material used for the manufacturing of the support structure was stainless steel 304. A clamp mechanism was designed to constrain the primary nozzle from any vertical movement and to ensure no air leakage occurs at the interface of the primary nozzle wall and the conical inlet. The material used for the manufacturing of the clamp mechanism was aluminium alloy 6082-T6. Detailed manufacturing drawings of the support structure and clamp mechanism are presented in APPENDIX B.

Figure 4-10 illustrates the designed individual components assembled and Figure 4-11 shows a section view of the conical inlet, clamp mechanism, primary nozzle, support structure, mixing duct and diffuser.

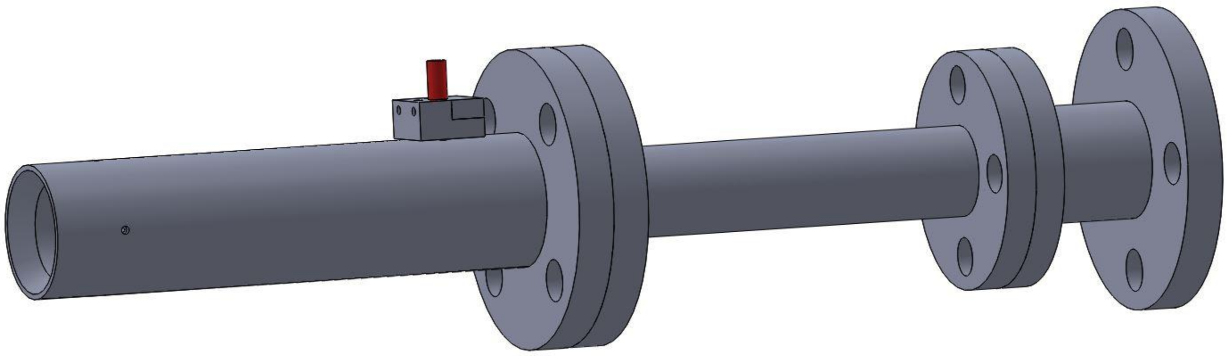

Figure 4-10 : Assembled conical inlet, ejector components and clamp mechanism

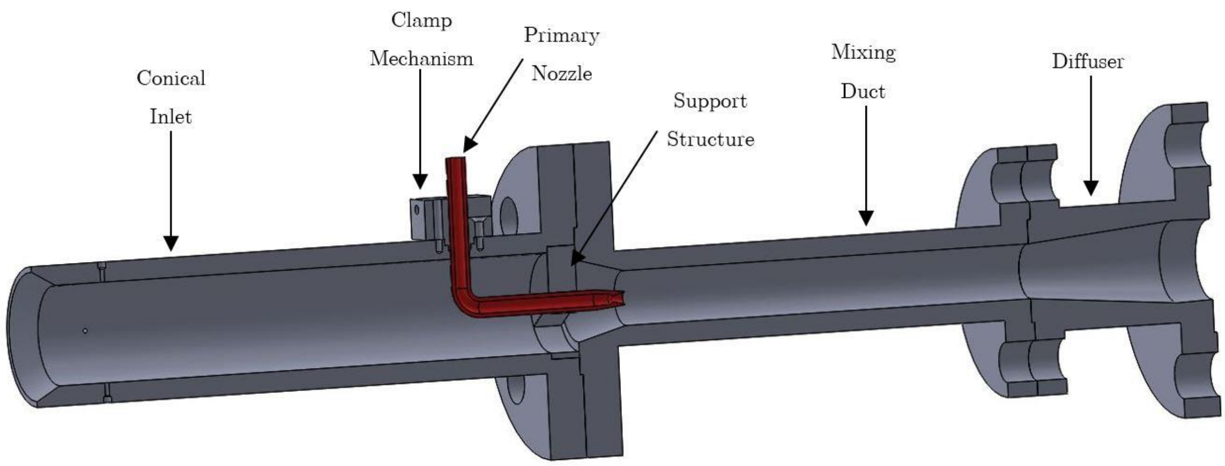

Figure 4-11 : Section view of conical inlet, clamp mechanism, primary nozzle, support structure, mixing duct and diffuser

4.1.4 Test Rig

The experimental test rig encompasses the conical inlet, all the ejector components, clamp mechanism and the meter run which are all assembled using bolts and nuts. A sealant was used between each flange to ensure no air leakage occurs during testing. Figure 4-12 illustrates the assembly of the experimental test rig and Figure 4-13 shows the manufactured experimental test rig assembled with bolts and nuts.

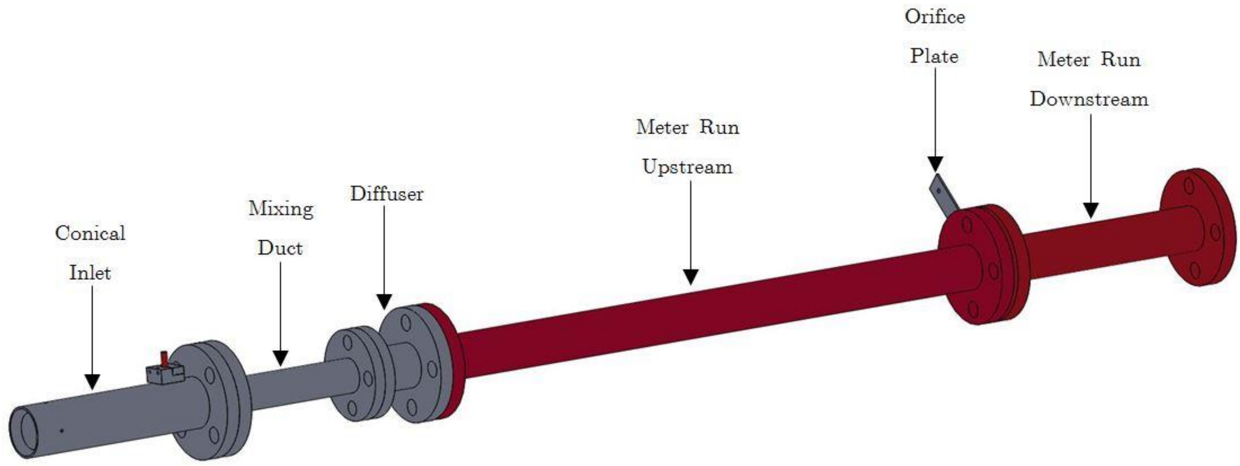

Figure 4-12 : Assembly of the experimental test rig

Figure 4-13 : Assembled manufactured experimental test rig

4.1.4.1 Instrumentation

The mass flow rate calculation for the conical inlet according to Equation 4.1 requires the static pressure at the conical inlet to be measured as well as the atmospheric pressure and temperature to allow for the determination of the upstream density. The mass flow rate determination for the meter run according to Equation 4.3 requires the static pressure at the flange taps to be measured in order to determine the pressure drop across the orifice plate. The Reynolds number according to Equation 4.8 requires the temperature in the pipe to determine the gas density and gas viscosity.

The atmospheric pressure was recorded using an electronic barometer and the atmospheric temperature in addition to the temperature in the meter run pipe was recorded using a thermometer. The static pressure at the conical inlet and the static pressure at the flange taps were measured using a Scanivalve ZOC33 electronic pressure scanning module which is presented in APPENDIX C.1. A R406 cylinder regulator presented in APPENDIX C.2 was utilised to regulate the primary pressure from an air cylinder containing synthetic air to 25bar. An integral bonnet needle valve as presented in APPENDIX C.3 was used to control the quantity of synthetic air passed to the primary nozzle.

4.2 Experimental Layout

The layout of the experimental test rig with various instrumentation is shown in Figure 4-14 and a schematic of the experimental layout showing the various instrumentation is shown in Figure 4-15. The experimental test rig is placed on three stands which allows for the vertical adjustment of the test rig. The cylinder regulator is attached to the air cylinder which allows for the regulation of the primary pressure to 25bar. A needle valve is located downstream of the cylinder regulator which ensures a controlled quantity of air passing to the primary nozzle. Stainless steel pipes are used to connect the primary nozzle to the needle valve and thence to the cylinder regulator. A thermometer is attached to a tripod and is positioned at the exit of the meter run pipe to allow for the determination of the air temperature.

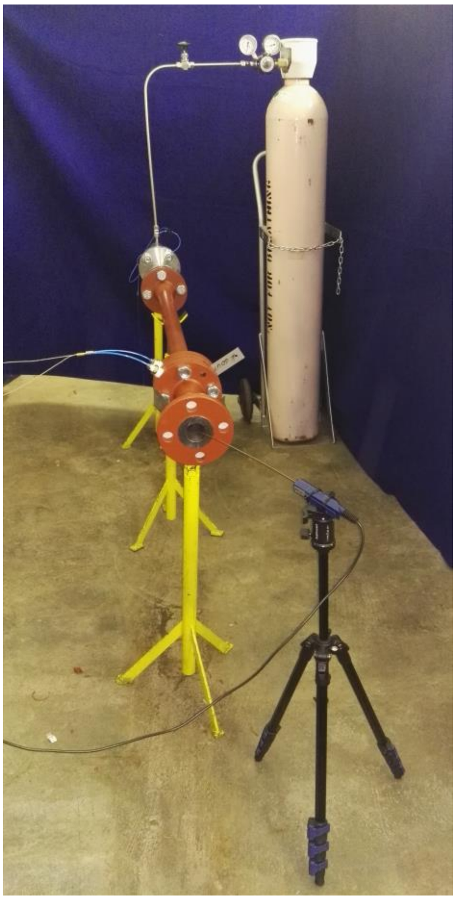

Figure 4-14 : Experimental layout of test rig with instrumentation

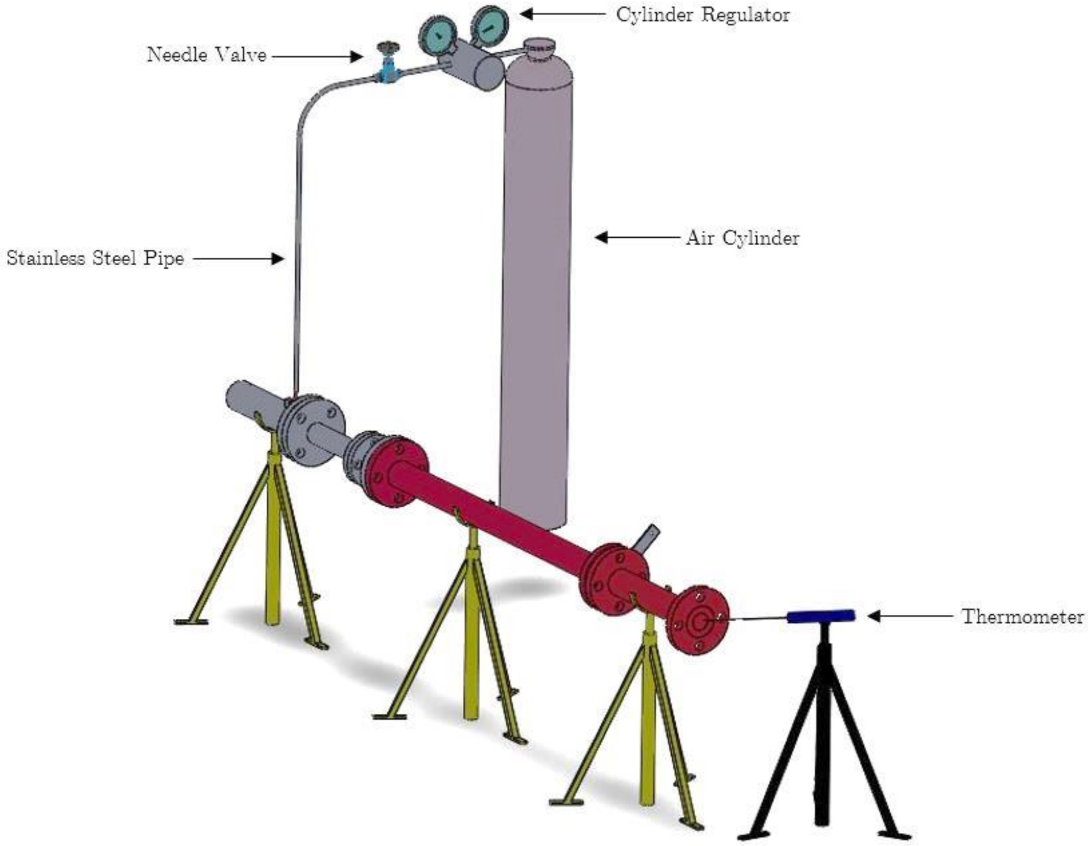

Figure 4-15 : Schematic of experimental layout with instrumentation

The Scanivalve electronic pressure scanning module is connected to the flange taps using tubing as shown in Figure 4-16(a) where P1 represents the downstream pressure measurement point of the meter run and P2 represents the upstream pressure measurement point of the meter run. Figure 4-16(b) shows the connection point of the Scanivalve to the conical inlet tubing where P3 represents the pressure measurements point.

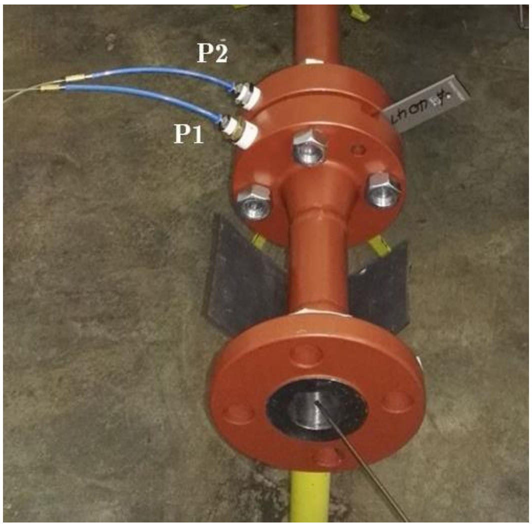

(a) Scanivalve connection at flange taps

(b) Scanivalve connection at conical inlet

Figure 4-16 : Scanivalve connection points

4.3 Methodology

The experiment was conducted in the Hot Gas Lab facility situated in the High Speed Wind Tunnel (HSWT) at the Council for Scientific and Industrial Research (CSIR). The method followed in order to conduct the experiment is outlined in the subsequent sections. The experiment was conducted for one operating point *i.e.* at a secondary pressure corresponding to ambient conditions, since the secondary pressure to the ejector could not be regulated. A risk assessment, presented in APPENDIX D.1, was performed in order to determine the risk factors associated with the experiment and to determine the accompanying precautions that should be followed.

4.3.1 Leak Test

4.3.1.1 Conical Inlet Tubing Connection

A leak test was performed to determine if any air leakage occurred at the tubing connections of the conical inlet. The setup for the leak test at the conical inlet tubing connection is illustrated in Figure 4-17. The holes of the pressure tappings on the inner surface of the conical inlet was sealed using aluminium tape as shown in Figure 4-17. The leak test was performed using the Druck DPI620 Advanced Modular Calibrator, presented in APPENDIX C.4, connected to the tubing to determine the leak rate per minute as illustrated in Figure 4-17.

Figure 4-17 : Conical inlet tubing connection leak test setup

The Druck DPI620 was used to pump 50kPa into the tubing of the conical inlet. The pressure was allowed to settle for five minutes before the leak rate per minute was determined. Figure 4-18 illustrates a leak rate of 2Pa per minute was obtained by the Druck DPI620 at the conical inlet tubing connection.

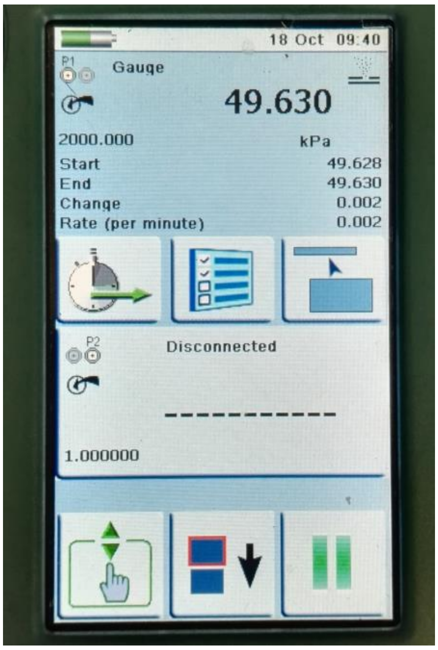

Figure 4-18 : Leak rate per minute for conical inlet tubing connection

4.3.1.2 Experimental Test Rig

A leak test was performed to determine if any air leakage occurred at the interface of the experimental test rig flanges. A sealing tape was used between the flanges and at the interface of the orifice plate and flanges. The leak test was conducted on the experimental test rig by sealing the entry of the conical inlet and the exit of the meter run with aluminium tape as illustrated in Figure 4-19.

(a) Conical inlet entry sealed

1. Meter run exit sealed

Figure 4-19 : Experimental test rig leak test setup

A stopper was inserted into the T-shaped push fitting of the conical inlet tubing connection to ensure no air escaped. A pressurised test rig was required to determine if any leaks were present. This was obtained by regulating the pressure from the air cylinder using the cylinder regulator. The needle valve was opened to allow air through to the primary nozzle, pressurising the test rig. A soapy water solution was sprayed on all flanges to determine if a leak was present. A cluster of bubbles appeared at the interface of the orifice plate and the flanges, indicating a leak. This leak was corrected by using a silicone sealant at the interface of the orifice plate and flanges. The leak test was repeated and no further leaks were obtained.

4.3.2 Calibration of Cylinder Regulator Pressure Gauge

A calibration was performed to check the accuracy of the cylinder regulator pressure gauge. The calibration test was performed using the Druck DPI620 Advanced Modular Calibrator, presented in APPENDIX C.4. The Druck DPI620 was used to increase the pressure in the gauge up until a 20bar reading was displayed on the pressure gauge. The corresponding pressure displayed on the Druck DPI620 was 17.75bar. A maximum pressure of 19.4bar was pumped to the pressure gauge using the Druck DPI620 which resulted in approximately 22bar being displayed on the pressure gauge as shown in Figure 4-20. Therefore for a required primary pressure of 25bar, an approximate pressure of 27bar should be displayed on the pressure gauge for the experiment.

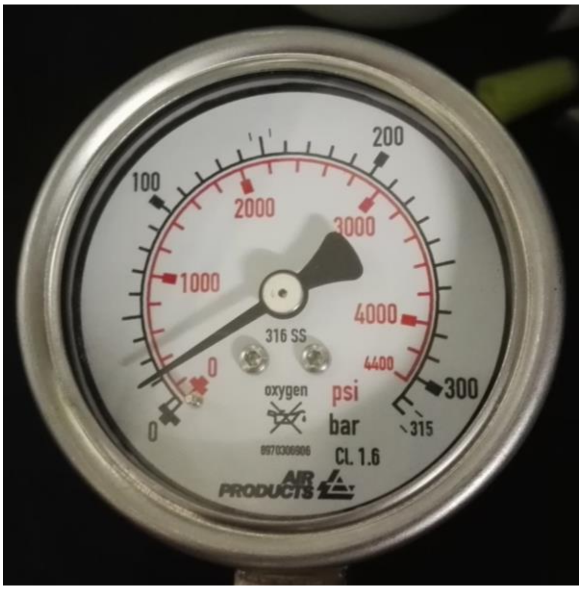

Figure 4-20 : Calibration of regulator pressure gauge

4.3.3 Calibration of Conical Inlet Standard and Orifice Meter Run Standard

A calibration was performed to determine if the conical inlet ISO 5801:2007(E) standard and the orifice meter run ASME MFC-14M-2001 standard resulted in equivalent calculated mass flow rate. The calibration test was performed using one vacuum cleaner at two different suction powers and using a small vacuum with a lower suction power. The experimental layout mentioned in Section 4.2 was used for the calibration test. A detail procedure of the calibration process is given below.

1. Switch on the Scanivalve and obtain a zero reading.
2. Switch on the barometer and thermometer.
3. Record the atmospheric pressure displayed by the barometer and the atmospheric temperature displayed by the thermometer.
4. Ensure proper precautions are followed according to the risk assessment.
5. The air cylinder, cylinder regulator and needle valve should all be closed.
6. Place the vacuum pipe at the exit of the meter run and switch on the vacuum.
7. Start recording data using the Scanivalve.
8. The vacuum should be on for approximately 10 seconds subsequently switch off the vacuum.
9. Stop recording data from the Scanivalve.
10. Determine the average P1 (downstream meter run pressure), P2 (upstream meter run pressure), P3 (conical inlet pressure) from the Scanivalve data readings.
11. Calculate the mass flow rate for the meter run according to the ASME MFC-14M-2001 standard using Equation 4.2 to Equation 4.9.
12. Calculate the mass flow rate for the conical inlet according to the ISO 5801:2007(E) standard using Equation 4.1.

Repeat steps 1 to 12 to determine the mass flow rates according to the ASME MFC-14M-2001 standard and the ISO 5801:2007(E) standard for two other vacuum suction powers.

4.3.4 Experimental Test Procedure

The experiment was conducted at ambient conditions with 3 different tests performed. The first test was required to determine the entrained mass flow rate at 25bar primary pressure and constant backpressure, the second test was required to determine the minimum pressure the ejector can pump down to and the third test was required to determine the entrained mass flow rates at 25bar primary pressure and various backpressures. The experimental layout mentioned in Section 4.2 was used for the experimental test. The following procedure describes the steps that should be followed for each test.

1. Switch on the Scanivalve and obtain a zero reading.
2. Switch on the barometer and thermometer.
3. Record the atmospheric pressure displayed by the barometer and the atmospheric temperature displayed by the thermometer.
4. Ensure proper precautions are followed according to the risk assessment.
5. The air cylinder and cylinder regulator should be closed.
6. The needle valve should be opened to the maximum.
7. Start recording data using the Scanivalve.

8. Open the air cylinder to the maximum.
9. Regulate the pressure to 27bar using the cylinder regulator.
10. The test should be conducted for approximately 10 seconds.
11. Stop recording data from the Scanivalve.
12. Close the air cylinder.
13. Record the meter run exit temperature displayed by the thermometer.
14. Determine the average P1 (downstream meter run pressure), P2 (upstream meter run pressure), P3 (conical inlet pressure) from the Scanivalve data readings.
15. Calculate the mass flow rate for the meter run according to the ASME MFC-14M-2001 standard using Equation 4.2 to Equation 4.9.
16. Calculate the mass flow rate for the conical inlet according to the ISO 5801:2007(E) standard using Equation 4.1.

The first test should be conducted following the procedure mentioned above from steps 1 to 16. The second test requires the entry of the conical inlet to be completely blocked. This is accomplished by using a steel plate covered with rubber, pushed against the conical inlet entry for the duration of the test. Steps 1 to 16 from the procedure mentioned above should be followed for the second test. For the third test, the downstream section of the meter run and the orifice plate should be removed from the experimental test rig, therefore P1 from the Scanivalve will be disconnected. The third test requires changing (*i.e.* progressively blocking) the exit area of the upstream section of the meter run which will result in a variation in backpressure. This is accomplished by using a metal plate pushed against the exit of the upstream section of the meter run, slowly moving the plate to ensure a change in exit area for the duration of the test. Steps 1 to 16 (excluding 15) from the procedure mentioned above should be followed for the third test.

5. RESULTS AND DISCUSSION

5.1 Flow Quantity Metering System

The results of the flow quantity metering system employing a conical mass flow plug operated in a choked condition are presented in this subsection. The 30° translating conical mass flow plug resulted in a slender more compacted arrangement allowing for approximately 100mm linear plug displacement. This linear plug displacement allows for a variation of mass flow rates to be obtained for a specific wind tunnel stagnation pressure.

A flow quantity metering analysis was conducted as described in Section 3.1.2. to determine the target backpressure to ensure choked conditions at the geometric throat for various wind tunnel stagnation pressures. One of the most important aspects in the determination of the target backpressure was the location of the normal shock in the annular diffuser. The different locations and effects of the normal shock in the annular diffuser using the process explained in Figure 3-6 will be shown for one tunnel stagnation pressure and plug displacement with three different target stagnation backpressures.

A normal shock located downstream in the annular diffuser but not aft of the conical mass flow plug, yields a low calculated target stagnation backpressure *i.e.* a high-pressure difference. This leads to an unreasonable demand on the performance required from the ejector. Figure 5-1 illustrates the Mach number and area ratio along the flow quantity metering system for a tunnel stagnation pressure of $P_{tunnel} = 100kPa$, a low target stagnation backpressure of $P_{b\_target} = 65kPa$ and a conical mass flow plug displacement of 70mm. The geometric throat occurs at the minimum area ratio which is represented graphically in Figure 5-1 at position 0. At this position the flow is sonic which depicts a choked throat. The annular diffuser is represented graphically in Figure 5-1 by the area ratio distribution from position 0 to 0.09m with the base of the conical mass flow plug located at position 0.07m. For the low target backpressure of 65kPa, the normal shock location is represented graphically in Figure 5-1 at position 0.06m, since the Mach number goes from supersonic to subsonic, which is downstream of the annular diffuser but not aft of the conical mass flow plug.

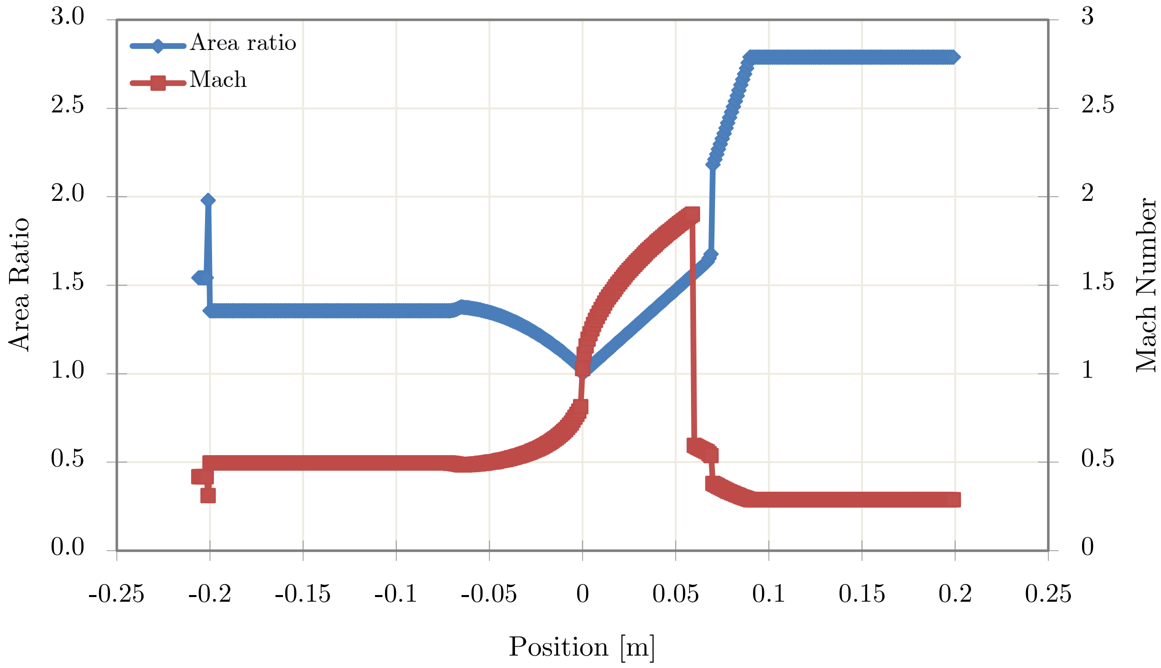

Figure 5-1 : Mach number and area ratio along the flow quantity metering system for $P_{tunnel} = 100kPa$, $P_{b\_target} = 65kPa$ and plug displacement of 70mm

A normal shock located upstream in the annular diffuser towards the geometric throat, yields a high calculated target backpressure *i.e.* a low-pressure difference, which may lead to the shock disappearing altogether hence the benefits of using a choked plug are lost. Figure 5-2 illustrates the Mach number and area ratio along the flow quantity metering system for a tunnel stagnation pressure of $P_{tunnel} = 100kPa$, a higher target stagnation backpressure of $P_{b\_target} = 85kPa$ and a conical mass flow plug displacement of 70mm. The geometric throat occurs at the minimum area ratio which is represented graphically in Figure 5-2 at position 0. This position represents sonic flow which depicts a choked throat. The annular diffuser is represented graphically in Figure 5-2 by the area ratio distribution from position 0 to 0.09m with the base of the conical mass flow plug located at position 0.07m. For the higher target backpressure of 85kPa, the normal shock location is represented graphically in Figure 5-2 at position 0.01m, since the Mach number goes from supersonic to subsonic, which is further upstream in the annular diffuser almost reaching the geometric throat.

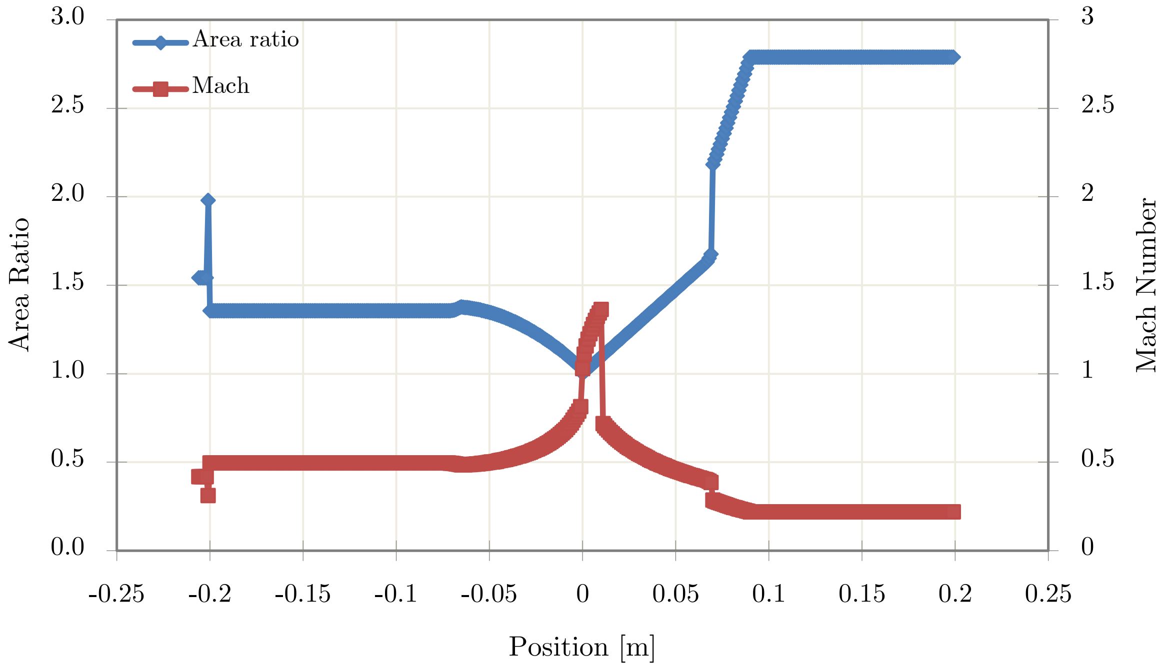

Figure 5-2 : Mach number and area ratio along the flow quantity metering system for $P_{tunnel} = 100kPa$, $P_{b\_target} = 85kPa$ and plug displacement of 70mm

It was determined from the flow quantity metering analysis that a normal shock location approximately central in the annular diffuser allows the system to be operated in a choked mode and the performance required from the ejector is achievable. Figure 5-3 illustrates the Mach number and area ratio along the flow quantity metering system for a tunnel stagnation pressure of $P_{tunnel} = 100kPa$, a target stagnation backpressure of $P_{b\_target} = 75kPa$ and a conical mass flow plug displacement of 70mm. The geometric throat occurs at the minimum area ratio which is represented graphically in Figure 5-3 at position 0. This position characterises sonic flow representing a choked throat. The annular diffuser is represented graphically in Figure 5-3 by the area ratio distribution from position 0 to 0.09m with the base of the conical mass flow plug located at position 0.07m. For a target backpressure of 75kPa, the normal shock location is represented graphically in Figure 5-3 at position 0.027m, since the Mach number goes from supersonic to subsonic, which is central in the annular diffuser.

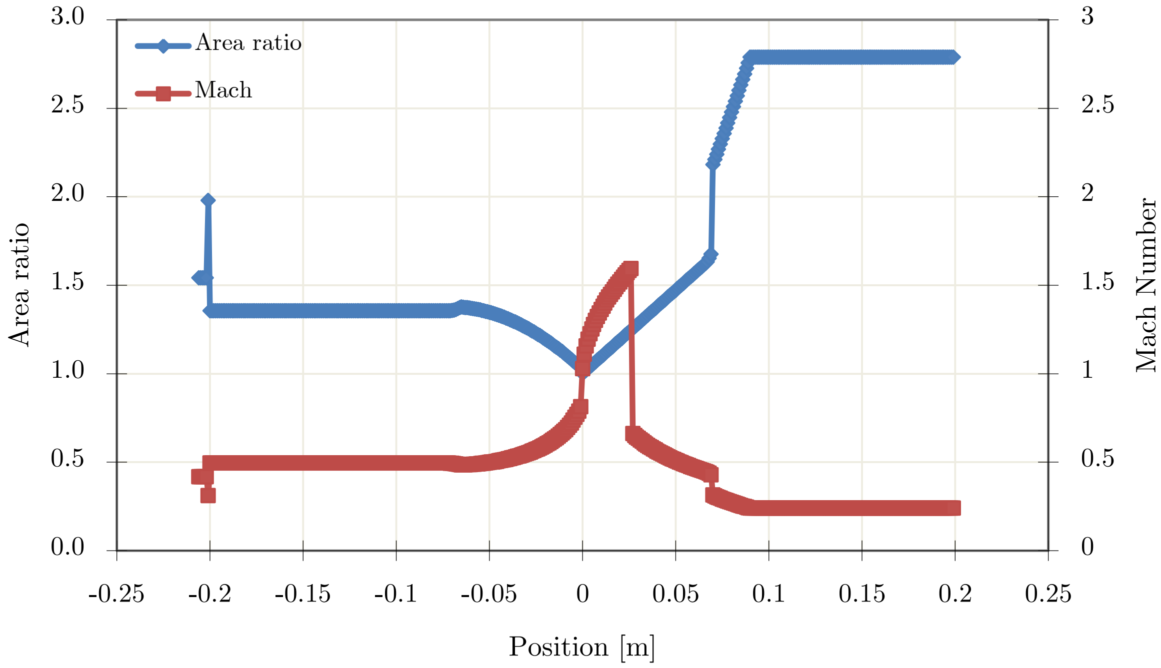

Figure 5-3 : Mach number and area ratio along the flow quantity metering system for $P_{tunnel} = 100kPa$, $P_{b\_target} = 75kPa$ and plug displacement of 70mm

It is required that the maximum Mach number at the engine face, or the "aerodynamic interface plane" (AIP), be in the range of 0.4 and 0.6 as mentioned in Section 3.1.1. The AIP location from Figure 5-1 to Figure 5-3 is approximately at position -0.2m which has a resulting Mach number in the region of 0.5. From the flow quantity metering analysis, a minimum plug displacement of 30mm is required to obtain a Mach number in the necessary range for the AIP. The effective converging – diverging nozzle created by the translating conical mass flow plug is illustrated graphically in Figure 5-1 to Figure 5-3 with reference to the area ratio distribution from position -0.07 to position 0.07.

The total pressure and Mach number distribution along the flow quantity metering system for tunnel stagnation pressure of $P_{tunnel} = 100kPa$, target stagnation backpressure of $P_{b\_target} = 75kPa$ and plug displacement of 70mm is illustrated in Figure 5-4. The dominant pressure losses incurred by the system are the intake loss which is 10% as mentioned in Section 3.1.2 and the normal shock losses represented graphically in Figure 5-4 at position 0.027m. Minor pressure losses occur at two sudden expansions in the system illustrated in Figure 5-4 at positions -0.2 and 0.07. Position -0.2 corresponds to the pressure loss caused by the expansion to house the rake support structure needed for the flow quality metering. The second expansion occurs at the base of the conical mass flow plug which corresponds to the pressure loss at position 0.07. Smaller pressure losses incurred by the annular diffuser, rake supports and pipe friction are not exclusively represented in Figure 5-4, however these pressure loss components collectively do have a significant effect in the determination of the target stagnation backpressure.

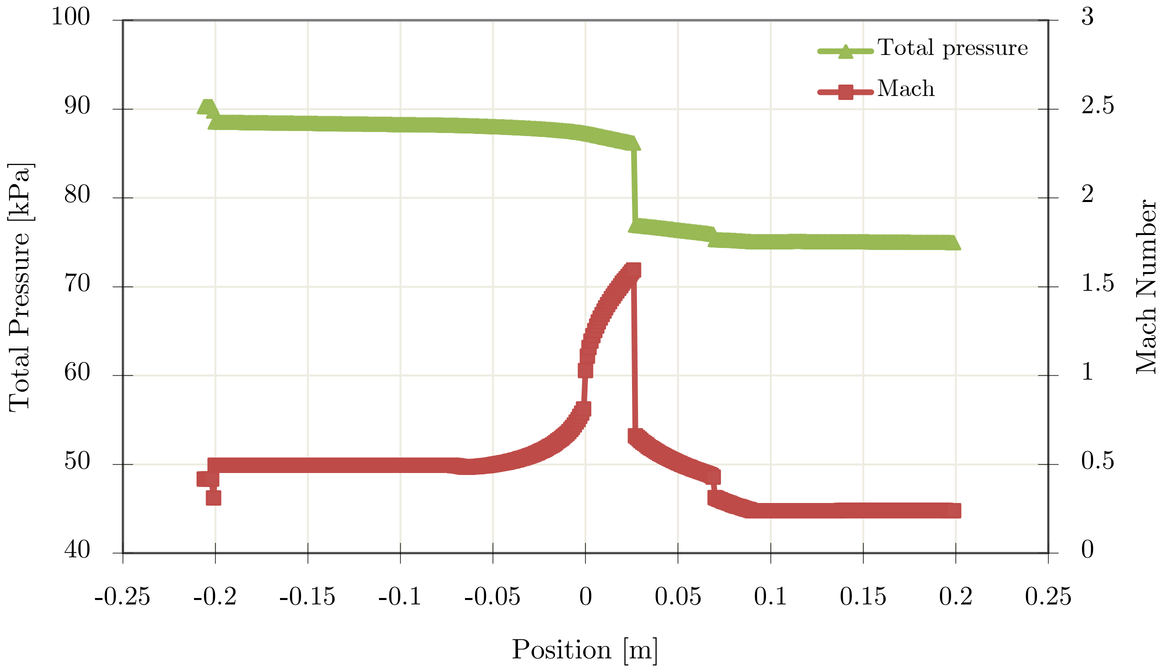

Figure 5-4 : Total pressure and Mach number distribution along the flow quantity metering system for $P_{tunnel} = 100kPa$, $P_{b\_target} = 75kPa$ and plug displacement of 70mm

The results of the flow quantity metering system employing a conical mass flow plug operated in a choked condition are listed in Table 5-1 and illustrated graphically in Figure 5-5. Linear conical mass flow plug displacements of 30mm results in the maximum mass flow rate, $\dot{m}$, attainable for each wind tunnel stagnation pressures, P_{tunnel}. The maximum mass flow rate that can be achieved for the designed flow quantity metering system is $\dot{m} = 1.91kg/s$ at $P_{tunnel} = 240kPa$ and for ambient conditions *i.e.* $P_{tunnel} = 100kPa$ the mass flow rate ranges between $\dot{m} = 0.50kg/s$ and $\dot{m} = 0.79kg/s$. As the plug translates upstream towards the geometric throat, the mass flow rate decreases as the geometric throat area decreases. This shows that the mass flow rate through the choked system is a function of the geometric throat area as stated in Section 2.1.2. The target stagnation backpressure, P_{b_target}, determined by the process illustrated in Figure 3-6 results in choked conditions at the geometric throat and a centrally located normal shock in the annular diffuser for various wind tunnel stagnation pressures and conical mass flow plug displacements. The results from the flow quantity metering system allows for an appropriate mass flow generation system to be designed.

Table 5-1 : Flow quantity metering analysis results

P_{tunnel} [kPa]	**Plug Displacement [mm]**	$\dot{m}$ [kg/s]	P_{b_target} [kPa]
240	-95	1.20	180
	-70	1.60	165
	-30	1.91	140
200	-95	1.00	160
	-70	1.33	145
	-30	1.59	125
150	-95	0.75	120
	-70	1.00	110
	-30	1.19	100
100	-95	0.50	80
	-70	0.67	75
	-30	0.79	70
50	-95	0.25	40
	-70	0.33	35
	-30	0.40	30

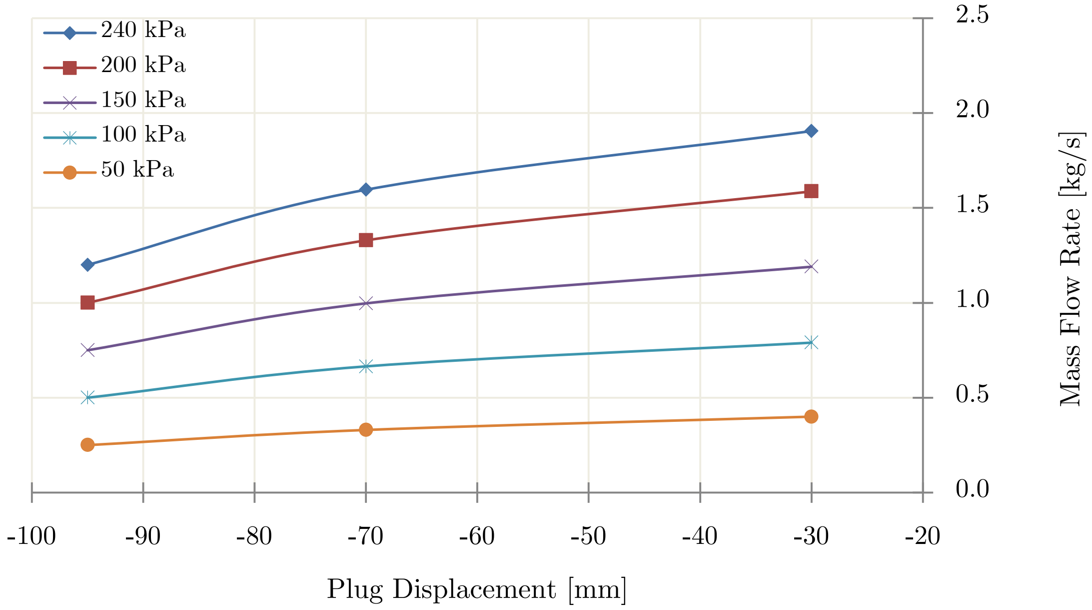

Figure 5-5 : Targeted mass flow rate for various wind tunnel stagnation pressures and plug displacements

5.2 Mass Flow Generation System

The mass flow generation system encompasses a constant-area mixing ejector. The ESDU 92042 software was chosen as the design tool for the determination of an ejector to meet the mass flow rate requirements from the flow quantity metering analysis. CFD simulations were performed to verify the ESDU 92042 software and to determine the performance of the ejector. The ejector was designed following the process described in Section 3.2.3 with the results presented in the subsequent sections.

5.2.1 Ejector Design Using ESDU 92042 and Verification of Design Tool

The results from the flow quantity metering analysis in Section 5.1 were required as the input parameters for the ESDU 92042 quick design procedure to determine the geometry of the ejector. The recommended diffuser wall angle range mentioned in Section 3.2.1 was investigated for various secondary pressures *i.e.* target backpressures, which led to a diffuser wall angle of 5° deemed feasible as it resulted in a shorter diffuser hence a shorter ejector being designed. The ejector was designed for two primary pressures, $P_{t1} = 25bar$ and $P_{t1} = 12bar$ with primary mass flow rates of $\dot{m}_p = 0.554kg/s$ and $\dot{m}_p = 1.28kg/s$ respectively. ESDU allows for the determination of ejector geometries for mass flow ratios, $\dot{m}_{entrained}/\dot{m}_p$, in the range of 0.05 to 1, as mentioned in Section 2.3. The maximum mass flow ratio that will allow an ejector to be designed by ESDU is 2, however the data obtained for the design will be less reliable. Ejector geometries were determined for $P_{t1} = 25bar$ with $\dot{m}_{entrained}/\dot{m}_p = 2$ as the maximum, which resulted in a limitation on the maximum mass flow rate $\dot{m}_{entrained} = 1.11kg/s$ as shown in Table 5-2.

Table 5-2 : ESDU maximum mass flow rate and mass flow ratio at $P_{t1} = 25bar$

P_{t0} [kPa]	$\dot{m}_{target}$ [kg/s]	$\dot{m}_{entrained}$ [kg/s]	$\dot{m}_{entrained}/\dot{m}_p$
30	0.40	0.40	0.72
40	0.25	0.25	0.45
70	0.79	0.79	1.43
80	0.50	0.50	0.90
100	1.19	1.11	2.00
120	0.75	0.75	1.35
125	1.59	1.11	2.00
140	1.91	1.11	2.00
160	1.00	1.00	1.81
180	1.20	1.11	2.00

Determining ejector geometries for $P_{t1} = 12bar$ resulted in all target mass flow rates from the flow quantity metering analysis being met as $\dot{m}_{entrained}/\dot{m}_p < 2$ listed in Table 5-3. However the ejector designs obtained for $\dot{m}_{entrained}/\dot{m}_p > 1$ will be unreliable.

Table 5-3 : ESDU maximum mass flow rate and mass flow ratio at $P_{t1} = 12bar$

$\boldsymbol{P_{t0}}$ [kPa]	$\boldsymbol{\dot{m}_{entrained}}$ [kg/s]	$\boldsymbol{\dot{m}_{entrained}/\dot{m}_p}$
30	0.40	0.31
40	0.25	0.20
70	0.79	0.62
80	0.50	0.39
100	1.19	0.93
120	0.75	0.59
125	1.59	1.24
140	1.91	1.49
160	1.00	0.78
180	1.20	0.94

The ESDU 92042 software was required to be verified as certain ejector designs were unreliable. Two-dimensional CFD simulations were performed according to Section 3.2.2 to determine the entrained mass flow rates obtained using the ejector designs developed by ESDU. The ejector designs for three secondary pressures were analysed with the results presented in Table 5-4. The entrained mass flow rates predicted for $P_{t1} = 25bar$ determined by CFD analysis achieved or exceeded the entrained mass flow rates from ESDU. The ejector design for $P_{t0} = 180kPa$ was for a mass flow ratio of two which is considered an unreliable ejector design. This ejector design resulted in an entrained mass flow rate greater than the limited ESDU entrained mass flow rate. The entrained mass flow rates predicted for $P_{t1} = 12bar$ determined by CFD analysis did not match any of the entrained mass flow rates from ESDU. A decrease in the entrained mass flow rate was achieved by the designed ejector geometries at $P_{t1} = 12bar$ therefore ejector geometries designed at this primary pressure were not considered to be a viable option. It was determined the design tool, ESDU 92042, provided reliable ejector designs when higher primary pressures were utilised and the entrained mass flow rates for ejectors designed at $\dot{m}_{entrained}/\dot{m}_p = 2$ exceeded the specified value in ESDU.

Table 5-4 : Entrained CFD mass flow rates at $P_{t1} = 25bar$ and $P_{t1} = 12bar$

	$P_{t1} = 25bar$		$P_{t1} = 12bar$	
P_{t0} [kPa]	$\dot{m}_{ESDU}$ [kg/s]	$\dot{m}_{CFD}$ [kg/s]	$\dot{m}_{ESDU}$ [kg/s]	$\dot{m}_{CFD}$ [kg/s]
30	0.40	0.40	0.40	0.14
80	0.50	0.50	0.50	0.33
180	1.11	1.45	1.20	1.11

Since the entrained mass flow rates predicted for $P_{t1} = 25bar$ determined by CFD analysis achieved or exceeded the entrained mass flow rates from ESDU, this primary pressure will be used in the design of the ejector. The ESDU mass flow rate results from Table 5-2 for $P_{t1} = 25bar$ is shown graphically in Figure 5-6. This is the performance operating envelop the designed ejector should meet. The blue line in Figure 5-6 shows the target maximum mass flow rates at the various secondary pressures that the ejector needs to meet. The designed ejector performance should lie at or above the blue line in order to be a successful final design.

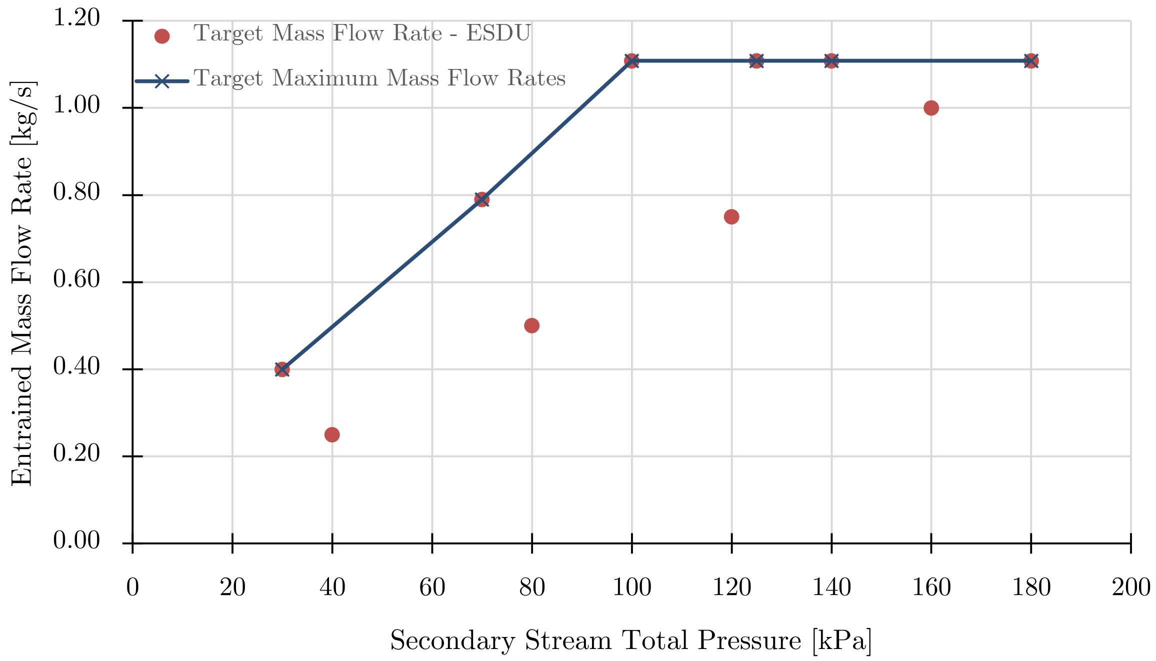

Figure 5-6 : Target maximum mass flow rates

The performance prediction calculation from ESDU 92042 was explored since this would allow for the outlet conditions and the flow conditions throughout a specified ejector geometry to be determined for various secondary pressures. The input for the performance prediction calculation was the geometry developed using the quick design procedure. A sample calculation using the geometry determined for $P_{t0} = 120kPa$ from the quick design procedure was investigated with the results shown in Table 5-5. The performance prediction calculation was unable to evaluate $P_{t1} = 25bar$ case, which was the original case for the specified geometry used as the input data. The entrained mass flow rate for $P_{t0} = 120kPa$ at $P_{t1} = 25bar$ was required to be $\dot{m}_{entrained} = 0.75kg/s$ as listed in Table 5-2. However, the performance prediction calculation determined that for the specified geometry, the targeted entrained mass flow rate of 0.75kg/s could be obtained at a lower primary pressure approximately 20bar. The results also showed that by decreasing the primary pressure, P_{t1}, for a specific ejector geometry, an increase in entrained mass flow rate could be attained as shown in Table 5-5.

Table 5-5 : Prediction performance calculation results for $P_{t0} = 120kPa$

P_{t1} [bar]	$\dot{m}_{ESDU}$ [kg/s]	$\dot{m}_p$ [kg/s]
25	-	-
24	0.13	0.53
23	0.43	0.51
22	0.58	0.49
21	0.69	0.47
20	0.77	0.44
17	0.93	0.38

ESDU 92042 stated that when the output from the design evaluation is taken as the input for a performance prediction calculation, the results obtained for the performance parameters should agree with the initial data input as mentioned in Section 3.2.1. However, this was incorrect as the original case could not be evaluated; instead the performance prediction calculated that the entrained mass flow rate could be obtained using a lower primary pressure. Since there was no correlation between the quick design procedure results and the performance prediction calculation, a different method for exploring the performance of an ejector needed to be determined.

5.2.2 Off-Design Ejector

Since ESDU 92042 determines the optimum ejector design for a specific set of input data, an off-design case was determined. The off-design case was determined by analysing each ejector design, obtained by ESDU 92042 for $P_{t1} = 25bar$ and secondary stream total pressures listed in Table 5-2, to determine which geometrical factors where significantly different. It was established that the mixing duct cross-sectional area, hence mixing duct diameter was the most significant factor that changed between each ejector design as shown in Table 5-6. It should be noted that the optimum mixing duct diameter for each ejector design is listed in Table 5-6.

Table 5-6 : Mixing duct diameters for various secondary stream total pressures

P_{t0} [kPa]	Mixing Duct Diameter [m]
30	0.10133
40	0.07058
70	0.09816
80	0.06975
100	0.11759
120	0.07277
125	0.10545
140	0.09980
160	0.08233
180	0.08817

Since the performance prediction calculation could not be utilised, CFD simulations were performed employing a test matrix shown in Table 3-6. The results from the CFD simulations performed are explained in Table 5-7. Three different ejector geometries where tested at three different secondary stream total pressures. It should be noted that three of the nine simulations performed were for the optimum design case *i.e.* ejector geometry obtained for specific input data. These optimum design cases occur for minimum geometry at $P_{t0} = 80kPa$, intermediate geometry at $P_{t0} = 180kPa$ and maximum geometry at $P_{t0} = 100kPa$. The maximum ejector geometry resulted in reverse flow for $P_{t0} = 80kPa$ and $P_{t0} = 180kPa$, however a successful simulation was obtained for $P_{t0} = 100kPa$ since this was the optimum design. The intermediate ejector geometry resulted in reverse flow for $P_{t0} = 80kPa$, however successful simulations were obtained for $P_{t0} = 100kPa$ and $P_{t0} = 180kPa$ since this was the optimum design. The minimum ejector geometry resulted in all CFD simulations being successful. This geometry yielded an entrained mass flow rate for all three secondary stream total pressures, however for $P_{t0} = 100kPa$ a significant reduction in the entrained mass flow rate occurred. The results from the CFD simulations performed indicated that for larger mixing duct diameters, reverse flow will be obtained for cases where the optimum design mixing duct diameters are smaller. However if smaller mixing duct diameters are employed, then a reduction in the entrained mass flow rate will be achieved for the cases where the optimum design mixing duct diameters are larger.

Table 5-7 : CFD results for determining off-design case

Mixing Duct Diameter [m]	Geometry	Secondary Stream Total Pressure - P_{to} 80kPa - Minimum	100kPa - Intermediate	180kPa - Maximum
0.06975	**Minimum - 80kPa**	✓	✓ Reduced Mass Flow Rate	✓
0.08817	**Intermediate - 180kPa**	× Reverse Flow	✓	✓
0.11759	**Maximum - 100kPa**	× Reverse Flow	✓	× Reverse Flow

The numerical results from the CFD simulations performed are listed in Table 5-8. The maximum and intermediate ejector geometries resulted in an unsuccessful determination in the entrained mass flow rate for specific secondary stream total pressures. The maximum ejector geometry produced results for only its optimum case with an entrained mass flow rate of $\dot{m}_{entrained} = 1.35kg/s,$ since the other two optimum design mixing duct diameters are smaller than the maximum ejector geometry. The intermediate ejector geometry resulted in a decrease in the entrained mass flow rate for $P_{t0} = 100kPa,$ since the optimum design mixing duct diameter for this specific case is larger than the intermediate ejector geometry. The entrained mass flow rate that was targeted for $P_{t0} = 100kPa$ was $\dot{m}_{entrained} = 1.35kg/s$ however an entrained mass flow rate of $\dot{m}_{entrained} = 1.14kg/s$ was achieved. The optimum design case for the intermediate ejector geometry resulted in an entrained mass flow rate of $\dot{m}_{entrained} = 1.45kg/s$. The minimum ejector geometry resulted in a decrease entrained mass flow rate for $P_{t0} = 100kPa$ and $P_{t0} = 180kPa$, since both these cases have optimum design mixing duct diameters larger than the minimum ejector geometry. The entrained mass flow rate that was targeted for $P_{t0} = 180kPa$ was $\dot{m}_{entrained} = 1.45kg/s$ however an entrained mass flow rate of $\dot{m}_{entrained} = 1.26kg/s$ was achieved. A more significant reduction in the entrained mass flow rate was obtained for $P_{t0} = 100kPa$. The targeted entrained mass flow rate for $P_{t0} = 100kPa$ was $\dot{m}_{entrained} = 1.35kg/s$, however the entrained mass flow rate that the minimum ejector geometry attained was $\dot{m}_{entrained} = 0.66kg/s$. This is due to the mixing duct diameter of the optimum design case of $P_{t0} = 100kPa$ being significantly larger than the mixing duct diameter of the minimum ejector geometry. Since the minimum mixing duct diameter ejector design was the only ejector to entrain mass flow for the various secondary stream entry total pressures, this ejector was considered to be the off-design case.

Table 5-8 : Numerical CFD results for determining off-design case

Mixing Duct Diameter [m]	Geometry	Entrained Mass Flow Rate [kg/s] P_{to} = 80kPa Minimum	P_{to} = 100kPa Intermediate	P_{to} = 180kPa Maximum
0.06975	**Minimum - 80kPa**	0.50	0.66	1.26
0.08817	**Intermediate - 180kPa**	-	1.14	1.45
0.11759	**Maximum - 100kPa**	-	1.35	-

5.2.3 Configuration 2 – 9 Ejectors Designed At $P_{t1} = 25bar$

The off-design case was converted into 9 single ejectors as described in Section 3.2.3. Two-dimensional CFD simulations were performed according to Section 3.2.2 to determine the entrained mass flow rates obtained using the ejector geometry of configuration 2 developed by ESDU. CFD simulations were performed for a range of secondary stream total pressures such that a significant pressure difference exists between each secondary stream total pressure. The entrained mass flow rate obtained from the CFD simulations at various secondary stream total pressures are listed in Table 5-9. The targeted entrained mass flow rate that the ejector had to achieve was according to the specified entrained mass flow rate from ESDU for $P_{t1} = 25bar$ in Section 5.2.1. The entrained mass flow rate obtained for $P_{t0} = 80kPa$ with 9 ejectors at $P_{t1} = 25bar$ was $\dot{m}_{CFD} = 0.51kg/s$ which correlates to the entrained mass flow rate of the off-design case, $\dot{m}_{entrained} = 0.50kg/s$. The entrained mass flow rate for $P_{t0} = 100kPa$ and $P_{t0} = 180kPa$ for the off-design case resulted in $\dot{m}_{entrained} = 0.66kg/s$ and $\dot{m}_{entrained} = 1.26kg/s$ respectively, which also correlates to the entrained mass flow rate achieved for the 9 ejectors at $P_{t1} = 25bar$ in Table 5-9. This shows that the method used to convert from a single nozzle ejector to multiple ejectors was correct.

The entrained mass flow rates achieved by the 9 ejectors at $P_{t1} = 25bar$ for $P_{t0} = 80kPa,\ P_{t0} = 160kPa$ and $P_{t0} = 180kPa$, exceeds the target mass flow rates from ESDU as listed in Table 5-9. However, for the remaining secondary stream total pressures the entrained mass flow rates obtained by the CFD simulations did not meet the targeted mass flow rates from ESDU as shown in Figure 5-7. This is due to the optimum ejector mixing duct diameters of these secondary stream total pressures, listed in Table 5-6, being significantly larger than the mixing duct diameter of the off-design ejector. Due to these entrained mass flow rates not meeting the targeted mass flow rates from ESDU, the ejector system was redesigned.

Table 5-9 : CFD simulation results for 9 ejectors designed at $P_{t1} = 25bar$

$\boldsymbol{P_{t0}}$ [kPa]	$\boldsymbol{\dot{m}_{CFD}}$ [kg/s]	$\boldsymbol{\dot{m}_{ESDU}}$ [kg/s]
30	0.14	0.40
70	0.45	0.79
80	0.51	0.50
100	0.68	1.11
125	0.86	1.11
160	1.09	1.00
180	1.23	1.11

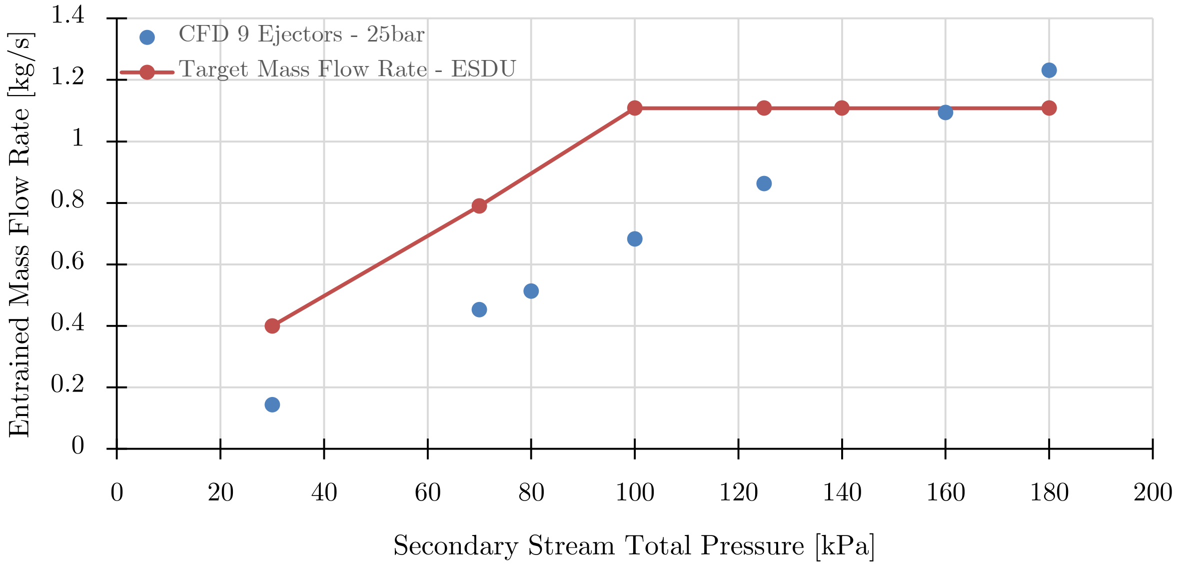

Figure 5-7 : CFD simulation results for 9 ejectors designed at $P_{t1} = 25bar$

5.2.4 Redesigned 9 Ejectors At $P_{t1} = 20bar$ and $\dot{m}_p = 0.277kg/s$

Since the 9 ejectors designed at $P_{t1} = 25bar$ did not meet the required entrained mass flow rate from ESDU, the ejector was redesigned at a lower primary pressure which would allow for the ejector to be run at a higher pressure entraining more mass flow and redesigning at a lower primary mass flow rate would allow for the addition of ejectors. The ejector was redesigned using ESDU 92042 with a primary pressure, $P_{t1} = 20bar$, and total primary mass flow rate of $\dot{m}_p = 0.277kg/s$ which results to a primary mass flow rate of $\dot{m}_p = 0.03078kg/s$ per nozzle. The ejector designed using ESDU 92042 for the above mentioned parameters can be found in APPENDIX E. Two-dimensional CFD simulations were performed as described in Section 3.2.2 with the redesigned ejector geometry simulating maximum primary pressure conditions *i.e.* $P_{t1} = 25bar$ to determine the entrained mass flow rates obtainable at various secondary stream total pressures. CFD simulations were performed for a range of secondary stream total pressures such that a significant pressure difference exists between each secondary stream total pressure. The entrained mass flow rate obtained for 9 ejectors from CFD simulations at various secondary stream total pressures are listed in Table 5-10 and illustrated graphically in Figure 5-8 with respect to the required entrained mass flow rate from ESDU. The entrained mass flow rates achieved by the 9 ejectors simulating $P_{t1} = 25bar$ exceeds the target mass flow rates from ESDU for most of the secondary stream total pressures. However, for $P_{t0} = 30kPa$, $P_{t0} = 70kPa$ and $P_{t0} = 100kPa$ the entrained mass flow rates obtained by the CFD simulations did not meet the targeted mass flow rates from ESDU.

Table 5-10 : CFD simulation results for 9 ejectors designed at $P_{t1} = 20bar$ and $\dot{m}_p = 0.277kg/s$

$\boldsymbol{P_{t0}}$ [kPa]	$\boldsymbol{\dot{m}_{CFD}}$ [kg/s]	$\boldsymbol{\dot{m}_{ESDU}}$ [kg/s]
30	0.26	0.40
70	0.68	0.79
80	0.79	0.50
100	1.02	1.11
125	1.17	1.11
140	1.20	1.11
160	1.37	1.00
180	1.55	1.11

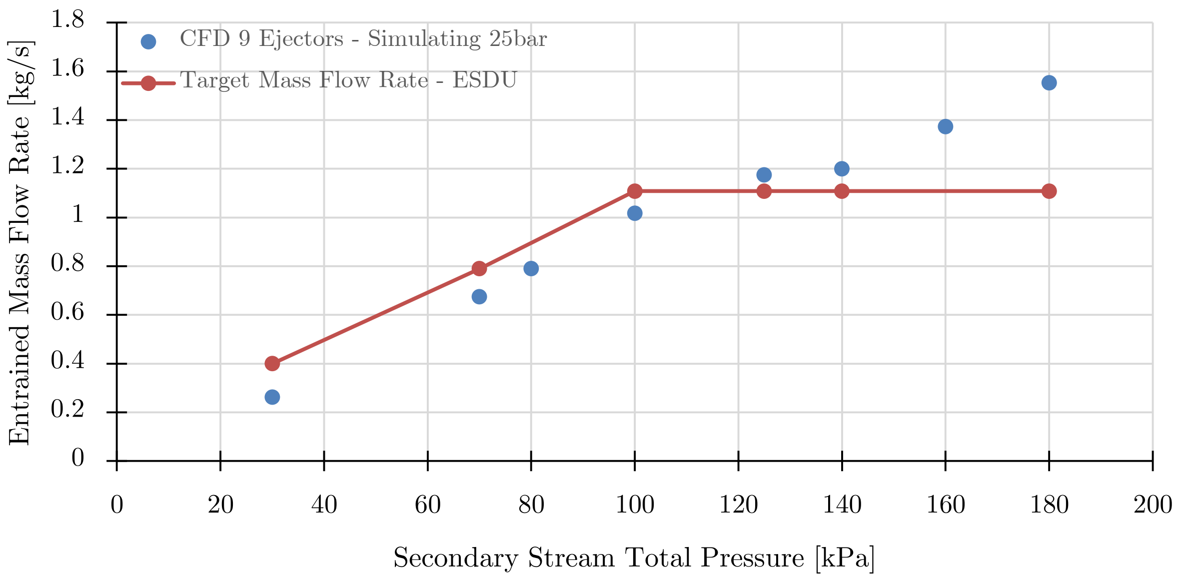

Figure 5-8 : CFD simulation results for 9 ejectors designed at $P_{t1} = 20bar$ and $\dot{m}_p = 0.277kg/s$

A comparison of results from CFD simulations for 9 ejectors designed at $P_{t1} = 25bar$ and 9 ejectors designed at $P_{t1} = 20bar$ and $\dot{m}_p = 0.277kg/s$ are illustrated in Figure 5-9. It can be seen that the entrained mass flow rates obtained for the ejector designed at $P_{t1} = 20bar$ and $\dot{m}_p = 0.277kg/s$ are significantly higher than the entrained mass flow rates obtained for the ejector designed at $P_{t1} = 25bar$. The results of the ejector designed at $P_{t1} = 20bar$ and $\dot{m}_p = 0.277kg/s$ follows the same trend as the ejector designed at $P_{t1} = 25bar$.

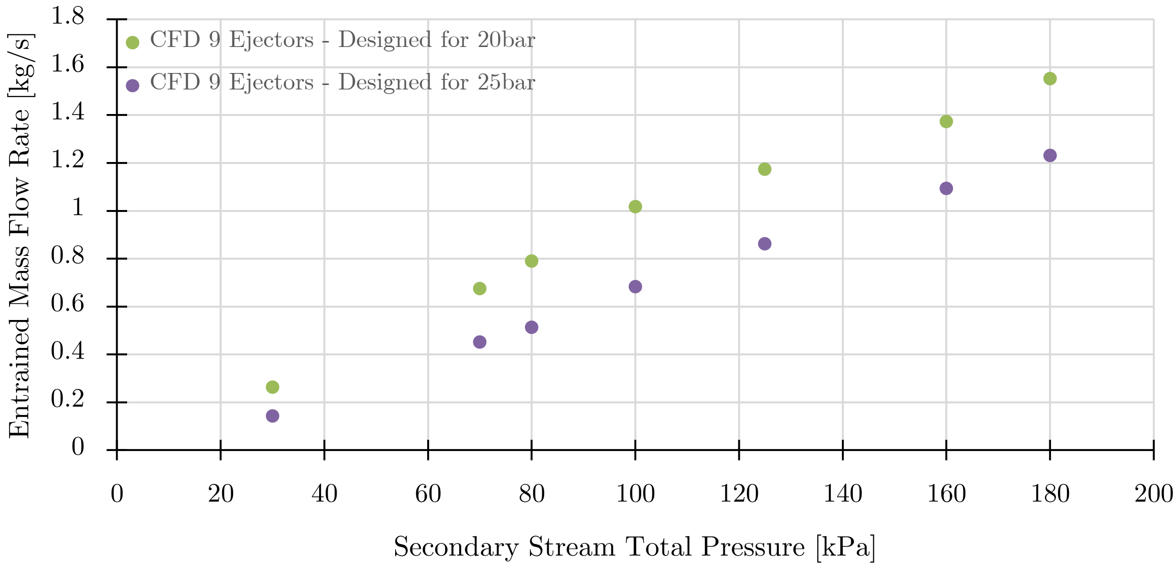

Figure 5-9 : Comparison of results for 9 ejectors designed at $P_{t1} = 25bar$ and 9 ejectors designed at $P_{t1} = 20bar$ and $\dot{m}_p = 0.277kg/s$

5.2.5 Design Integrating 14 Ejectors At $P_{t1} = 20bar$ and $\dot{m}_p = 0.277kg/s$

It was established that the entrained mass flow rate determined with the redesigned ejector at $P_{t1} = 20bar$ and $\dot{m}_p = 0.277kg/s$, simulating maximum primary pressure $P_{t1} = 25bar$, did not meet all the required entrained mass flow rates from ESDU, hence the option of increasing the number of ejectors were explored. The mass flow rate through the primary nozzle designed for the ejector at $P_{t1} = 20bar$ and $\dot{m}_p = 0.277kg/s$ resulted in a primary mass flow rate per nozzle $\dot{m}_{per\_nozzle} = 0.0395kg/s$. Using this information, the maximum number of ejectors that will satisfy the maximum primary mass flow rate available ($\dot{m}_p = 0.554kg/s$) resulted in 14 ejectors. The entrained mass flow rate results from Table 5-10 for the ejector designed at $P_{t1} = 20bar$ and $\dot{m}_p = 0.277kg/s$ was used to calculate the entrained mass flow rates for 14 ejectors with the results listed in Table 5-11 and shown graphically in Figure 5-10 with respect to the required entrained mass flow rate from ESDU. From Table 5-11 and Figure 5-10 it can be seen that the calculated entrained mass flow rates for 14 ejectors designed at $P_{t1} = 20bar$ and $\dot{m}_p = 0.277kg/s$, simulating $P_{t1} = 25bar$, will meet or exceed the required entrained mass flow rates from ESDU. It should be noted that the entrained mass flow rate for $P_{t0} = 30kPa$ meets the required mass flow rate from ESDU, whereas the entrained mass flow rates for $P_{t0} = 80kPa$ up until $P_{t0} = 180kPa$ are significantly higher than the required mass flow rates from ESDU. Since the design integrating 14 ejectors yields the required entrained mass flow for the various secondary stream entry total pressures, this ejector configuration was deemed feasible.

Table 5-11 : Calculated entrained mass flow rates for 14 ejectors designed at $P_{t1} = 20bar$ and $\dot{m}_p = 0.277kg/s$

P_{t0} [kPa]	$\dot{m}_{Calc}$ [kg/s]	$\dot{m}_{ESDU}$ [kg/s]
30	0.41	0.40
70	1.05	0.79
80	1.23	0.50
100	1.58	1.11
125	1.83	1.11
140	1.87	1.11
160	2.14	1.00
180	2.41	1.11

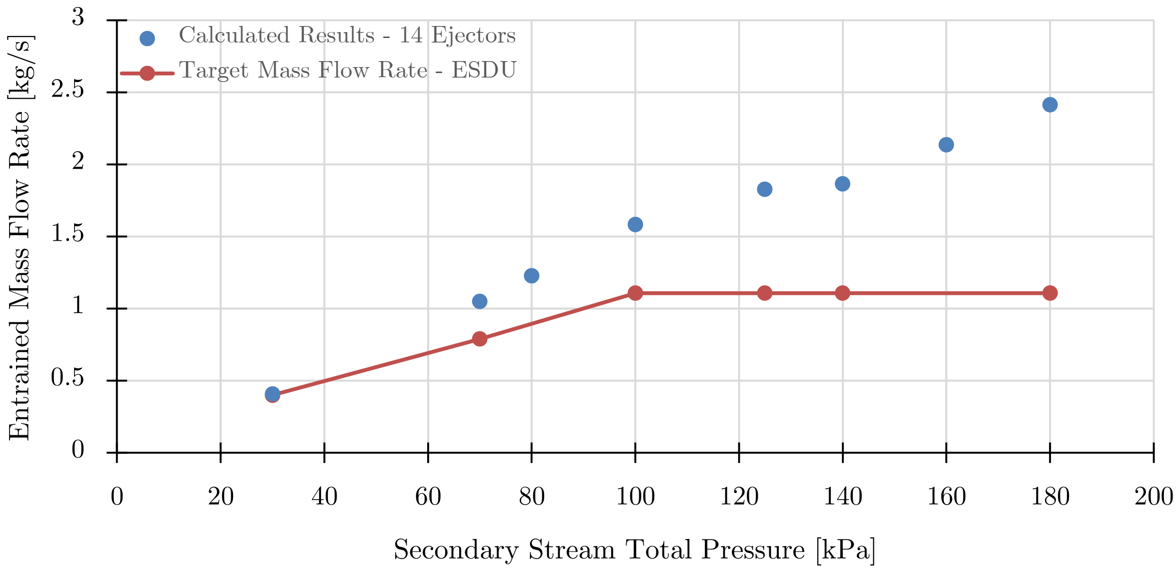

Figure 5-10 : Entrained mass flow rate calculated for 14 ejectors designed at $P_{t1} = 20bar$ and $\dot{m}_p = 0.277kg/s$

5.2.6 Multi-Nozzle Ejector

The configuration employing 14 ejectors was used to develop a multi-nozzle ejector as described in Section 3.2.3 and illustrated in Figure 3-18. Three-dimensional CFD simulations were performed according to Section 3.2.2 to determine the entrained mass flow rate for various secondary stream total pressures. CFD simulations were performed for a range of secondary stream total pressures such that a significant pressure difference exists between each secondary stream total pressure. The results extracted from the CFD simulations are listed in Table 5-13 and shown graphically in Figure 5-12 with respect to the calculated entrained mass flow rate for 14 ejectors from Section 5.2.5. For secondary stream total pressures $P_{t0} = 30kPa$, $P_{t0} = 70kPa$ and $P_{t0} = 80kPa$ the entrained mass flow rates obtained by the CFD simulations did not meet the calculated entrained mass flow rate for 14 ejectors by a small fraction. However, $P_{t0} = 160kPa$ yielded an entrained mass flow rate $\ddot{m}_{CFD-MN} = 2.16kg/s$, which was slightly higher than the calculated entrained mass flow rate for 14 ejectors. The remaining secondary stream total pressures *i.e.* $P_{t0} = 100kPa$, $P_{t0} = 125kPa$ and $P_{t0} = 180kPa$ did not meet the calculated entrained mass flow rate by a significant margin.

Table 5-12 : CFD simulation results for multi-nozzle ejector

P_{t0} [kPa]	$\ddot{m}_{Calc}$[kg/s]	$\ddot{m}_{CFD-MN}$[kg/s]
30	0.41	0.31
70	1.05	0.89
80	1.23	1.15
100	1.58	0.91
125	1.83	0.73
160	2.14	2.16
180	2.41	2.04

It can be seen from Figure 5-11 that the entrained mass flow rate peaks at two points followed by a decrease in entrained mass flow rate. The entrained mass flow rate increases from $P_{t0} = 30kPa$ and peaks at $P_{t0} = 80kPa$, followed by a decrease in entrained flow. However, after the decrease in mass flow rate, the entrained mass flow peaks again at $P_{t0} = 160kPa$ followed by a decrease. For secondary stream total pressures $80kPa < P_{t0} < 160kPa$ the multi-nozzle ejector does not perform as required. The multi-nozzle ejector employs an annular mixing duct as opposed to a cylindrical mixing duct. ESDU stated that the mixing duct employed by an ejector need not be cylindrical. However, employing an annular mixing duct as an alternative to a cylindrical mixing duct has an effect on the performance of the multi-nozzle ejector. The shear layer developed in the annular mixing duct of the multi-nozzle ejector may have not represented the shear layer developed in the cylindrical mixing duct of a single ejector affecting the mixing process of the two streams and hence the entrained mass flow rate.

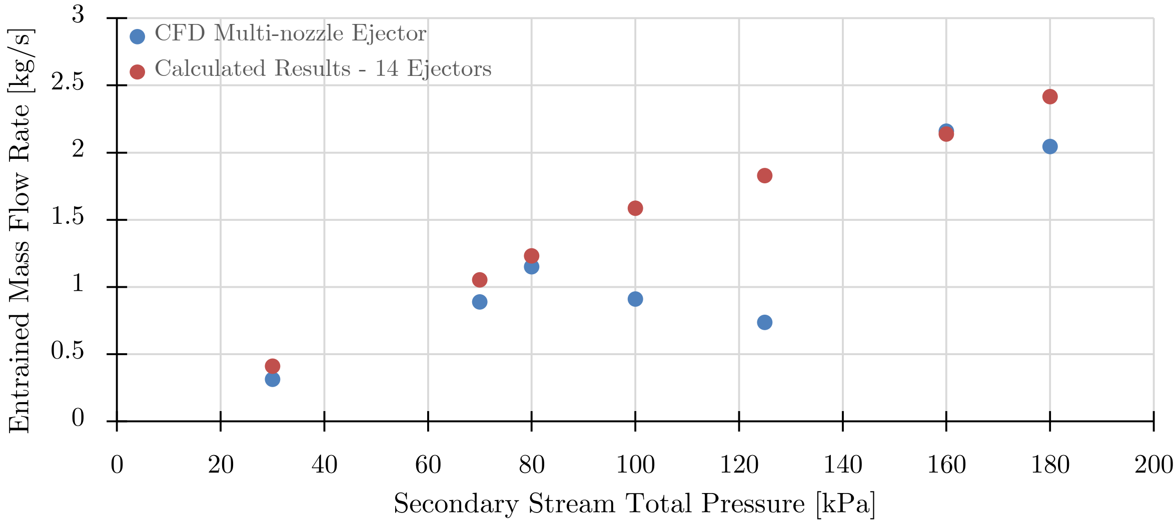

Figure 5-11 : CFD simulation results for multi-nozzle ejector

A comparison of the CFD simulation results for the multi-nozzle ejector and the target entrained mass flow rate from ESDU are listed in Table 5-13 and illustrated graphically in Figure 5-12. It can be seen that for various secondary stream total pressures, the entrained mass flow rate obtained by the multi-nozzle ejector exceeds the target entrained mass flow rate from ESDU. However, for $P_{t0} = 30kPa$, $P_{t0} = 100kPa$ and $P_{t0} = 125kPa$ the entrained mass flow rate obtained by the multi-nozzle ejector does not meet the targeted entrained mass flow rate from ESDU as shown graphically in Figure 5-12. Since no correlation exists between the CFD multi-nozzle ejector results and the calculated entrained mass flow rates for 14 ejectors, as well as the target entrained mass flow rate from ESDU, the multi-nozzle ejector design was deemed not feasible.

Table 5-13 : Comparison of CFD simulation results for multi-nozzle ejector and target entrained mass flow rate from ESDU

$\boldsymbol{P_{t0}}$ [kPa]	$\dot{\boldsymbol{m}}_{\boldsymbol{ESDU}}$ [kg/s]	$\dot{\boldsymbol{m}}_{\boldsymbol{CFD-MN}}$[kg/s]
30	0.40	0.31
70	0.79	0.89
80	0.50	1.15
100	1.11	0.91
125	1.11	0.73
160	1.00	2.16
180	1.11	2.04

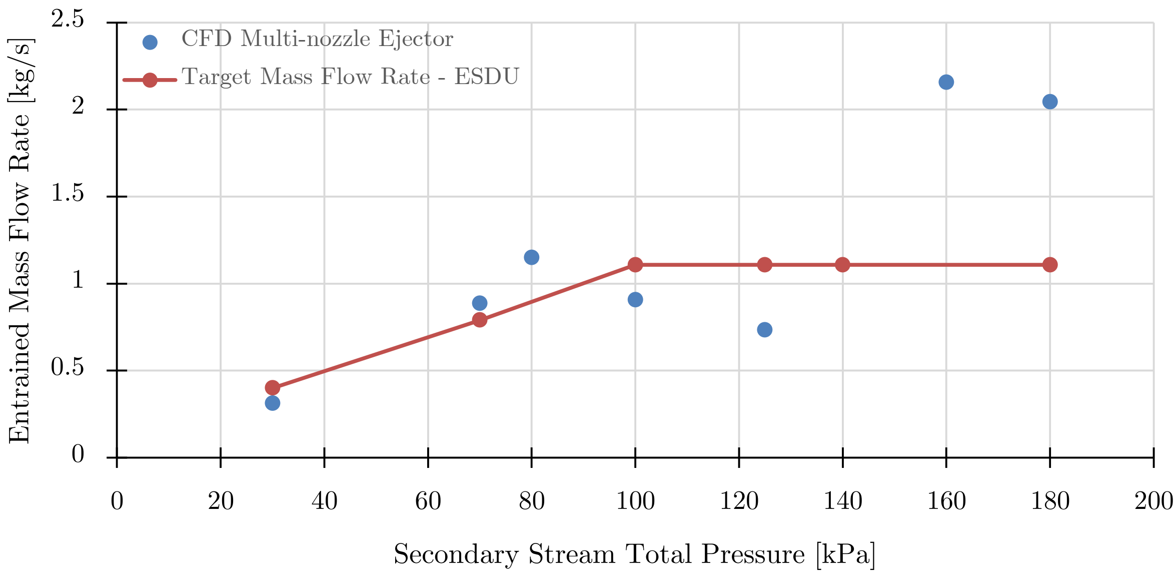

Figure 5-12 : Comparison of CFD simulation results for multi-nozzle ejector and target entrained mass flow rate from ESDU

5.2.7 Staggered Multi-Ejector

The staggered multi-ejector, as illustrated in Figure 3-21, employs 14 individual ejectors arranged around an annulus. Three-dimensional CFD simulations, as described in Section 3.2.2, were performed to determine the entrained mass flow rate for various secondary stream entry total pressures. CFD simulations were performed for a range of secondary stream total pressures such that a significant pressure difference exists between each secondary stream total pressure. The results extracted from the CFD simulations are listed in Table 5-14 and shown graphically in Figure 5-13 with respect to the calculated entrained mass flow rate for 14 ejectors from Section 5.2.5. It can be seen from Table 5-14 and Figure 5-13 that for all secondary stream total pressures, the achieved entrained mass flow rate from CFD simulations for the staggered multi-ejector has virtually met and exceeded the calculated entrained mass flow rate for 14 ejectors. For the staggered multi-ejector designed at a primary pressure of $P_{t1} = 25bar$, the minimum entrained mass flow rate achieved $\dot{m}_{CFD-ME} = 0.44kg/s$ occurs at $P_{t0} = 30kPa$, whereas a maximum entrained mass flow rate $\dot{m}_{CFD-ME} = 2.72kg/s$ occurs at $P_{t0} = 180kPa$. The entrained mass flow rate that can be achieved at ambient conditions, *i.e.* $P_{tunnel} = 100kPa$ from Table 5-1, ranges from $\dot{m}_{CFD-ME} = 1.06kg/s$ for $P_{t0} = 70kPa$ to $\dot{m}_{CFD-ME} = 1.21kg/s$ for $P_{t0} = 80kPa$. Since the CFD results obtained by the staggered multi-ejector met or exceeded the calculated entrained mass flow rate for 14 ejectors, this staggered multi-ejector design was deemed feasible.

Table 5-14 : CFD simulation results for staggered multi-ejector

P_{t0} [kPa]	$\dot{m}_{Calc}$ [kg/s]	$\dot{m}_{CFD-ME}$ [kg/s]
30	0.41	0.44
70	1.05	1.06
80	1.23	1.21
100	1.58	1.56
125	1.83	1.91
140	1.87	2.14
160	2.14	2.42
180	2.41	2.72

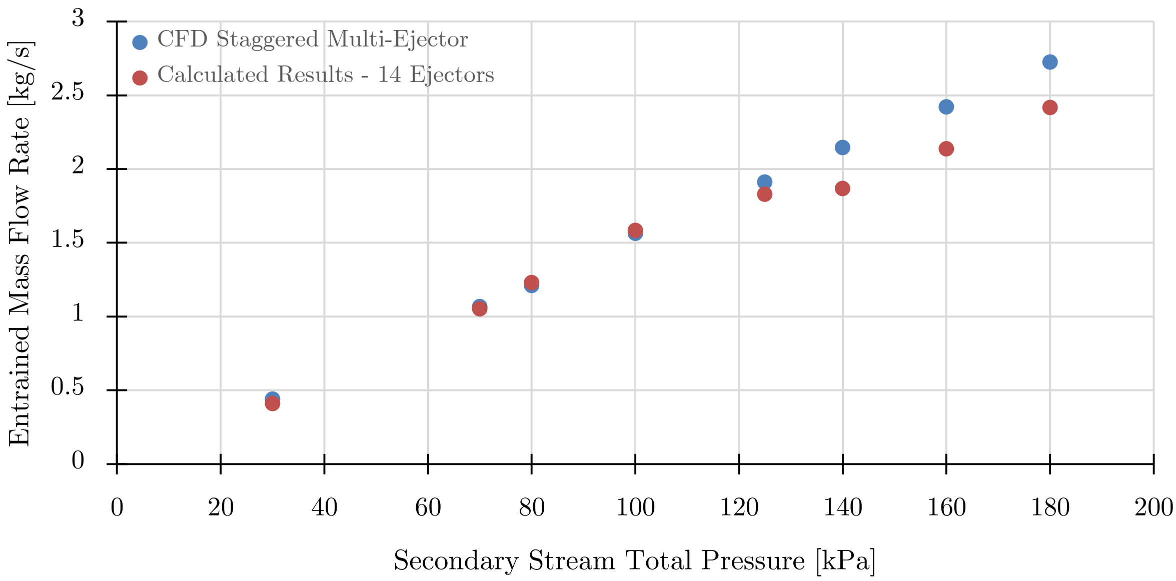

Figure 5-13 : CFD simulation results for staggered multi-ejector

The entrained mass flow rate obtained from CFD simulations for the staggered multi-ejector at various secondary stream total pressures are shown graphically from Figure 5-14(a) to Figure 5-14(h). The mass flow inlet chamber monitor represents the mass flow rate entrained by the staggered multi-ejector. It can be seen that the entrained mass flow rate converged at the various secondary stream total pressures for the staggered multi-ejector.

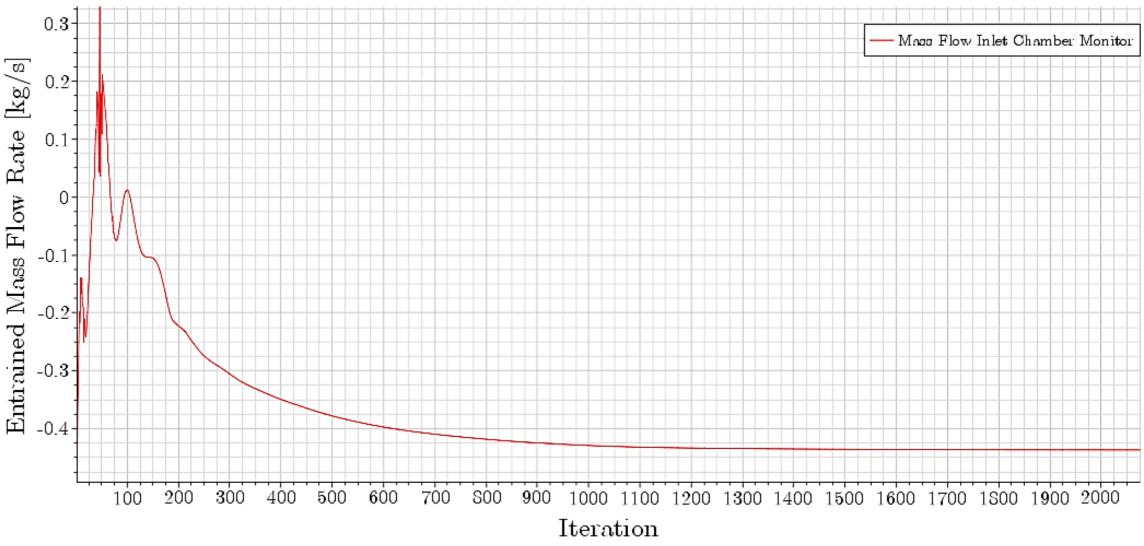

(a) Entrained mass flow rate plot at $P_{t0} = 30kPa$

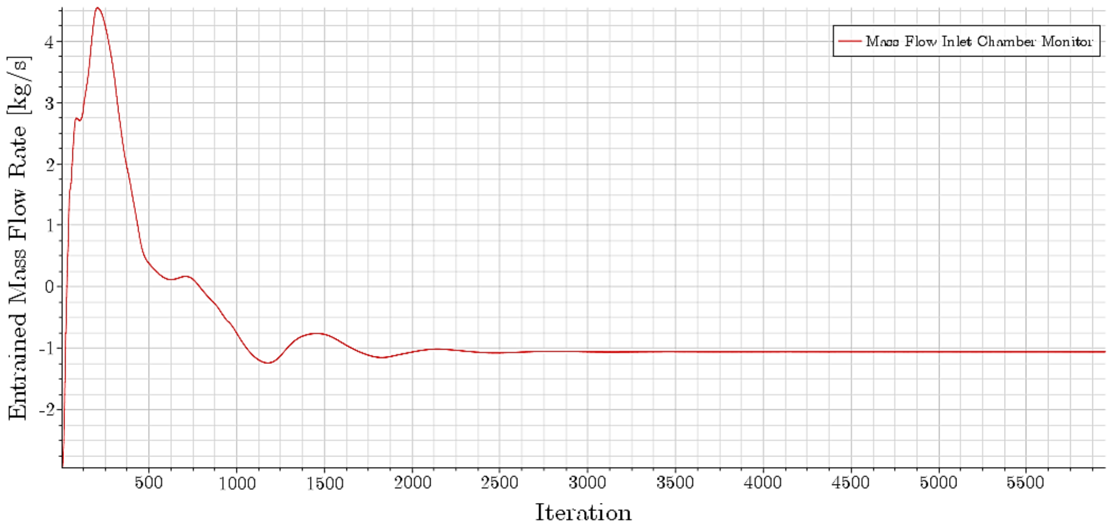

(b) Entrained mass flow rate plot at $P_{t0} = 70kPa$

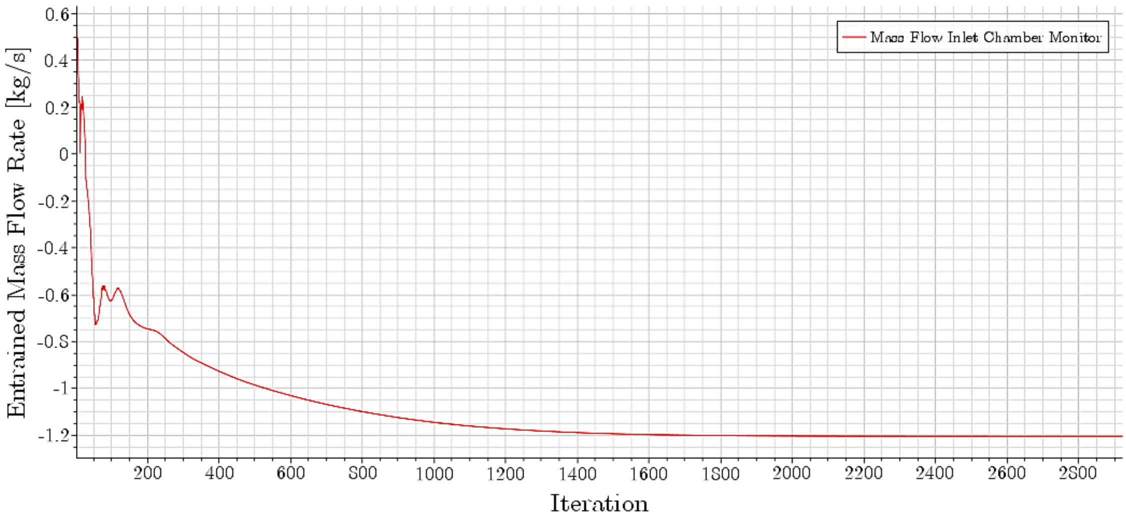

(c) Entrained mass flow rate plot at $P_{t0} = 80kPa$

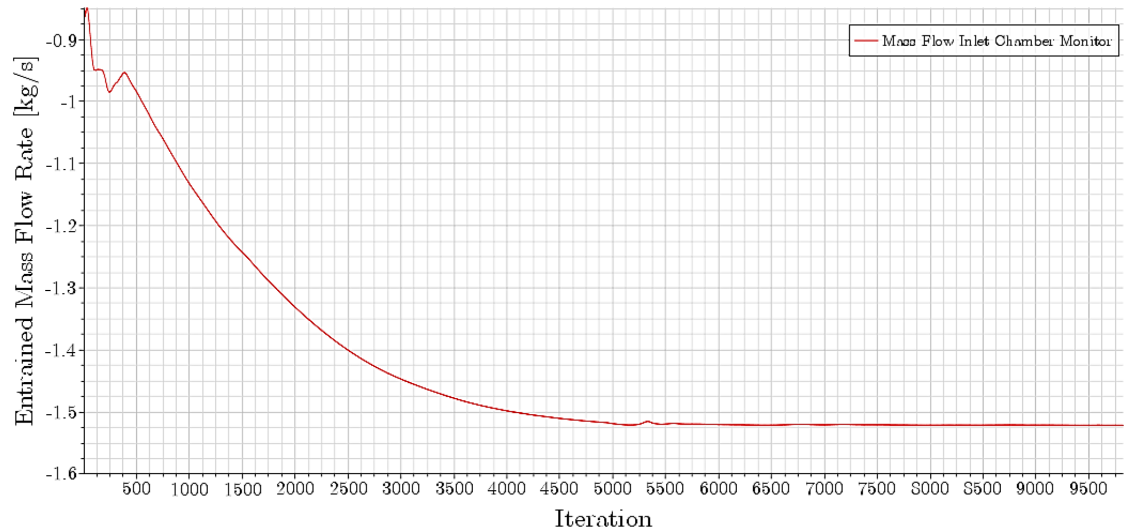

(d) Entrained mass flow rate plot at $P_{t0} = 100kPa$

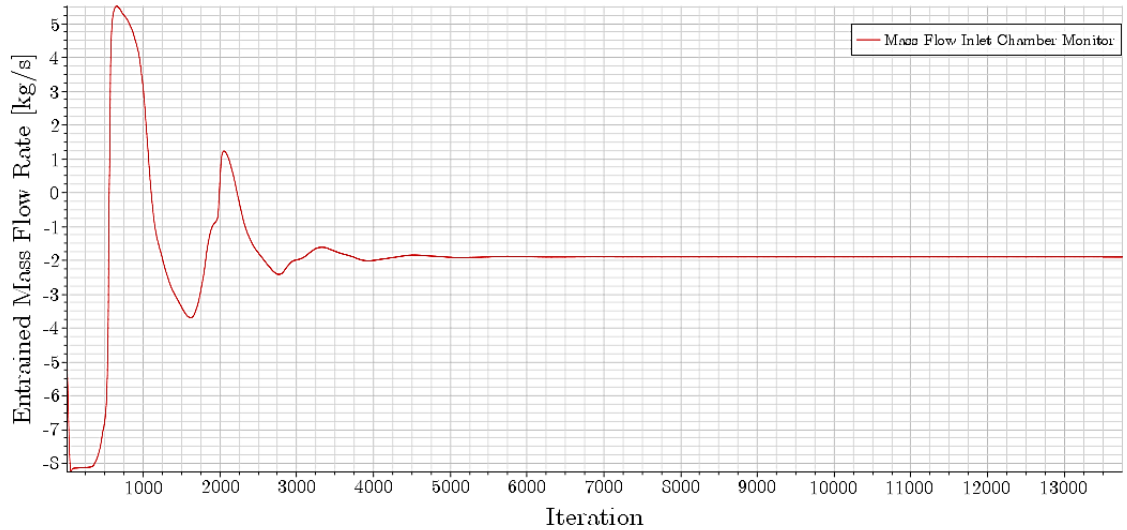

(e) Entrained mass flow rate plot at $P_{t0} = 125kPa$

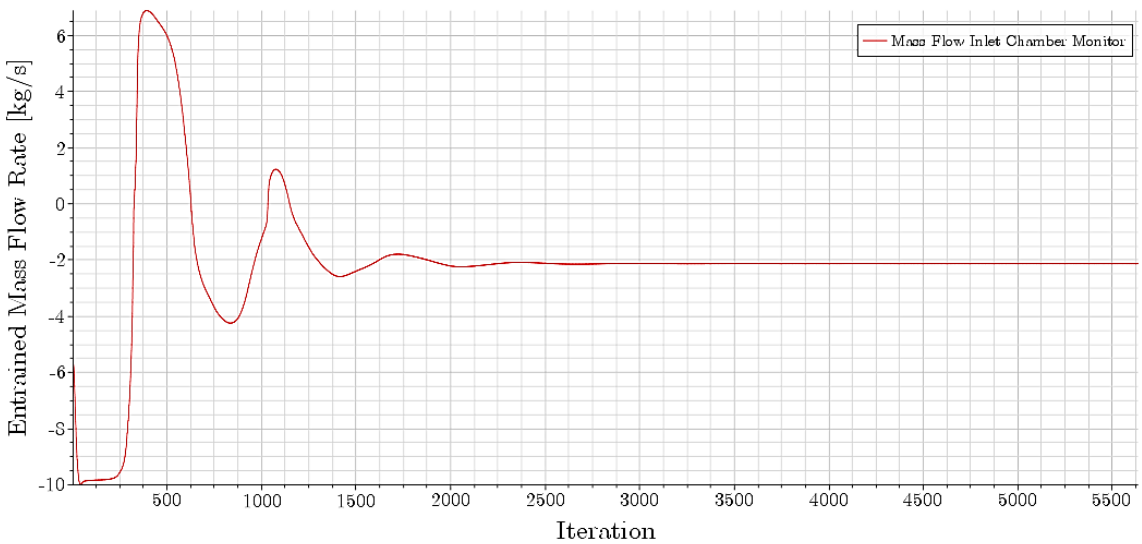

(f) Entrained mass flow rate plot at $P_{t0} = 140kPa$

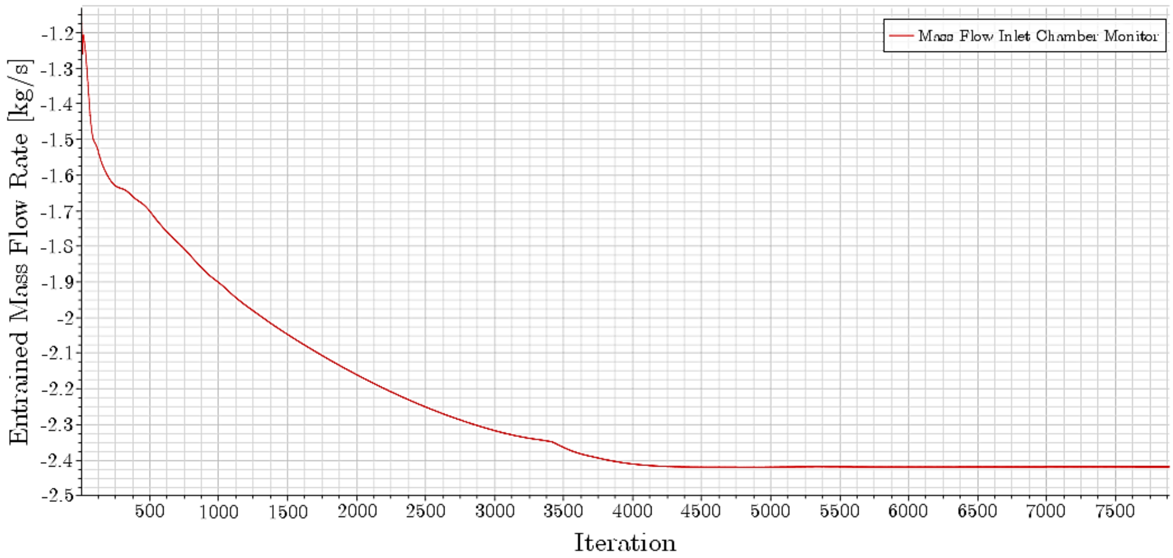

(g) Entrained mass flow rate plot at $P_{t0} = 160kPa$

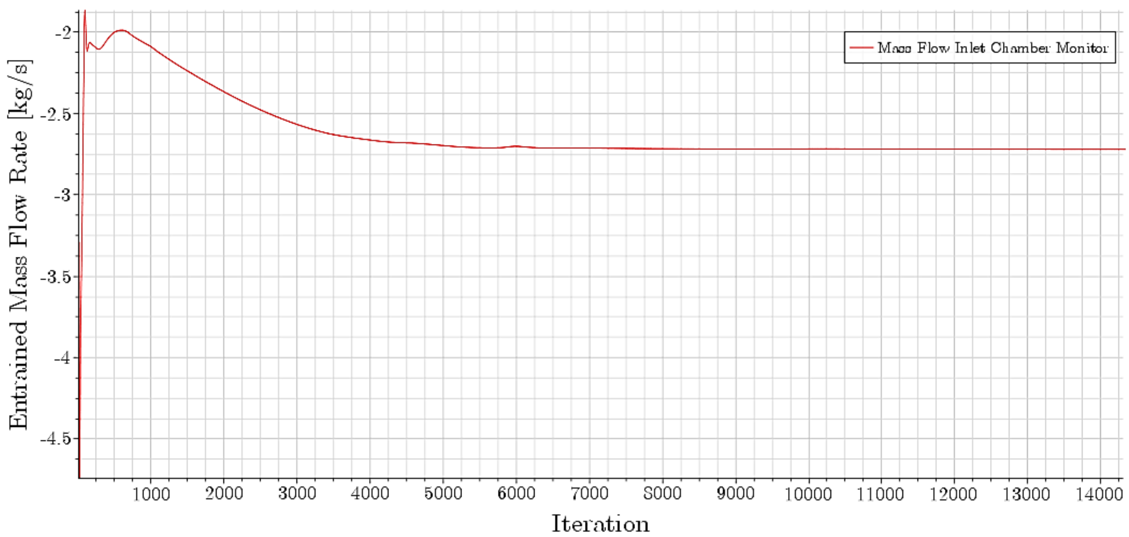

(h) Entrained mass flow rate plot at $P_{t0} = 180kPa$

Figure 5-14 : CFD simulation entrained mass flow rate plot at various secondary stream total pressures for the staggered multi-ejector

A comparison of the CFD simulation results for the staggered multi-ejector and the target entrained mass flow rate from ESDU are listed in Table 5-15 and illustrated graphically in Figure 5-15. It can be seen that for all secondary stream total pressures, the entrained mass flow rate obtained by the staggered multi-ejector exceeds the target entrained mass flow rate from ESDU. For $P_{t0} = 30kPa$ the entrained mass flow rate obtained by the staggered multi-ejector $\dot{m}_{CFD-ME} = 0.44kg/s$ is slightly greater than the targeted entrained mass flow rate from ESDU, whereas for the remaining secondary stream total pressures the entrained mass flow rate obtained by the staggered multi-ejector is significantly greater than the entrained mass flow rate from ESDU. This is due to the mass flow ratio limitation imposed by ESDU which resulted in a maximum mass flow rate $\dot{m}_{ESDU} = 1.11kg/s$ as shown in Table 5-2.

Table 5-15 : Comparison of CFD simulation results for staggered multi-ejector and target entrained mass flow rate from ESDU

P_{t0} [kPa]	$\dot{m}_{ESDU}$ [kg/s]	$\dot{m}_{CFD-ME}$ [kg/s]
30	0.40	0.44
70	0.79	1.06
80	0.50	1.21
100	1.11	1.56
125	1.11	1.91
140	1.11	2.14
160	1.00	2.42
180	1.11	2.72

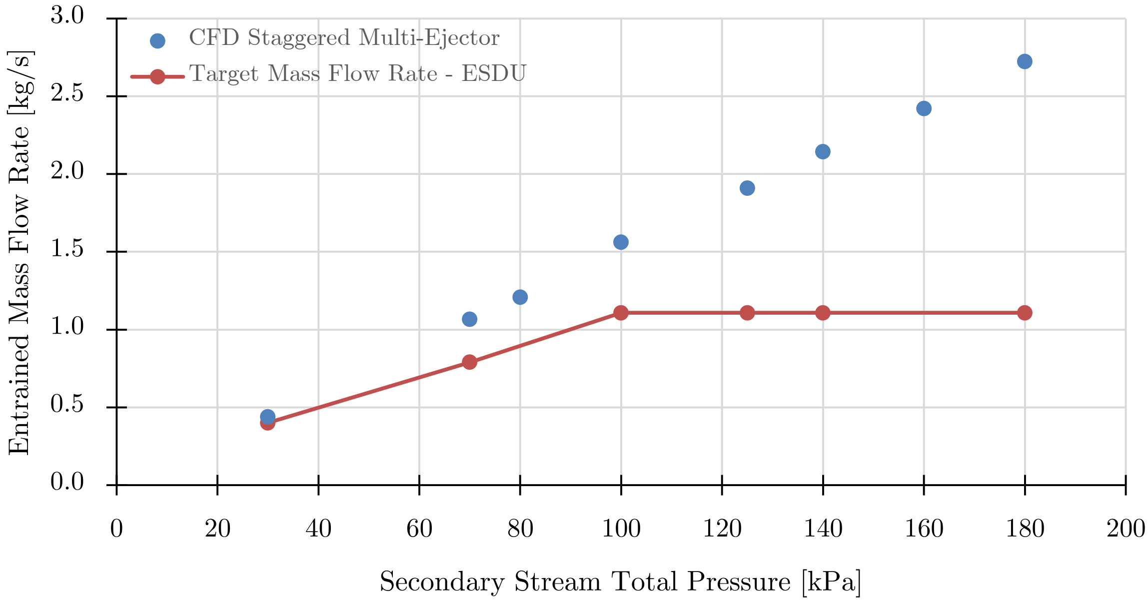

Figure 5-15 : Comparison of CFD simulation results for staggered multi-ejector and target entrained mass flow rate from ESDU

A comparison of the CFD simulation results for the staggered multi-ejector and the results obtained from the flow quantity metering analysis, listed in Table 5-1, for various secondary stream total pressures are illustrated in Figure 5-16. The results from the flow quantity metering analysis are illustrated in Figure 5-16 for different plug displacements. It can be seen that for all secondary stream total pressures, the entrained mass flow rate obtained by the staggered multi-ejector exceeds the results obtained from the flow quantity metering analysis. This ensures that the designed staggered multi-ejector will be able to entrain the required mass flow rate determined by the designed flow quantity metering system for all secondary stream total pressures, hence wind tunnel stagnation pressures.

Since the designed staggered multi-ejector employs 14 individual ejectors, this provides an option of employing all 14 individual ejectors or allowing for an appropriate number of ejectors to be run collectively depending on the mass flow rate required to be entrained. From Figure 5-16 it can be seen that for plug displacements of 30mm, all 14 ejectors should be employed for $P_{t0} = 30kPa$. However, for plug displacements of 95mm a reduced number of ejectors run collectively could be used to entrain the required mass flow rate at $P_{t0} = 80kPa$, $P_{t0} = 160kPa$ and $P_{t0} = 180kPa$.

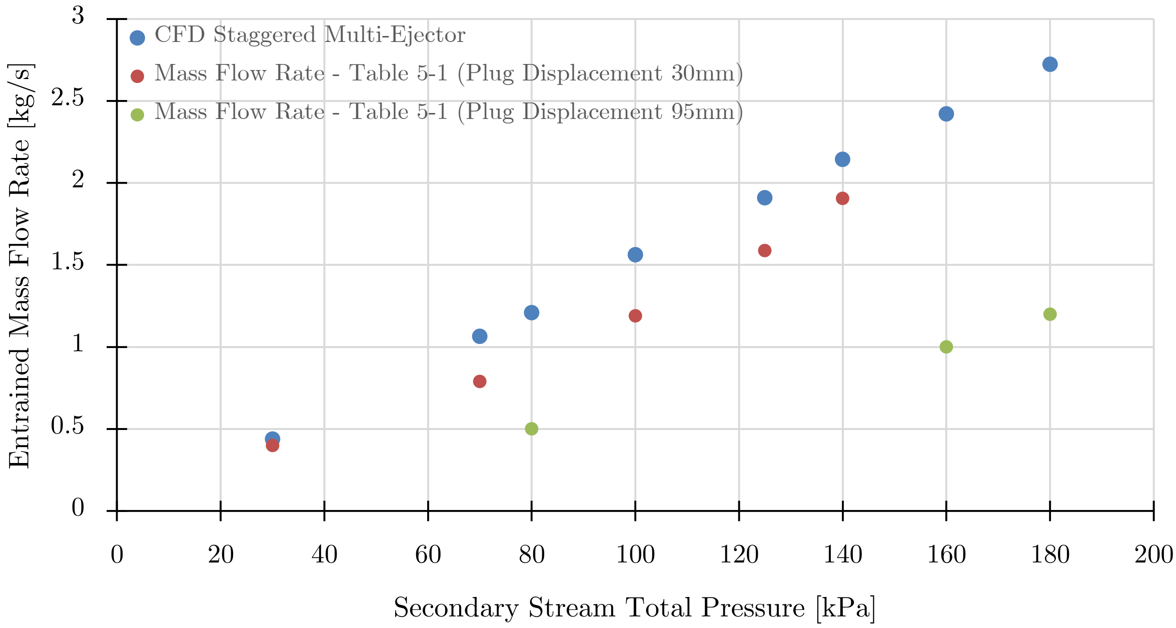

Figure 5-16 : Comparison of CFD simulation results for staggered multi-ejector and flow quantity metering analysis results

The mass flow ratios, $\dot{m}_{CFD-ME}/\dot{m}_p$, determined for various primary to secondary pressure ratios, P_{t1}/P_{t0}, for the staggered multi-ejector are illustrated in Figure 5-17. It should be noted that the staggered multi-ejector was designed for a primary pressure $P_{t1} = 25bar$ with a primary mass flow rate $\dot{m}_p = 0.554kg/s$. From Figure 5-17 it can be seen that a maximum mass flow ratio $\dot{m}_{CFD-ME}/\dot{m}_p = 4.92$ is obtained by the staggered multi-ejector at a low pressure ratio $P_{t1}/P_{t0} = 13.89$, indicating a high entrained mass flow rate at a high secondary pressure. For higher pressure ratios, a lower mass flow ratio is observed indicating a low entrained mass flow rate at lower secondary pressures.

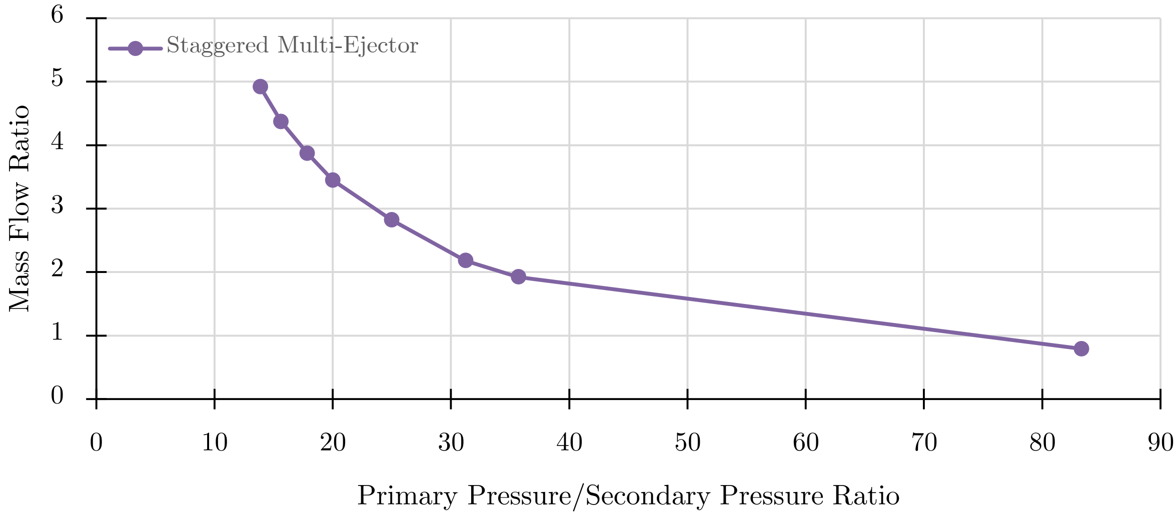

Figure 5-17 : Staggered multi-ejector $\dot{m}_{CFD-ME}/\dot{m}_p$ for various P_{t1}/P_{t0}

Three-dimensional CFD simulations, as described in Section 3.2.2, were performed to determine the entrained mass flow rates for a secondary stream entry total pressure of $P_{t0} = 80kPa$ and various backpressures (discharge pressures) for the staggered multi-ejector. The results extracted from the CFD simulations are listed in Table 5-16 and shown graphically in Figure 5-18. It can be seen from Table 5-16 and Figure 5-18 that the critical backpressure for the ejector operating at $P_{t0} = 80kPa$ occurs at $P_b = 78.4kPa$. For the staggered multi-ejector at $P_{t0} = 80kPa$ the critical operation mode, *i.e.* where the secondary flow is choked in the mixing duct, occurs for backpressures $P_b \leq 78.4kPa$ and the sub-critical operation mode, *i.e.* where the secondary flow is unchoked, occurs for $P_b \geq 78.4kPa$. For backpressures lower than the critical backpressure, the entrained mass flow rate remains constant. Hence the staggered multi-ejector should be operated in the critical mode to allow for maximum efficiency.

Table 5-16 : CFD simulation results for $P_{t0} = 80kPa$ and various backpressures for the staggered multi-ejector

P_b [kPa]	$\dot{m}_{entrained}$ [kg/s]	$\dot{m}_{per\_nozzle}$[kg/s]
120	0.42	0.030
116	0.67	0.048
110	0.98	0.070
105	1.11	0.079
100	1.15	0.082
94	1.16	0.083
78.4	1.21	0.086
65.6	1.21	0.086
41.3	1.21	0.086

Figure 5-18 shows that the entrained mass flow rate does not immediately reduce when the backpressure increases above the critical backpressure. However a gradual decrease in entrained mass flow rate occurs follow by a radical decrease in entrained mass flow rate. The staggered multi-ejector result for $P_{t0} = 80kPa$ was determined with a backpressure of $P_b = 65.6kPa$ which resulted in an entrained mass flow rate of $\dot{m}_{CFD-ME} = 1.21kg/s$ as listed in Table 5-14.

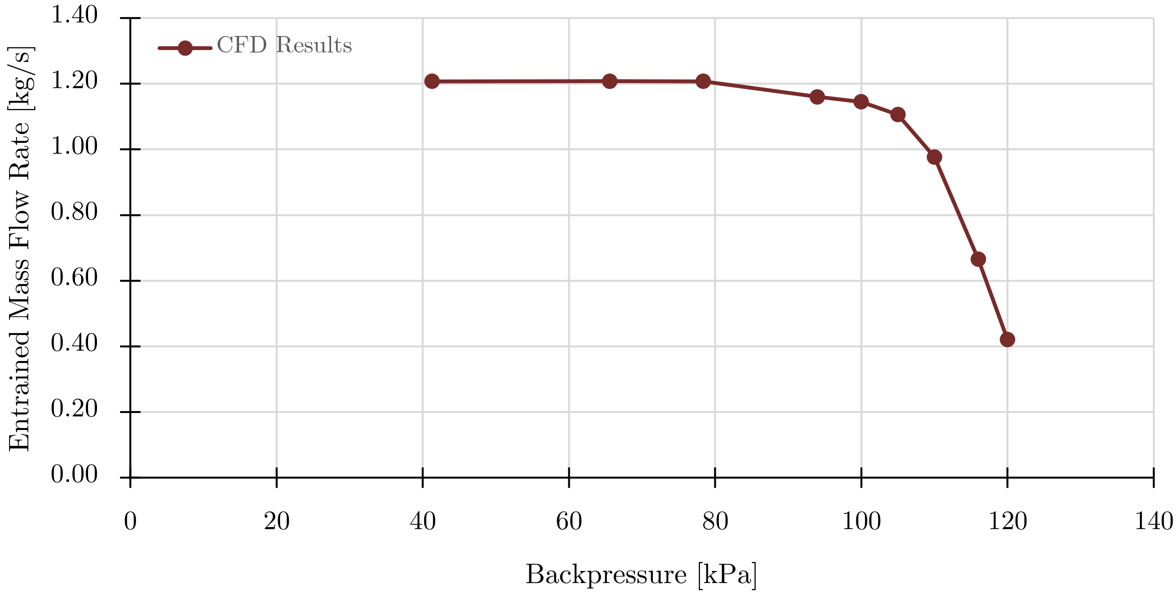

Figure 5-18 : CFD simulation results for $P_{t0} = 80kPa$ and various backpressures for the staggered multi-ejector

A three-dimensional CFD simulation, as described in Section 3.2.2, was performed with the secondary stagnation inlet boundary specified as a wall boundary condition and with ambient conditions at the exit. The CFD simulation was performed to determine the minimum secondary stream total pressure the ejector can pump down to. The result extracted from the CFD simulation show a minimum secondary pressure of $P_{t0} = 41.7kPa$ obtained at an exit ambient pressure of 86.85kPa.

5.2.8 Skewed Inlet Velocity Profile With/Without Inclined Exit

CFD simulations were performed to determine the effects a skewed inlet velocity profile and inclined exit conditions relative to the free stream wind tunnel test section conditions have on the entrained mass flow rate for the staggered multi-ejector. The CFD simulations were performed for a secondary stream total pressure $P_{t0} = 80kPa$, targeting an entrained mass flow rate of $\dot{m}_{CFD-ME} = 1.21kg/s$. Three-dimensional CFD simulations, as described in Section 3.2.2, were performed to determine the entrained mass flow rate for a skewed secondary inlet velocity profile with and without a 30° inclined exit. A 30° inclined exit was chosen since this represents the maximum angle of attack the staggered multi-ejector system will perform at in the Medium Speed Wind Tunnel (MSWT). The entrained mass flow rate results extracted from the CFD simulations are presented in Table 5-17 for each inlet ring, as illustrated in Figure 3-25, and summed up for each case. For the skewed inlet velocity profile case without an inclined exit, the entrained mass flow rate achieved is $\dot{m}_{CFD} = 1.20kg/s$ and for the case with an inclined exit of 30°, the entrained mass flow rate achieved is $\dot{m}_{CFD} = 1.20kg/s$. The entrained mass flow rate achieved for the skewed inlet velocity profiles with and without an inclined exit has virtually met the target entrained mass flow rate of $\dot{m}_{CFD-ME} = 1.21kg/s$ at $P_{t0} = 80kPa$. This shows that a skewed velocity profile at the inlet with and without an inclined exit of 30° does not affect the entrained mass flow rate and hence the performance of the staggered multi-ejector. Therefore the staggered multi-ejector can be used in the MSWT at different angle of attacks without affecting the performance or mass flow rate entrainment.

Table 5-17 : CFD simulation entrained mass flow rate results at $P_{t0} = 80kPa$ for skewed inlet velocity profile with and without 30° inclined exit

	Without inclined exit	**With 30° inclined exit**
	$\dot{m}_{CFD}$ [kg/s]	
Ring 1	0.32	0.32
Ring 2	0.28	0.28
Ring 3	0.24	0.24
Ring 4	0.20	0.20
Ring 5	0.16	0.16
Total	1.20	1.20

The entrained mass flow rate obtained from the CFD simulation for the staggered multi-ejector at secondary stream total pressure $P_{t0} = 80kPa$ and a skewed inlet velocity profile without an inclined exit is illustrated in Figure 5-19. It can be seen that the entrained mass flow rate converges to $\dot{m}_{CFD} = 1.20kg/s$ at a secondary stream total pressure $P_{t0} = 80kPa$. Figure 5-20 illustrates the entrained mass flow rate obtained from the CFD simulation at secondary stream total pressure $P_{t0} = 80kPa$ for the skewed inlet velocity profile with an inclined exit of 30°. It can be seen that the entrained mass flow rate converges to $\dot{m}_{CFD} = 1.20kg/s$ at a secondary stream total pressure $P_{t0} = 80kPa$.

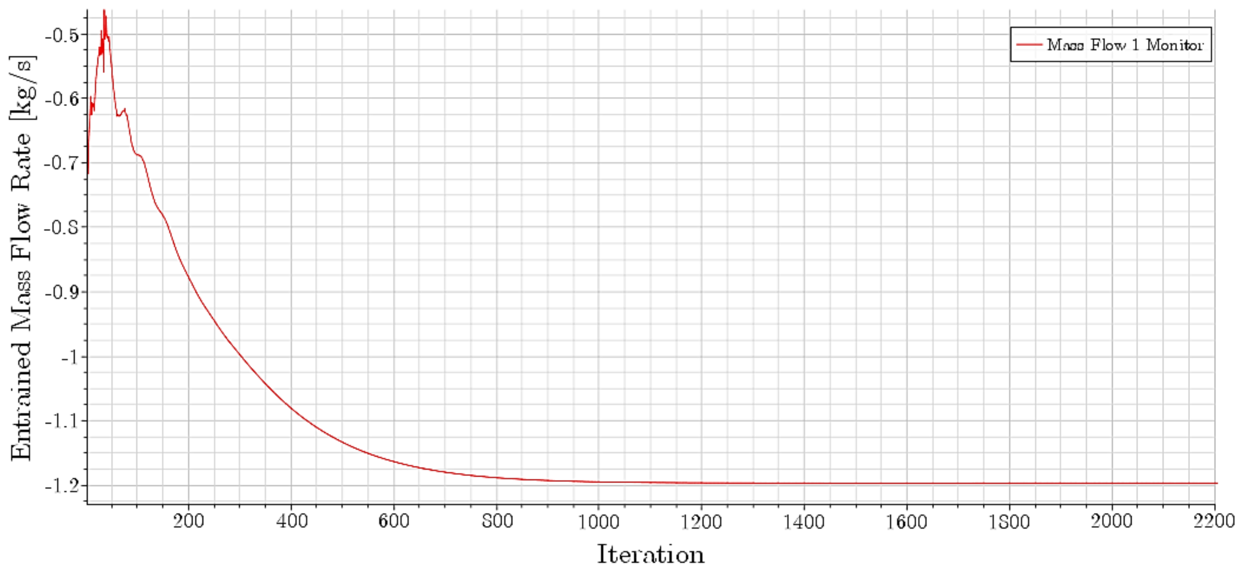

Figure 5-19 : CFD simulation entrained mass flow rate plot at $P_{t0} = 80kPa$ for skewed inlet velocity profile without inclined exit

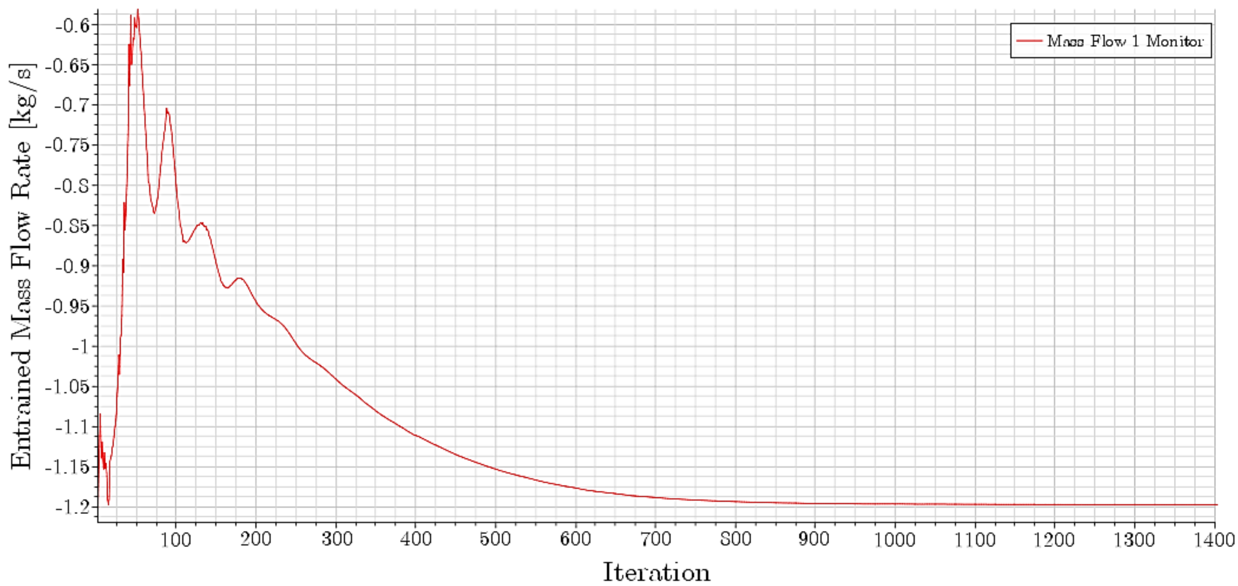

Figure 5-20 : CFD simulation entrained mass flow rate plot at $P_{t0} = 80kPa$ for skewed inlet velocity profile with an inclined exit of 30°

5.2.9 Primary Nozzle – MLN and Rao TOP

Two nozzle designs were investigated, the minimum length nozzle as described in Section 2.4.1.1 and Rao thrust optimised parabolic nozzle as described in Section 2.4.1.2. The nozzles were designed for $A_e/A_{th} = 3.348$ where the primary nozzle exit radius is $r_e = 2.818mm$ and primary nozzle throat radius is $r_{th} = 1.54mm$ which was determined from ESDU for the ejector designed in Section 5.2.4. Figure 5-21 illustrates the MLN design determined using the Matlab code as shown in APPENDIX A.1 and Figure 5-22 illustrates the Rao TOP nozzle design determined using the Matlab code in

APPENDIX A.2. The Matlab code used to develop the MLN contour produces only the divergent section profile as shown in Figure 5-21. The Rao TOP nozzle contour developed using the Matlab code produces the entire nozzle profile including the convergent section and nozzle throat section as shown in Figure 5-22. It can be seen that the designed Rao TOP nozzle exhibits a shorter nozzle length compared to the MLN resulting in a lower weight primary nozzle being manufactured. Two-dimensional CFD simulations were performed at $P_{t0} = 30kPa$ to determine the entrained mass flow rate employing a MLN design and a Rao TOP nozzle design. The entrained mass flow rate obtained using the ejector designed from Section 5.2.4 with the MLN profile yielded $\dot{m}_{entrained} = 0.024kg/s$ per nozzle and the Rao TOP profile yielded $\dot{m}_{entrained} = 0.029kg/s$ per nozzle. This shows that a Rao TOP nozzle design entrains more mass flow than a MLN design. Since the Rao TOP nozzle exhibits a shorter nozzle length and entrains more mass flow than the MLN design, it was considered feasible to be employed as the design for the primary nozzle.

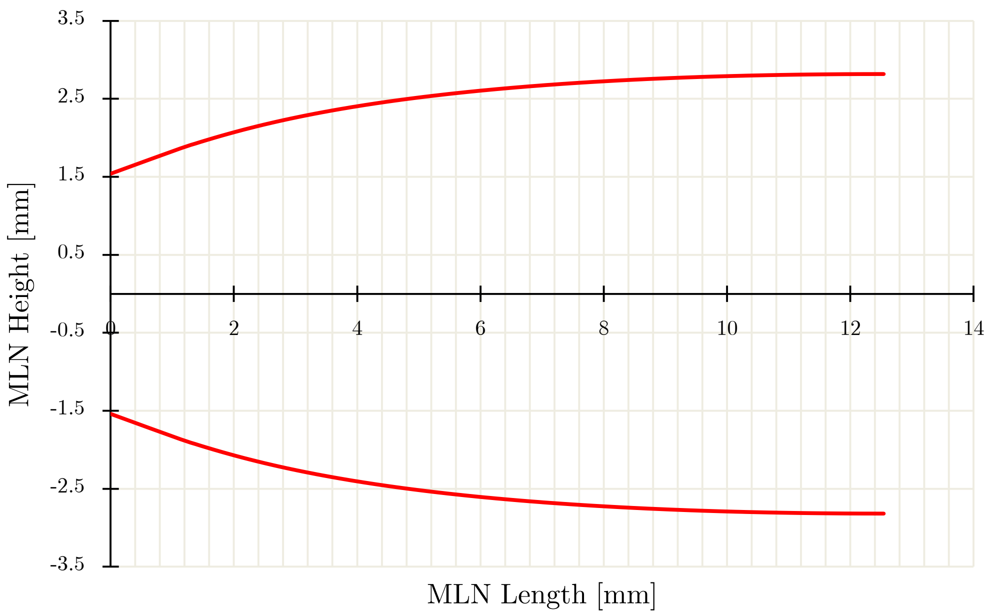

Figure 5-21 : Minimum length nozzle designed for $A_e/A_{th} = 3.348$

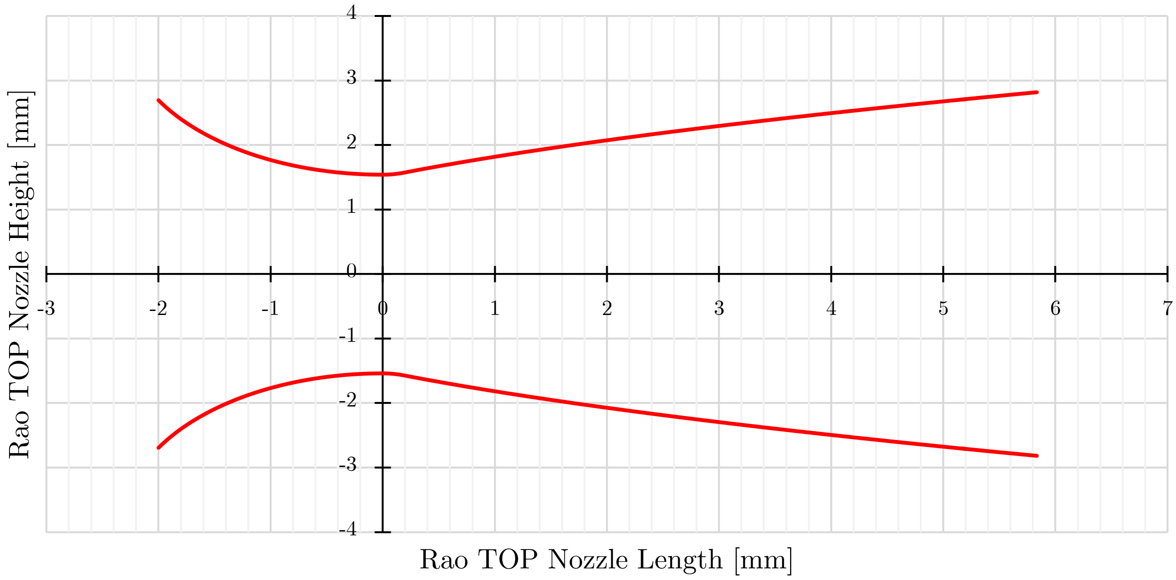

Figure 5-22 : Rao TOP nozzle designed for $r_e = 2.818mm$ and $r_{th} = 1.54mm$

5.3 Experimental Ejector Test

An experimental test was required to determine the entrained mass flow rate of a single ejector from the designed staggered multi-ejector and to determine the accuracy of the CFD model. The experimental tests were conducted at ambient conditions in the Hot Gas Test Facility at the Council for Scientific and Industrial Research (CSIR). The designed and manufactured test rig allows for a single operating secondary pressure of the ejector to be tested which corresponds to atmospheric pressure in Pretoria; approximately 86kPa. The results from the experimental test are compared to the CFD results from the staggered multi-ejector at $P_{t0} = 80kPa$. It should be noted that the CFD simulation result at $P_{t0} = 80kPa$ was determined with a backpressure of $P_b = 65.6kPa$ which resulted in an entrained mass flow rate of $\dot{m}_{CFD-ME} = 1.21kg/s$ as listed in Table 5-14.

5.3.1 Calibration of Conical Inlet Standard and Orifice Meter Run Standard

A calibration procedure, as mentioned in Section 4.3.3, was performed to determine if the conical inlet ISO 5801:2007(E) standard and the orifice meter run ASME MFC-14M-2001 standard resulted in equivalent calculated mass flow rate. Figure 5-23 illustrates the results obtained from the calibration procedure for the conical inlet and the orifice meter run. It can be seen from Figure 5-23 that the conical inlet mass flow rate results are marginally higher than the orifice meter run results. Although the comparison falls within the uncertainty of the two devices, more consistent results may be achieved by referring the measurements to a single standard, effectively removing the bias from the other standard. Note that two mass flow rate measurements were required to deduce the unknown primary mass flow rate. A linear trendline was fitted to the results to determine a correction factor, *i.e.* 1.01 from Figure 5-23, which will be applied to the experimental test results of the orifice meter run. Thus all of the results were referred to a single mass flow rate standard, which was the conical inlet.

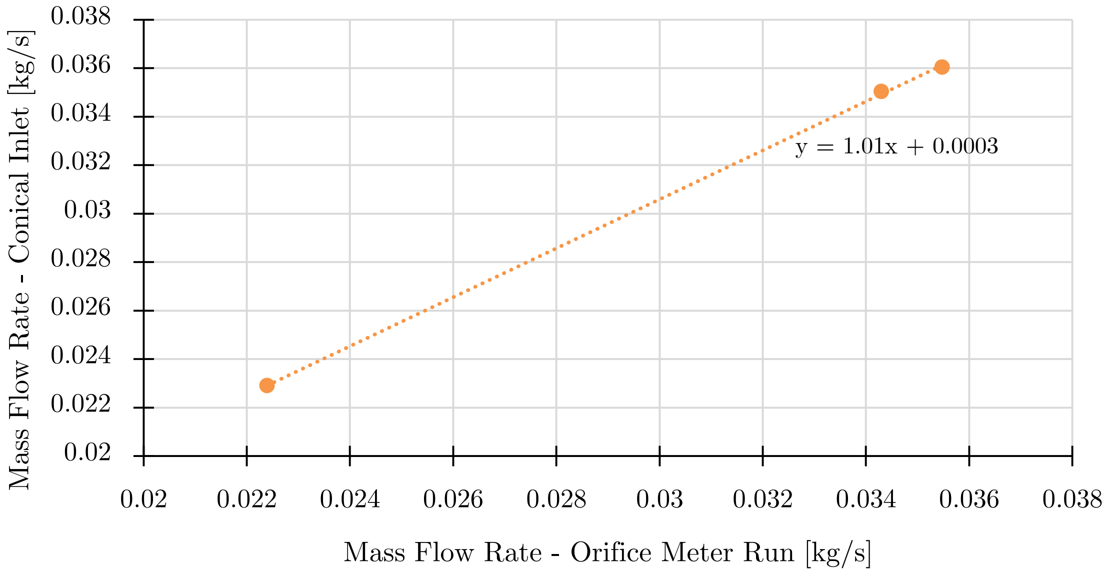

Figure 5-23 : Calibration results of conical inlet standard and orifice meter run standard

5.3.2 Experimental Tests

Three experimental tests were conducted on the designed and manufactured test rig as mentioned in Section 4.3.4. The first test was required to determine the entrained mass flow rate at a primary pressure of 25bar and constant backpressure, the second test was required to determine the minimum pressure the ejector can pump down to and the third test was required to determine the entrained mass flow rates at a primary pressure of 25bar and various backpressures.

5.3.2.1 Entrained Mass Flow Rate at Constant Backpressure

The first test required the determination of the entrained mass flow rate of the ejector at a constant backpressure. This backpressure corresponds to the upstream pressure in the meter run. The results from the experimental test are listed in Table 5-18. An atmospheric pressure of $P_{atm} = 86.96kPa$ and an atmospheric temperature of $T_{atm} = 26.1°\text{C}$ was recorded in the test facility before the experiment was performed. A pressure drop across the orifice, $\Delta P = 28.21kPa$, resulted in a mass flow rate of $\dot{m}_{orifice} = 0.097kg/s$, however this mass flow rate was corrected using the correction factor from Section 5.3.1. Hence a mass flow rate of $\dot{m}_{corrected} = 0.098kg/s$ exits the meter run. An entrained mass flow rate of $\dot{m}_{conical} = 0.064kg/s$ through the conical inlet was determined from the experimental test. The calibration of the conical inlet ISO 5801:2007(E) standard and the orifice meter run ASME MFC-14M-2001 standard allows for the determination of the primary mass flow rate. The total exit mass flow rate determined by the orifice meter run ASME MFC-14M-2001 standard is the sum of the entrained mass flow rate determined by the conical inlet ISO 5801:2007(E) standard and the primary mass flow rate. Hence the primary mass flow rate is calculated by subtracting the entrained conical inlet mass flow rate from the total exit mass flow rate. This results in a primary mass flow rate of $\dot{m}_p = 0.034 kg/s$ through the primary nozzle.

Table 5-18 : Experimental results for constant backpressure

P_{atm} [kPa]	86.96
T_{atm} [°C]	26.1
P_1 [kPa]	75.18
P_2 [kPa]	103.39
P_3 [kPa]	86.37
T_{exit} [°C]	16.9
$\ddot{m}_{conical}$ [kg/s]	0.064
$\ddot{m}_{orifice}$ [kg/s]	0.097
$\ddot{m}_{corrected}$ [kg/s]	0.098
$\dot{m}_p$ [kg/s]	0.034

The primary nozzle of the staggered multi-ejector was designed for a primary pressure of 25bar and a primary mass flow rate of $\dot{m}_p = 0.0396 kg/s$, however from the experimental test a primary mass flow rate of $\dot{m}_p = 0.034 kg/s$ was determined. This may be due to the nozzle profile being altered during the manufacturing process. The backpressure for the experimental test corresponds to the upstream pressure of the meter run, P2. From the CFD simulation results listed in Table 5-16, the ejector is operating in the sub-critical mode during the experiment. It should be noted that for the experimental test conditions, an entrained mass flow rate of approximately $\ddot{m}_{per\_nozzle} = 0.079 kg/s$ should be expected. However, a 19% deviation in the experimental result was obtained for the ejector in the sub-critical mode. This indicates that the CFD model over-predicted the entrained mass flow rate of the staggered multi-ejector at this test condition.

An experimental and numerical investigation on the global performance and internal flow of a supersonic air ejector was conducted by Chong et al. [44]. The ejector was designed for a primary pressure of 1MPa and a secondary pressure of 0.2MPa, and modelled using FLUENT CFD software package with a RNG k-epsilon model. The entrainment ratio results from the experiment and CFD simulations are shown in Figure 5-24 [44]. Chong et al. [44] concluded that the results from the experiment and the CFD simulation agreed well on the trend and the value of critical backpressure as shown in Figure 5-24(a). However, the CFD numerical model over-predicted the entrainment ratio. Figure 5-24(b) shows the deviations are less than 15% when the ejector operates in critical mode and less than 30% in sub-critical mode.

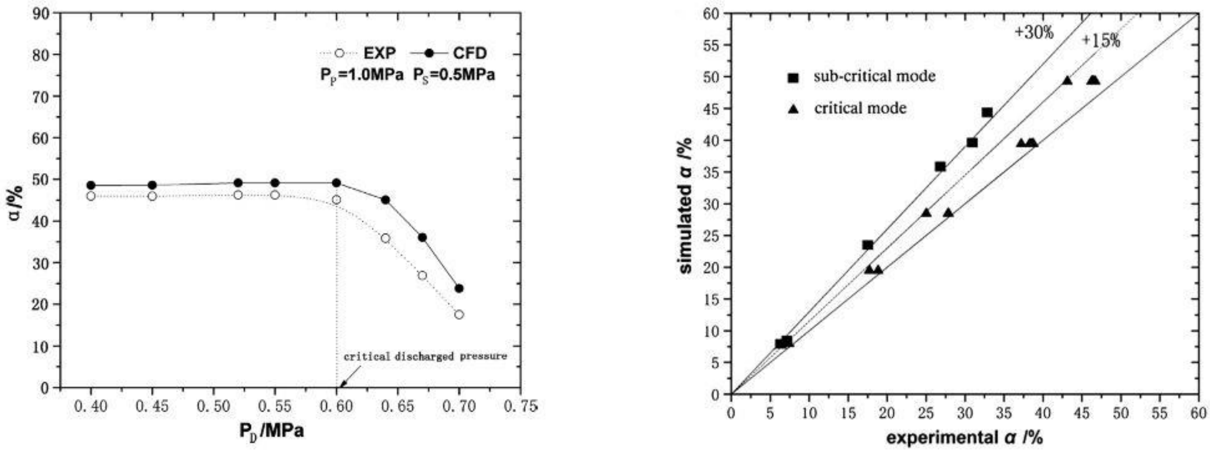

(a) Variation of entrainment ratio with discharge pressure (b) Deviation of entrainment ratios

Figure 5-24 : Experimental and numerical results [44]

The over-prediction of the entrained mass flow rate in the sub-critical region is consistent with Chong et al. [44] although there were significant differences in the operating conditions which may be contributing to the different deviations between simulation and experiment. This shows that the 19% deviation in the experimental results obtained for the ejector in the sub-critical mode follows the same trend observed by Chong et al. [44].

5.3.2.2 Minimum Secondary Pressure

The second test required the determination of the minimum secondary pressure the manufactured ejector can pump down to. A minimum secondary pressure of $P_{t0} = 51.38kPa$ was obtained from the experimental test. The backpressure determined from the experimental test corresponds to the upstream pressure in the meter run $P_2 = 86.49kPa$. The result extracted from the CFD simulation show a minimum secondary pressure of $P_{t0} = 41.70kPa$ was obtained at a backpressure of 86.85kPa. A 19% deviation was found between the experimental and CFD simulation results for the minimum secondary pressure. From the CFD simulation results in Table 5-14, the minimum secondary entry total pressure the ejector can pump down to is $P_{t0} = 30kPa$ at an exit pressure of 32.80kPa. The experimental test rig does not allow the exit pressure to be reduced to below ambient conditions, therefore the minimum secondary pressure the actual ejector can pump down to cannot be determined.

5.3.2.3 Entrained Mass Flow Rates at Various Backpressures

The third test required the determination of the entrained mass flow rates of the ejector at various backpressure. The backpressure corresponds to the upstream pressure in the meter run. For the third test, the downstream section of the meter run and the orifice plate were removed from the experimental test rig. The main purpose of the orifice plate was to deduce the primary mass flow rate. By removing the orifice plate the data range of the experiment expanded to lower backpressures. The entrained mass flow rate results from the experimental test are illustrated graphically in Figure 5-25 with respect to the CFD simulation results from Table 5-16. An atmospheric pressure of $P_{atm} = 86.96kPa$ and an atmospheric temperature of $T_{atm} = 26.2°\text{C}$ was recorded in the test facility before the experiment was performed. The entrained mass flow rate result at constant backpressure $P_2 = 103.39kPa$ (*i.e.* first experimental test) is illustrated graphically in Figure 5-25 by the yellow point, which shows that the result obtained from the first experimental test relates to the results from the third experimental test. Figure 5-25 shows that as the backpressure decreases, an increase in entrained mass flow rate through the ejector is achieved. The experimental results indicate that the ejector is operating in sub-critical mode. A maximum entrained mass flow rate of $\dot{m}_{entrained} = 0.091kg/s$ is obtained at a backpressure of $P_2 = 87.31kPa$. However, this entrained mass flow rate is not the maximum mass flow rate the ejector can entrain, since the ejector is operating in sub-critical mode. For the ejector to operate in critical mode, the backpressure should decrease below $P_2 = 87.31kPa$ to determine the maximum entrained mass flow rate, however the experimental test rig does not allow the backpressure to be reduced to below ambient conditions. It can be seen from Figure 5-25 that the maximum entrained mass flow rate determine from the experiment is greater than the maximum entrained mass flow rate predicted by CFD. The maximum entrained mass flow rate predicted by CFD for the ejector in critical mode is $\dot{m}_{CFD} = 0.086kg/s$, whereas the experimental entrained mass flow rate in sub-critical mode is $\dot{m}_{exp} = 0.091kg/s$. From the experimental results, the ejector is predicted to entrain a higher maximum mass flow rate than that predicted from the CFD simulations for backpressures lower than $P_2 = 87.31kPa$. The ejector is required to operate in critical mode to allow for maximum entrainment. If the ejector operates in critical mode, the entrained mass flow rate will be higher than the required mass flow rate, which will result in an increase in ejector performance. Figure 5-25 indicates that the CFD model over-predicts the entrained mass flow rates of the ejector in the sub-critical mode and will envisage it to under-predict the entrained mass flow rates in the critical mode.

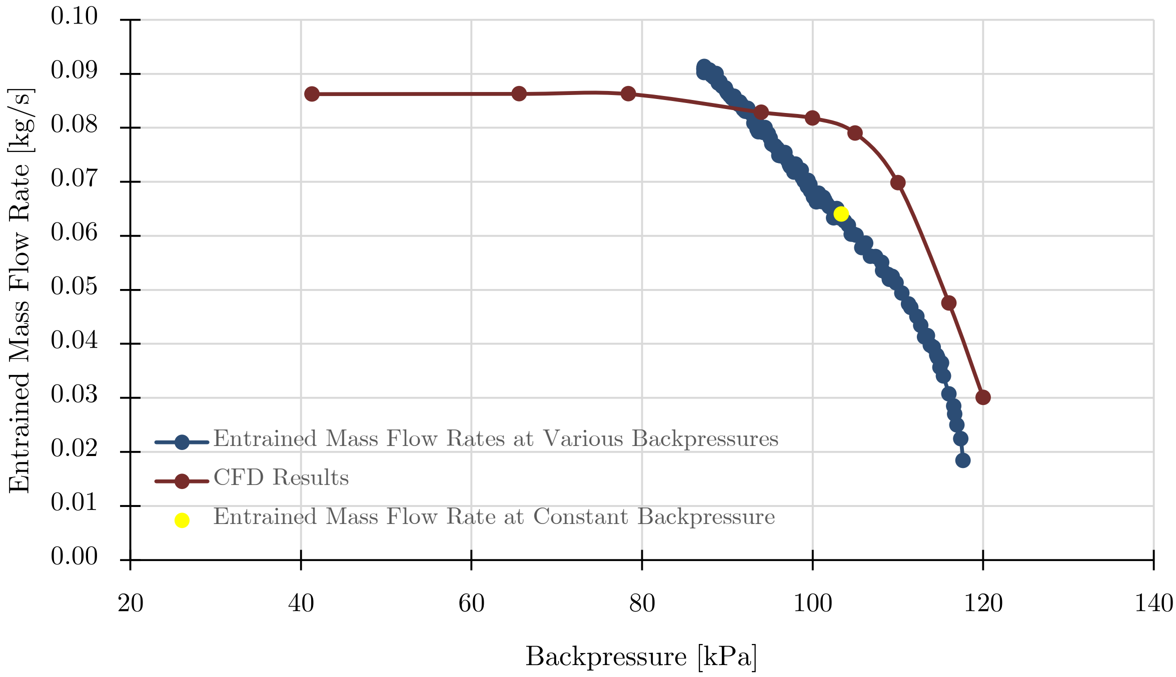

Figure 5-25 : Experimental and CFD simulation entrained mass flow rates at various backpressures

6. CONCLUSIONS

An induced mass flow system was designed featuring ejector driven mass flow generation and flow regulation and metering. The flow regulation and metering system employs a translating conical mass flow plug which is operated in a choked mode to provide an accurate measurement of airflow through an inlet. The results from the flow regulation and metering system analysis showed that a linear conical mass flow plug displacement of 30mm towards the geometric throat, yielded in the maximum mass flow rate attainable for each wind tunnel stagnation pressure. The linear conical mass flow plug is capable of translating approximately 100mm which allows for a variation of mass flow rates to be obtained for specific wind tunnel stagnation pressures.

The mass flow generation system employs 14 individual ejectors arranged in a staggered formation around an annulus. The ejector design tool, ESDU 92042 software was verified using CFD simulations. The results from the CFD simulations showed that the ESDU 92042 software provided reliable ejector designs when higher primary pressures were utilised and for ejectors designed at mass flow ratios equal to two, the entrained mass flow rate was greater than that determined by the ESDU 92042 software. The performance prediction calculation in the ESDU 92042 software was unable to provide a correlation to the quick design procedure results. The entrained mass flow rate predicted by the CFD model for the staggered multi-ejector exceeds the target entrained mass flow rate determined by the ESDU 92042 software and it exceeds the mass flow rate target from the flow regulation and metering system. CFD simulations of the 14-ejector unit were conducted featuring a skewed velocity profile at the entrance to the ejector duct with and without an inclined exit angle of 30° to the bulk flow. The entrained mass flow rate was not affected by the distortion at the mixing duct entrance, by the inclined jet exit angle, or the combination of these effects. Therefore the staggered multi-ejector can be used in the Medium Speed Wind Tunnel at different angles of attack without affecting the entrained mass flow rate.

The experimentally determined entrained mass flow rate was higher than the predicted CFD entrained mass flow rate at low backpressures but was lower than the predicted CFD entrained mass flow rate at high backpressures. The CFD model under-estimated the entrained mass flow rate at the critical point. The CFD simulations predicted that, with reducing back pressure, the critical mode would be reached when the entrained mass flow rate would peak and remain constant. In the experiment, the entrained mass flow rate continued to increase up to the minimum backpressure achievable, and was greater than the CFD predicted maximum entrained mass flow rate. The experimental results for the single ejector suggest that the designed operating envelope predicted for the staggered multi-ejector should be reached.

7. RECOMMENDATIONS

- The primary nozzle exit position should be explored computationally and experimental to determine the effect the primary nozzle exit position has on the ejector performance.
- The experimental test rig allows for only one secondary pressure to be experimentally tested *i.e.* ambient conditions. A technique for regulating the secondary pressure during the experiment should be explored to allow for more secondary pressures to be experimentally tested.
- For the manufactured ejector to operate in critical mode, the backpressure should decrease below ambient conditions to determine the maximum entrained mass flow rate. Since the experimental test rig does not allow the backpressure to be reduced to below ambient conditions, a modification to the test rig should be explored in order for the maximum mass flow rate to be determined. This will also allow for the critical backpressure to be determined.

REFERENCES

1. P.J. Skinner, "*KT 471006, P150001/P04A Chevron 1.4, Task T04a, Wind Tunnel Test Training. Milestone M01, Inlet System Concept Study FY 2008/2009*". February 2009.
2. STARCS Experimental Aerodynamics, "*Air Inlet Testing Capability in the Transonic Wind Tunnel T1500*", Sweden, December 2008.
3. C.H. Boccadoro, B.G. Franco, "*An Ejector Augmented Choking Valve for the Metering and Control of Inlet and Bleed Duct Flows*", AIAA 12th Aerodynamic Testing Conference, March 22-24, 1982.
4. Calspan Jet Engine Air Intake Testing, *URL: http://www.calspan.com/services/subsonic-transonic-wind-tunnel/military-aircraft-weapons/forebody-inlet-optimization/*, Last Accessed on the 24th of January 2017.
5. F.J. Capone, L.S. Bangert, S.C. Asbury, C.T.L. Mills, and E.A. Bare, "*The NASA Langley 16-Foot Transonic Tunnel*", NASA Technical Paper 3521, Langley Research Center, Hampton, Virginia, September 1995.
6. M. Davis, W. Baker, G. Power, D. Beale, "*A Proposal for Integration of Wind Tunnel and Engine Test Softwares for the Evaluation of Airframe-Propulsion Compatibility Using Numerical Simulations*", ASME Journal of Engineering for Gas Turbines and Power, Vol. 124, pp. 447-458, July 2002.
7. K. Zhang, S. Shen, Y. Yang, "*Numerical investigation on performance of the adjustable ejector*", International Journal of Low-Carbon Technologies, February 2010.
8. S. Daneshmand, C. Aghanajafi, A. Bahrami, *"Analytical and Experimental Methods of Design for Supersonic Two-Stage ejectors"*, World Academy of Science, Engineering and Technology, Vol: 26 0000-00-00, 2009.
9. Fox Valve, *URL: http://www.foxvalve.com/l2_ air_ ejectors_fuelcells.aspx*, Last Accessed on the 25th of January 2017.
10. ESDU, *"Ejectors and jet pumps: Computer software for design and performance for compressible gas flow"*, ESDU 92042, June 2011.
11. CRYSTAL TCS PVT. LTD., Multi Jet Ejectors, *URL: http://www.crystaltcs.com/multi-jet-ejectors.php*, Last Accessed on the 25th of January 2017.
12. D. Wang, *"Analysis and design of air-jet pumps for pneumatic transportation of bulk solids in pipelines"*, University of Wollongong, 1995.
13. W.A. Aissa, *"Effect of Multiple Nozzles on Air Ejector Performance"*, High Institute of Energy, Aswan, Mech. Power Department, ISABE-2005-1291, 2005.

14. R.S. Castner, *"The Nozzle Acoustic Test Rig; An Acoustic and Aerodynamic Free-Jet Facility"*, NASA Technical Memorandum 106495, June 1994.
15. R.K. McGovern, K.V. Bulusu, M.A. Antar, J.H. Lienhard V, *"One-dimensional Model of an Optimal Ejector and Parametric Study of Ejector Efficiency"*.
16. Society of Automotive Engineers, *"Gas Turbine Engine Inlet Flow Distortion Guidelines*", ARP 1420, March 1978.
17. D.P. Turner, *"Analysis of Taxi Test Data for an Unmanned Aerial Vehicle Implemented with Fluidic Flow Control"*, North Carolina State University, 2006.
18. J.H. Keenan, E.P. Neumann, F. Lustwerk, *"An Investigation of Ejector Design by Analysis and Experiment"*, ASME Journal of Applied Mechanics, Vol 72, pp. 299-309, September 1950.
19. S. Hooseria, *"Research and Development of Unconventional Air Breathing Propulsion Systems"*, CSIR, February 2017.
20. G.V.R. Rao, "*Exhaust nozzle contour for optimum thrust*" Jet Propulsion, Vol. 28, pp. 377-382, 1958.
21. J. Anderson, "*Modern Compressible Flow with Historical Perspective*", 3rd ed. New York: McGraw-Hill, 2003, pp. 397-401.
22. G.V.R. Rao, *"Approximation of optimum thrust nozzle contour"*, ARS Journal, Vol. 30, pp. 561, 1960.
23. W.B.A. van Meerbeeck, B.T.C. Zandbergen, L.J. Souverein, *"A Procedure for Altitude Optimization of Parabolic Nozzle Contours Considering Thrust, Weight and Size",* 5th European Conference for Aeronautics and Space Sciences (EUCASS), DOI: 10.13140/RG.2.1.1118.0006, Munchen, Germany, 2012.
24. C. Liao, *"Gas Ejector Modeling for Design and Analysis"*, Ph.D. Texas A&M University, December 2008.
25. Council for Scientific and Industrial Research, *URL: http://defsec.csir.co.za/aeronautical-systems-as/wind-tunnel-testing*, Last Accessed on the 31st of January 2017.
26. H.I.H. Saravanamuttoo, G.F.C. Rogers, H. Cohen, P.V. Straznicky, *"Gas Turbine Theory"*, Sixth Edition, Pearson, Prentice Hall, p. 107.
27. B.W. Skews, *"Course Notes – MECN4021 and MECN4024 Compressible Flow"*, University of the Witwatersrand, Johannesburg, School of Mechanical Engineering, 2013.
28. Wolfram Math World, *URL: http://mathworld.wolfram.com/ConicalFrustum.html*, Last Accessed on the 2nd of February 2017.
29. S.E. Tournier, J.D. Paduano, D. Pagan, *"Flow Analysis and Control in a Transonic Inlet"*, Technical Report, American Institute of Aeronautics and Astronautics, 2005.

30. E.J. Saltzman, *"In-Flight Gains Realized by Modifying a Twin Side-Inlet Induction System"*, NACA Research Memorandum, RM-H57J09, December 1957.
31. T.S. Zhao, Q.C. Bi, *"Pressure drop characteristics of gas-liquid two-phase flow in vertical miniature triangular channels"*, International Journal of Heat and Mass Transfer, pp. 2523-2534, 2001.
32. F.M. White, *"Fluid Mechanics"*, Fifth Edition, McGraw-Hill, pp. 19-28.
33. LMNO Engineering Research and Software, Gas Viscosity Calculator, *URL: http://www.lmnoeng.com/Flow/GasViscosity.php*, Last Accessed on the 7th of February 2017.
34. ESDU, *"Flow through a sudden enlargement of area in a duct"*, ESDU 72011, March 2007.
35. ESDU, *"Pressure losses caused by obstructions in ducts and pipes"*, ESDU 81021, March 2007.
36. J.R. Henry, C.C. Wood, S.W. Wilbur, *"Summary of Subsonic-Diffuser Data"*, Research Memorandum NACA RM L56F05, NACA, October 1956.
37. C. Beckey, R. Hartfield, M. Carpenter, *"Compressor Modeling for Engine Control and Maintenance"*, Air Force Flight Test Centre, Edwards Air Force Base, California, July 2011.
38. International Organization for Standardization, *"Natural Gas-Standard Reference Conditions"*, ISO 13443, Switzerland, 1996.
39. N.Krishnamoorthy, Exploring STAR-CCM+ Capabilities, Enhancements and Practices for Aerospace Combustion, STAR GLOBAL CONFERENCE, San Diego, 2015, *URL : https://mdx2.plm.automation.siemens.com/sites/default/files/Presentation/SGC2015_ CD-adapco_ Krishnamoorthy.pdf*, Last Accessed 29th of September 2017.
40. C. Dodson, MathWorks, Minimum Length Nozzle Design Tool, Version 1.2, *URL: https://www.mathworks.com/matlabcentral/fileexchange/39499-minimum-length-nozzle-design-tool?requestedDomain=www.mathworks.com*, Last Accessed 29th of September 2017.
41. CD-Adapco, STAR-CCM+9.06 User's Guide.
42. International Standard, *"Industrial fans – Performance testing using standardized airways"*, ISO 5801:2007(E), December 2007.
43. Excel Calculations, Small-Bore Gas Orifice Meter Flow Calculator, *URL: http://excelcalculations.blogspot.co.za/2011/10/small-bore-gas-orifice-meter-flow.html*, Last Accessed on the 6th of September 2017.
44. D. Chong, M. Hu, W. Chen, J. Wang, J. Liu, J. Yan, *"Experimental and Numerical Analysis of Supersonic Air Ejector"*, Elsevier Journal, Applied Energy, China, 2014.

APPENDIX A

A.1 Minimum Length Nozzle Matlab Code [40]

```
function MinLengthNozzle(G,Me,n)

%{
    Defines geometry for a minimum length nozzle based on a design exit
    mach number for a certain gas, given a finite number (n) of mach waves.
    Based on the information described in Anderson, Modern Compressible
    Flow 3rd Edition (Library of Congress CN: 2002067852).

Input parameters
    G is gamma, the ratio of specific heats (Cp/Cv)
    Me is the design exit mach number
    n is the finite number of expansion waves used in approximation

%}

%% Initialize datapoint matrices
Km = zeros(n,n);     % K- vlaues (Constant along right running characteristic
lines)
Kp = zeros(n,n);     % K- vlaues (Constant along left running characteristic
lines)
Theta = zeros(n,n); % Flow angles relative to the horizontal
Mu = zeros(n,n);     % Mach angles
M = zeros(n,n);      % Mach Numbers
x = zeros(n,n);      % x-coordinates
y = zeros(n,n);      % y-coordinates

%% Find NuMax (maximum angle of expansion corner)
[~, B, ~] = PMF(G,Me,0,0);
NuMax = B/2;

%% Define flow of first C+ line
y0 = 1;
x0 = 0;

dT = NuMax/n;
Theta(:,1) = (dT:dT:NuMax);

Nu = Theta;
Km = Theta + Nu;
Kp = Theta - Nu;
[M(:,1) Nu(:,1) Mu(:,1)] = PMF(G,0,Nu(:,1),0);

%% Fill in missing datapoint info along first C+ line
y(1,1) = 0;
x(1,1) = x0 - y0/tand(Theta(1,1)-Mu(1,1));
for i=2:n;

    s1 = tand(Theta(i,1)-Mu(i,1));
    s2 = tand((Theta(i-1,1)+Mu(i-1,1)+Theta(i,1)+Mu(i,1))/2);
    x(i,1) = ((y(i-1,1)-x(i-1,1)*s2)-(y0-x0*s1))/(s1-s2);
    y(i,1) = y(i-1) + (x(i,1)-x(i-1,1))*s2;
```

```
end

%% Find flow properties in characteristic web
for j=2:n;
    for i=1:1+n-j;

        Km(i,j) = Km(i+1,j-1);

        if i==1;

            Theta(i,j) = 0;
            Kp(i,j) = -Km(i,j);
            Nu(i,j) = Km(i,j);
            [M(i,j) Nu(i,j) Mu(i,j)] = PMF(G,0,Nu(i,j),0);
            s1 = tand((Theta(i+1,j-1)-Mu(i+1,j-1)+Theta(i,j)-Mu(i,j))/2);
            x(i,j) = x(i+1,j-1) - y(i+1,j-1)/s1;
            y(i,j) = 0;

        else

            Kp(i,j) = Kp(i-1,j);
            Theta(i,j) = (Km(i,j)+Kp(i,j))/2;
            Nu(i,j) = (Km(i,j)-Kp(i,j))/2;
            [M(i,j) Nu(i,j) Mu(i,j)] = PMF(G,0,Nu(i,j),0);
            s1 = tand((Theta(i+1,j-1)-Mu(i+1,j-1)+Theta(i,j)-Mu(i,j))/2);
            s2 = tand((Theta(i-1,j)+Mu(i-1,j)+Theta(i,j)+Mu(i,j))/2);
            x(i,j) = ((y(i-1,j)-x(i-1,j)*s2)-(y(i+1,j-1)-x(i+1,j-1)*s1))/(s1-
s2);
            y(i,j) = y(i-1,j) + (x(i,j)-x(i-1,j))*s2;

        end

    end
end

%% Find wall datapoint info
xwall = zeros(1,n+1);
ywall = zeros(1,n+1);

xwall(1,1) = x0;
ywall(1,1) = y0;

walls = tand(NuMax);
webs = tand(Theta(n,1)+Mu(n,1));

xwall(1,2) = ((y(n,1)-x(n,1)*webs)-(ywall(1,1)-xwall(1,1)*walls))/(walls-
webs);
ywall(1,2) = ywall(1,1)+(xwall(1,2)-xwall(1,1))*walls;

for j=3:n+1;

    walls = tand((Theta(n-j+3,j-2)+Theta(n-j+2,j-1))/2);
    webs = tand(Theta(n-j+2,j-1)+Mu(n-j+2,j-1));
    xwall(1,j) = ((y(n-j+2,j-1)-x(n-j+2,j-1)*webs)-(ywall(1,j-1)-xwall(1,j-
1)*walls))/(walls-webs);
    ywall(1,j) = ywall(1,j-1) + (xwall(1,j)-xwall(1,j-1))*walls;

end

%% Provide wall geometry to user and plot
```

```
assignin('base','xwall',xwall)
assignin('base','ywall',ywall)

grid=1;
if grid == 1

    plot(xwall,ywall,'-')
    axis equal
    axis([0 ceil(xwall(1,length(xwall))) 0 ceil(ywall(1,length(ywall)))])
    hold on

    for i=1:n
        plot([0 x(i,1)],[1 y(i,1)])
        plot([x(n+1-i,i) xwall(1,i+1)],[y(n+1-i,i) ywall(1,i+1)])
    end

    for i=1:n-1
        plot(x(1:n+1-i,i),y(1:n+1-i,i))
    end

    for c=1:n
        for r=2:n+1-c
            plot([x(c,r) x(c+1,r-1)],[y(c,r) y(c+1,r-1)])
        end
    end

xlabel('Length [x/y0]')
ylabel('Height [y/y0]')

end

end
```

A.2 Rao TOP Nozzle Matlab Code [19]

```
clc; clear all; close all; format long;

% Selected Throat Diameter
Dt = 28.56;
Rt = Dt/2;

% Selected Exit Diameter
De = 58.77;
Re = De/2;

%-----COMPUTES ENTRANCE CURVE ANGLES: THETA_E & THETA_N FROM RESPONSE
SURFACES-----%
EXP_Rat = (Re/Rt)^2;
K = 1;
Lf = K*100;

%  Length Parameter
Ln = K*(sqrt(EXP_Rat)-1)*Rt/tand(15);

%Theta_e Response Surface
Theta_e  = 82.63455429...                              %Constant
-(1.438585863*EXP_Rat)...                              %A
```

```
-(1.705517217*Lf)...                              %B
+(0.005706602*EXP_Rat*Lf)...                      %A*B
+(0.050171718*EXP_Rat^2)...                       %A^2
+(0.01567885*Lf^2)...                             %B^2
-(7.02175E-05*(EXP_Rat^2)*Lf)...                  %A^2*B
-(0.000929959*EXP_Rat^3)...                       %A^3
-(5.70618E-05*Lf^3)...                            %B^3
+(7.14837E-06*EXP_Rat^4);                         %A^4

%Theta_n Response Surface
Theta_n  = 93.4106155515...                       %Constant
+(0.7636870374*EXP_Rat)...                        %A
-(2.0094058273*Lf)...                             %B
+(0.0016662045*EXP_Rat*Lf)...                     %A*B
-(0.0221445827*EXP_Rat^2)...                      %A^2
+(0.0181722597*Lf^2)...                           %B^2
+(0.0000106195*(EXP_Rat^2)*Lf)...                 %A^2*B
-(0.0000108031*EXP_Rat*(Lf^2))...                 %A*B^2
+(0.0002578244*EXP_Rat^3)...                      %A^3
-(0.0000581932*Lf^3)...                           %B^3
-(0.0000011586*EXP_Rat^4);                        %A^4

%-----COMPUTES ENTRANCE CURVE 1-----%
res1 = 0.005;
coeff1 = 1.5;
Theta1 = 45;
E_xmin1 = -1*round(coeff1*Rt*sind(Theta1));
Ex1 = (E_xmin1:res1:-res1)';
Ey1 = -sqrt((coeff1*Rt)^2-Ex1.^2)+(1+coeff1)*Rt;

%-----COMPUTES ENTRANCE CURVE 2 UP TO POINT N-----%
res2 = 0.005;
ceoff2 = 0.382;
E_xmax2 = (ceoff2*Rt*sind(Theta_n));
Ex2 = (0:res2:E_xmax2)';
Ex2(end) = E_xmax2;
Ey2 = -sqrt((ceoff2*Rt)^2-Ex2.^2)+(1+ceoff2)*Rt;

%-----COMPUTES THRUST OPTIMISED PARABOLA (RAO TOP) FROM POINT N TO POINT E---
--%
% PARABOLIC FORMULA: x = ay^2 + by + c
xN = Ex2(end);
yN = Ey2(end);
yE = Re;

%Solve for coeffiecient a
a = (cotd(Theta_e) - cotd(Theta_n))/(2*(yE-yN));
aa = (cotd(Theta_n) - cotd(Theta_e))/(2*(yN-yE));

%Solve for coeffiecient b
b = cotd(Theta_n)-2*a*yN;
bb = cotd(Theta_e)-2*a*yE;

%Solve for coeffiecient c
c = xN - (a*yN^2 + b*yN);

% Solves Profile
res3 = 0.005;
Py = ((yN+res3):res3:yE)';
Py(end) = yE;
```

```
Px = a*(Py.^2)+b*(Py) + c;
xE = Px(end);

Profile_X = [Ex1;Ex2;Px];
Profile_Y = [Ey1;Ey2;Py];

% Plots Profile
    Heading = char('Rao Bell Nozzle Contour (');
    Dts = num2str(Dt,3);
    Des = num2str(De,3);
    Ks = num2str(K,3);
    Title = strcat(Heading,'  ','Dt= ',Dts,',','De= ',Des,',','K= ',Ks,')');
    figure(1)
    hold on;
    plot(Profile_X,Profile_Y,'-ro','MarkerFaceColor','r','MarkerSize',3);
    plot(Profile_X,-Profile_Y,'-ro','MarkerFaceColor','r','MarkerSize',3);
    grid on;
    box on;
    title(Title,'fontsize',20);
    xlim([Profile_X(1) Profile_X(end)]);
    ylim([-Profile_Y(end) Profile_Y(end)]);

set(gca,'XTick',round(Profile_X(1)):round((Profile_X(end)/5)):round(Profile_X
(end)),'FontSize',20);
    set(gca,'YTick',-
Profile_Y(end):(Profile_Y(end)/5):Profile_Y(end),'FontSize',20);
    xlabel(texlabel('X (mm)'),'fontsize',20);
    ylabel(texlabel('R (mm)'),'fontsize',20);
    legend(texlabel('Rao Bell Nozzle'),'Location','NorthWest');
    legend('boxoff');
    hold off;

% Writes Profile to Excel Document
    Profile = [Profile_X,Profile_Y];
    [status,message] = xlswrite('Rao_Nozzle',Profile);
```

APPENDIX B

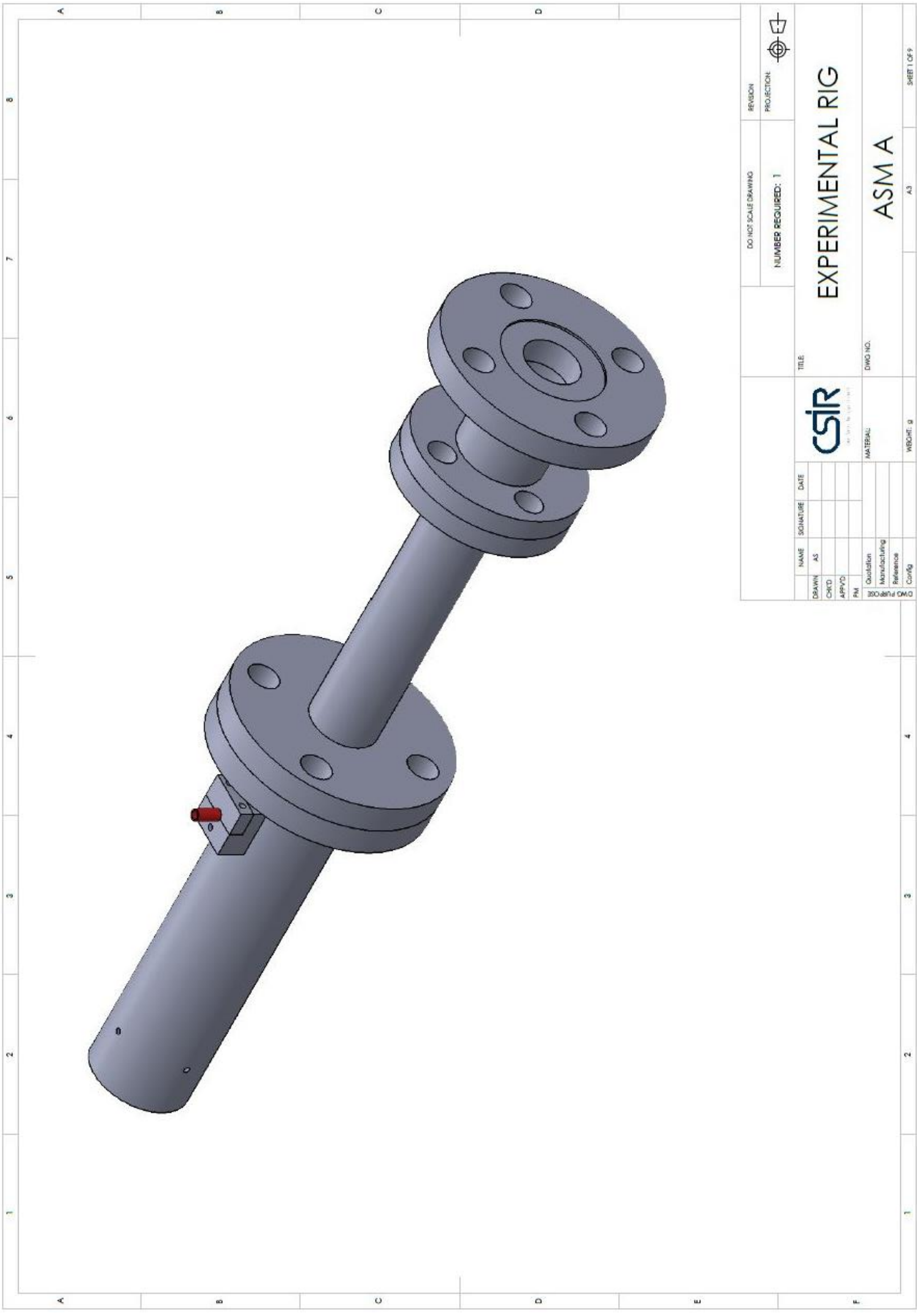
DO NOT SCALE DRAWING
REVISION
NUMBER REQUIRED: 1
PROJECTION:
TITLE:
EXPERIMENTAL RIG
DWG NO.
ASM A
A3
SHEET 1 OF 9
NAME
SIGNATURE
DATE
DRAWN
AS
CHK'D
APPV'D
PM
DWG PURPOSE
Quotation
Manufacturing
Reference
Config
MATERIAL:
WEIGHT: g
CSIR

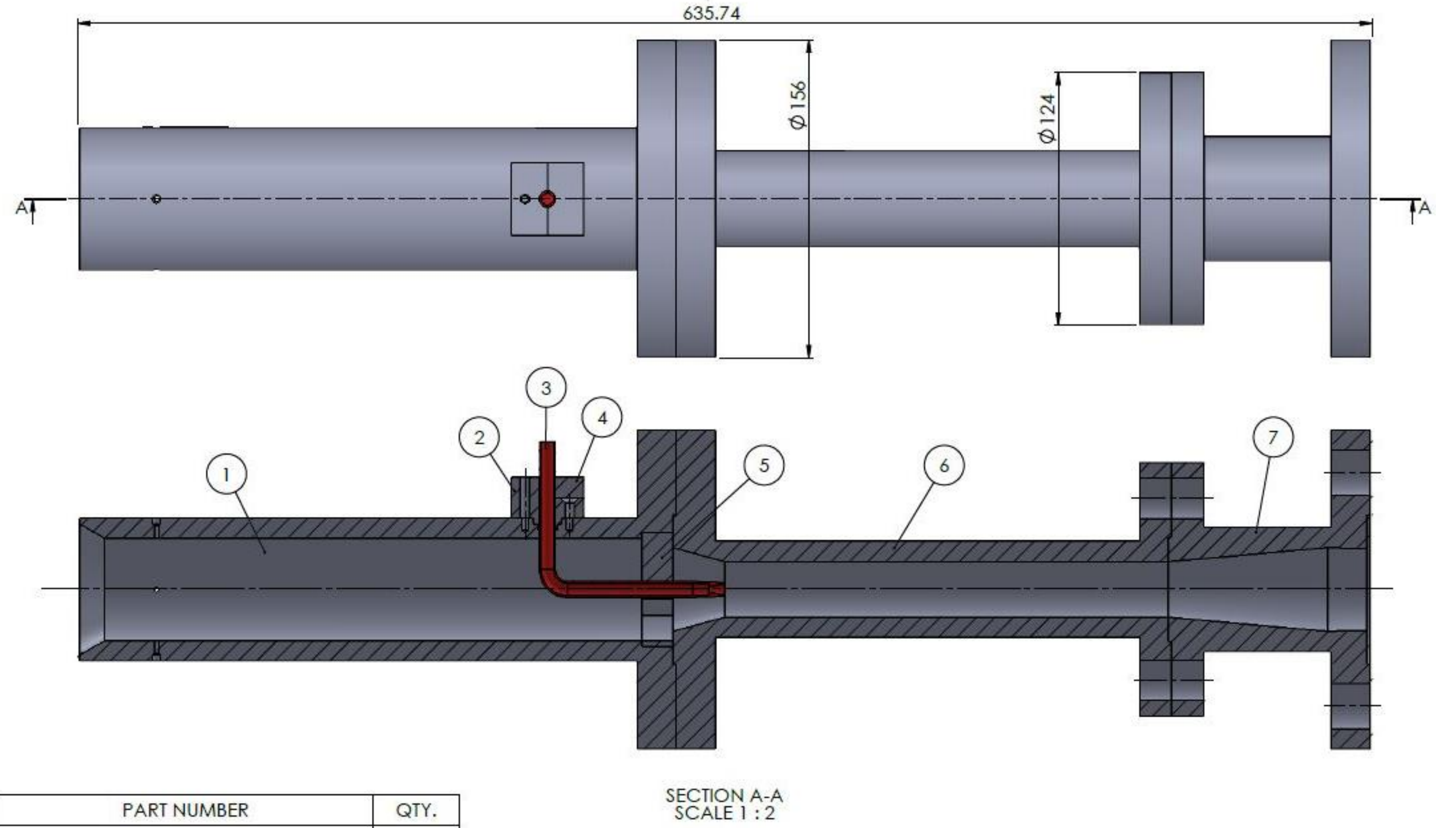

ITEM NO.	PART NUMBER	QTY.
1	Conical Inlet	1
2	Clamp Part 1	1
3	Nozzle	1
4	Clamp Part 2	1
5	Support Structure for Nozzle	1
6	Mixing Duct and Cone Inlet	1
7	Diffuser	1

DO NOT SCALE DRAWING | REVISION
NUMBER REQUIRED: | PROJECTION:

	NAME	SIGNATURE	DATE
DRAWN	AS		
CHK'D			
APPV'D			
PM			

DWG PURPOSE: Quotation / Manufacturing / Reference / Config

CSIR

TITLE: EXPERIMENTAL RIG SECTION VIEW

MATERIAL: | DWG NO. ASM B

WEIGHT: g | A3 | SHEET 2 OF 9

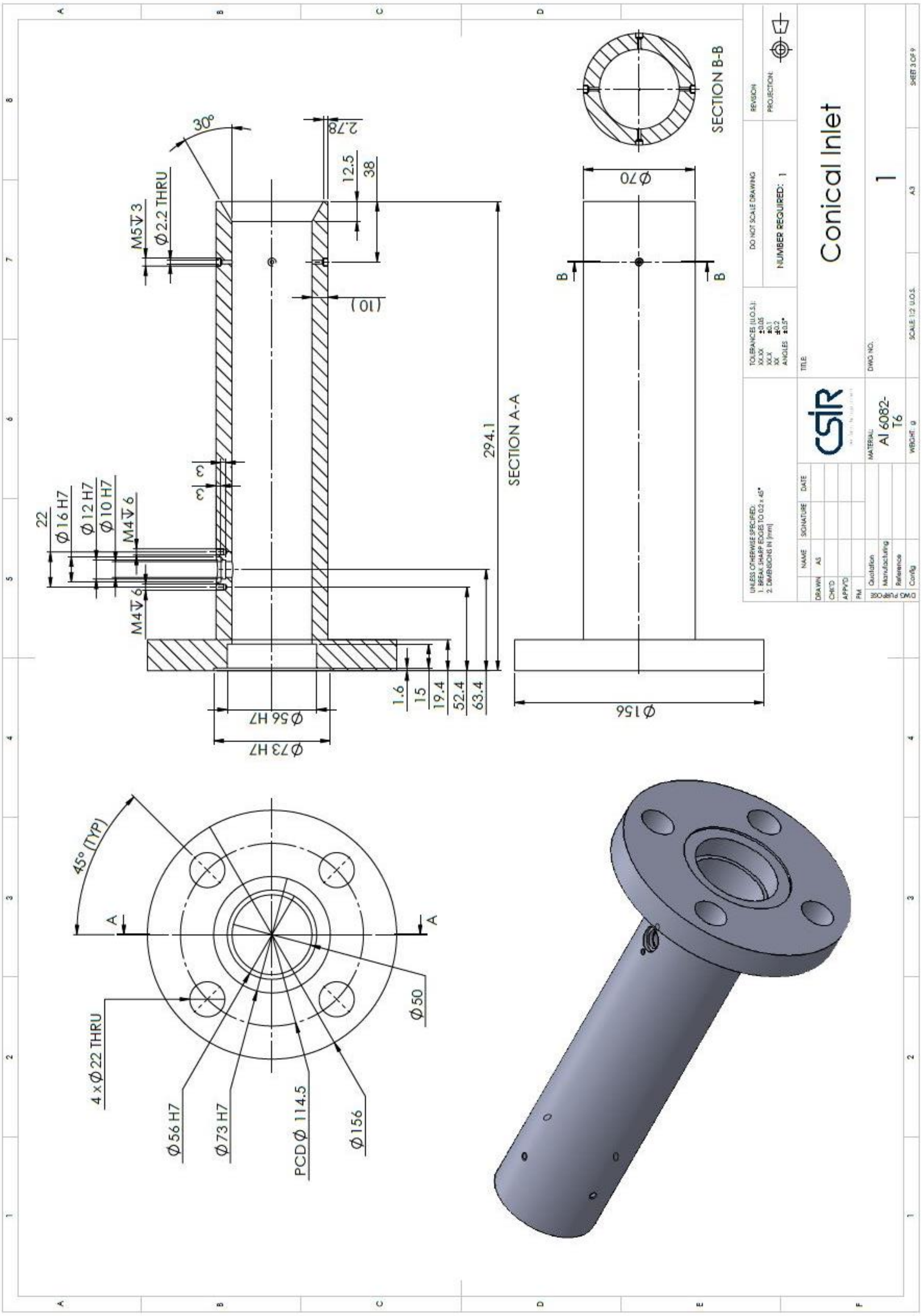

Conical Inlet
SECTION A-A
SECTION B-B
30°
2.78
12.5
38
M5 3
Ø2.2 THRU
(10)
294.1
3
3
22
Ø16 H7
Ø12 H7
Ø10 H7
M4 6
M4 6
1.6
15
19.4
52.4
63.4
Ø56 H7
Ø73 H7
Ø70
Ø156
45° (TYP)
4 x Ø22 THRU
Ø50
PCD Ø 114.5
Al 6082-T6
NUMBER REQUIRED: 1
DO NOT SCALE DRAWING

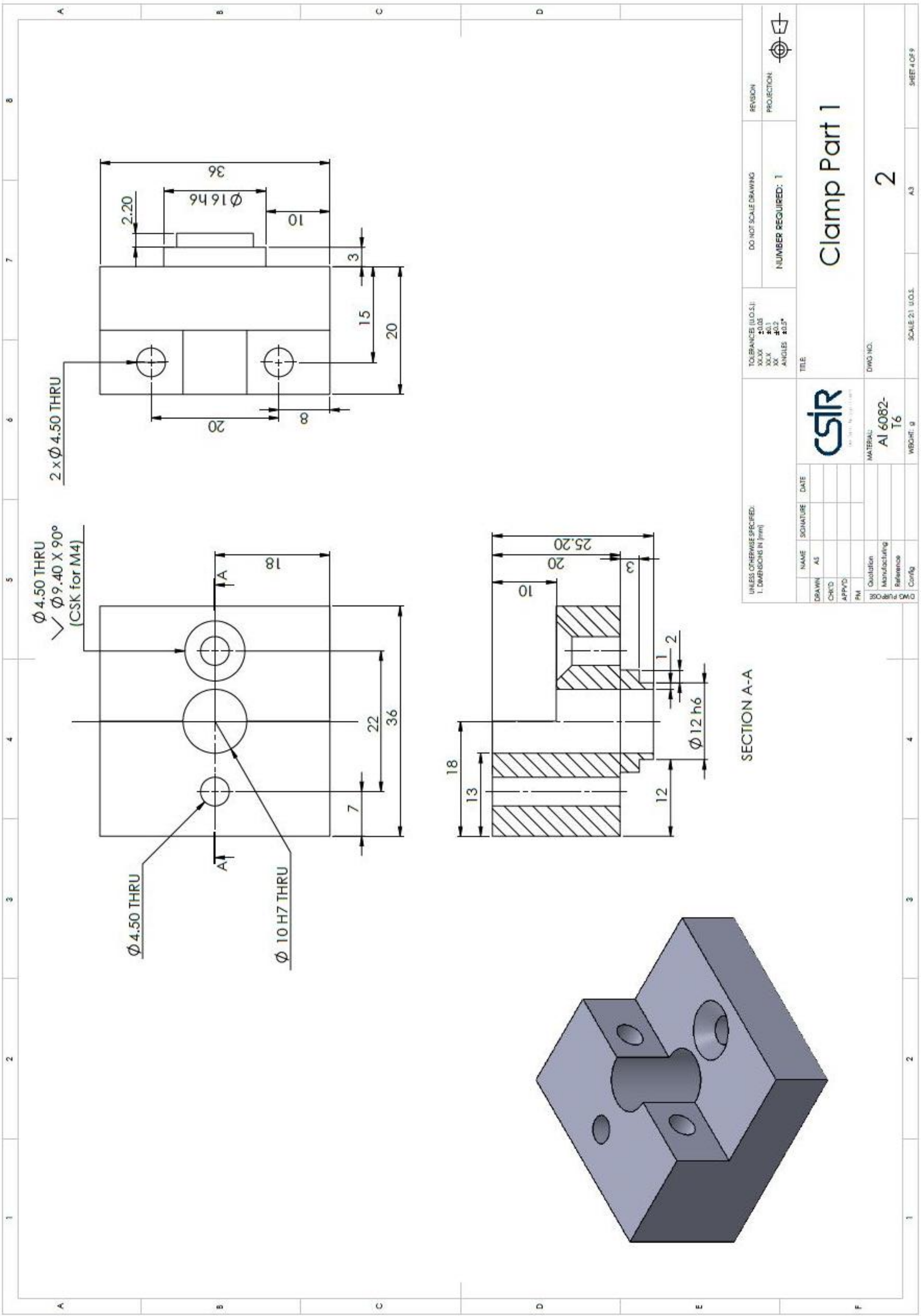

2 x Ø4.50 THRU
Ø4.50 THRU
Ø9.40 X 90°
(CSK for M4)
Ø4.50 THRU
Ø 10 H7 THRU
Ø16 h6
Ø12 h6
SECTION A-A
36
2.20
10
3
15
20
8
18
22
7
25.20
13
12
UNLESS OTHERWISE SPECIFIED:
1. DIMENSIONS IN [mm]
DO NOT SCALE DRAWING
NUMBER REQUIRED: 1
REVISION
PROJECTION:
TITLE:
Clamp Part 1
MATERIAL:
Al 6082-T6
DWG NO.
2
SCALE 2:1 U.O.S.
A3
DRAWN AS
CHK'D
APPV'D
Quotation
Manufacturing
Reference
Config
WEIGHT: g

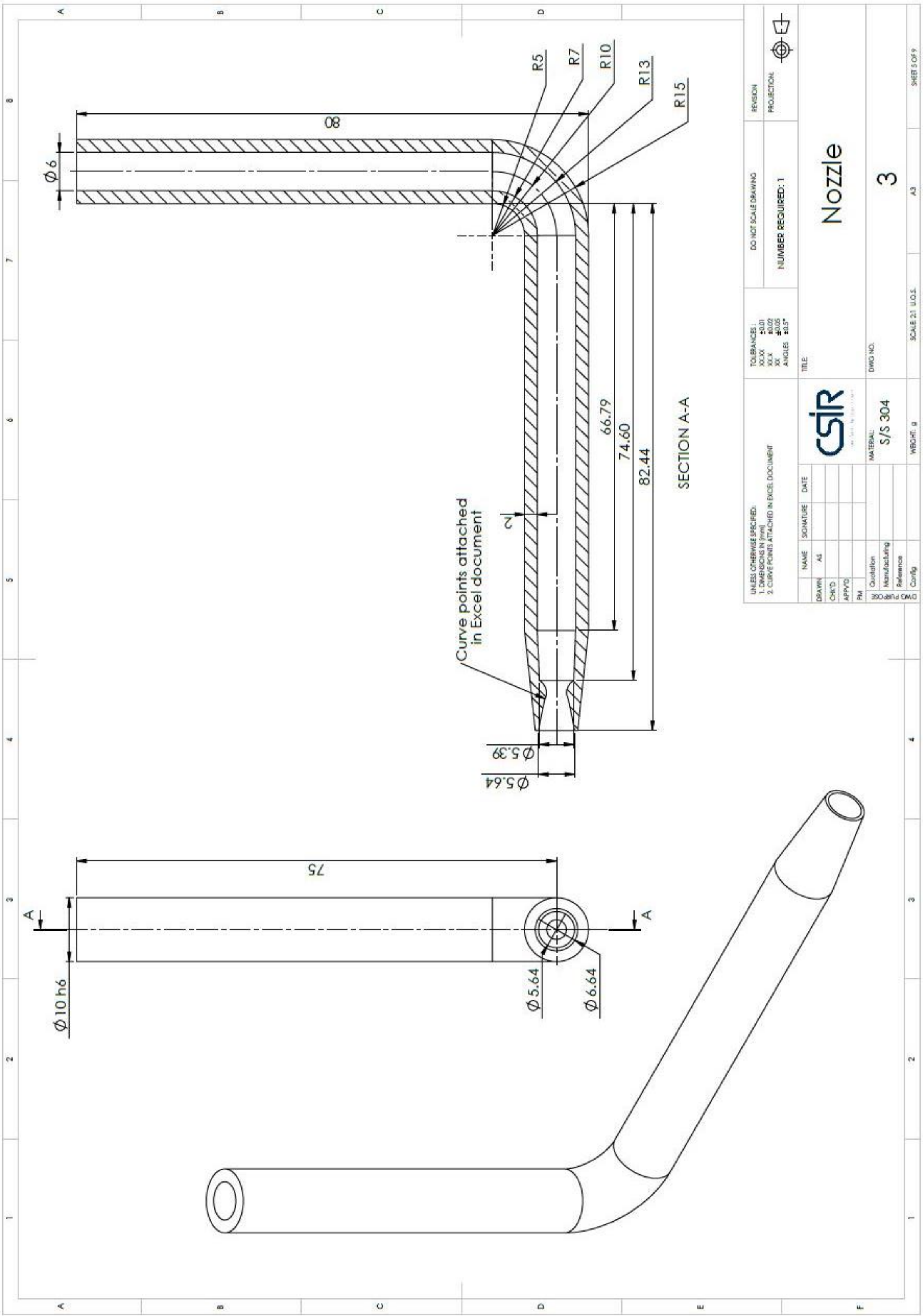
R5
R7
R10
R13
R15
80
Ø6
66.79
74.60
82.44
SECTION A-A
Curve points attached in Excel document
Ø5.39
Ø5.64
75
Ø10 h6
Ø5.64
Ø6.64
A
A
UNLESS OTHERWISE SPECIFIED:
1. DIMENSIONS IN [mm]
2. CURVE POINTS ATTACHED IN EXCEL DOCUMENT
DO NOT SCALE DRAWING
NUMBER REQUIRED: 1
REVISION
PROJECTION:
TITLE:
Nozzle
DWG NO.
3
MATERIAL:
S/S 304
WEIGHT: g
SCALE 2:1 U.O.S.
A3
DRAWN
CHK'D
APPV'D
NAME
SIGNATURE
DATE
AS
Quotation
Manufacturing
Reference
Config

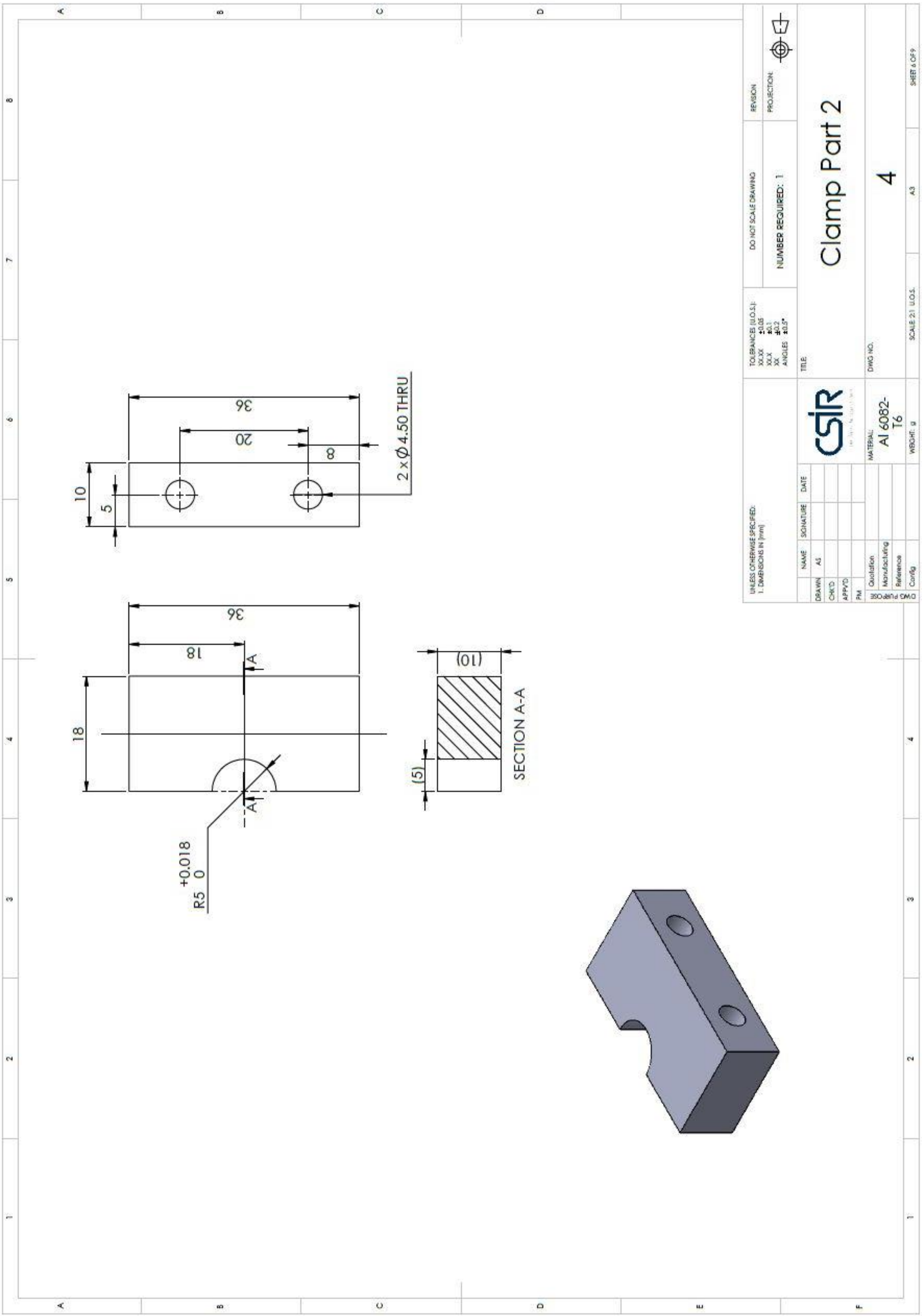
36
20
8
2 x Ø4.50 THRU
10
5
36
18
A
A
18
+0.018
R5 0
(10)
(5)
SECTION A-A
UNLESS OTHERWISE SPECIFIED:
1. DIMENSIONS IN [mm]
NAME SIGNATURE DATE
DRAWN AS
CHK'D
APPV'D
PM
Quotation
Manufacturing
Reference
Config
DWG PURPOSE
CSIR
MATERIAL:
Al 6082-T6
WEIGHT: g
TOLERANCES (U.O.S.):
XX.XX ±0.05
XX.X ±0.1
XX ±0.2
ANGLES ±0.5°
TITLE:
DWG NO.
SCALE 2:1 U.O.S.
DO NOT SCALE DRAWING
NUMBER REQUIRED: 1
Clamp Part 2
4
A3
REVISION
PROJECTION:
SHEET 6 OF 9

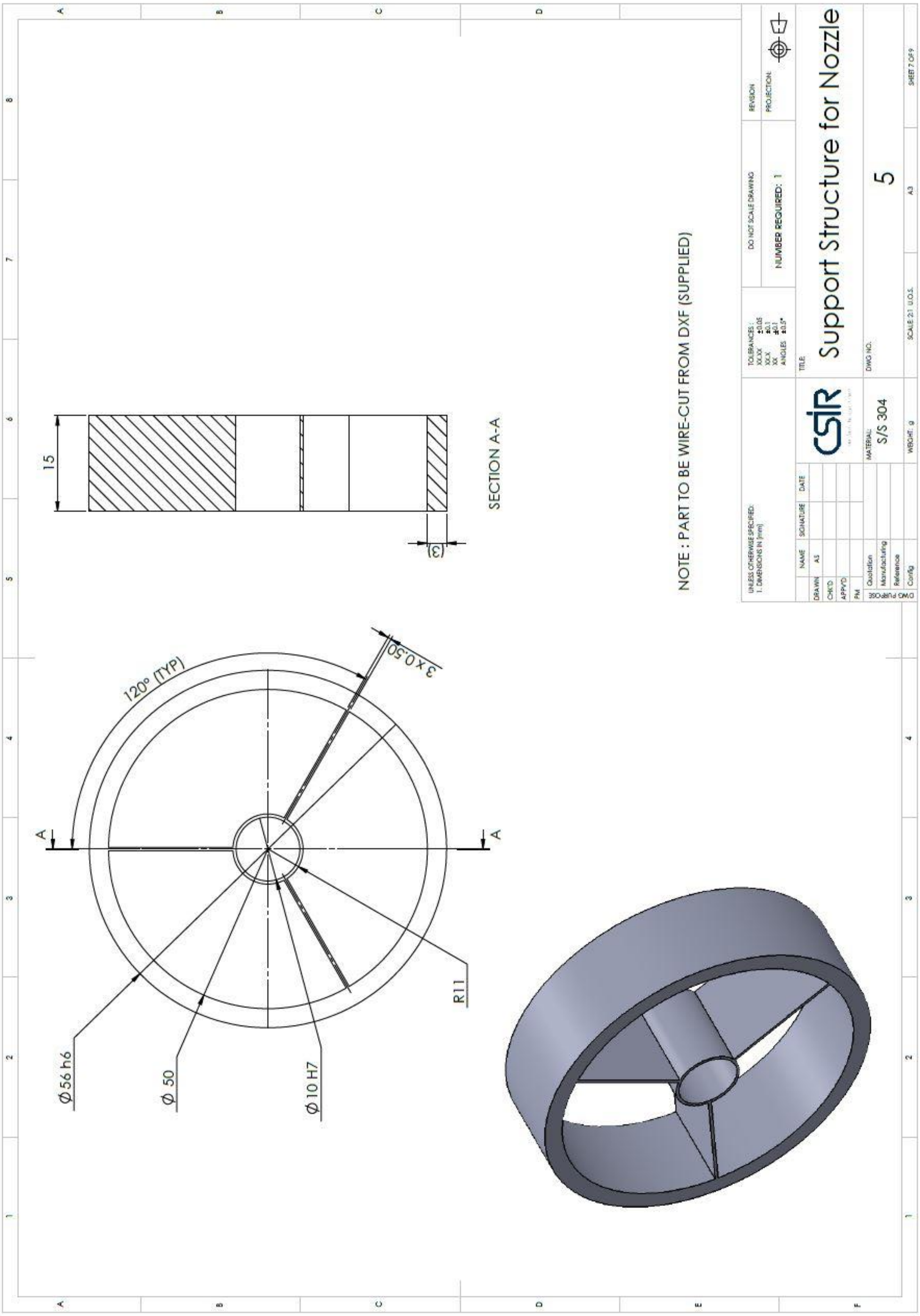

Support Structure for Nozzle
5
S/S 304
NOTE : PART TO BE WIRE-CUT FROM DXF (SUPPLIED)
SECTION A-A
15
(3)
120° (TYP)
3 x 0.50
R11
Ø56 h6
Ø 50
Ø10 H7
A
A
UNLESS OTHERWISE SPECIFIED:
1. DIMENSIONS IN [mm]
TOLERANCES :
X.X.XX ±0.05
X.XX ±0.1
X.X ±0.1
ANGLES ±0.5°
DO NOT SCALE DRAWING
NUMBER REQUIRED: 1
REVISION
PROJECTION:
TITLE:
NAME
SIGNATURE
DATE
DRAWN AS
CHKD
APPVD
PM
Quotation
Manufacturing
Reference
Config
DWG Purpose
MATERIAL:
DWG NO.
WEIGHT: g
SCALE: 2:1 U.O.S.
A3
SHEET 7 OF 9

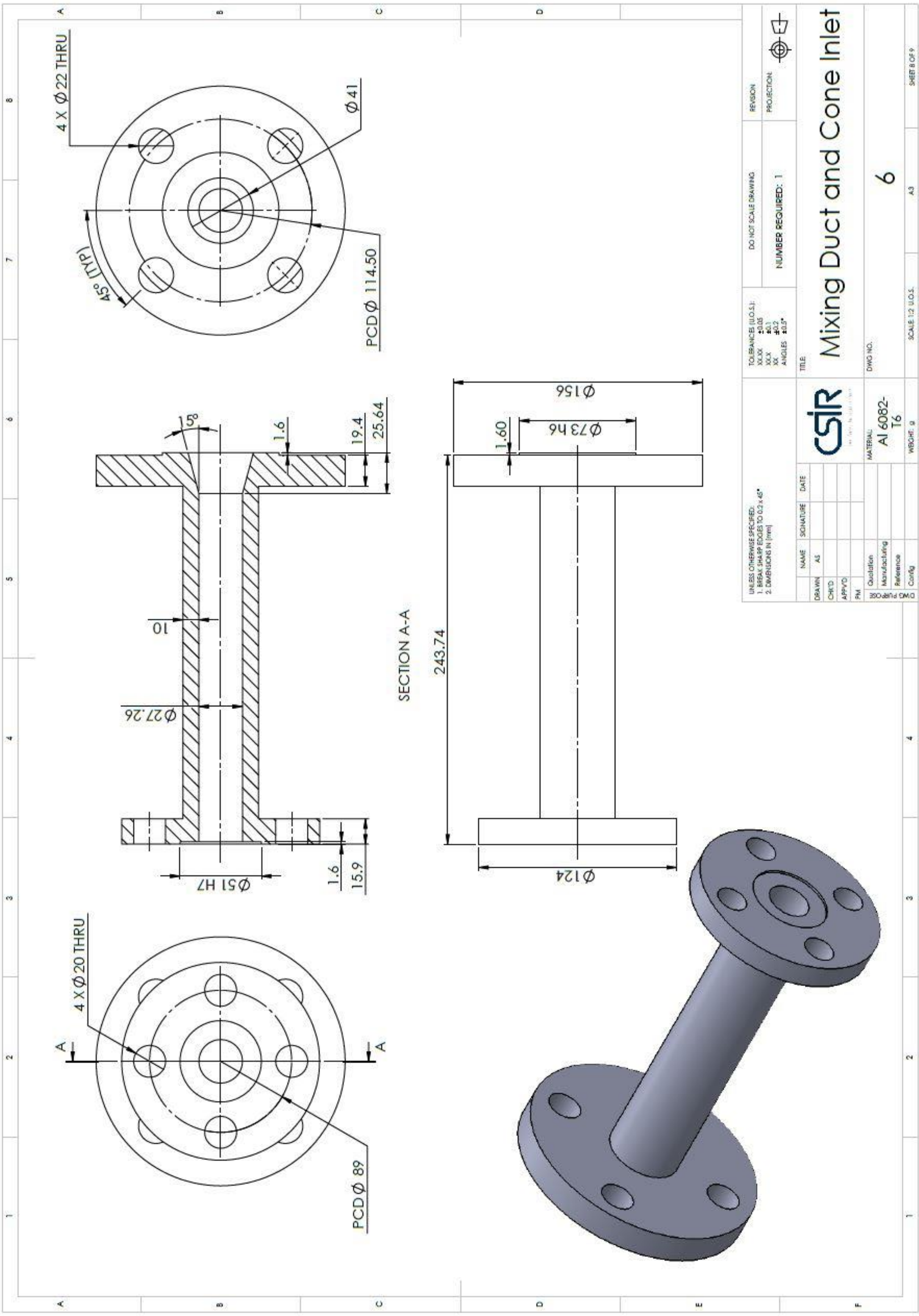
Mixing Duct and Cone Inlet
4 X Ø22 THRU
Ø41
PCD Ø 114.50
45° (TYP)
15°
1.6
19.4
25.64
1.60
Ø73 h6
Ø156
10
Ø27.26
SECTION A-A
243.74
Ø51 H7
1.6
15.9
Ø124
4 X Ø20 THRU
PCD Ø 89
A
A
DO NOT SCALE DRAWING
NUMBER REQUIRED: 1
REVISION
PROJECTION:
TITLE:
DWG NO.
6
MATERIAL:
Al 6082-T6
WEIGHT: g
SCALE: 1:2 U.O.S.
SHEET 8 OF 9
A3
UNLESS OTHERWISE SPECIFIED:
DRAWN AS
CHK'D
APPV'D
PM
Quotation
Manufacturing
Reference
Config
DWG PURPOSE

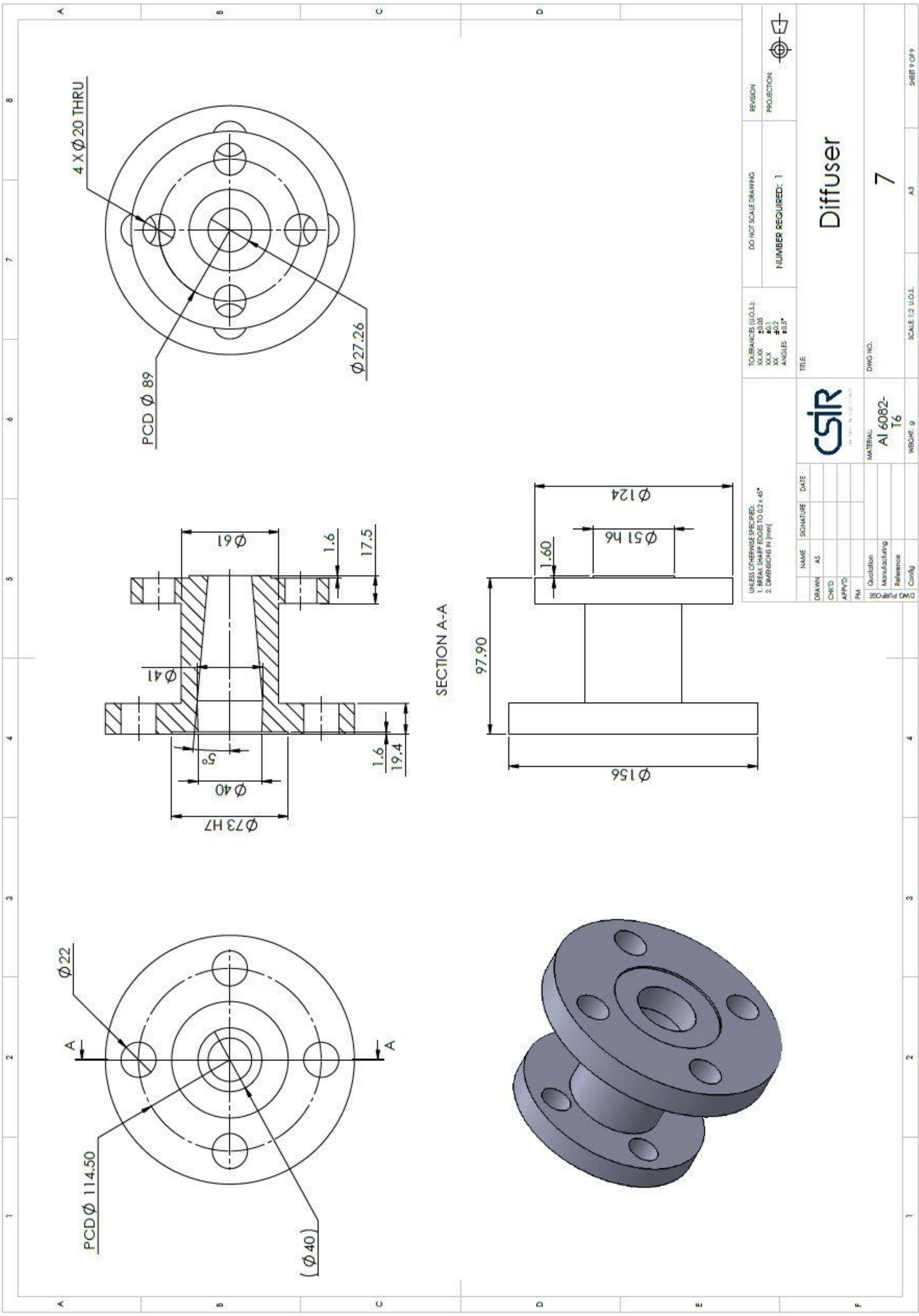

4 X Ø20 THRU
PCD Ø 89
Ø27.26
Ø61
1.6
17.5
Ø41
5°
Ø40
Ø73 H7
1.6
19.4
SECTION A-A
97.90
1.60
Ø51 h6
Ø124
Ø156
Ø22
A
A
PCD Ø 114.50
(Ø40)
UNLESS OTHERWISE SPECIFIED:
1. BREAK SHARP EDGES TO 0.2 x 45°
2. DIMENSIONS IN [mm]
DO NOT SCALE DRAWING
REVISION
PROJECTION:
NUMBER REQUIRED: 1
TITLE:
Diffuser
DRAWN AS
MATERIAL:
Al 6082-T6
DWG NO.
7
A3
SCALE 1:2 U.O.S.
SHEET 9 OF 9

APPENDIX C

C.1 Scanivalve ZOC33 Electronic Pressure Scanning Module

Scanivalve Corp.

Model **ZOC 33**

Electronic Pressure Scanning Module

Data Sheet No. G480

Features

- 0 - 50 psid pressure range
- Field replaceable pressure sensors
- 45kHz scan rates
- Duplex 128 pressure inputs with 64 pressure sensors
- On board sensor excitation

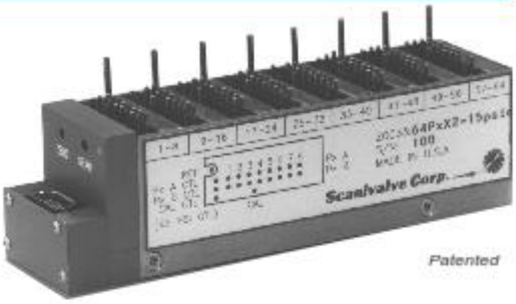

ZOC33/64Px
Pressure Scanner (shown)

General Description

The Model ZOC33 electronic pressure scanning module is extremely compact and accepts up to 64 pneumatic inputs and converts them to high level electronic signals. Each ZOC33 module incorporates 64 individual silicon pressure sensors, calibration valving, a high speed multiplexer (45kHz), and an instrumentation amplifier. An integral "duplexing" valve is available to allow the ZOC33's 64 sensors to service up to 128 input pressures.

The integral calibration valve has 4 modes of operation: operate, calibrate, purge, and leak test. Each group of 8 pressure sensors has its own calibration valving and multiplexer which allows the ZOC33 module to incorporate multiple pressure ranges and easy sensor replacement. This calibration valve allows the ZOC sensors to be automatically calibrated on-line.

The ZOC33's extremely compact design (approximately .1 cu. in. per channel) permits installation within the very confined spaces typically available in wind tunnel models.

Three versions are available:

ZOC33/64Px - 64 Px inputs each with its own dedicated sensors.

ZOC33/64PxX2 - 128 Px inputs duplexed* between 64 sensors.

ZOC33/64Px - Valveless (no calibration valve).

Applications

The ZOC33 electronic pressure scanning module is specifically designed for use in wind tunnel and flight tests where operational conditions are very space constrained and pressures do not exceed 50 psi. It is ideal for use inside small supersonic wind tunnel models.

It may be mounted in any position so the pressure sensors may be close coupled to the pressure sources to be measured. A removable header allows for easy installation and removal without breaking the pneumatic lines. When the ZOC33 is used for flight test, it must be installed in a thermostatically controlled heater jacket.

The ZOC33 module is designed to be used in conjunction with our Model ERAD4000 Remote A/D or our Model DSM3400 Digital Service Module. Each ZOC33 pressure scanner incorporates an embedded RTD to monitor the temperature of the pressure sensors. The ERAD4000 communicates via Ethernet. The DSM3400 communicates via Ethernet, RS-232, or ARINC 429.

*Duplexing shares 2Px inputs with one pressure sensor. This doubles the usefulness of a ZOC33 module without increasing the installation volume.

Px = Pressure Input

ISO 9001:2008

Specifications

Inputs (Px): 128 or 64 .042 inch (1.067mm) O.D. tubulations

Full Scale Ranges: ±10, ±20 inch H_2O, ±1, ±2.5, ±5, ±15, 50 psid (2.5, 5, 7, 17, 35,100, 350 kPa)

Accuracy:[1]

10 to 20 in.H_2O	±0.15% F.S.
1 psid	±0.12% F.S.
2.5 psid	±0.10% F.S.
5 to 50 psid	±0.08% F.S.

Sensor Addressing: 6 bit binary, CMOS level

Full Scale Output: Standard: ±2.5Vdc
Optional: ±5Vdc, ±10Vdc

Resolution: Infinite

Scan Rate: 45kHz

Operating Temperature: 0° to 60°C

Temperature Sensitivity:

Range	Zero	Span
10 inch H_2O	0.25% FS/°C	0.10% FS/°C
20 inch H_2O	0.20% FS/°C	0.08% FS/°C
1 to 50 psid	0.10% FS/°C	0.05% FS/°C

Connector Type: Cannon 15 pin MDM 15SL2P

Power Requirements: ± 15Vdc @ 110mA

Control Pressure Requirements: 65 psi instrument grade air

Overpressure Capability: (With no damage) 10 inch H_2O, 20 inch H_2O, 1 psid = 10 psi (70kPa) 2.5-50 psid = 400% or 75 psi (517kPa) (whichever is less)

Maximum Reference Pressure: 50 psig (345kPa)

Media Compatibility: Gases compatible with silicon, silicone, aluminum, and Buna-N

Weight: ZOC33/64Px: 11 ozs. (312 gm)
ZOC33/64PxX2: 13 ozs. (369 gm)

Ordering Information

ZOC33 / 64Px - 1 psid

Model

Pressure Ranges

Write "Valveless" here for this option only.

Inputs
64Px, for 64 Inputs
64PxX2, for 128 inputs
Duplexed

[1]Note: Accuracies are following a calibration with Scanivalve DSM3400 or ERAD4000 data systems.

† 10 inch H_2O = 25.4 cm H_2O = .36127 psi

‡ 20 inch H_2O = 50.8 cm H_2O = .72254 psi

Dimensions Inches (mm)

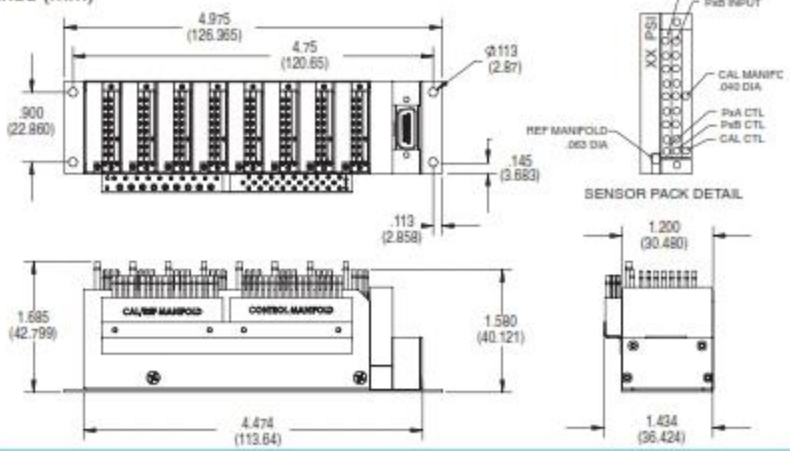

Scanivalve Headquarters
1722 N. Madson Street
Liberty Lake, WA 99019
Tel: 509-891-9970
800-935-5151
Fax: 509-891-9481
e-mail: scanco@scanivalve.com

Scanivalve Corp.
www.scanivalve.com

1106

C.2 R406 Cylinder Regulator

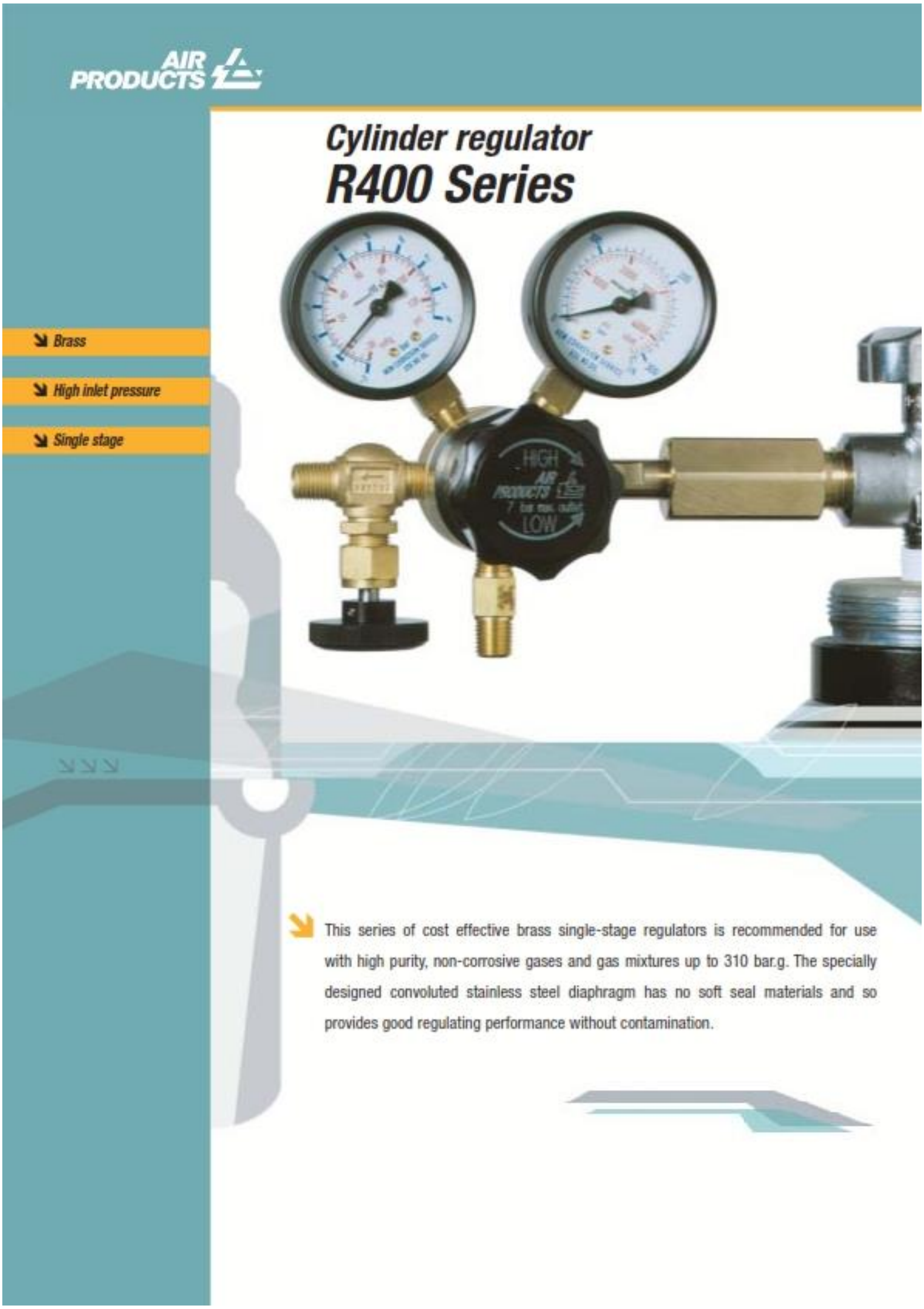

AIR PRODUCTS

Cylinder regulator

R400 Series

- Brass
- High inlet pressure
- Single stage

This series of cost effective brass single-stage regulators is recommended for use with high purity, non-corrosive gases and gas mixtures up to 310 bar.g. The specially designed convoluted stainless steel diaphragm has no soft seal materials and so provides good regulating performance without contamination.

Specifications

Material
Body: brass
Bonnet: nickel plated brass
Seat: Teflon®
Inlet filter: bronze
Diaphragm: 316L stainless steel
Gauge: brass, 64 mm diameter
Outlet valve: brass

Pressure/Temperature rating
Maximum inlet pressure: 310 bar.g
Temperature range:
-40 °C to +74 °C

Connections
Inlet: cylinder connection
Outlet: 1/4 inch NPT male
Relief valve: 1/4 inch NPT male

Flow
CV=0.06
The flow coefficient expresses the flow capability of the regulator.
CV is the flow of air in standard ft^3/min for each psi of inlet pressure.

Design leak rate
< 2 x 10^{8} mbar.l/sec He equivalent

Weight
1.8 kg

Installation dimensions
WxHxD: 220 mm x 140 mm x 125 mm

Design features

- Inlet filter for maximum reliability
- Ultrasonically cleaned for high purity gas handling
- Relief valve fitted as standard for protection against over pressurisation
- Individually tested and certified to assure maximum leak-tightness and reliability
- Panel mounting facility using 2 threaded holes in the rear of the regulator
- High standard finish

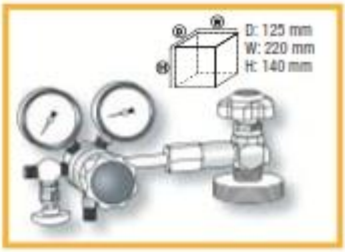

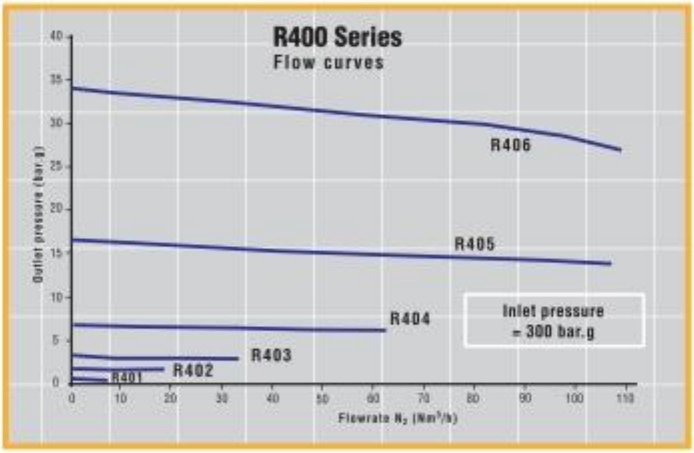

Ordering information

Order Code	Recommended outlet pressure range (bar.g)	Design capacity at maximum outlet pressure (*) (Nm^3/h)	Inlet gauge range (bar.g)	Outlet gauge range (bar.g)
R401	0.1 to 0.7	7	0 to 315	-1.0 to +1.5
R402	0.2 to 1.7	18	0 to 315	-1.0 to +3.0
R403	0.5 to 3.5	33	0 to 315	-1.0 to +5.0
R404	1.0 to 7.0	62	0 to 315	-1.0 to +9.0
R405	5.0 to 17.0	106	0 to 315	0.0 to +25.0
R406	5.0 to 35.0	108	0 to 315	0.0 to +40.0

(*) For outlet pressure drops, refer to the flow curves.

OPTIONS

- **C** Cleaning for oxygen service
- **D** Helium leak rate certification
- **E** Panel mounting kit, consists of 2 nuts
- **F** Extra 5 micron inlet filter
- **G** Purge system (see datasheet)
- **H** Compression fitting on outlet (available in various sizes)
- **M** Mounting on a back plate
- **R** No relief valve

Ireland
Air Products Ltd.
52, Broomhill Road - Tallaght - Dublin 24
Tel. : +353 (1) 463 4242
Fax : +353 (1) 463 4292
E-mail : ordergas@airproducts.com
www.airproducts.ie

United Kingdom
Air Products PLC
2 Millennium Gate, Westmere Drive - Crewe
Cheshire CW1 6AP
Tel.: +44 (0) 845 777 8800
Fax: +44 (1270) 614170
E-mail: getgas@airproducts.com
www.airproducts.co.uk

250-04-046-GB

C.3 Integral Bonnet Needle Valve

Swagelok

10/11/2017 3:29:55 AM

www.swagelok.com

Integral Bonnet Needle Valves

Part No.

SS-1RS10MM

Part Description

Stainless Steel Integral Bonnet Needle Valve, 0.73 Cv, 10 mm Swagelok Tube Fitting, Regulating Stem

Specifications

General	
Body Material	316 Stainless Steel
Cleaning Process	Standard Cleaning and Packaging (SC-10)
Connection 1 Size	10 mm
Connection 1 Type	Swagelok® Tube Fitting
Connection 2 Size	10 mm
Connection 2 Type	Swagelok® Tube Fitting
eClass (4.1)	37010203
eClass (5.1.4)	37010201
eClass (6.0)	37-01-02-03
eClass (6.1)	37-01-02-03
Flow Pattern	Straight (2-way)
Handle Color	Black
Handle Style	Phenolic Knob
Lubricant	Perf. Polyether/Tung. Disulfide (WL7)
Max Temperature with Pressure Rating	450°F @ 3435 PSIG /232°C @ 236 BAR
Orifice	0.250 in
Packing	PFA
Room Temperature Pressure Rating	5000 PSIG @ 100°F /344 BAR @ 37°C
Stem Tip Material	316 Stainless Steel
Stem Type	Regulating
UNSPSC (10.0)	40141602
UNSPSC (11.0501)	40141602
UNSPSC (13.0601)	40141602
UNSPSC (15.1)	40141602
UNSPSC (17.1001)	40141600
UNSPSC (4.03)	40141602
UNSPSC (SWG01)	40141602
Valve Material	Stainless Steel

PART NO. SS-1RS10MM

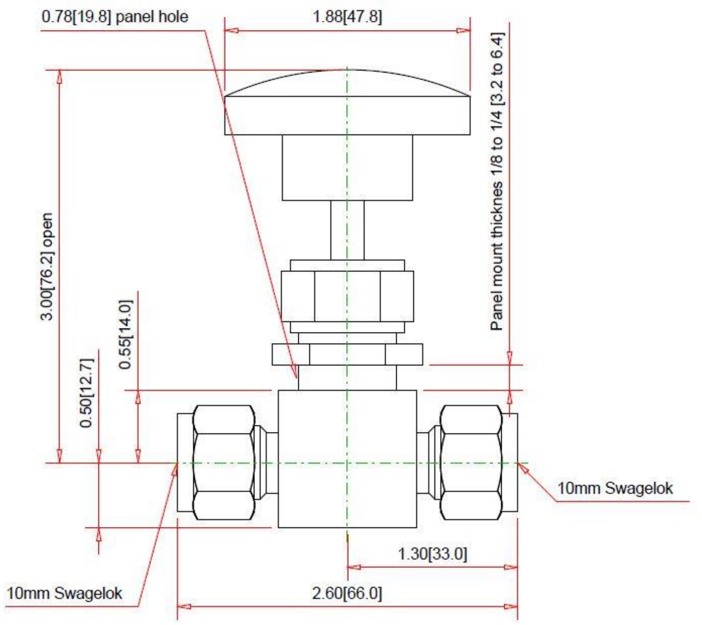

CUSTOMER DRAWING

Swagelok

- DRAWING NOT TO SCALE
- DIMENSION ARE INCHES NEXT TO [MILIMETRES]
- DRAWING IS SUBJECT TO CHANGE WITHOUT NOTICE.
- ALL ASSEMBLED NUTS AND FERRULES ARE SHOWN AT FINGER TIGHT DIMENSIONS.
- ALL HEX CALL-OUT ARE ACROSS FLATS.

TITLE: Integral Bonnet Needle Valves "O","1" & "18" Series

PART NO. SS-1RS10MM

C.4 Druck DPI620 Advanced Modular Calibrator

GE
Sensing & Inspection Technologies

DPI 620 Series

Advanced Modular Calibration and HART® Communication System

HART COMMUNICATION PROTOCOL

System Features

- Modular concept provides greater flexibility
- Re-range during use
- Expand over time
- Adapt by application
- Allows significant inventory reduction
- Simplifies user training
- Reduces cost of ownership
- A complete HART communicator and multifunction calibrator in one device

Multifunction Calibrator and HART Communicator

- Accuracy from 0.0025%rdg + 0.002%FS
- Measure, source and simulate mA, mV, V, ohms, frequency, RTDs and thermocouples
- HART digital communicator—complete device library for all HART devices
- Free-of-charge upgrades and new device descriptions
- Easy-to-use with video quality touch screen
- Hand-held PC version with Windows CE
- USB and WiFi IEEE 802.11g connectivity

GE imagination at work

Pressure Measurement Modules

- 25 mbar to 1000 bar/10 inH_2O to 15000 psi
- Accuracy from 0.005%FS
- Fully interchangeable modules with no need for set-up, calibration or tools

Pressure Generation Stations

- Advanced pressure generation
  - 95% vacuum to 20 bar (300 psi) pneumatic
  - 95% vacuum to 100 bar (1500 psi) pneumatic
  - 0 to 1000 bar (0 to 15,000 psi) hydraulic
- Stand-alone pressure stations can replace hand pumps and can be used as comparators

Applications

- Instrumentation installation, commissioning, maintenance and calibration
- HART test, configuration and calibration
- System measurement and monitoring
- Indicator, recorder and controller testing
- Process loop set up and diagnostics
- Switch, trip and safety system testing

For...

- Plant and process engineers
- Service companies and site contractors
- Installation and commissioning engineers
- Laboratory technicians

Modularity Brings a Whole New Perspective to Multi-Function Test Instruments, Calibrators and HART Communicators

The DPI 620 Series Advanced Modular Calibration and HART Communication System uses three basic components to provide the multi-functionality to perform duties formerly requiring a wide range of different instruments.

- Its basic component is an ultra-compact, electrical, frequency and temperature calibrator and HART communicator, which provides simultaneous measurement and source capabilities with full-featured HART digital interface.
- Pressure measurement is provided by interchangeable pressure modules that can be attached to the calibrator by a pressure module carrier.
- If pressure generation is required, the calibrator and pressure module can be attached to one of three pressure generation stations to form a fully-integrated pressure calibrator of unparalleled performance.

The DPI 620 - a Compact and Powerful Electrical Calibrator

The DPI 620 electrical calibrator can measure and source mA, mV, V, Ohms, frequency and a variety of RTDs and T/Cs. It provides an isolated 24V loop power supply to energize devices and control loops. A stabilized DC voltage supply is available for ratio metric transducers.

High Performance HART Communicator

The DPI 620 multifunction calibrator now incorporates a fully featured HART® communicator that surpasses market-leading communicators in functionality, ease of use and upgrade support. With the DPI 620, a single hand-held device can now configure the full range of HART devices and perform mA trims and sensor calibrations without the need for secondary equipment such as ammeters, calibrators, power supplies and loop resistors. This can significantly reduce equipment inventory, cost of ownership and greatly simplify maintenance activities. The DPI 620 contains the latest application software and a complete library of registered HART device descriptions. Upgrades can be simply downloaded free of charge from our website.

The DPI 620 CE

The Windows CE-driven version of the electrical calibrator provides all the computing power of a conventional hand-held PC or PDA. This means that operators can consult user manuals, training and safety material, datasheets, and installation drawings while in the field or in the plant.

The DPI 620 CE WiFi

The DPI 620 CE version can be further enhanced with wireless IEEE 802.11g communications. For the first time, in a calibrator of this type, it is possible to link to Internet and remote networks in order to access information and to transfer data. This powerful feature will benefit service technicians who spend extended periods away from the office and for those who need instant access to data, safety information, system drawings, and product datasheets while on the move. It will also provide an interface to future system modules when a physical connection is difficult.

Pressure Modules

The pressure modules can be used in conjunction with the relevant pneumatic or hydraulic pressure station and the DPI 620 multifunction calibrator to form an integrated pressure calibrator for test and calibration of pressure instruments including transmitters, transducers, switches, gauges, indicators and recorders

Pressure Stations

There are three pressure generation bases: the PV 621, a pneumatic pressure generator for pressures up to 20 bar (300 psi); the PV 622, a pneumatic pressure generator for pressures up to 100 bar (1500 psi); and the PV 623, a hydraulic pressure generator for pressures up to 1000 bar (15000 psi).

DPI 620 Series Accessories

- Intecal Calibration Software
- 300 V AC measurement probe
- Soft carry case
- Hard transit case
- Spare rechargeable battery
- External battery charging station
- Main power adaptor
- USB cable
- USB to RS 232 converter
- USB to IDOS converter
- Overpressure protection valves
- Pneumatic hose kits
- Hydraulic hose kits
- Pressure adaptor sets
- Comparator adaptor

www.gesensinginspection.com

920-449D

APPENDIX D

D.1 RISK ASSESSMENT

HAZARD	RISK	MITIGATION
High Pressure Air in tanks and equipment	Hoses and equipment separating; compressed air or air-borne loose items causing eye injuries	PPE – Safety glasses mandatory at all times while working with test equipment
Noise levels while testing. (Possible Noise Zone > 85dBA)	Noise Induced Hearing Loss	PPE - Ear plugs mandatory at all times while working with test equipment
High Instability of Equipment on tripods and stands	• Personal injuries to feet from falling or knocked-over items. • Damage to equipment from falling	• PPE – Safety boots mandatory at all times while working with test equipment • Cordon off test equipment with bunting tape
HGTF - Confined/limited working space and tight passage past equipment.	• Personal injuries to feet from falling or knocked-over items. • Damage to test equipment from being knocked over • Tripping hazard	• PPE – Safety boots mandatory at all times while working with test equipment • Ensure clearly demarcated passage using bunting tape • Limit access by non-test personnel • Ensure floor kept clean of non-essential equipment
High velocity air into inlet and out exit	• Damage to downstream HGTF equipment (eg. mirrors) • Damage to test equipment (instability due to the exit air stream) • Flying components may be entrained through the inlet.	• Remove all HGTF equipment upstream of test equipment • Additional weights to tripod feet if required • PPE – Safety glasses and boots mandatory at all times while working with test equipment

APPENDIX E

ESDUpac A9242 v2.0

Ejectors and jet pumps. Design and performance for compressible gas flow.

Input | Results

```
Customer 'CSIR (Motodi Maserumule)' using session id: 'csir99_1160823084042lxp'
Run at 9:49:10 AM GMT on Tuesday, August 23, 2016

 ***************************************************************************

 ESDU International plc

 Program                 A9242

 ESDUpac Number:         A9242
 ESDUpac Title:          Ejectors and jet pumps.  Design and
                         performance for compressible gas flow
                         with conical mixing chamber
 Data Item Number:       92042
 Data Item Title:        Ejectors and jet pumps.  Design and
                         performance for compressible gas flow
                         with conical mixing chamber
 ESDUpac Version:        2.0    Issued December 1993

 See Data Item for full input/output specification and interpretation.

 ***************************************************************************


                            S T A R T   O F   R U N
                            -----------------------



               *******************************************

                                  SI  UNITS
                                  ---------

                 Pressures:        kPa      Lengths:  m
                 Mass flow rates:  kg/s     Areas:    m^2

               *******************************************


GAS PROPERTIES
--------------

     The Quick Design Method is based on experimental data for air.
     The primary nozzle throat area is evaluated from equation (5.1)
     of Data Item No. 84029 with ratio of specific heats = 1.4 and
     gas constant = 287 J/kg K.
```

```
DESIGN REQUIREMENTS
-------------------

Pressure
--------

Absolute total pressure at:
        Secondary flow entry plane                          pt0 = 80.00
        Primary nozzle entry plane                          pt1 = 2000.

Mass flow rate
--------------

        Mass flow rate of secondary stream              (mdot)" =0.5556E-01
        Mass flow rate of primary stream                (mdot)' =0.3078E-01

Entry temperature
-----------------

Absolute total temperature (K) at:
        Secondary flow entry plane                          Tt0 = 313.3
        Primary nozzle entry plane                          Tt1 = 383.1

Geometry
--------

        Mixing duct length/diameter ratio              (S+L)/d4 = 8.000
        Diffuser duct exit diameter                          d5  =0.4100E-01
        Diffuser wall angle (degrees)                      phi_d = 5.000

        ---------------------------------------------------------------


                          OUTPUT OF RESULTS
                          -----------------


QUICK DESIGN METHOD
-------------------

                        *   a required design value
                        Q   derived by the Quick Design Method

  Secondary entry pressure                        pt0 = 80.00      (*)
  Primary entry pressure                          pt1 = 2000.      (*)
  Exit pressure                                   pt5 = 100.9      (Q)
  Secondary stream mass flow                  (mdot)" =0.5556E-01 (*)
  Primary stream mass flow                    (mdot)' =0.3078E-01 (*)
  Discharge mass flow                 (mdot)"+(mdot)' =0.8633E-01 (*)

  Primary pressure ratio                      pt1/pt5 = 19.83      (Q)
  Secondary pressure ratio                    pt5/pt0 = 1.261      (Q)
  Primary/secondary pressures                 pt1/pt0 = 25.00      (*)
  Mass flow ratio                     (mdot)"/(mdot)' = 1.805      (*)

***  N O T E:  Data Item No. 84029 Figure 1 is utilised forrm > 1
               where data are less reliable

Primary nozzle exit area to throat area ratio          Ae'/Ath = 3.348

***  N O T E:  Data Item No. 84029 Figure 2 is utilised forrm > 1
```

```
               where values are based on theory

Primary nozzle throat area          Ath     =0.7452E-05      (dth =0.3080E-02)
Primary nozzle exit area            Ae'     =0.2495E-04      (de' =0.5636E-02)

Mixing duct cross-sectional area    A4      =0.5838E-03      (D   =0.2726E-01)
Contraction or diffuser exit area   A5      =0.1320E-02      (d5  =0.4100E-01)

Area ratio (AR*)                    A4/Ath = 78.34
Area ratio (AR)                     A4/Ae' = 23.40
Diffuser area ratio                 A5/A4  = 2.261

Mixing duct length                  S+L     =0.2181
Diffuser length                     Ld      =0.7850E-01
Diffuser length/diameter ratio      Ld/d4  = 2.879

END OF OUTPUT  -------------------------------------------------------------
```